Modelling mechanisms of organometallic reactions from surface deposition to heterogeneous catalysis

by

Sofia Donnecke
A.B., Harvard University, 2018

A Dissertation Submitted in Partial Fulfillment of the
Requirements for the Degree of

DOCTOR OF PHILOSOPHY

in the Department of Chemistry

Modelling mechanisms of organometallic reactions from surface deposition to heterogeneous catalysis

by

Sofia Donnecke
A.B., Harvard University, 2018

Supervisory Committee

Dr. Irina Paci, Supervisor
(Department of Chemistry)

Dr. J. Scott McIndoe, Supervisor
(Department of Chemistry)

Dr. Hausi A. Müller, Departmental Member
(Department of Computer Science)

ABSTRACT

Theoretical and experimental methods are applied to study the elementary steps taking place in the gas phase and on the surface to help guide the rational design of new precursors and catalysts. The body of this work sets out to improve our fundamental understanding of the reactions taking place on various surfaces. A number of reaction pathways are modelled on the surface ranging from benchmarking the energetics of known reactions to modelling new systems and unexplored reaction pathways. Atomic layer deposition (ALD) of cobalt thin films is desirable in the fabrication of complex nanodevices and development of effective precursors requires a mechanistic understanding of the deposition pathways. The first two projects set out to understand the reactivity and deposition pathways of a number of existing and new Co precursors for ALD, and identify promising precursors to improve deposition. In a third project, the catalyzed oxygen reduction reaction (ORR) is studied to both benchmark computational methods and identify electronic trends across different metals and systems. DFT is shown to perform relatively well compared to CCSD(T) on difficult, high spin systems and modest model reduction in molecular catalysts is found to improve cost and convergence, while retaining the calculated chemical trends. A large number of reaction pathways are computed for known and new transition metal systems and the results are reported herein.

Table of Contents

List of Tables

List of Figures

List of Figures

ACKNOWLEDGEMENTS

I would like to thank:

my husband, Brett for staying up to work during these past several months, for answering countless questions about computers, for teaching me most of the python I know (starting in 2017), for pushing me to be my best, and for holding me in my lowest moments.

Irina and Scott for their mentoring, support, encouragement, and patience. I somehow won the lottery twice. They both had a profound impact on my life as a graduate student and I am very grateful to them. I will carry their advice with me well beyond my PhD.

David McGillivray and his family for their generous award. It was very special to receive the David McGillivray Scholarships in Chemistry. David McGillivray worked with my father during this PhD and he still speaks fondly of their time in the mass spec lab.

Each of us must work for his own improvement, and at the same time share a general responsibility for all humanity, our particular duty being to aid those to whom we think we can be most useful.

Marie Curie

DEDICATION

To my father, who's footsteps I followed.

Chapter 1

Introduction

1.1 Background

1.1.1 Organometallic reactions on surfaces

Innumerable natural processes take place on surfaces, spanning from capture and transport across biological membranes, to rock weathering and formation.[1] Over the past century, researchers have harnessed the gas-solid and liquid-solid reactions to perform specific functions such as carbon capture using zeolites, metal-organic frameworks (MOFs) or silicates[2, 3, 4, 5], harnessing energy in electrochemical reactions[6, 7, 8], and industrial-scale catalysis.[9, 10, 11] Unlike the bulk phase of a material, the surface is in constant equilibrium with its environment, continuously facilitating adsorption and desorption processes. A surface can host an abundance of sites with varying reactivities. The activity on each site often depends on the surface morphology and defects such as grooves and edges, which alter the saturation of the metal atoms, play a key role in the chemical activity.[12, 13, 14, 15] Catalytic processes take place on active sites where surface atoms serve as a stabilizing scaffold and electron library to facilitate molecular transformations. To increase the relative number of surface sites available to catalyse reactions, rough or porous structures, crystallite particles, and nanoparticles of the catalyst material are commonly used.[9, 11, 15]

Heterogeneous catalysis is a centerpiece for numerous important industrial processes including Haber Bosch,[16] olefin metathesis,[17] hydrogenation,[18, 19, 20] and the synthesis of many chemical reagents. Having a solid-phase cata-

lyst allows for easy separation from reagents and reuse of the catalyst after the reaction is complete. Electrochemical processes also rely on surface chemistry to facilitate reactions. In electrochemistry, two paired yet physically separated charge-transfer reactions take place, only linked by electronic and ionic conductors. Instead of transferring heat to and from the surroundings through chemical collisions, the reactants collide with the electrodes to exchange energy in the form of electricity.[6, 10] During electrolysis, endothermic reactions are driven by an electrical current to generate a desired product, while in galvanic cells a spontaneous set of redox reactions drive the current.[6] Fuel cells are a type of galvanic cell which generate electricity by harnessing the free energy from spontaneous redox reactions by a continuous source of reactants (fuel).[21, 22] H_2 is split at the anode to provide electrons to the cathode for the reduction of oxygen. The catalyzed transformation of O_2 to H_2O on the surface is the topic of Chapter 5.

Adsorption and desorption refer to the processes of association and dissociation of molecules on the surface. The adsorption and desorption properties of a catalyst have direct implications on catalytic activity.[23, 24, 25] Adsorption is further classified into two processes: chemisorption and physisorption. Physisorption occurs when a molecule becomes attached to a surface through van der Waals interactions. During chemisorption, electrons on the surface are shared with the molecule. Physisorption is often a precursor state for chemisorption[26] and physiosorbed compounds will often sample the surface until an eligible chemisorption site is encountered. In heterogenous catalysis, turnover is often determined by rate of adsorption and/or desorption.[15, 26] The barrier for desorption must be higher than the desired reaction step however low enough for the product to desorb readily. For example, selectivity for hydrogenation of ethylene on various doped Ni catalysts can be predicted by comparing the hydrogenation barrier against the desorption barrier.18 Understanding what factors govern adsorption and desorption allows for rational catalyst design for optimized performance.

Surface chemistry drives the deposition of thin films and materials. There is a growing demand for the fabrication of materials possessing specific electronic and optoelectronic properties for energy conversion, semiconductor applications, and magnetism.[27, 28] Heterojunction solar cells, transistors, and circuits are all examples of devices that exploit materials formed by surface deposition and/or etching methods. Physical vapor deposition (PVD) proceeds through physisorption while chemical vapor deposition (CVD) harnesses chemisorption to deposit

layers onto a substrate surface. However, these “line of sight” methods offer little control over layer thickness and uniformity, and films often suffer from defects (ie. shunting).[29, 30] With increased knowledge over the chemical processes that occur on the surface comes increased ability to tune and control the deposition process. A method which harnesses chemical knowledge to offer the most control over uniformity, thickness and selectivity of a deposited thin film is atomic layer deposition (ALD).

1.1.2 Atomic layer deposition

Atomic layer deposition (ALD) is a cyclic gas phase deposition technique used to grow highly conformal layers of an inorganic material.[31, 32] The birth of ALD is largely credited to Finnish scientist Suntola in 1974 for patenting atomic layer epitaxy (ALE).[33] However, a technique coined molecular layering emerged in the Soviet Union in the 1960’s which remained unrecognized by the scientific communities in Europe and North America until recently.[34, 35] ALD is becoming the deposition method of choice for the fabrication of complex semiconductor materials and microelectronic devices around the globe[31, 36, 37] because it offers new possibilities for advanced nanopatterning through selective deposition[38, 39, 40] and deposition onto high aspect ratio substrates.[32, 41]

What sets ALD apart from other thin film fabrication techniques such as chemical vapour deposition (CVD) are the discrete steps and self-limiting surface reactions which take place. An ALD cycle entails the deposition of a gas phase precursor followed by the introduction of a co-reactant, separated by a purge or rinse step (Figure 1.1). In step 1, the gas phase precursor is introduced into the ALD chamber and coordinates to available surface sites. Once deposited, a well-designed ALD precursor will self-limit deposition to one molecular layer per cycle by retaining enough ligands to shield the metal center from remaining gas phase species. Once the surface sites are fully occupied, the remaining gaseous species are evacuated from the chamber (step 2). Step 3 marks the second half-cycle which involves either cleaving the remaining ligands from the surface-bound precursor, introducing a second precursor for multi-elemental films or, in the case of thermal ALD, heating the film.42 To remove the remaining ligands, a reactive co-reagent is introduced into the chamber to reduce the metal center. However, step 3 can also involve exposure to high temperatures (thermal ALD) or plasma (plasma

assisted ALD) to scrub auxiliary species from the surface. In the final step, the chamber is once again evacuated to remove gas phase species previously generated, leaving behind an atomic layer of material. These series of steps form one complete ALD cycle which can be repeated to achieve a desired film thickness. The self-limiting deposition mechanism allows for uniform thin films to be grown on high aspect structures with thickness control down to the Angstrom level.[31, 42]

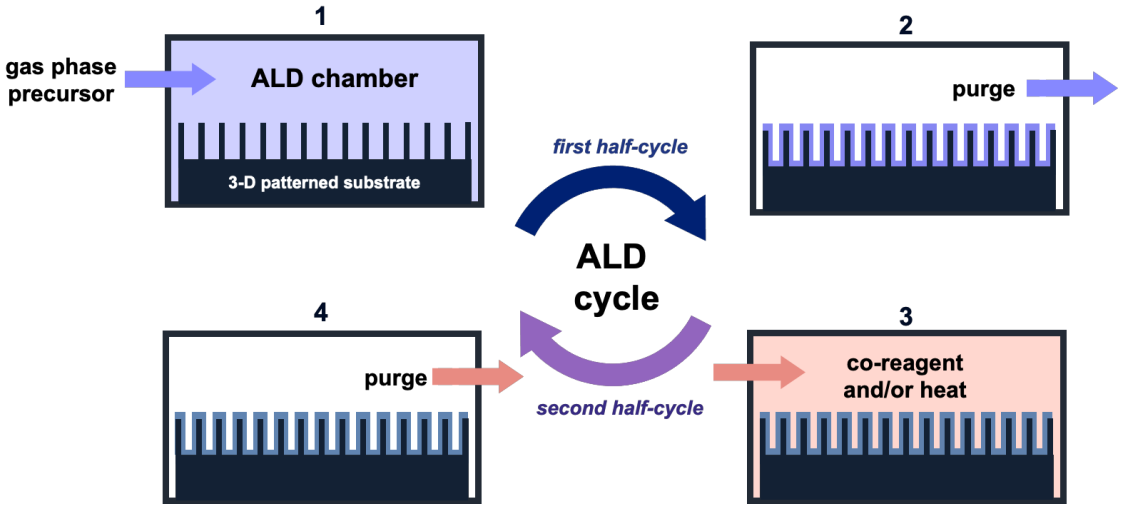

Figure 1.1: Schematic depiction of an ALD cycle with numbered steps which can repeated until a desired film thickness is achieved.

While ALD offers high precision it is an expensive process where a large portion of the precursor dosage becomes waste.[43] Thus, there is a need to maximize the efficiency of precursor deposition by improving targeted reactivity towards the surface. Moreover, despite the growing popularity and demand for the technique, ALD mechanisms remain poorly understood[44, 45] and there are only a limited number of known reaction pathways for ALD.[31] The rational design of new successful metal ALD precursors requires a detailed understanding of the deposition mechanisms.[44, 46, 47]

A number of studies have accomplished *in situ* monitoring of deposition to monitor growth rate, reaction products, surface species and film properties such as thickness using methods such as quartz crystal microbalance, infrared spectroscopy (IR), quadrupole mass spectrometry (QMS), and spectroscopic ellispometry. [48, 49, 50, 51, 52, 53, 54, 55, 56] Goldstein et al.[57] performed *in situ* monitoring of Al_2O_3 ALD using Fourier transform infrared (FTIR) spectroscopy to characterize surface species along with QMS to track gas-phase products from the

reaction of O_3 with $AlMe_3$. However, conventional characterization takes place *ex situ*, after deposition is complete or between cycles.[48]

Spectroscopic methods including X-ray photoelectron spectroscopy (XPS), IR and Raman are commonly used to characterize the chemical environment on the surface while microscopy methods such as atomic force microscopy (AFM) and scanning electron microscopy (SEM) can be used to characterize the morphology of surface layers.[49, 58, 59, 60] For depositing multielemental layers, observing which types of bonds are formed on the surface reveals information about the bonding environment and potential side-reactions that take place.

Computational chemistry is an emerging method for supplementing experimental methods applied to advance ALD precursors. Simulations offer molecular level insight and feedback for predicting the elementary steps during deposition.[61, 62, 63, 64, 65, 66] Moreover, chemical trends can be used to predict and screen more stable, and/or effective precursors.[67, 68] The capabilities of modern materials chemistry software allow researchers to simulate realistic surfaces to obtain information about adsorption energies, reaction intermediates, activation barriers, thermal stability, and electronic properties. These methods will be discussed in Chapter 2.

1.1.3 Cobalt and ALD

The deposition of metallic cobalt has important applications in microelectronics. Atomic layers of Co can act as a diffusion barrier between interposed materials, preventing charge drift across material junctions, or as a seed layer at interfaces with poor adhesion such as Cu, an important conductor material, and SiO_2.[44, 69, 45] Metallic cobalt is also a desirable material for semiconductors, spintronics and super-magnetoresistance in memory storage devices.[70, 71] $CoSi_2$ also serves as a common contact material in microelectronics where Co deposited and then annealed on Si contacts.[44, 45] These applications require the deposition of highly uniform Co layers onto high aspect-ratio surfaces, a task well-suited to ALD. The layout of microelectronic devices is rapidly shrinking towards the nanoscale, and thus the demand only grows for the function and precision offered by ALD for Co precursors.

As mentioned, there are only a handful of known ALD precursors and fewer still proposed reaction pathways for the deposition of cobalt.[44, 59, 45, 72, 73, 74]

While deposition of Co onto metal surfaces remains fairly straightforward, deposition onto Si and SiO_2 have posed challenges.[69] The optimal conditions for deposition are unique to each compound being deposited, thus precursor design continues to limit the substrates that can undergo ALD.[31, 47] Cobalt is particularly challenging to deposit as a pure metal because of its relatively low reduction potential.[44, 45, 66] Metals with more negative electrochemical reduction potentials require stronger reducing agents during the second half-cycle (Figure 1.1) to reduce them to metals at the surface.

Despite their inherent uniqueness, successful metal ALD precursors share a number of basic qualities including: adequate volatility such that the substrate temperature is higher than that required to evaporate the precursor, sufficient thermal stability throughout the ALD process, reactivity which results in only volatile by-products and, of course, reasonable reaction yields.[75] As the demand for depositing Co grows more diverse and broad across different applications, identifying precursors which are most suited for ALD onto a specific substrate will increase efficiency, decrease waste and improve the quality of thin films deposited.

Cobalt precursors have been tested for ALD with varying success (Figure 1.2).[76] In particularl, cobalt carbonyl complexes have gathered attention as promising precursors due to well-established syntheses, their relatively good volatility, and the easy cleavage of carbonyls as neutral species.[77, 78, 79, 80] While most proposed Co precursors have an oxidation state of +1, oxidation state ranges between 0 (**A**) and +2 (**D**, **F**). While uncommon, trivalent Co(+3) species have been tested for ALD as well.[76] For precursor **A**, a reducing agent is not required; instead, an annealing step above 125 °C after adsorption is performed to bake off remaining ligands. For precursor **B**, the key parameter to deposition was the partial pressure of the coreagent, H_2.[58] For Co(+2) complexes, formic acid has been used to reduce the metal center.[81] Other common reducing agents used includes H_2 (sometimes in combination with plasma) hydrazine, and ammonia.[76] In some cases, a finely tuned mixture of H_2/NH_3 has shown to affect deposition (ie. for precursors **D** and **F**).[82, 83]) While deposition onto metal surfaces works well, limited success with Co deposition onto SiO_2 drives a demand for precursors with better reactivity towards SiO_2.[76, 84, 39, 85] The use of silyl-based ligands has shown some success over simple alkyl groups in depositing low-resistivity Co metal films without the use of a co-reagent.[86] Cobalt-silyl complexes will be the primary focus of Chapter 4.

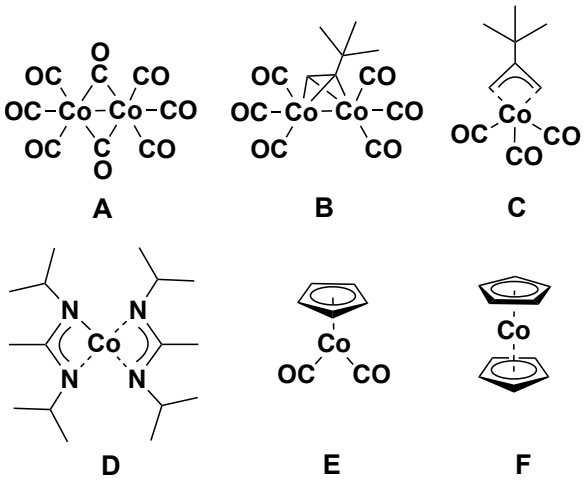

Figure 1.2: Examples of cobalt precursors that have been proposed and tested for ALD. **A** shows $Co_2(CO)_8$, **B** shows tBu-Acetylene-dicobalthexacarbonyl,[72] **C** shows tBu-AllylCo$(CO)_3$,39 **D** is bis(N,N'-diisopropylacetamidinato)cobalt,[87] and **E** and **F** show CoCp$(CO)_2$ and Co$(Cp)_2$.[84]

There are multiple studies that have harnessed computational chemistry and ex situ experimental methods to deduce Co ALD reaction pathways. Kim et al.[59] deposited cobalt carbonyl (**A**) onto Si(100) substrate by remote plasma ALD and examined the impurity content by Auger electron spectroscopy (AES). They found that incomplete decomposition of the Co-CO bonds resulted in carbon and oxygen incorporation into the Co film which in turn suppressed the formation of the desired $CoSi_2$ layer in a subsequent annealing step. Kwon et al.[72] used IR spectroscopy to characterize the bonds formed on SiO_2 and Si surfaces after ALD with CCTBA (**B**). Bridging carbonyls were observed during intermediate steps of the ALD process on Si(111). However after the final ALD step, Co$-$Si bonds were observed on Si(111) and Co$-$O bonds on SiO_2(111). Another observation on Si(111) was the incorporation of C-Si bonds, suggesting that hydrosilation is taking place with the terminal alkyne. Subsequent growth was inhibited on sites occupied by carbon species. They also noted that deposition onto SiO_2 required much higher temperatures and resulted in more impurities over the course of multiple cycles. In Chapter 3, the experimental and computational results from modifying CCTBA to suppress unwanted reactivity of the alkyne are discussed. In another study, Kwon et al.[39] investigated the deposition of ^{t}Bu-AllylCo$(CO)_3$ (**C**) using AFM, XPS and computational methods. They measured a striking selectivity for the Si(111) over the SiO_2(111) surface during Co deposition. Simulated reaction pathways show an

energy difference of over 0.8 eV for initial chemisorption steps on Si versus SiO_2 which is largely attributed to the thermodynamic difference in activating a Si−H surface bond versus the O−H surface bond.

The theme of poor reactivity between Co ALD precursors and SiO_2 is pursued in Chapter 4. Although the positive reduction potential of cobalt limits the reactive nature of the metal center, a molecular design which targets specific deposition mechanisms can help overcome the lack in reactivity on silica substrates. In Chapter 4, a set of ALD precursors specifically target reactivity with a SiO_2 substrate. Understanding the deposition pathways of existing precursors can propel the design of improved or specialized precursors. Broadening the scope of cobalt ALD will open the opportunity for more industrial applications and allow the design of smaller and more complex devices. This thesis is motivated by the opportunity and need for the rational design of cobalt precursors (Chapters 3 and 4) and catalysts (Chapter 5) using computational chemistry.

1.2 Agenda

Chapter 1 has introduced background and the motivation for this research. A general background on the facets of organometallic surface chemistry is given from a brief discussion of heterogeneous catalysis, the basics of adsorption and desorption processes followed by an introduction to atomic layer deposition (ALD). ALD of Cobalt is then introduced along with a discussion of current progress and ongoing challenges in the field.

The methods used in this dissertation are introduced in **Chapter 2**. A general overview of computational chemistry along with the selection of computational chemistry methods applied to simulate various types of chemical systems are explained. A background of the mass spectrometric methods used to monitor reactions in real-time follows the quantum computational section.

Chapter 3 describes the first project which studies the gas phase decomposition of two cobalt carbonyl alkynyl precursors using the mass spectrometric and computational methods that were introduced in Chapter 2. Kinetic experiments were also conducted by reaction monitoring to compare the formation of the two Co precursors. Finally, simulations of precursor deposition onto the silicon surface showed were used to compare the reactivities of the metal center. NEB was ap-

plied to show the decreased reactivity of the modified alkyne ligand and suggests this ligand may lead to lower amounts of carbon impurities.

Chapter 4 is a computational study on a set of silyl-based Co ALD precursors and their deposition mechanisms onto various surfaces. These precursors offer an alternative deposition pathway during ALD on SiO_2 which has not been explored. Results show promising energetics for deposition onto silica through this new pathway.

Methods for simulating the catalytic conversion of oxygen to water are benchmarked in **Chapter 5**. This work was conducted during an internship in collaboration with OTI Lumionics in an effort to benchmark their quantum algorithm for describing the electronic structure of small high spin systems. This work is ongoing, however we also achieved extensive results from DFT benchmarking of atomic, molecular and periodic catalyst systems. The results and computational trade-offs of various methods and systems are discussed.

A collection of shorter projects and collaborations are assembled in **Chapter 6**. Simulations of transitions states of molecular catalysts were performed to pair with experimental work done by collaborators. Python tools created for kinetic analysis and generating figures are also summarized in this chapter.

Finally, **Chapter 7** concludes the dissertation, summarizes its contributions to the scientific community and reflects on the lessons learned from simulating a large variety of organometallic reaction pathways.

Chapter 2

Methodology

Theoretical chemistry lends itself well to understanding the chemical processes taking place on the surface. Calculations can identify stable geometric arrangements of atomic nuclei and the relative energies of these structures can be used to gain information about their reactivity. Furthermore, molecular properties such as electronic spin, dipole moments and stability can be assessed. Providing information before any experiments are conducted in a lab provides valuable chemical insights to help direct synthetic targets and understand key mechanisms.

Selecting a suitable level of theory to describe a system and evaluating the quality of the results lies at the center of theoretical chemistry. To simulate atoms with multiple electrons, let alone many interacting atoms making up molecules, means tackling the many-body problem. The implementation of several approximations has made chemical problems tractable on classical computers. The computational chemist must regularly deliberate the trade-off between accuracy and system-size (or computational cost).

This dissertation tackles many transition metal systems, ranging from surfaces to molecules to single atom catalysts. Hence, a variety of computational methods are used to describe these systems as well as to benchmark the results. While density functional theory remains the method of choice because of its reliability and scaling, wavefunction methods provide a way to prepare the Hamiltonian of a system for emerging quantum algorithms. Furthermore, DFT and wavefunction methods in combination produce some of the most reliable and accurate electronic structure calculations of molecular systems.

2.1 Quantum chemistry

At the molecular level, electromagnetic interactions dictate the behaviour of particles, which is captured in Coulomb's law.[88] The Coulombic equation is an expression of potential energy as a function of distance,

$$V_{Coulomb}\left(r_{ij}\right) = \frac{q_i q_j}{r_{ij}}$$

where r_{ij} is the distance between two charged particles and q is the charge of the particle. The total energy of a chemical system is the sum of the kinetic and potential energies of all particles constituting the system. The distinct interacting particles are electrons and nuclei and therefore the molecular Hamiltonian becomes

$$H_{tot} = T_e + V_{ne} + V_{ee} + V_{nn} + T_n$$

The potential energy terms arise from the interactions between each type of particle where V_{ne} is the coulombic interaction between the nuclei and the electrons, V_{ee} is the interaction between the electrons and V_{nn} is the interaction between nuclei.

$$V_{ne} = -\sum_i \sum_j \frac{Z_i e^2}{4\pi\varepsilon_0 \left|R_i - r_j\right|}$$

$$V_{ee} = \sum_i \sum_{j>i} \frac{e^2}{4\pi\varepsilon_0 \left|r_i - r_j\right|}$$

$$V_{nn} = \sum_i \sum_{j>i} \frac{Z_i Z_j e^2}{4\pi\varepsilon_0 \left|R_i - R_j\right|}$$

where e is the elemental charge of a particle, Z is the atomic number which corresponds to the number of protons in the nucleus, R and r are the nucleic and electronic positions and $\frac{1}{4\pi\varepsilon_0}$ is Coulomb's constant containing the vacuum permittivity, ε_0. Note that V_{ne} is an attractive term and the negative sign comes from the elemental charge q of an electron and the protons in the nucleus having opposite signs.

To allow for separation of variables, the kinetic energy must be expressed as a function of a particle's coordinates and momenta rather than their velocities as they are in $\frac{1}{2}mv^2$. The linear momentum operator of a quantum particle is $p = \left(\frac{\hbar}{i}\frac{\partial}{\partial r}\right)$.

Substituting this operator into the expression of kinetic energy in terms of p and r yields

$$\frac{1}{2}mv^2 = \frac{p^2}{2m} = \frac{1}{2m}\left(\frac{\hbar}{i}\frac{\partial}{\partial r}\right)^2 = -\frac{\hbar^2}{2m}\left(\frac{\partial}{\partial r}\right)^2$$

As a result, the kinetic energy operators for the nuclei (T_n) and electrons (T_e) of a system respectively are

$$T_n = -\frac{\hbar^2}{2M_i}\sum_i \nabla_i^2$$

$$T_e = -\frac{\hbar^2}{2m_e}\sum_i \nabla_i^2$$

Where $\hbar$ is Planck's constant, M_i is the mass of the nucleus or m_e the mass of an electron and ∇_i^2 is the Laplace operator of particle i,

$$\nabla_i^2 = \frac{\partial^2}{\partial x_i^2} + \frac{\partial^2}{\partial y_i^2} + \frac{\partial^2}{\partial z_i^2}$$

One measure to greatly reduce the many-body problem is to apply the Born-Oppenheimer approximation[89] which solves the motion of the nuclei and electrons separately. Because of the difference in mass between an electron and the nucleus, there is a large separation in their dynamical timescales. The positions of the nuclei can essentially be considered fixed when assessing to the motion of an electron. Therefore, the electronic Hamiltonian H_e can be solved in terms of a stationary set of nuclei,

$$H_e = T_e + V_{ne} + V_{ee} + V_n$$

and the electronic potential obtained subsequently contributes to the motion of the nuclei. The Born-Oppenheimer approximation excels in systems with heavier nuclei, however even in the case of lighter atoms such as the hydrogen molecule, or when multiple solutions to the Schrodinger equations exist close in energy.[90, 91]

There are several methods of modelling chemical systems within computational chemistry. Molecular models span from classical modelling, which wrap the electronic and nucleic charges into a single classical potential, to quantum methods including semi-empirical or *ab initio* wavefunction methods and density function theory (DFT). To describe bonds breaking and forming, the electrons involved in

these interactions must be treated separately from the nuclei which demands a quantum mechanical approach.

2.1.1 Wavefunction methods

Hartree-Fock (HF) theory is central to *ab initio* methods,[92, 93] in which each electron is described by a single orbital and the full wavefunction is the combination of those orbitals. By addressing electron repulsion term with a mean-field interaction depending only on the electron's position, the equation describing each electron becomes separable into n hydrogen-like equations. The HF solution must be sought iteratively through the self-consistency cycle (SCF) until an acceptable convergence is reached. Slater introduced a mathematical formulation for anti-symmetric spin orbitals in the linear combination of atomic orbitals.[94] While the HF solution itself neglects electron correlation, post-HF methods offer energetic corrections to address the electron-electron repulsion more rigorously and correct the V_{ee} term . The true energy of a modelled system is the sum of the electronic correlation energy and the Hartree Fock energy (E_{HF}).[90]

$$E_{sys} = E_{HF} + V_{ee}$$

For high spin systems, unrestricted Hartree-Fock (UHF) and restricted open shell Hartree-Fock (ROHF) allow for singly occupied wavefunctions. UHF breaks the wavefunction into a set of singly occupied anti-symmetric orbitals[95] while ROHF assigns doubly occupied orbitals for the core electrons and allows open shell assignment of unpaired valence electrons.[96] However, spin contamination can influence the ground state energy by mixing different spin states, which leads to error in estimating the energy in stretched and equilibrium structures.[97, 98]

Once the HF wavefunction has been solved, there are a range of options for incorporating electronic correlation into the total energy. From completely ignoring the repulsive interaction to accounting for a complete active space, the researcher must assess the level of theory to use for their system under study. As mentioned, HF includes in the interaction between an electron and the mean field at its position. However, an electron's position will instantaneously influence the positions of the other electrons in its proximity which is not captured in the mean field approach.

Perturbation theory can address electron correlation by adding higher order

correction terms to the simplified Hamiltonian. Møller–Plesset (MP) perturbation theory[99] is a common post-HF perturbative method which involves usually a second order (MP2) correction of the natural orbitals to account for electron correlation effects and dispersion interactions by mixing in some added occupancies into the wavefunction. Full configurational interaction (CI) is a linear variational approach for including all electron-electron interactions and includes all possible electronic configurations possible within the basis function.[100] Coupled cluster (CC) is another post-HF method for handling the many-body problem[101] and is considered the gold standard in quantum chemistry methods. Starting from the HF wavefunction, CC uses an exponential excitation operator to mix electronic excited states into the wavefunction to account for correlation. However, with n^6 scaling with system size, CC and full CI quickly become impossible to apply using current computers, even for moderately small molecules.[100] There are ways to work around the scaling issue by selecting an active space to treat using CC or CI. The problem of size consistency arises if these energies are compared against different reaction steps, for example. There is no sure-fire way to ensure that each system got the same "CAS" treatment since the electronic structure changes across a reaction. Nevertheless, thoughtful CAS selection can give accurate and valuable insight on the electronic structure of reactive centers for larger molecules. In Chapter 5, an appropriate CAS selection was necessary to prepare the one and two-electron integrals of the oxygen reduction intermediates for OTI's qubit coupled cluster method.[102]

2.1.2 Density functional theory

Rather than solving a large set of orbitals, the electrons can be viewed as a non-uniform density.[103] Hence, density functional theory (DFT) applies a functional which is a function of the electron density which is a function of position. The Kohn-Sham equations evaluate the kinetic energy of the electrons as if they are non-interacting.[103] This mostly accounts for the kinetic energy, but corrections can be added in after which take into consideration the effect of electron correlation on the kinetic energy. DFT has established itself as a pillar in computational chemistry for the evaluation of electronic structures, geometries, and reaction profiles at much lower costs than HF methods.[104, 105, 106]

The exact exchange-correlation functional is not known and different levels

of approximations can be made. The simplest approximation is the semi-local exchange-correlation functional which only depends on the local charge density and its gradient. The local density approximation (LDA) is the simplest exchange-correlation functional which evaluates $E_{xc}(r)$ using a homogeneous electron density. However, the LDA functional results in large errors and is insufficient for describing chemical reactions.[107] The generalized gradient approximation (GGA)[108, 109] marked a significant advance in the accuracy of DFT functionals. In GGA, a gradient approximation is applied to the exchange functional instead of a homogeneous density distribution, as done in the local spin density approximation (LSDA/LDA). GGA offers significant improvement over LDA for computing binding energies and energetic barriers in chemical reactions, including adsorption processes.[110, 111, 112]

DFT methods can be divided into non-empirical and semi-empirical approaches, both finding ongoing use in chemistry research. The non-empirical route involves *ab initio* methods while semi-empirical methods use established parameters to fit coefficients to previously calculated reference values. While semi-empirical methods tend to achieve closer agreement with experimental values, their accuracy relies on the agreement between fitted empirical parameters and the system of study. Non-empirical methods on the other hand attempt to describe a variety of systems with more consistent chemical accuracy by describing each system from first principles.[113]

There are a vast number of DFT functionals with varying weaknesses, capabilities and cost.[114] Hybrid functionals combine contributions from Hartree Fock, LDA and Becke's gradient-based exchange correction and the Lee, Yan and Parr (LYP) correlation functional. Among the most reliable hybrid functionals is B2-PLYP, introduced by Grimme in 2005.[115] B2-PLYP is a double hybrid function because it mixes electronic exchange from Becke's GGA with electronic correlation by Lee, Yan and Parr (LYP) with HF exchange and second order MP-type correlation.

$$E_{xc} = (1 - a_x) E_x^{GGA} + a_x E_x^{HF} + b E_c^{GGA} + c E_c^{PT2}$$

Where a_x is the HF-exchange mixing parameter and b and c scale the contributions of GGA and perturbative correlation contributions. While B2-PLYP shows good performance even for transition metal systems, it is computationally expensive and does not scale well for larger systems. A less expensive but reliable

alternative to B2-PLYP is the PBE0 hybrid functional, which behaves consistently across a variety of systems. Both PEB0 and B2-PLYP were the functionals of choice for studying modest systems because they tend to be dependable for transition metal complexes.[115, 116, 117]

Despite many advancements, strong electron correlation remains difficult to capture using DFT, and there is no straightforward way to systematically improve these functionals.[106] Nevertheless, over the past few decades, DFT has offered considerable improvement over HF-based methods in chemical accuracy and especially in computational scaling with system size.[104]

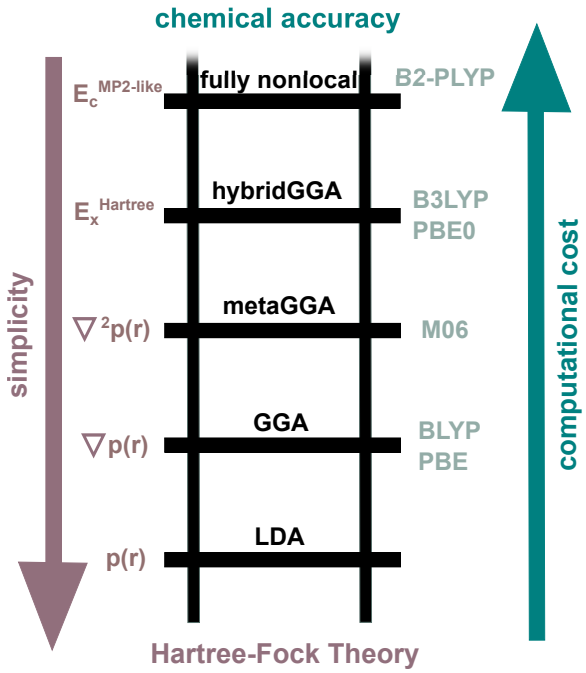

Figure 2.1: The Jacob's Ladder of computational accuracy.[118] Each of the rungs represent a step up in describing electron-electron interactions. The rungs starting from the bottom are i) the local spin density approximation, ii) the generalized gradient approximation (GGA), iii) the meta-GGA approximation iv) the hybrid functional, and v) the generalized random phase approximation. The lower semi-local rungs are computationally efficient, can be constructed non-empirically, and can serve as inputs to fourth-rung functionals.

2.1.3 Choice of basis sets

All quantum-chemical calculations are performed using a finite set of basis functions which are used to build the molecular orbitals of a system.[119, 120] Both

HF and DFT methods start from a linear combination of atomic orbitals (or plane waves for some periodic methods). An infinite number of basis functions would be needed to form a complete basis set (CBS). Regardless of whether a wavefunction, DFT or hybrid method is used, the basis set approximation will continue to limit the description of a system. An inadequate basis set will give poor results no matter the method used to describe the electrons occupying that basis set.

A basis set is defined by number of orbitals used to describe each atom as well as the type of functions used to describe each orbital. Minimal basis sets are adequate to describe single atoms, which only include enough atomic orbital functions to contain the electrons of the neutral atoms. However, additional functions allow for asymmetry and flexibility about the nucleus when molecular orbitals are formed. One improvement over a minimal basis set is to introduce a split valence basis in which the number of functions used to describe each valence orbital is doubled (double-zeta, DZ), tripled (triple-zeta, TZ), quadrupled (QZ), and so forth. Split valence basis sets combine multiple functions to describe a single orbital. Especially in valence orbitals, split valence basis sets allow the electron density to spatially redistribute in response to a particular environment.

Furthermore, polarization functions can be added to provide higher angular momentum functions to describe the electron distribution along a bond. For example, polarization can be achieved by mixing p-orbitals to polarize s-orbitals or d-orbitals to polarize p-orbitals and so forth. Adding polarization functions is a reliable way for improving the accuracy of binding energies in molecules.[121, 122] Finally, diffuse functions are small exponential functions which add a “tail” to the atomic orbitals. These help account for long loosely bound electrons and are very important for capturing vdW interactions, stabilize anionic species, and accurate modeling of long-range interactions. Diffuse functions are especially useful for describing anions and excited states.[123, 124]

The complex bonding environment of organometallic complexes makes them costly to describe sufficiently. The valence electrons involved in forming bonds originate from d-orbitals and there are often a number of degenerate or near-degenerate electronic states. Capturing the flexible shape of the bonding and nonbonding orbitals requires a higher number of basis functions per orbital. Even small changes in the spatial description of the orbitals can result in a different ordering of near-degenerate energy states and therefore different minimum energy descriptions of a system. In order to capture these subtle energy differences in

transition metal catalysts, we opt for triple-zeta basis sets with added polarization and diffuse functions. However, this can become costly fast and, depending on the system at hand, performing geometry optimizations with a smaller basis set followed by a final single point energy using a larger basis set is an effective way to obtain the best possible electronic structure while managing computational cost.

Gaussian bases from the Ahlrichs def2 basis set family were selected for calculations involving finite structures. In a benchmarking of DFT geometry optimizations, def2-TZVP bond lengths remained within 1 *pm* and angles within 1°.[125] In particular, DFT calculations paired with the def2-TZVPP basis set tend to improve results towards the basis set limit.[125] It is important to be selective over the use of augmented basis sets in DFT because excess diffuse functions can increase the cost of the calculation, cause SCF convergence issues and do not necessarily improve basis set superposition error (BSSE).[126, 127, 128] However, describing the coordination in transition metal systems differs greatly from main-group elements and adding diffuse functions (def2-TZVPPD) will generally improve electronic structure, particularly for systems with loosely bound electrons.[129, 128, 117] A common workflow throughout this dissertation is to perform DFT geometry optimizations using a smaller basis set followed by a single-point energy calculation using def2-TZVPPD. Effective core potentials (ECP) were often used for heavy elements to reduce computational cost with minimal sacrifice of accuracy since the core electrons are not involved in bond breaking and formation.[125] The def2-ECPs[130] were applied for heavy atoms such as Pt in Chapter 5 and for Pd and Zr in complexes discussed in Chapter 6.

While large basis sets can be implemented for molecular scale systems as described above, a large portion of this dissertation is focused on surface chemistry. A common approach to describing periodic materials is to use plane wave basis sets which repeat periodically. However, when describing localized reactions taking place on a surface, a plane wave description of the localized interactions becomes cumbersome. Another periodic basis set which involves numerical atomic orbitals is implemented by the SIESTA method.[131] What sets this basis set apart is that the bases functions have a numerically defined radial dependence and are only non-zero within a finite space.[132] This cancels all interactions in regions where the bases are defined as zero. Selecting an appropriate radius cut-off is essential to preserve accuracy while also considering added cost and this value can be set using the PAO.EnergyShift keyword. For all SIESTA calculations, a cutoff of 0.001

Ry was applied. Moreover, the number of basis functions are kept small by using effective core potentials. These approximations allow for N-scaling with system size. Because of this scaling, we are able to monitor metal substrates and atomic layer deposition pathways on various surfaces with large cell sizes (200+ atoms).

2.1.4 *Ab initio* studies of surfaces

The two main classes of models to simulate surfaces stem from a molecular and solid-state chemistry approach.[133] Cluster models are used to simulate a finite collection of atoms which resemble a surface site. This molecular approach allows for adjustment of the system size to match the computational method applied. On the other hand, solid-state chemistry describes the surface as a slab in a repeating cell of specified dimension. The surface reaction must fit into a single cell and the periodic distance must be taken into consideration when designing a slab. Periodic boundary conditions enable a continuous material to be modeled while only simulating cell containing a finite number of atoms which repeat in each spatial dimension. In some cases, a 2-D surface is required to truly simulate the bonding environment on the surface (ie. to account for crowding effects).[62] Depending on the property of interest, both periodic and cluster approaches can serve as models for systems from first principles.

For both the cluster and periodic approach, DFT generally gives structures that are in good agreement with crystallographic results. Exchange-correlation approximations, basis set completeness and the accuracy of pseudopotentials are all factors which contribute to the accuracy of DFT results. While hybrid functionals tend to describe adsorption processes more accurately,[134] they are not easily evaluated for periodic systems, making exact electronic exchange difficult to access.[118, 107] For simulating periodic surfaces, the popular GGA based Perdew, Becke and Ernzerhof's PBE functional[135] has become prevalent in materials simulations. A leading influence on the accuracy of surface interactions, particularly involving transition metals, is the inclusion of dispersive van der Waals interactions. Including some form of dispersion correction in DFT greatly influences the energy landscape of a system, offering higher accuracy for interaction energies and geometries.[136] In particular, periodic systems which are limited to pure DFT functionals show considerable improvement in calculated adsorption energies when empirical dispersion corrections are included.[137] Semi-empirical[115, 138]

or empirical[139] corrections can used to account for long-range dispersive interactions.

Dispersion corrections to supplement DFT calculations involve adding a pairwise interatomic C_6R^{-6} term (E_{vdW}) to the DFT energy.

$$E_{vdW} = -\frac{1}{2}\sum_{A,B} f_{damp}\left(R_{AB}, R_A^0, R_B^0\right) C_{6AB} R_{AB}^{-6}$$

Where R_{AB} is the distance between atoms A and B, C_{6AB} is the isotropic C_6 term to describes the vdW interaction between two atoms or molecules, R_A^0 and R_B^0 are the vdW radii for each atom. A short-range damping function f_{damp} is incorporated to eliminate unrealistic behaviour at short distances. When simulating a material such as a surface, accounting for screened interactions is important.[140] Screened vdW interactions are best described by a different set of values for calculating E_{vdW}. Tkatchenko's screened vdW parameters are implemented for all surface calculations performed in this work.[140]

Whether the electronic Hamiltonian is treated as a wavefunction or electron density, tackling large systems and materials requires solutions to scaling. For heavier elements past the second row, the use of pseudopotentials greatly decreases the number of orbitals and interactions that need to be accounted for. A pseudopotential wraps the inert core electrons into a single potential, leaving only the reactive valence electrons which are involved in bonding to be optimized.[141, 142] All Troullier-Martins pseudopotentials used in surface calculations were obtained from SIESTA's GGA Pseudopotential Database.

2.1.5 *Ab initio* molecular dynamics

Molecular dynamics is a simulation of the movement of atoms in molecules. Each simulation results in a trajectory containing a specified number of steps. Commonly, the movement of the nuclei are governed by Newtonian equations of motion. After each step, the energy of the system is calculated using either classical or, in the case of *ab initio* molecular dynamics (AIMD), quantum chemical methods. The Nosé-Hoover thermostat[143] provides a thermal bath in which the kinetic energy of the system can fluctuate. During these calculations, volume V and temperature T are kept constant. The number of particles N is also held fixed, resulting in a canonical NVT ensemble. By using a quantum mechanical approach to describe

the electrons in the system, bond breaking and forming can occur. However, AIMD is an expensive method; each MD step spans only up to one femtosecond and for each step an electronic structure calculation must take place. If an appropriate method is chosen and enough computational resources are available, these calculations provide a unique opportunity to simulate the dynamics of the study system. In this work, PBE/DZP with semi-empirical dispersion corrections was paired with AIMD to simulate periodic systems.

AIMD trajectories carried out allow for the system to sample the potential energy surface freely. Geometry optimizations for obtaining minimum structures are highly dependent on the starting geometry. When optimizing binding configurations for a reaction on the surface, a common issue is to become energetically trapped in the nearest local minimum of a shallow PES. AIMD allows the system to traverse the PES and sample many configurations to start geometry optimizations from. This method was applied to find and confirm complex surface binding configurations throughout Chapters 3 and 4.

2.1.6 Transition State Methods

Determining the transition state of a reaction is an interesting problem for the computational chemist. Because transition states do not exist long enough to observe experimentally, computational methods offer a unique approach for studying transition state configurations. Unlike optimizing a structure to a potential energy minimum, finding a saddle point, let alone the correct saddle point is a challenging task. The two approaches involve interpolation methods and local surface-walking algorithms and combining these techniques often yields the most success in identifying reaction barriers.

A reaction pathway can be represented by the minimum energy path (MEP) which connects the starting energy to the final energy across the potential energy surface (PES). Depending on the number of elementary steps in the reaction, the MEP will encounter saddle points corresponding to each transition state. The highest point along the MEP connecting the reactant and product determines the energy barrier of a reaction so it is necessary to have an estimate of the MEP.[144] There are several computational techniques that are used to identify the coordinates of the saddle point connecting the start and endpoints. Generally, finding the transition state can be done using interpolation methods, surface walking al-

gorithms or a combination of both. A sound strategy is to use interpolation techniques such as growing string[145] or nudged elastic band (NEB)[146] to establish the MEP.[144] These methods attempt to connect the final and initial state of the system along the most energetically favorable pathway. NEB is an interpolation method that minimizes a set of images connecting the two endpoints. A spring force is applied to adjacent images to ensure continuity and control the spacing of these images. To improve the estimation of the transition state, the climbing image (CI) NEB method was implemented.[147] CI-NEB is designed to increase the resolution around the saddle point by forcing images closer towards the energy barrier. One of the images is selected to converge at the highest saddle point.

Once an interpolation method establishes a MEP, the maximum can become the initial guess for a local saddle point search algorithm. These methods use local gradient and second derivative information to converge upon the true saddle point. Dimer methods,[148] the Lanczos method[149] and partitioned rational functionalized methods of Baker[150] are all surface walking methods that can be used for finding transition states in molecular systems.[151] Starting a saddle point search from an arbitrary or biased point may result in convergence upon a saddle point which does not connect the endpoints. While MEPs become very expensive to converge as the system grows, even a rough interpolation calculation provides an initial guess that incorporates information about where the saddle point must lie to connect the endpoints.

NEB calculations were performed for various systems using ORCA and NWChem, and will be discussed in more details in the coming chapters. Recently, NEB has also been implemented for SIESTA calculations through the Atomic Simulation Environment (ASE), allowing for transition state searches on surfaces. Previously, a homemade python script was implemented and used to perform relaxed scans on the surface by linear transit (see AppendixA). These normally resulted in very rough MEPs and overestimations of saddle points because of their brute-force nature. However, implementing a step-size smaller than 0.05 $\mathring{A}$ resulted in fairly smooth energy curves. More refined methods such as NEB allow for much higher chemical accuracy with fewer computational steps.

2.1.7 Quantum chemistry software

Academic free license chemical software used for simulating systems includes SIESTA,[131] ORCA,[152, 153] ASE,[154] PySCF[155, 156] and NWChem.[157] SIESTA was primarily used to perform DFT geometry optimizations (using both "DZP" and "TZP") and *ab initio* molecular dynamics on periodic surface slabs. ORCA was used to perform geometry optimizations, transition state searches and free energy calculations with more rigorous hybrid DFT functionals and basis sets. Finally, NWChem was also used to perform geometry optimizations and transition state calculations for small transition metal systems. UHF electronic structure calculations were also performed to generate one and two electron integrals as inputs for quantum codes.

Transition metals remain a difficult subject for computational chemists as there are many interacting electrons and degenerate or proximal orbitals. Wavefunction methods such as coupled cluster are more expensive but can fully incorporate the electronic interactions when given enough computational resources. Oftentimes, parameterizing a system can achieve adequate results with a fraction of the computational cost which can be particularly helpful in the simulation of materials containing transition metals. It is the duty of the computational chemist to weigh the benefits and drawbacks of each compromise, which is often facilitated by benchmarking these methods.

2.2 Experimental methods

2.2.1 Electrospray ionization mass spectrometry

Electrospray ionization (ESI) is a widely used soft ionization technique to produce gas phase ions from solution.[158, 159] ESI is well suited to the mass spectrometric monitoring of fragile species because it is gentle enough to prevent decomposition of macromolecules[158, 160] and, in our case, organometallic complexes.[161] The high sensitivity and fast acquisition rate of mass spectrometry (MS) make it excellent for observing transient or low abundance species that may be undetectable by other methods. To be detected, the analyte must carry a charge before entering the source of the instrument and must undergo a desolvation process where it is transformed into gas phase ions. In the case of ESI, the charged analyte is carried

by solvent through a charged capillary and ejected as fine droplets from a Taylor cone. A nebulizer gas is applied, and the droplets shrink, eventually releasing gaseous ions which enter the source of the instrument for mass analysis.[162]

There are different models for how gas phase ions are formed from the fine droplet spray proceeding the Taylor cone. The ion evaporation model first introduced by Iribarne and Thomson suggests that once a droplet shrinks to a critical radius such that the field strength at the surface of the droplet exceeds the energy required to disrupt the surface, ions are expelled from the droplet.[163, 164, 165] Alternatively, the charge residue model, first introduced by Dole, suggests that the droplet undergoes cycles of solvent evaporation followed by fission when the Raileigh limit has been reached until a single gas-phase ion remains.[160, 166, 167] While a theory for the ionization process has not been proven, the general consensus is that the ion evaporation is likely the ionization process for smaller ions while the charge residue model best describes the mechanism for ions over 1000 Da and/or organometallic species with long, flexible ligands.[159] In the case of organometallic species, it might depend on both the size of the species the nature of the ligand. Compact species may be easier to expel while larger, elongated molecules may remain in the droplet while neutral species evaporate.

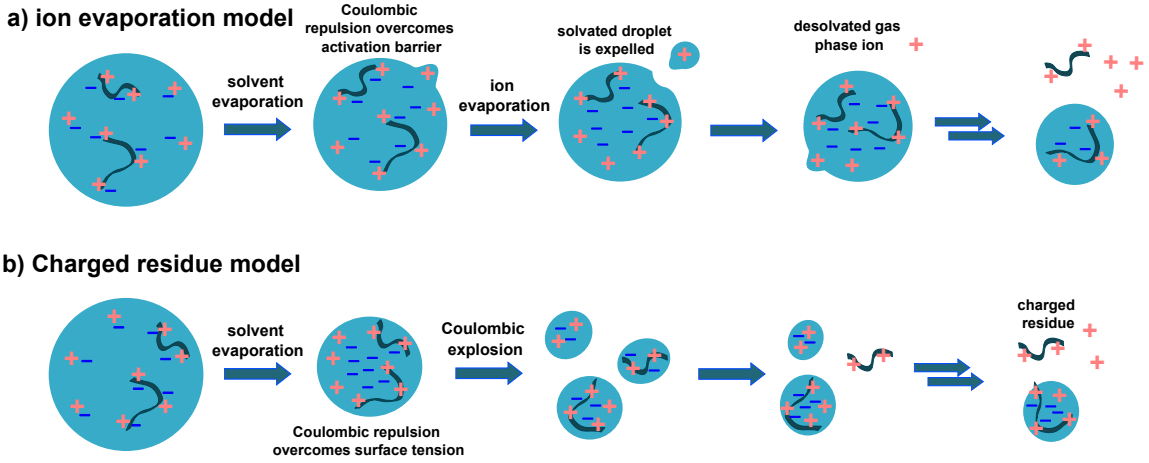

Figure 2.2: Models for the ionization processes. In both description of ionization, solvent is evaporating throughout, however ion evaporation (**a**) shows the gradual release of intact ions from the surface while the charged residue model (**b**) predicts for coulombic explosion once the shrinking droplet reaches a critical charge density.

2.2.2 Collision induced dissociation

Tandem mass spectrometry offers a highly selective method of separating species based on their mass to charge ratio (*m/z*). The electronic field exerts a unique force on each ion depending on their charge. Using an oscillating electric field, only ions of a particular mass-to-charge remain between the quadrupoles to continue towards the detector. [168] Those ions are accelerated into the collision cell where they collide with argon atoms. The fragmented ions plus any remaining intact precursor are passed onto the detector. As the collision voltage increases, these collisions become more energetic and cause increased levels of fragmentation (unimolecular decomposition through deposition of internal energy).

Currently, there are no common experimental methods for characterizing the behaviour of ALD precursors in the gas phase. However, using collision induced dissociation (CID) we can directly observe the gas phase decomposition of a charged analyte. The high energy, gas phase environment in the collision cell simulates the high temperature, gas phase environment precursors encounter during ALD. In both ALD and CID, the weakest bonds will tend to break first and the strongest bonds last. Therefore, we can use CID to predict how ALD precursors may behave in the moments before they bind to the surface.

2.2.3 Pressurized sample infusion

In 2010, the McIndoe group introduced the pressurized sample infusion (PSI) technique to monitor chemical reactions. Pressurized sample infusion (PSI) is a method used in conjunction with ESI-MS for online reaction monitoring of charged species. A continuous flow into the mass spectrometer paired with continuous data acquisition provides unique access to observing short-lived intermediates and elucidating catalytic steps. Reactions involving high-spin intermediates cannot be easily observed by NMR yet make prime candidates for PSI monitoring if they are or can become charged. Many air-sensitive reactions have been monitored successfully by ESI-PSI-MS including copper-free Sonogashira and Suzuki-Miyaura cross coupling reactions.[169, 170]

In PSI, the reaction mixture is prepared in a sealed Schlenk flask (or adapted flask) which is connected to the mass spectrometer using PEEK tubing. The reaction monitoring begins when an overpressure is applied (usually an inert gas such

as Ar or N_2), injecting the reaction mixture into the capillary. Reagents can then be added through the septum via syringe to initiate the reaction step of interest. A large benefit of PSI is the addition of reagents does not interrupt the continuous data collection. However, formation of solid particulates may lead to blocking of the capillary.

There are a variety of good candidates when selecting a charged-tag to attach to the analyte. In general, a good charged-tag is chemically inert yet also does not hinder the reactive center. The counterion must also be chemically inert during the reaction. In most cases, a well selected charged-tag and counter ion will not interfere with a reaction. Triphenyl phosphonium with a hexafluorophosphate counterion were selected for this work because (i) triphenyl phosphonium is fairly inert and easy to attach to alkyl halides through SN2 and (ii) hexafluorophosphate is more inert towards transition metals than the halogen it was exchanged for while also improving the solubility of the ionic complex.

One advantage of PSI-ESI-MS over other reaction monitoring techniques such as nuclear magnetic resonance (NMR) and infrared (IR) spectroscopy is the enhanced time resolution. While a reaction may have up to tens of data points when collected by IR spectroscopy and NMR, during PSI-ESI-MS a new spectrum is collected every second. This high frequency of data collection provides a unique opportunity to observe short-lived intermediates. Furthermore, the high sensitivity of the instrument gives access to processes occurring in the baseline. While NMR and IR work at mmol/L, an appropriate concentration for a MS sample is on the order of μmol/L.

Some challenges we face with MS are in fact due to this high sensitivity.[171] Saturation effects can easily occur when a sample is too concentrated which makes it problematic to run reactions at standard concentrations. Lowered concentrations will not only suppress the reaction rate, but it will also increase the relative fraction of catalyst that is consumed by poisoning. Excess reagent and solvent impurities become more prevalent as a reaction becomes more dilute. Finally, ESI-MS only identifies charged species. Therefore, to study the behaviour of a neutral species requires the synthesis of a charge-tagged analog which will be further discussed in detail.

Chapter 3

Gas phase decomposition of ALD precursors

3.1 Abstract

Cobaltcarbonyl-tert-butylacetylene (CCTBA) is a conventional precursor for the selective atomic layer deposition of Co onto silica surfaces. However, the limited understanding of the deposition mechanism of such cobalt precursors curbs rational improvements on their design for increased efficiency and tuneable selectivity. The impact of using a less reactive internal alkyne to a terminal alkyne was investigated using experimental and computational methods. Electrospray-ionization mass spectrometry was used to monitor the formation of CCTBA analogs and study their gas phase decomposition pathways. Gas phase analysis show that an internal alkyne dissociates at slightly lower energies than a terminal alkyne, suggesting that an internal alkynyl ligand may be more suited to low temperature ALD. Furthermore, the less reactive internal alkyne will result in fewer carbon impurities embedded in surfaces, in particular due to its reduced reactivity with Si-H bonds on the surface of Si wafers. Computational analysis also predicts increased surface binding in the metal centers of the internal alkynyl complex.

3.2 Introduction

Atomic layer deposition (ALD) is an emerging technique for depositing thin films with high conformity in a self-limiting manner. However, the development of precur-

sors with better performance or specific function is limited by a lack of fundamental knowledge over mechanistic pathways taking place on the surface during ALD. Cobalt is specifically used as a seed layer for copper interconnects to prevent defects and atom migration across the interface between the conductive and dielectric layers of devices,[172, 45] however there is a limited number of established Co precursors for ALD. The organometallic complex $Co_2(CO)_6(\mu^2\text{-}HCCCMe_3)$ (known as CCTBA, cobaltcarbonyl-tert-butylacetylene) is a common precursor for the chemical vapour deposition (CVD) and ALD of cobalt.[172, 58, 173, 174, 175, 176, 76, 177, 72] Its high vapour pressure and relatively small molecular size enhances the performance of CCTBA as a volatile source of Co, making it desirable compared to many other Co precursors.[174] Furthermore, the synthesis of cobalt-alkyne complexes is straightforward and well-established across a wide range of alkynes.[**?**] The ease of cleaving ligands as neutral molecules minimizes surface impurities and improves the atom economy during the ALD process. However, during deposition Co precursors, including CCTBA, participate in undesired side-reactions which embed impurities into the surface during deposition. In the case of CCTBA, thermally driven hydrosilation is thought to occur between the alkyne and Si-H terminated surfaces, leaving behind carbon to disrupt the desired material uniformity and properties such as conductivity.[72] Modifying the properties of the alkyne can help reduce undesired impurities and direct the surface reactivity towards the metal center.[72, 31]

Altering the ligands of CCTBA can tune the precursor for deposition onto specific surfaces. However, these modifications require insight on the mechanisms by which precursors such as CCTBA undergo during ALD.[47] Studying heterogenous reactions on surfaces is notoriously difficult using experimental methods. Mass spectrometric studies have been used for in situ monitoring of the gaseous biproducts from ALD of Al_2O_3[57, 52] and ZrO_2.[51] Researchers often turn to computational chemistry to understand the behavior of such systems, however there is a general lack in experimental data probing Co-ALD mechanisms.[44] For the cobalt carbonyl complex to interact strongly with a surface, it must first lose ligands, and the mechanism by which this occurs is currently obscure. Understanding which ligands are lost first, whether the alkyne leaves intact or in parts and how changing the ligand might affect these gas-phase processes is a necessary insight into what chemical processes occur during ALD.

We set out to identify what effect replacing the terminal alkyne with an internal

alkyne might have on the gas phase behaviour of the precursor. The postulated hydrosilation mechanism taking place on a treated Si-H surface will be more hindered by an internal alkyne. While cobaltcarbonyl-tert-butylmethylacetylene (CCTMA) has a slightly higher melting point than CCTBA, it has been shown to produce lower resistivity films on silica, which suggests a lower carbon content.[173] By synthesizing charged analogs of these alkynyl cobalt carbonyl complexes we can probe their gas phase reactivity through collision induced dissociation (CID) and determine whether CCTMA demonstrates similar gas phase decomposition to that of CCTBA. Insight upon the gas phase decomposition of these alkynyl cobalt carbonyl complexes can guide targeted modifications to the precursor and determine whether CCTMA demonstrates similar behaviour to CCTBA.

3.3 Methods

3.3.1 Synthesis of CCTBA analogs

The conventional synthesis of CCTBA for ALD involves substitution of two carbonyl ligands for TBA (tert-butylacetylene) (Equation 1 where R=H).[177] This reaction is fast (minutes) at room temperature and possible across a range of alkynes, including internal alkynes. The traditional complex containing a terminal alkyne (R=H) was compared against an internal alkyne (R=Me) to identify differences in reactivity.

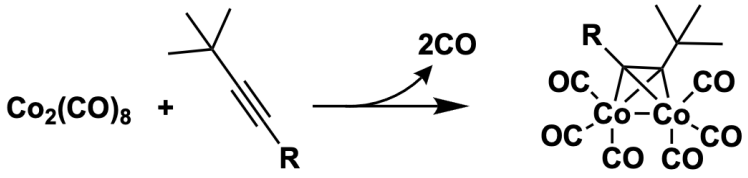

Figure 3.1: The formation of CCTBA. This reaction can be performed either neat or in a nonpolar solvent at RT.

The prospect of a model system to enable direct probing of the decomposition of CCTBA was appealing, and accordingly we designed and synthesized a charge-tagged acetylene ligand that would react with $Co_2(CO)_8$ analogously to CCTBA. A charged alkyne enables direct analysis of the ligand using electrospray ioniza-

tion mass spectrometry (ESI-MS)[178] to observe its reactivity with $Co_2(CO)_8$ in real-time,[179] and the gas-phase decomposition of the product complex using collision-induced dissociation (CID) in the mass spectrometer.

Two charged tags were prepared, one a terminal alkyne $[HCC(CH_2)_4PPh_3][PF_6]$ (**1**$[PF_6]$) and the other an internal alkyne $[CH_3CC(CH_2)_2PPh_3][PF_6]$ (**2**$[PF_6]$). Triphenylphosphonium groups were attached to alkynyl compounds through S_N2 reactions in toluene and the insoluble product was filtered out of solution after approximately 24 hrs at room temperature. We chose hexafluorophosphate as a counterion to eliminate any chance of the halide ion acting as a ligand itself, and to improve the solubility of **1** and **2** in the low-polarity solvents preferred for ESI-MS.

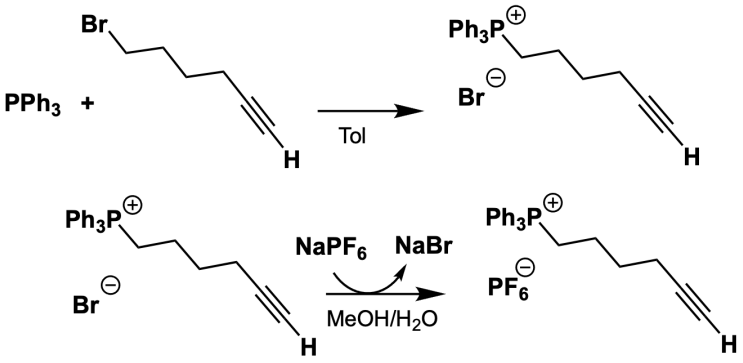

Figure 3.2: Synthesis of a charged analog ligand of CCTBA [**1**].

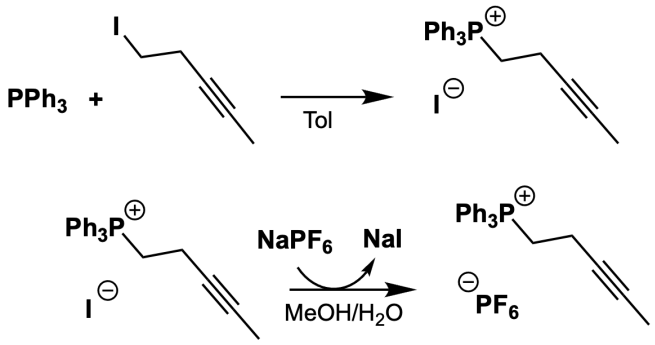

Figure 3.3: The synthesis of a charged analog ligand of CCTMA [**2**].

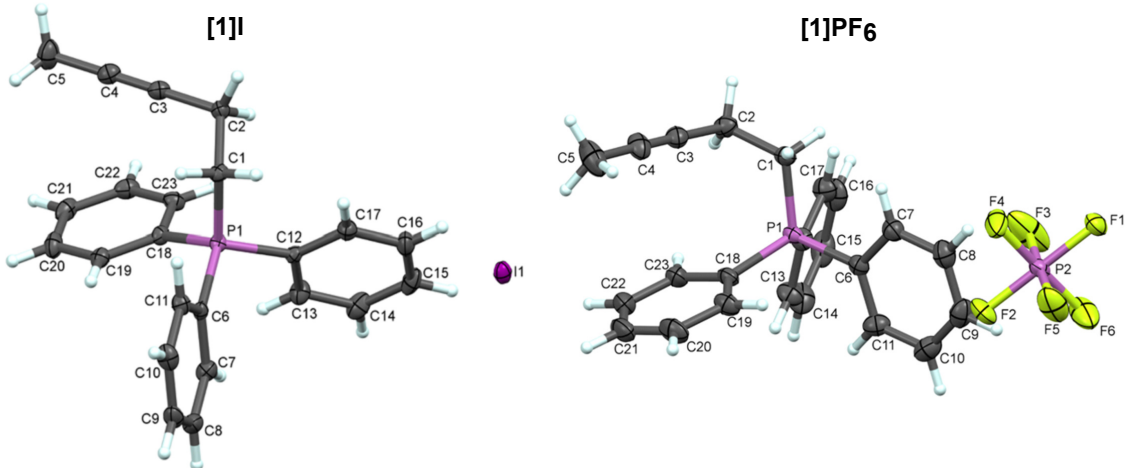

Figure 3.4: Crystal structures of [**2**][I] (left) and [**2**][PF_6] (right). [**2**][PF_6] was used in the formation of a charged analog of CCTMA.

3.3.2 Characterization of CCTBA analogs

Once compounds [**1**][PF_6] and [**2**][PF_6] were synthesized as described in Figure 3.2 and 3.3, [**2**]$^+$ was recrystallized with both I^- and PF_6^- counterions. The solid state molecular structures were obtained using X-ray crystallography (Figure 3.4). To generate charged analogs of CCTBA and CCTMA, [**1**][PF_6] and [**2**][PF_6] were each combined with $Co_2(CO)_8$ in the same manner as neutral alkynes (Figure 3.1). We were able to successfully characterize these internal and terminal alkynyl complexes by anaerobic ESI-MS[180] (Figure 3.5). These alkynyl complexes were prepared to be used as charged analogs of CCTMA ([**3**]$^+$) and CCTBA ([**4**]$^+$) for further gas phase analysis.

3.3.3 Computational methods

Density functional theory (DFT) was employed to compute the geometries of gas phase decomposition species using a PBE0/def2-TZVP approach with dispersive interaction treated using the Becke-Johnson D3 model[181] in the NWChem/v6.8.1 program.[157] For calculations involving surface reactions, a PBE-vdW-TS/DZP approach was used in the SIESTA 4.0.1 program.[131] Periodic Si(111) slabs consisting of four atomic layers and repeating every six atoms in the x and y direction were surface-capped with hydrogen. Troullier-Martins effective core potentials from the SIESTA database [182] were used alongside a DZP basis for atomic and

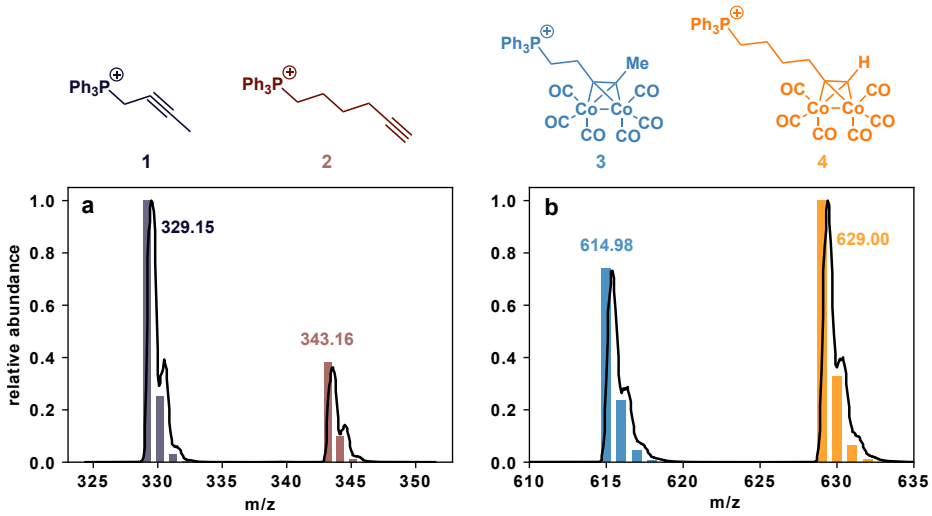

Figure 3.5: Mass spectra of species **1**, **2**, **3** and **4** plotted with their respective isotope patterns. Panel **a** plots the *m/z* of the internal and terminal alkyne charged tags and **b** plots the charged analogs of CCTBA and CCTMA.

cell optimizations. A spacing of 50 *Å* was included between slabs in the direction perpendicular to the surface. All calculations were done at the Γ point.. The orbital energy shift was set to a cutoff energy of 0.001 Ry. Nose-Hoover molecular dynamics calculations were performed in SIESTA to sample the binding configurations of key intermediates on the surface.[183] Surface-bound transition states were then identified using the nudged elastic band (NEB) approach. NEB calculations were performed using the Atomic Simulation Environment (ASE)[154] in conjunction SIESTA.

3.4 Results and Discussion

3.4.1 Experimental monitoring of CCTBA formation

Having the readily available charged alkynes provided the opportunity to directly probe the formation of CCTBA. The reaction of [**1**][PF_6] and [**2**][PF_6] at concentrations of 10 μM with excess $Co_2(CO)_8$ in dichloromethane was monitored in real time using PSI-ESI-MS.[184, 185] The reaction proceeded cleanly to $Co_2(CO)_6(\mu^2$-alkyne) (Figure 3.1). No intermediate $Co_2(CO)_7(\mu^1$-alkyne) ions were observed in either case, even at trace levels. The reaction of **1** with $Co_2(CO)_8$ was approximately twice as fast as the reaction between **2** and $Co_2(CO)_8$. The reaction was

zero order in **1** and **2** at conversions below 70%.

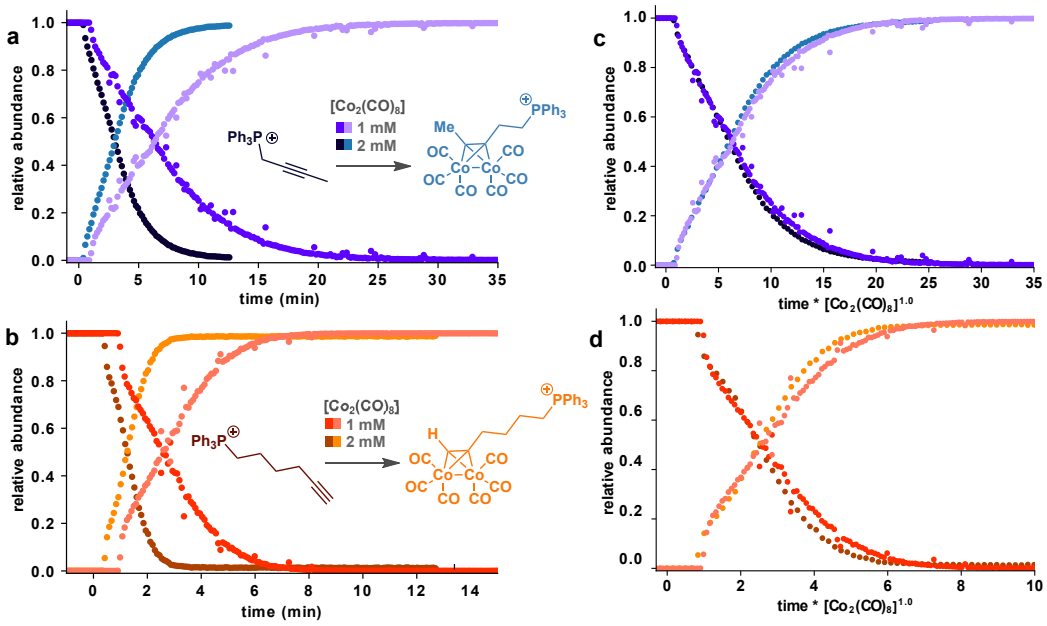

Figure 3.6: PSI-ESI-MS chromatograms show the rate dependence on the concentration of cobalt carbonyl. Formation of **3** (**a**) and **4** (**b**) are shown and concentrations of 1 *mM* (purple and red) and 2 *mM* (blue and orange). Note that the first thirty seconds of reactivity are missing due to the lag between addition of the $Co_2(CO)_8$ and arrival of the reacting solution in the mass spectrometer. Panels **b** and **d** show the time normalized traces of **a** and **b**.

Two conclusions can be drawn from monitoring the charged alkynes forming alkynyl complexes. Firstly, the internal alkyne (Figure 3.6**a**) reacts significantly slower than the terminal alkyne (Figure 3.6**b**). This is expected with increased steric hindrance introduced by the methyl group and by the phenyl groups in closer proximity. Secondly, the rate of the reaction depends on the concentration of $Co_2(CO)_8$. When doubling the $Co_2(CO)_8$ from 1 *mM* to 2 *mM* while keeping [**1**] and [**2**] at 10 μM, the rate of reaction doubles, indicating the reaction is first order in $Co_2(CO)_8$. This observation was corroborated by performing variable time normalization analysis (VTNA) to overlay the chromatograms (Figure 3.6**c,d**).[186] Normalizing the time axis by the constant concentration of $Co_2(CO)_8$ raised to the first power results in good overlay for the PSI traces in the formation of [**3**][PF_6] (Figure 3.6**c**) and [**4**][PF_6] (Figure 3.6**d**). This confirms that the reaction is first order in $Co_2(CO)_8$.

3.4.2 Computational modelling of CCTBA formation

The formation of CCTBA was computationally modelled without the charge tag to obtain the energy of isomers, potential intermediates, and the overall reaction. Geometry optimizations were used to analyze the effect of an internal alkyne on the overall structure and bonding character at the metal center. Two geometries were optimized for $Co_2(CO)_8$ with differing symmetry. The C_2v isomer has been reported in crystal structures,[187] and is 7 kJ/mol lower in energy than the D_3d isomer. This relative stability has been confirmed by solution phase studies with IR spectroscopy.[188, 189] For the alkyne to associate to the metal complex, CO must first dissociate. We expect CO dissociation to be the rate determining step of the reaction, thus predicting the overall formation of CCTBA. The electronic energy cost of losing a carbonyl to form a $Co_2(CO)_7$ intermediate was calculated to be +110 kJ/mol and the overall transformation to CCTBA was +39 kJ/mol for both the internal and terminal alkyne (Figure 3.7). No heptacarbonyl species were observed during PSI-ESI-PSI-MS experiments which suggests that either both carbonyls are removed before the alkynyl complex fully forms or that the steps following alkyne binding (CO loss and rearrangement) are concerted or very fast.

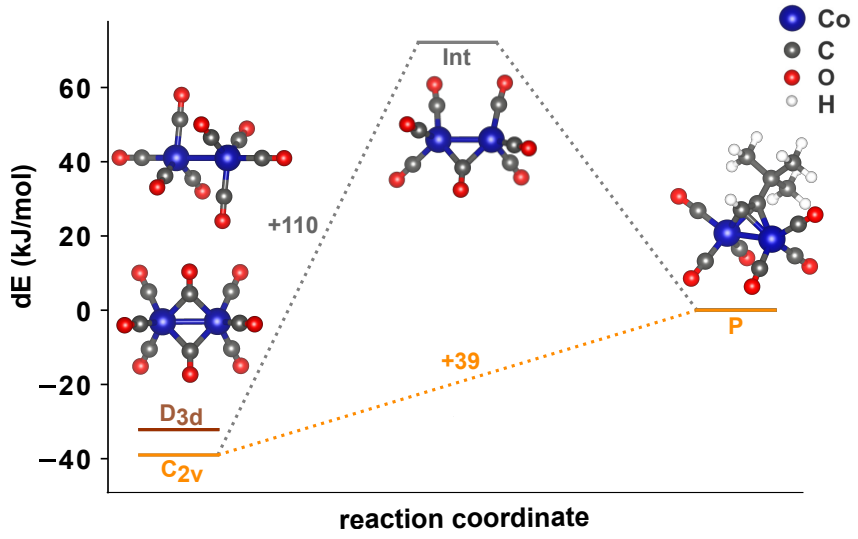

Figure 3.7: The change in energy (kJ/mol) during formation of CCTBA. The energies of D_3d (red) and C_2v (orange) isomers of $Co_2(CO)_8$ are shown with respect to the product **P** (CCTBA). The relative energy of a possible $Co_2(CO)_7$ intermediate (**Int**) is shown in grey.

The geometry optimizations for both the internal and terminal alkynyl complexes

revealed consistent changes in hybridization in the coordinating carbons. C−C and Co−Co bond lengths remain nearly identical between the internal and terminal alkyne (Figure **??**). Both alkynes change from a linear configuration (R−C−C = 180°) to a bent configuration with increased p character (R−C−C = 143 $\AA$) when coordinating across the Co−Co bond, which agrees with the known trend for general cobalt carbonyl alkynyl complexes.[**?**] Furthermore, upon coordination the C1−C2 triple bond lengthens to resemble a typical alkene double bond (C−C = 1.34 $\AA$). These findings suggest that the metal centers in CCTBA are closer to an oxidation state of Co(+1) than Co(0) oxidation state as usually presumed for late transition metal complexes.[72] Oftentimes, alkynes are considered dative ligands which normally do not affect the oxidation state of a metal, binding side-on and serving as a 2e σ donor. However, the metal center can donate electrons into the π^* orbital carbon to rehybridize the triple bond,[190, 191] forming a metallacyclopropene complex.[192, 193] Regardless of the metal oxidation state, all ligands on CCTBA can dissociate as neutral ligands, making thermal ALD an effective ligand stripping/reduction technique.

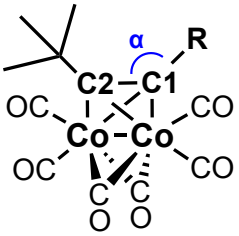

compound	d_{C1-C2}	d_{Co-Co}	$\alpha_{R-C1-C2}$
terminal alkyne	1.201		180.0°
internal alkyne	1.203		179.8°
CCTBA	1.336	2.423	142.6°
CCTMA	1.338	2.424	143.3°
$Co_2(CO)_8$ (C_2v)		2.495	
$Co_2(CO)_8$ (D_3d)		2.637	

Figure 3.8: Tabulated bond lengths ($\AA$) and bond angles of computed structures of CCTBA and CCTMA. Values remain consistent across the internal and terminal alkyne and coordination to Co results in lengthening of the C1−C2 bond and departure from a linear C1−C2−R bond angle.

3.4.3 Gas phase decomposition of ALD precursors

The gas phase decomposition of the precursors were probed by mass spectrometry and modelled computationally. There are no conventional experimental methods to capture information about the gas phase processes that occur in an ALD chamber. To our knowledge, the decomposition pathway of CCTBA has not been studied despite it being the main process by which the precursor comes to bind with the surface. Mass spectrometric techniques can provide a rare glimpse into what gas phase species are produced by a high energy environment to interact with the surface. CID increases the internal energy of the ionic complexes through multiple energetic interactions with a collision gas (argon in this case), resulting in a series of unimolecular decomposition reactions. CID also offers specific control over the collision energy which allows one to track the decomposition pathways as the internal energy gradually increases.

The synthesis of charged CCTBA and CCTMA analogs using **2** and **3** respectively has allowed the inspection of their gas-phase decomposition pathways using CID experiments summarized in Figure 3.9. This process resulted in two main fragmentation pathways: loss of the alkyne, and carbonyl dissociation. While the two mass spectra in Figure 3.9 show some differences in the relative abundances of decomposition products, the speciation of the **3** (*m/z* 629, Figure 3.9**a**) and **4** (*m/z* 615, Figure 3.9**c**) remains consistent between each precursor, with corresponding peaks separated by a mass-to-charge ratio of 15 Da (the mass difference between the internal and terminal charged tags). For both **3** and **4**, the intermediates from the sequential loss of all six carbonyls are observed and the loss of four carbonyls results in an exceptionally stable $Co_2(CO)_2-$alkynyl intermediate (*m/z* 503 and 517 produced from **4** and **3**). For the internal alkynyl complex **4**, the loss of one CO also results in a prominent decomposition product (*m/z* 587) while for **3**, loss of two carbonyls was more a prominent step (*m/z* 573) and occurs slightly earlier than the loss of the alkynyl. Both species result in very low abundance of daughter ions where the Co-Co bond was broken (*m/z* 444, 458). We observed no evidence of other breakdown products, such as decomposition of the charged tag itself, or loss of neutrals that would suggest C-H activation processes at work (such as H_2 loss).

The decomposition products are plotted with respect to the collision energy in Figure 3.9**c** and **d** to rank relative bond strengths. Loss of the first carbonyl occurs at very low collision voltage (5 V) for both complexes. Loss of the alkyne

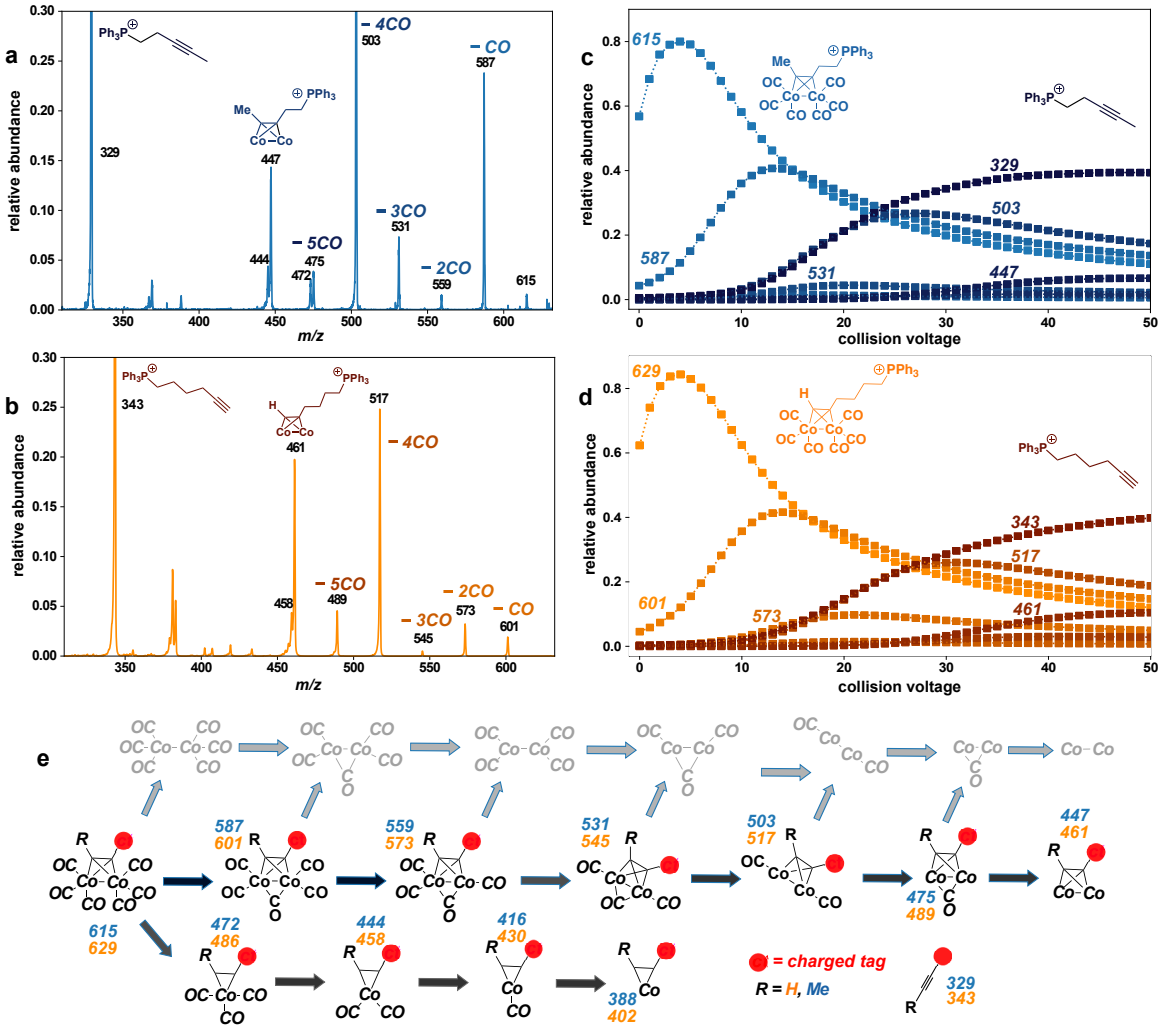

Figure 3.9: CID experiments reveal the gas phase decomposition of **3** and **4**. Spectra **a** and **b** plot the *m/z* values of the daughter ions detected over the course of the experiment. Panels **c** and **d** plot the abundance of daughter ions as the collision voltage is increased. Predominant traces are labelled with the corresponding ion mass. Panel **e** shows the decomposition pathways and the *m/z* values for charged species that can be observed by MS labelled in blue (internal alkyne) and orange (terminal alkyne). The charged components of **3** and **4** are denoted by a red circle.

ligand occurs after 10 V and competing closely with the loss of one or two and four carbonyls. Intermediates resulting from cleavage of the Co-Co bond were not abundant, which is reflected in the calculated metal-metal bond strength versus the weaker metal-carbonyl bonds. According to the computational results, the loss of CO requires on average +50 kJ/mol less than cleavage of the Co-Co bond at any

given decomposition step (Figure 3.10). The ability for the alkyne to be removed intact even after loss of several CO ligands is interesting because it suggests that C-H activation of the alkyne is not necessary in the decomposition pathway, and this is doubtless a contributing factor towards the success of CCTBA as a cobalt ALD precursor. C-H activation can result in tenaciously bound, carbon-containing fragments that are difficult to release from the metal and contaminate the metal layer with unwanted carbon.[76]

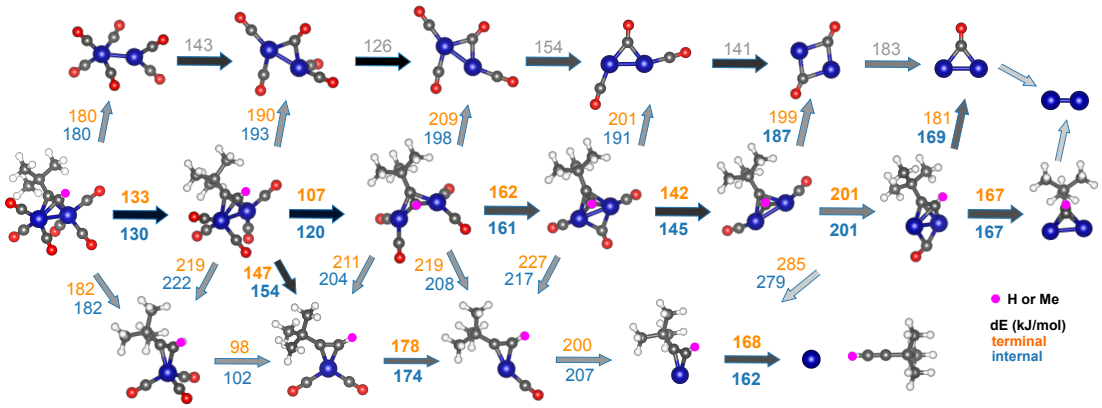

Figure 3.10: The predominant decomposition pathways computed for CCTBA. Orange/top numbers represent dEs for terminal alkyne and blue/bottom numbers for the internal alkyne. A pink sphere represents the position of H or Me.

These experimental findings were supported by computational results. The decomposition pathways of the neutral internal and terminal alkynyl complexes were investigated to directly compare the pathways of the ionic fragmentation observed by MS to pathways involving neutral species (Figure 3.10). Geometry optimizations were performed to obtain the minimum energy structure and electronic energy for each intermediate. The electronic *dE*s in Figure 3.10 are very similar between the terminal and internal alkyne which agrees with the similarities observed between decomposition of **3** and **4**. The most probable first and second steps were found to be CO dissociation and the cleavage of the Co-Co bond is less energetically feasible than loss of CO. Computational results also suggest that as carbonyl ligands are lost, the terminal alkyne binds more tenaciously than the internal alkyne. The *dE* increases for removing the terminal alkynyl in later decomposition steps. This is also in agreement with CID data in Figure 3.9 where the internal alkyne is removed slightly more easily than the terminal alkyne. Furthermore, the difference

in stability between the complexes after loss of one versus two carbonyls is also reflected in the *dE* for steps 1 and 2 in the middle pathway of Figure 3.10. The terminal alkyne proceeds through the first two CO losses with dEs of 133 and 107 kJ/mol for the first and second loss respectively, whereas the internal alkyne proceeds with a slightly lower energy of 130 kJ/mol for the first CO loss. The second loss of CO is significantly higher in the inernal alkyne, costing 120 kJ/mol. Hence, *m/z* 587 is a more prominent intermediate than *m/z* 601 (Figure 3.9**a**,**b**). The calculated cost of removing an initial CO is similar to the known experimental BDE of CO from $Co_2(CO)_8$ measured to be 138 kJ/mol.[77]

3.4.4 Surface deposition simulations

Simulations involving the Si(111) surface identified additional advantages of an internal alkyne for deposition. The weakened alkyne−Co bond was found to strengthen the interaction between Co and the surface during precursor decomposition. Furthermore, the internal alkyne also shows reduced reactivity towards the silicone surface, suggesting fewer impurities embedding into the film during ALD.

Decomposition by sequential loss of carbonyls was simulated on Si(111) for CCTBA and CCTMA to identify the stabilizing role played by the surface (Figure 3.11**a**). As in the gas phase, the carbonyl bond dissociation energies (BDE) are very similar between the internal and terminal alkyne. Strong chemisorption interactions formed in Step 4 after the loss of three carbonyls (Figure 3.11**a**). Chemisorption may also take place in earlier decomposition steps in the presence of a surface defect or with an opportune collision. The *dE*s were heavily dependent on the functional used to assess the carbonyl BDEs. Calculating accurate BDEs of metal-carbonyl complexes requires adequate inclusion of electron correlation.[194] In the periodic calculations using PBE/DZP, the metal-carbonyl bond strength was overestimated in the gas phase compared to results from PBE0/def-TZVP calculations (Figure 3.11**b**,**c**. However, trends across reaction paths for both precursors were consistent between methods. Observing surface interactions at a molecular level is a useful tool in understanding the deposition of these ALD precursors.

Over the course of precursor decomposition, the surface played an increasing role in stabilizing the precursor (Figure 3.11**b**). For both precursors, Step 3 of deposition shows a weakened surface interaction relative to the other steps (Figure 3.11 **b**,**c**; −172 and −115 kJ/mol) which precedes Step 4 where chemisorption interac-

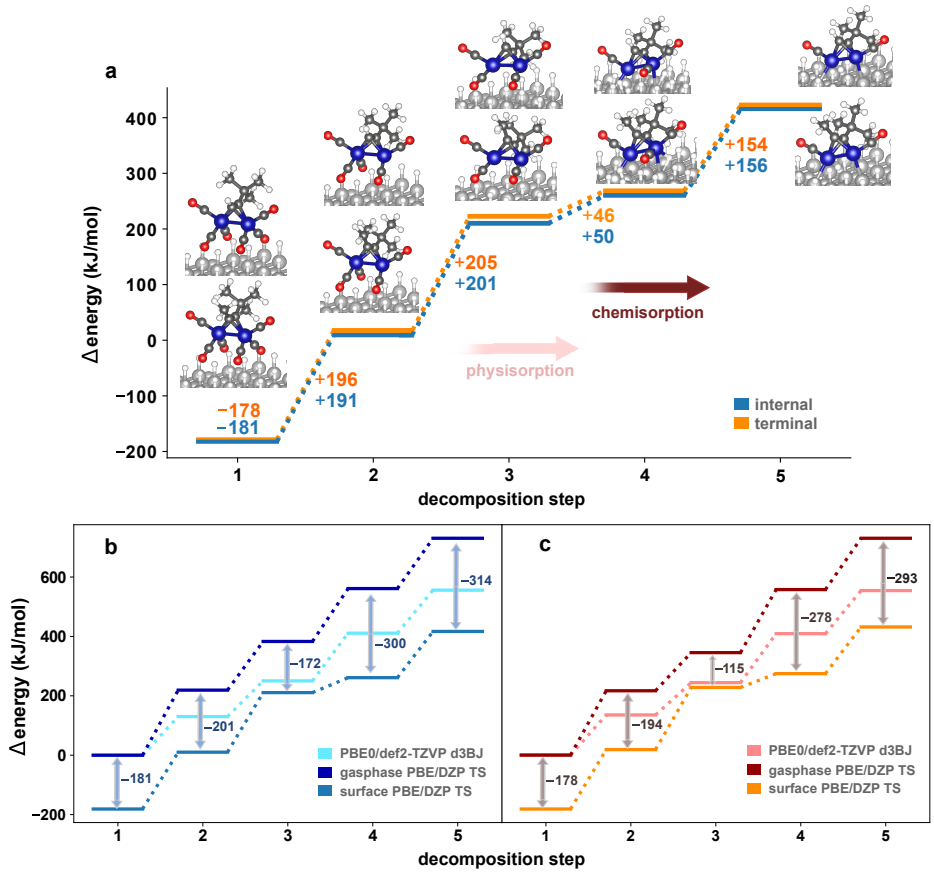

Figure 3.11: Delta Es plotted for the initial deposition steps on an intact Si(111) surface. Panel **a** shows the decomposition steps of CCTMA (blue) and CCTBA (orange) on the surface with corresponding adsorption geometries for each step. The ddEs values are labeled in orange for CCTBA and blue for CCTMA. Red arrows mark the transition from physisorption to chemisorption as the Co sequentially loses CO. These energies were benchmarked against gas phase data for CCTMA (**b**) and CCTBA (**c**) and the energetic stabilization offered by the surface is marked by arrows and numbers at each step. Light blue (**b**) and salmon (**c**) denote phase data obtained with PBE0/def2-TZVP(d3BJ), dark blue (**b**) and dark red (**c**) mark gas phase data obtained with PBE/DZP(TS) which was also the method used for surface calculations (blue **b**, orange **c**).

tions start to form and surface interactions strengthen significantly. Figure 3.11**b** and **c** show that or every decomposition step, CCTMA shows stronger interactions with the surface than CCTBA. These trends suggest that the internal alkyne in CCTMA allows Co to interact more strongly with the surface while a terminal alkyne is more tenaciously bound to the metal centers as observed in the experimental results from CID.

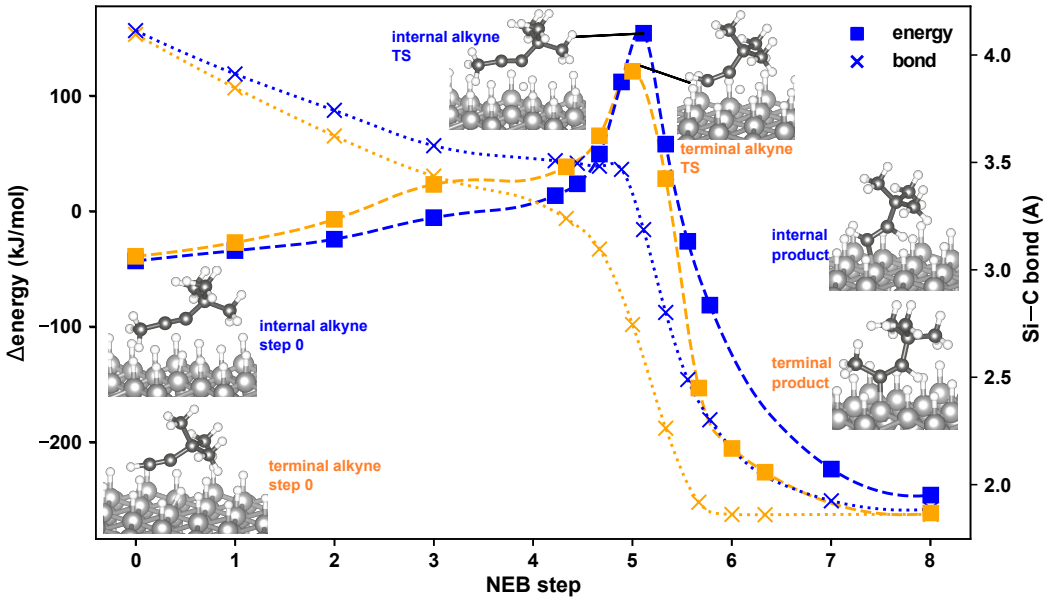

Figure 3.12: NEB results for hydrosilation of each alkyne on Si(111) surface. The bond length (x's) of the newly forming Si-C bond and delta Es (squares) for the internal alkyne (blue) and the terminal alkyne (orange) are plotted over the course of the reaction. Snapshots for the initial, transition state and the final step of the NEB calculation are labelled on the plot.

Finally, the reactivity of the terminal and internal alkyne ligand with Si(111) was investigated. NEB calculations were performed for an uncatalyzed hydrosilation reaction step on Si(111) (Figure 3.12). As expected, the reaction barrier for the terminal alkyne (120 kJ/mol) is lower than the internal alkyne (154 kJ/mol), supporting higher reactivity between the surface and a terminal alkyne. The newly forming carbon-silicon bond lengths are plotted over the course of the reaction path, showing a shorter bond distance for the terminal alkynyl carbon than the internal alkyne (yellow dotted lines in Figure 3.12 versus blue dotted lines). The internal alkyne remains farther from the surface until the transition state is complete, likely due to the steric hindrance introduced by the methyl group. These findings support an expected decrease in carbon impurities embedded into the Si surface in the presence of an internal alkynyl ligand.

3.5 Conclusions

The charged analogs of CCTBA and CCTMA precursors displayed trends that were consistent with computational results for the neutral species. Furthermore, the terminal and internal alkynyl cobalt carbonyl complexes shared very similar decomposition pathways both in the gas phase and on the surface. However, the experimental and computational data indicate that the internal alkyne is lost from the complex at a lower energy than the terminal alkyne. This suggests that CCTMA and other variants containing an internal alkyne have an increased facility of alkyne loss. Easy removal of the alkynyl ligand may be more desirable for ALD requiring low substrate temperatures. In computational studies, CCTMA showed stronger interactions with Si(111) during carbonyl loss compared to CCTBA. Finally, the reaction barrier of inserting each alkyne into a Si-H bond on the surface shows a higher barrier for a methylated alkyne, suggesting a lower rate of reaction with the surface and thus likely decreased carbon impurities embedded in Si during ALD.

This work suggests that internal alkyne alternatives will make deposition at lower temperatures possible due to easier removal of the alkynyl ligand and increased reactivity with the surface. Future work should involve the monitoring of other alkynes and perhaps new metal carbonyls to fully explore the potential of alkynyl ligands for ALD. CID data gave a first glimpse at what product ion species form in the gas phase under energetic stress and is a valuable tool for accessing gas phase information about precursor reactivity. ALD of CCTMA on Si should be performed and benchmarked against CCTBA to test the effects of temperature and measure the carbon-content of the deposited films. Internal alkynes are as affordable as the terminal TBA (e.g. 2-butyne, 2-pentyne, 2- and 3-hexyne are all cheaper than the $30/g cost of TBA) (Table S1). Testing the behavior of these simple alkynes will determine whether an inexpensive alternative to TBA can be paired with cobalt carbonyl for ALD to optimize the deposition of Co.

Chapter 4

Surface mechanisms during atomic layer deposition of cobalt silyl complexes

4.1 Introduction

Despite desirable properties of known precursors such as CCTBA including good volatility, thermal stability, and liquid state, deposited films often suffer from high carbon content.[195, 72] Furthermore, the deposition of cobalt onto silica surfaces using ALD is difficult due to the reluctant reactivity between the Co center and the terminal hydroxyl groups, requiring higher temperatures (above 400 K). Rather than forming an uniform monolayer of metal over the course of an ALD cycle, island growth is observed after depositing CCTBA onto Si and SiO_2 surfaces.[72, 39, 85] As mentioned previously, island growth is likely caused by impurities such as carbon binding to the surface and blocking further growth.[72] The Co species that do bind to the surface act as nucleation sites for further deposition and result in patchy, uneven layers which is what ALD is designed to avoid. However, an inherent lack of reactivity between Co and oxygen species on the surface is a challenging problem to tackle by modifying the precursor without also providing alternate mechanism for deposition. A precursor with better reactivity towards SiO_2 would have a profound impact on the versatility of ALD.

We propose and test a set of cobalt silyl precursors (patented by industrial collaborators at Seastar)[196] that show promise for incorporating of the first layer of

Co atoms into the surface. Rather than forming a Co-O bond with the surface (Figure 4.1**a**), the silyl group acts as a linker between the metal center and the terminal oxygen. (Figure 4.1**b**). In the perfect case, the silyl will react with two surface sites and eliminate two R groups; however, the first covalent bond formed with the surface can still encourage uniform coverage and avoid island growth. Then a second ALD step can be performed to target remaining carbonyl and R groups and leave behind a single layer of Si-Co on the silica surface. Introducing an additional layer of silicon atoms at the SiO_2–Co interface does not change the composition of the substrate since it simply acts as an extension of the bulk lattice. As depicted in Figure 4.1, the CoSi complex can deposit onto the surface via Pathway 1 by loss of carbonyl (**a**). We propose an alternative deposition Pathway 2 (**b**) available to $Co(CO)_4SiR_3$ species which is facilitated by targeted reactivity between the surface and silyl group.

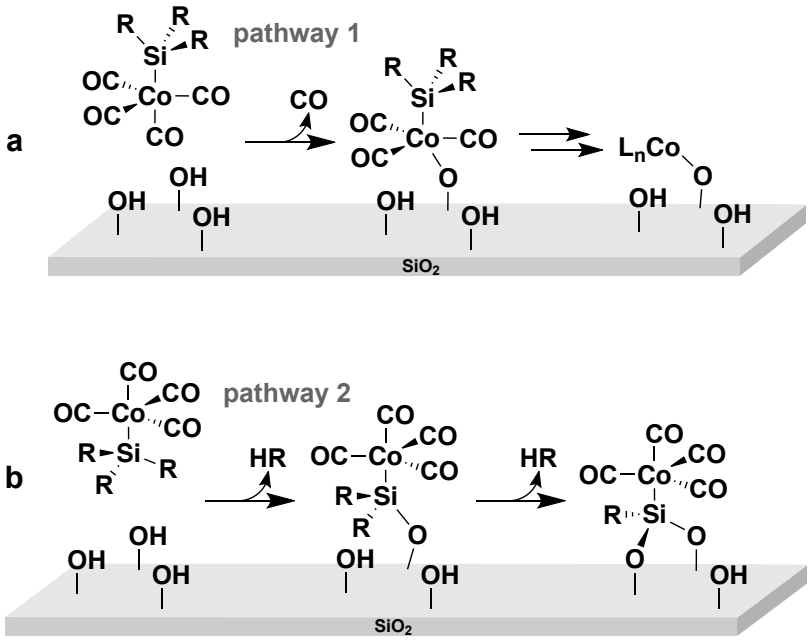

Figure 4.1: The two main deposition pathways of Co-silyl precursors onto SiO2. The common Co-down pathway proceeds through loss of CO (**a**). Pathway 2 depicts a deposition pathway facilitated by SiR_3 (**b**). R represents amine, halogen, alkyl and alkoxy groups. Note that a varying number of carbonyl groups may dissociate from the complex throughout the reaction.

4.2 Methods

4.2.1 CoSi precursor species

Cobalt-silyl (CoSi) complexes can be synthesized in a single step from cobalt carbonyl and the corresponding silane. The silane can carry a range of functional groups, making it a versatile handle for tuning the reactivity of the precursor. For this reason, CoSi precursors make promising candidates for the deposition of seed layers onto SiO_2. In this work, the deposition pathways of CoSi species (Figure 4.3) were modelled to understand the interaction between precursor ligands and various surfaces. Specifically, silyl groups were exchanged to probe the effect of the R groups on the most favored surface binding configurations and overall deposition mechanism (Figure 4.1). The gas phase decomposition pathways of 19 candidate precursors were benchmarked in addition (Figure 4.2). Of these nineteen CoSi complexes, we chose four representative compounds for closer investigation (SiR_3 where R = Me, Cl, NH_2, OMe).

Different silyl groups were modeled to probe the effects of functional groups on deposition (SiR_3 where R = Me, Cl, NH_2, OMe). Strong reactivity is not expected with trimethylsilyl ligands in CoSi1 while CoSi4 is expected to deliver chlorine to tenaciously bind to the surface. In practice, a silyl containing a bulkier amine than CoSi3 such as tris(dimethylamino)silyl should be used to provide better stability. There are many examples for aminosilanes with good thermal stability for deposition.[195, 197] By-products such as methanol and amines are preferable for their lower corrosivity towards metal substrates compared to reactive bipoducts containing halogens.[31, 198] Figure 4.2 shows R groups chosen to identify differences in stability, reactivity, and decomposition energy on the surface. In practice, mixing R groups can retain the selectivity for pathway 2 while offering the opportunity to tune properties of the CoSi precursor. The third R group, designed to be removed in the second ALD half-cycle, can be used to manipulate properties such as stability and solubility. Such precursors are included in the larger set studied in the gas phase.

Deposition pathways were modelled for CoSi1-4 on surface slabs (Figure 4) with periodic boundary conditions (PBC) using dispersion-corrected density functional theory (PBE-vdW-TS/DZP) in SIESTA. Periodic boundary conditions were applied for all calculations. The number of atoms per unit cell ranged between 100

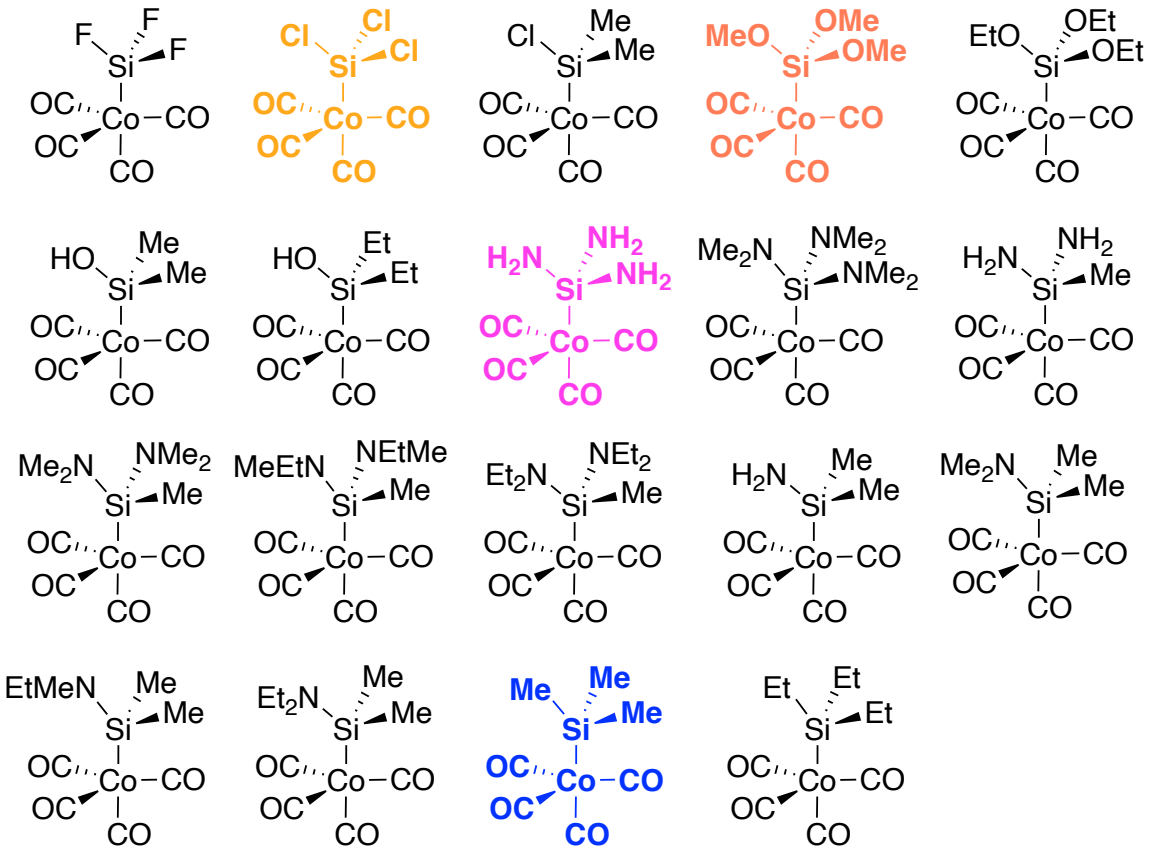

Figure 4.2: The nineteen precursors selected for computational gas phase benchmarking. From these, four complexes (**CoSi1** blue, **CoSi2** orange, **CoSi3** pink, **CoSi4** yellow) were selected for in-depth simulations of surface deposition Pathways 1 and 2.

and 200 to allow for ample spacing between reactive sites. Starting from crystallographic structures, the bulk atoms and lattice vectors were optimized (SIESTA, PBE/DZP). Finally, 50 angstroms of vacuum were introduced along the z axis and the terminal atoms in silicon and silica slabs were surface-capped with hydrogens or hydroxyls. In addition to silicon and silicon dioxide, copper surface was generated to gain information on performance on metallic surfaces.

All reaction energies were calculated using the general formula

$$\Delta E = \sum E_{prod} - \sum E_{react}$$

where E is the calculated absolute electronic energy of a given species. Adsorption energies E_{ads}, were calculated by taking the difference between a species in the

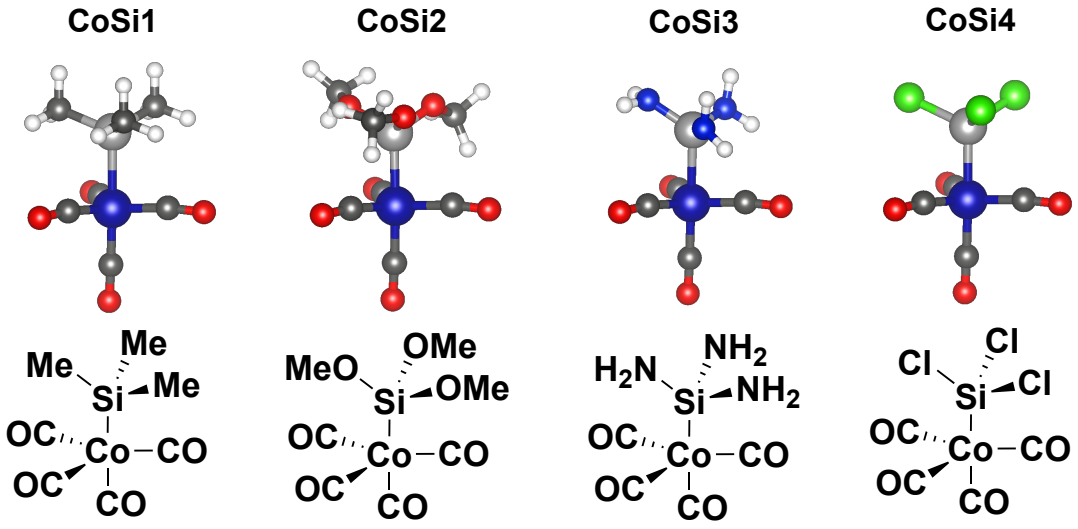

Figure 4.3: CoSi complexes with trimethylsilyl (CoSi1), trimethoxysilyl (**CoSi2**), triaminosilyl (**CoSi3**), and trichlorosilyl (**CoSi4**) ligands to facilitate surface deposition.

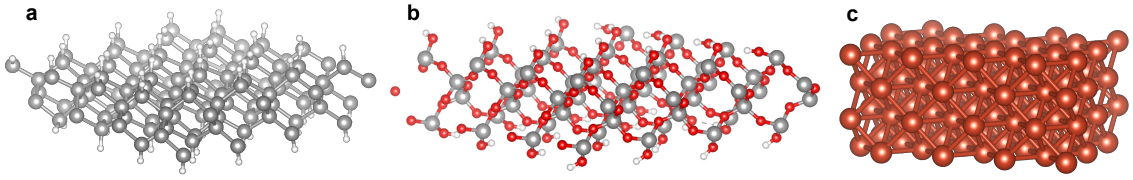

Figure 4.4: Silicon (a), silicon dioxide (b) and copper (c) surface slabs simulated in SIESTA. Deposition was simulated on the exposed 100 surface.

gas phase versus it adsorbed.

Three specific mechanisms were considered for the deposition of CoSi complexes (Figure 4.5) which differ slightly from generic Pathways 1 and 2. The deposition of metal carbonyls generally proceeds via loss of the volatile carbonyl ligands[80] as the metal strengthens its bond to the surface (Pathway A). Two silyl down pathways were compared to pathway 1. In Pathway B, the first R group is replaced by a bond to the surface. The remaining R groups are removed in subsequent steps before cleaving carbonyls. In Pathway C, however, one R groups is left on the silyl while carbonyls are removed. Modelling only the first step of the silyl-down pathway (Pathway B and C) provides a more direct energetic comparison to pathway 1 (Pathway A) in which Co coordinates to just one oxygen in the first ALD cycle. In the subsequent steps, the CoSi species was decomposed to observe

how the surface stabilizes the precursor during later stages of the ALD process (Figure 4.5). Comparing the minimum energy structures available for each pathway determines which pathway is more likely and how exchanging the R groups may affect these intermediate steps. If the initial steps of Pathway B are less uphill in energy than Pathway A, it suggests that the silyl will facilitate deposition onto SiO_2.

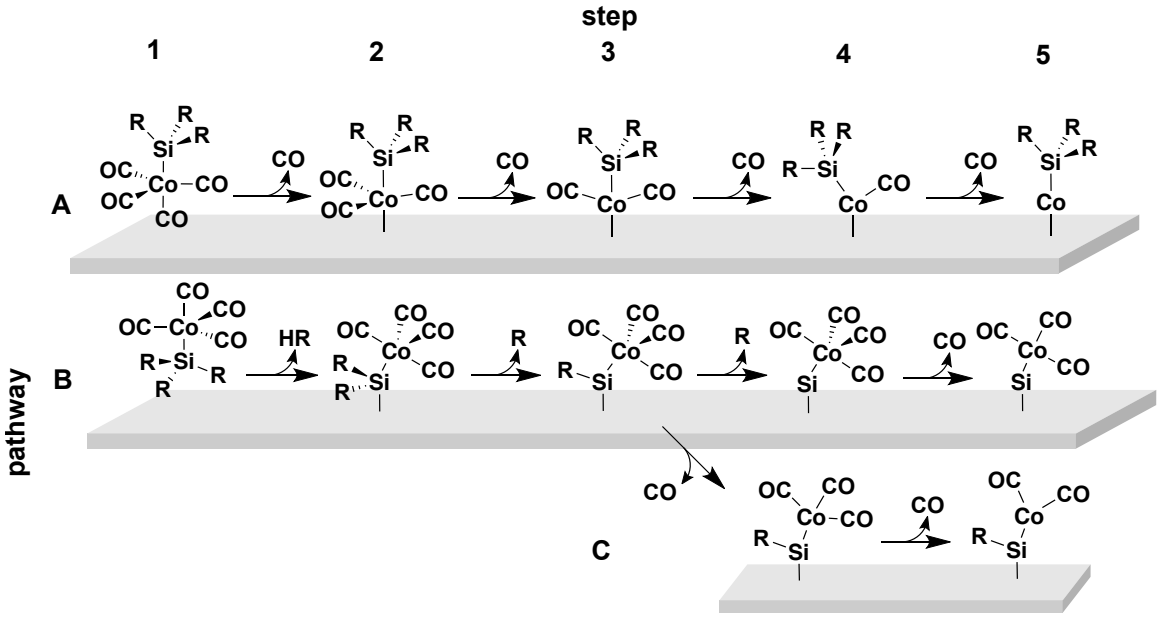

Figure 4.5: The three deposition mechanisms explored in this work. Pathway A is analogous to Pathway 1. Pathway B proceeds via the initial steps of Pathway 2 and is followed by loss of the third R group before loss of CO while Pathway C proceeds through loss of CO while retaining the third R group.

Ab initio molecular dynamics (AIMD) was employed to produce system trajectories at constant temperature and pressure. This was done to both (i) observe the interaction between the precursor and the surface over a brief time window ($\sim$1000 fs) and (ii) to ensure the most optimized intermediate structures and energies were found along the deposition pathway. The high dimensionality of the silica surface provides countless potential binding configurations which should be sampled beyond the local potential well of the starting geometry. AIMD samples these configurations freely from which new starting points can be selected for geometry optimization based on their energy and geometry.

Snapshots from local minima are only selected if they lie along the reaction pathway. For example, when a carbonyl dissociates from the CoSi complex, the

trajectory has progressed beyond chemical space containing the reaction step and cannot be used as a starting geometry (Figure 4.6**a**). However, this trajectory does demonstrate progress along the reaction coordinate between step 3A and 4A (dissociation of CO of Pathway A) for CoSi3 deposition on SiO_2. When a timestep samples a local minimum corresponding to the original reaction step, a geometry optimization can be performed to determine if it leads to a better structure (Figure 4.6**b**). In Figure 4.6**b**, a geometry optimization starting from 741 fs yields a 0.074 eV improvement over the original optimized geometry. Performing AIMD often leads to finding lower energy structures and, in a few cases, new configurations were nearly 1 eV lower in energy.

Although expensive, incorporating AIMD into the regular workflow greatly increased the confidence in the geometries obtained. In many cases, starting two geometry optimizations from slightly different positions on the surface resulted in a significant energy difference ($>$0.2 eV). AIMD combats this by escaping shallow minima and falling into deeper potential wells. In many cases, a single 600 fs simulation yielded one or more alternative configurations of the same reaction step. Figure 5 shows the workflow for computing reaction paths with precursors and surfaces containing high degrees of freedom. Once the surface is prepared as discussed previously, precursors are placed near the surface and optimizations are performed to obtain an initial guess for the binding configuration. Other structures can be sampled by performing AIMD to generate alternative binding configurations.

4.3 Results and discussion

4.3.1 Adsorption and surface binding

Surface adsorption energies were investigated for atomic Cobalt and the biproducts from decomposition of the CoSi precursors. These interactions are influenced by properties such as electronegativity and intermolecular forces such as hydrogen bonding. Three cases were considered for writing balanced reactions for CoSi deposition onto the surface (Figure 4.8). Case one is the simple adsorption of a ligand such as CO. Case two results in the elimination of H (using heat and/or a co-reagent). Case three involves the elimination of two hydrogens, one from the ligand and one from a capped surface. Note a catalyst and co-reagents which may be involved to help the reaction proceed have not been included. H_2 was used

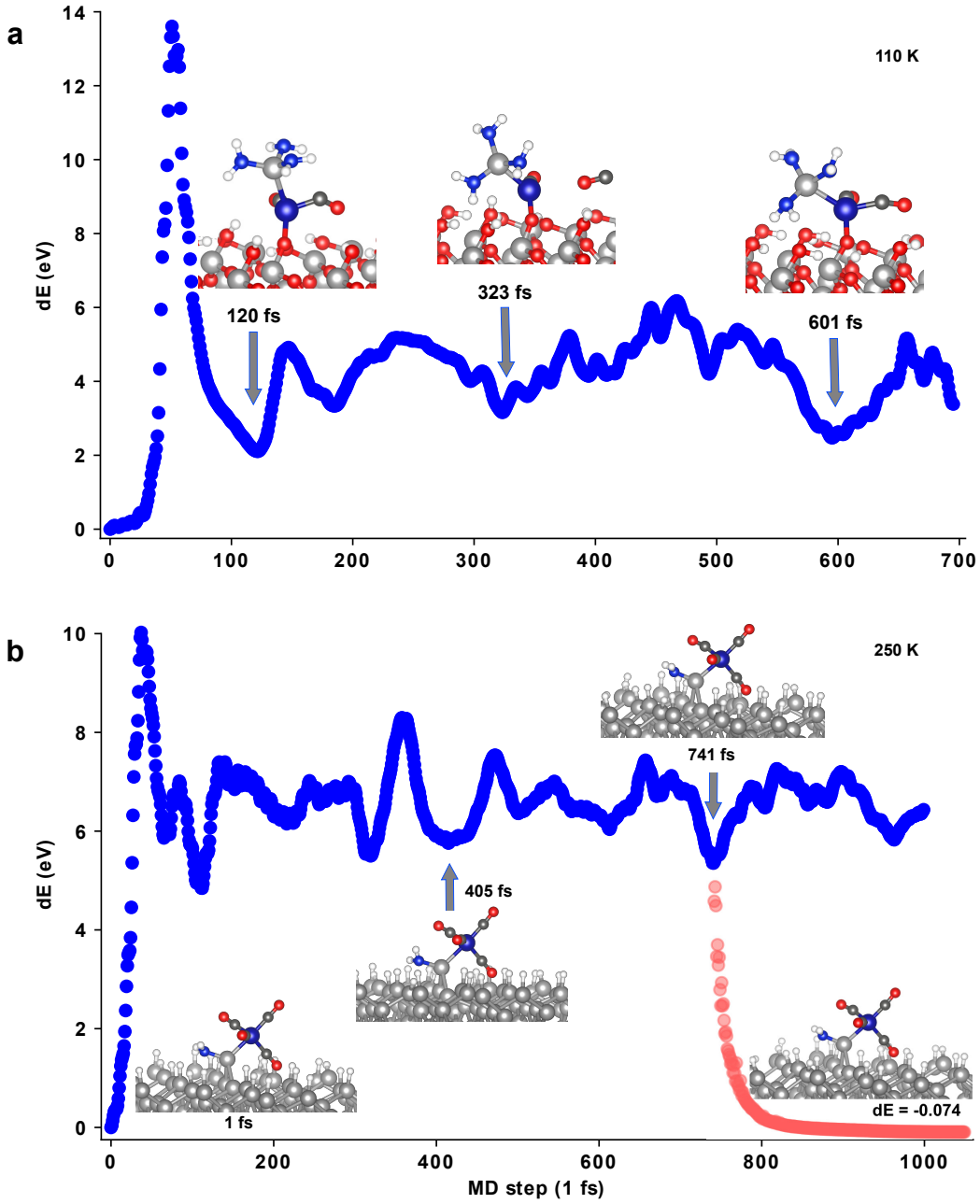

Figure 4.6: Example plots of the MD trajectory. Energies are plotted from an AIMD trajectory of CoSi3 on SiO_2 in step 3A (**a**) and CoSi3 on Si in step 3B (**b**). In a, 120 and 601 fs are good candidates for geometry optimization. However, while passing 323 fs, the trajectory shows the dissociation of a carbonyl. In **b**, a geometry optimization is shown in red, starting from 741 fs and yields a 0.074 eV improvement over the original geometry.

as a source of hydrogen as a consistent benchmark for energy. Adsorption energies were calculated from the difference in absolute energies between the gas

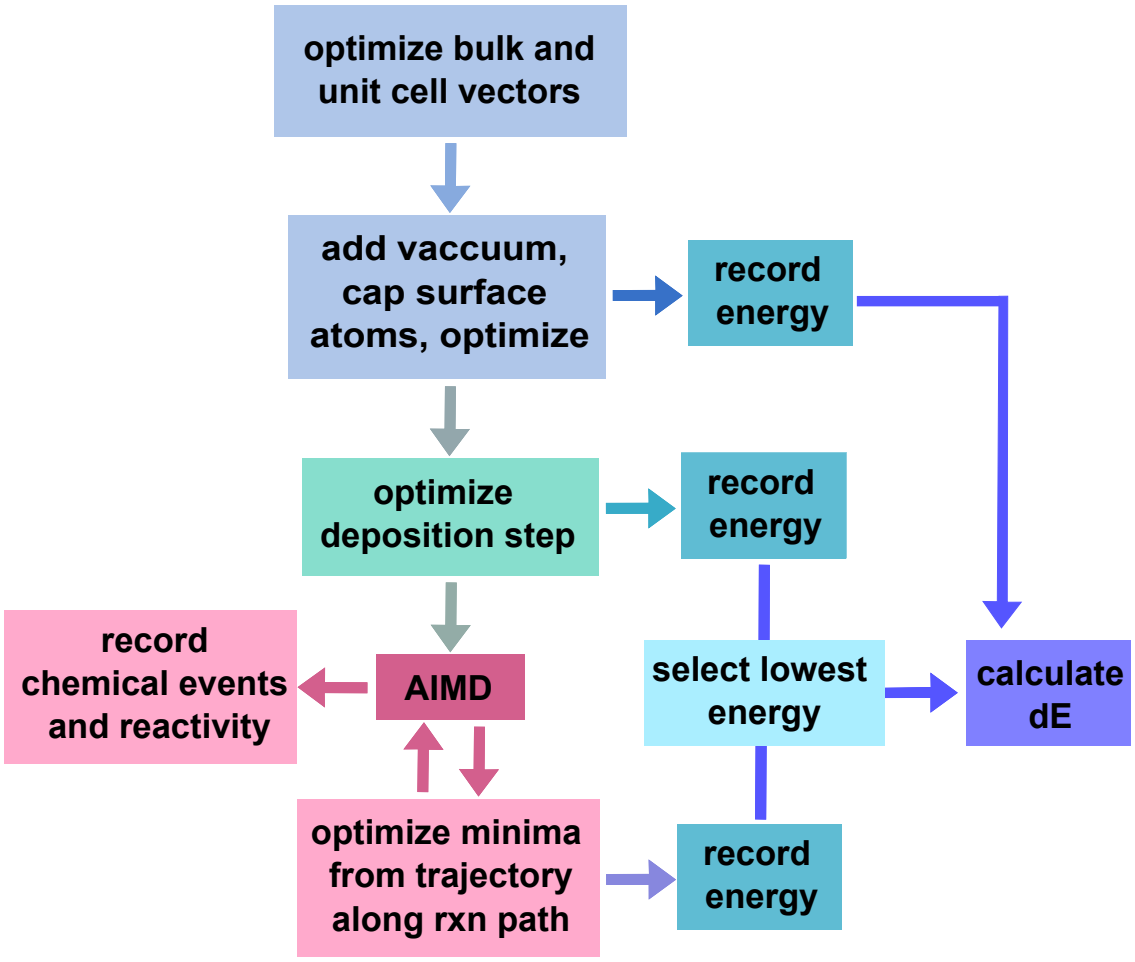

Figure 4.7: The workflow for modelling the deposition reaction pathway using SIESTA. AIMD (red) was used to sample multiple possible binding configurations and choose the lowest energy structure per reaction step.

phase adsorbate and the bound adsorbate (Figure 4.8 Case 1). They represent how strongly Co interacts with the surface and how difficult it is to remove various impurities from the surface.

Case 1: no hydrogens	$CO + surf \longrightarrow surf-CO$
Case 2: one hydrogens	$HR + surf \longrightarrow surf-R + 0.5\,H_2$
Case 2: two hydrogens	$HR + H-surf \longrightarrow surf-R + H_2$

Figure 4.8: Three cases to consider when writing balanced reactions on the surface. Case 1 is the simple adsorption of a ligand such as CO. Case 2 results in the elimination of hydrogen (using heat and/or a co-reagent). Case 3 involves the elimination of two hydrogens, one from the ligand and one from a capped surface

As expected, Co exhibits very strong binding with the Si surface (Figure 4.9). Despite starting from a position above the surface, atomic Co embeds itself deep into the surface layer of silicon. On the other hand, a reaction between Co and SiO_2 involves overcoming an activation barrier. During geometry optimization, Co remains loosely bound to a single terminal oxygen and hovers above the surface layer. If manually moved or simulated for enough time by AIMD with enough energy to overcome the barrier, Co will form a much stronger bonding interactions with the first bulk layer of SiO_2 (Figure 4.18, bulk layer refers to the start of bridging Si-O-Si). However, notably fewer AIMD trajectories led to the described strong bonding interactions on SiO_2 when compared to the Si surface. The "guarding" OH groups likely explain the inherent lack in reactivity between Co and SiO_2.

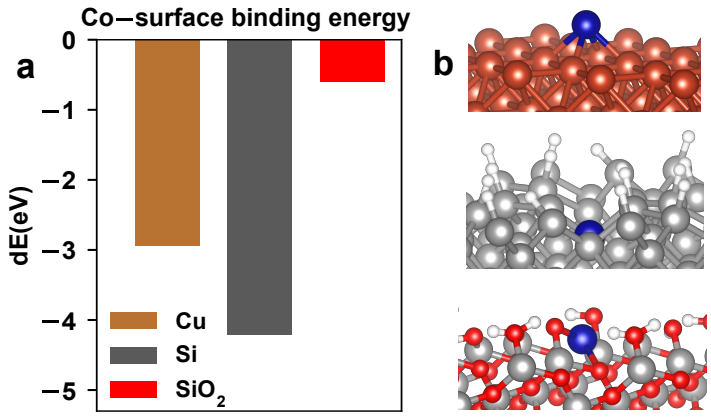

Figure 4.9: The surface binding energy of a single Co atom onto Cu (brown), Si (grey) and SiO_2 (red) (**a**). Panels on the right **b** show the corresponding geometries of Co adsorbed onto Cu, Si, and SiO_2 (top to bottom).

Furthermore, it is important to consider the affinity of decomposition products towards the surfaces to identify side reactions that might take place during ALD. Therefore, the surface reaction energy was calculated for CO and the R group of each silyl which are produced and exposed to the surface during ALD. Since surface deposition results in the formation of HR product species, Case 2 should be considered on copper and 3 should be considered on SiO_2 and Si surfaces when writing the balanced reactions show in Figure 4.8. Shown in Figure 4.10, HR adsorption onto SiO_2 is unfavorable and generally worsens with electronegativity of the R group. While methyl most easily binds to the surface oxygen species, Cl and methoxy species showed the least favourable reaction energies with SiO_2. The

coordination of R species to the Si atoms beneath the OH capped SiO_2 surface was not explicitly performed and AIMD simulations did not reach these configurations (over the course of 1000-2000 fs simulations). However, these Si atoms may be involved in the adsorption of reactive species and should be further investigated.

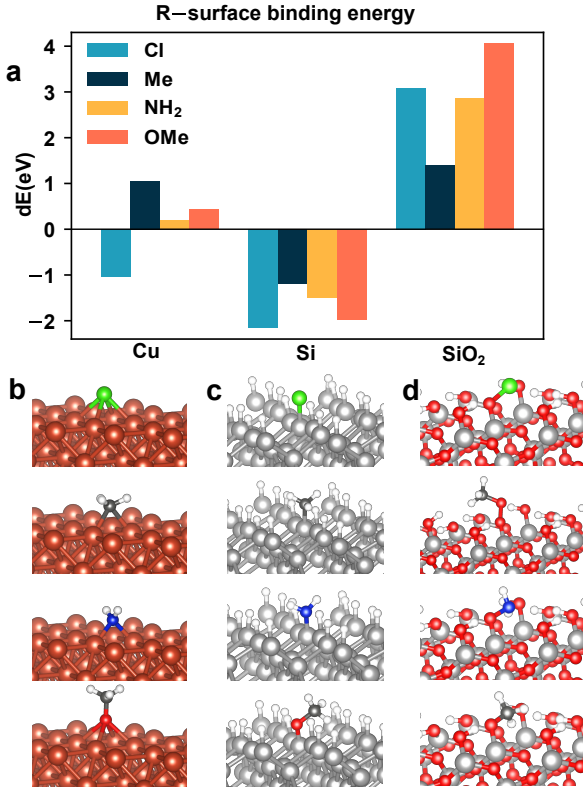

Figure 4.10: The surface binding energy of each R group. Plot a shows the binding energy of Cl (teal), Me (navy), NH_2 (yellow), OMe (red) onto Cu (brown), Si (grey) and SiO_2 (red). The optimized geometries are shown for binding on copper (**b**), silicon (**c**), and SiO_2 (**d**).

The adsorption energies of CO were calculated to highlight the differences across surfaces as well as provide a benchmark for other adsorption energies (Figure 4.11). Carbonyls are a popular ligand for ALD precursors because they are relatively inert and dissociate as neutral ligands upon adding heat. CO adsorbs strongly onto silicon while its interaction is only somewhat favorable towards Cu. However, CO adsorption onto SiO_2 is unfavorable suggesting any side reactions with carbonyl during deposition onto SiO_2 are unlikely.

Step 1 for Pathways A and B represents the adsorption of the CoSi species onto the surface. Despite observing a mixture of favorable and unfavorable interactions between decomposition products and the surface, the precursors themselves

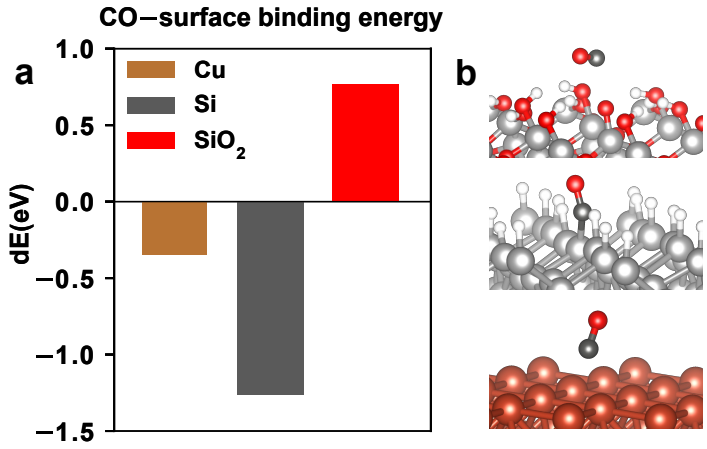

Figure 4.11: Adsorption energies of CO on Cu, Si and SiO_2 surfaces. Panel **a** shows adsorption energies on Cu (brown), Si (grey) and SiO_2 (red), and panel **b** shows the corresponding geometries.

all demonstrate favorable adsorption energies to each surface (Figure 4.12). The silyl groups demonstrate a strong influence over these trends. While CoSi4 tends to have weaker interactions with the surface, the methoxy groups on CoSi2 correspond to enhanced adsorption energy across all surfaces. While these interactions do not describe a change in chemical bonding, they are the first step in deposition. If a precursor experiences a strong attraction to the surface, it is more likely to spend greater amounts of time by the surface. This increases the likelihood of a reaction taking place.

4.3.2 Deposition mechanisms

The primary gas-phase decomposition pathway of all 19 CoSi species were calculated, showing very similar dEs across different silyl groups throughout the sequential loss of CO (Figure 4.13). Interestingly, the third loss of CO is the easiest reaction step and shows the tightest agreement across all species. Steps 4 and 5 show the most disagreement between all species however the most common outliers are the silyls containing halogens. As the most electron-withdrawing groups, they demonstrate the effect of induction on the decomposition pathway; stabilizing intermediates 2 and 3 during loss of CO whilst resisting steps 4 and 5 with higher dEs than the rest. Because coordination to CO involves back-donation into the π^* orbital from the meta center, a strong EWG on the silyl may remove some elec-

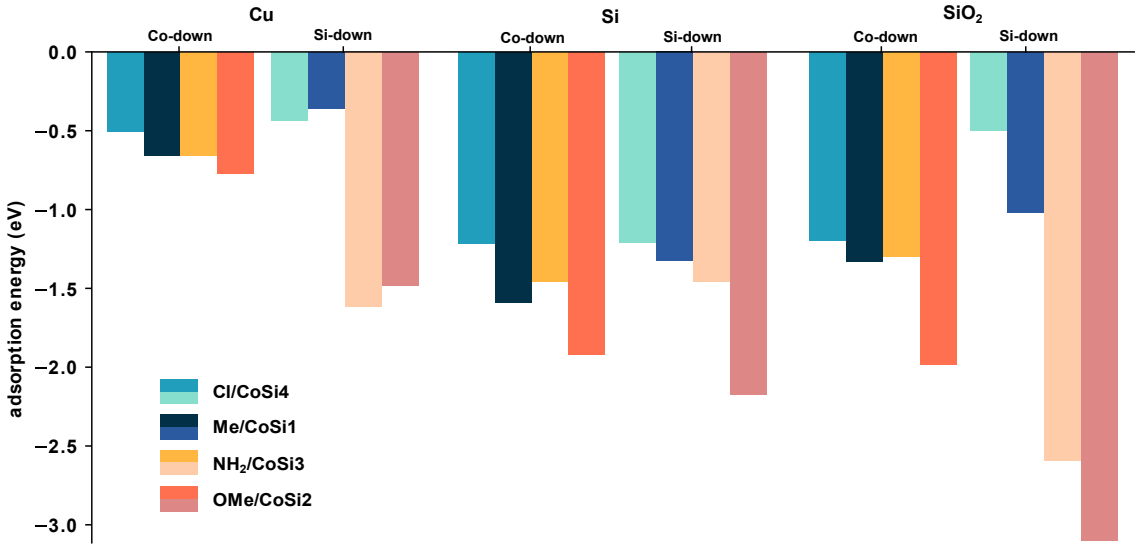

Figure 4.12: The adsorption energies of all precursors in both orientations for each surface plotted. Eight bars show the adsorption energy of the 4 precursors in the silyl down and Co down for Cu, Si and SiO_2 (left to right). Co-down pathways are plotted in the first cluster while Si-down pathways are depicted in the second cluster with light colors.

tron density available to the carbonyls, weakening their bonds to the metal. On the other hand, homolytic cleavage of the metal—silyl bond is more difficult when the EWG on the silyl are bound tenaciously to the metal as seen during formation of step 5.

As mentioned, later steps in the decomposition do not occur in the same ALD step and are often facilitated by a co-reagent. Therefore, early steps in the pathway (steps 1-3) are the most important indicators of even coverage with minimal side reactions. The more uniform the behaviour of the precursor, the more an ALD procedure can be optimized for a specific deposition pathway. Therefore, an energy separation between the pathways is desirable to avoid both taking place under the same conditions.

Pathway A and Pathway B were modeled for CoSi1-4 on Cu, Si and SiO_2 surfaces. AIMD was used to confirm binding configurations of intermediate species and their absolute energies were collected and plotted in reaction coordinate diagrams. In all cases, the surface stabilized the decomposition pathway. However, the preferred Pathway changed depending on the surface (Figure 4.14). The copper surface showed no strong preference for one pathway over the other. However, Si and SiO_2 both showed preference for one pathway over the other. Si prefers

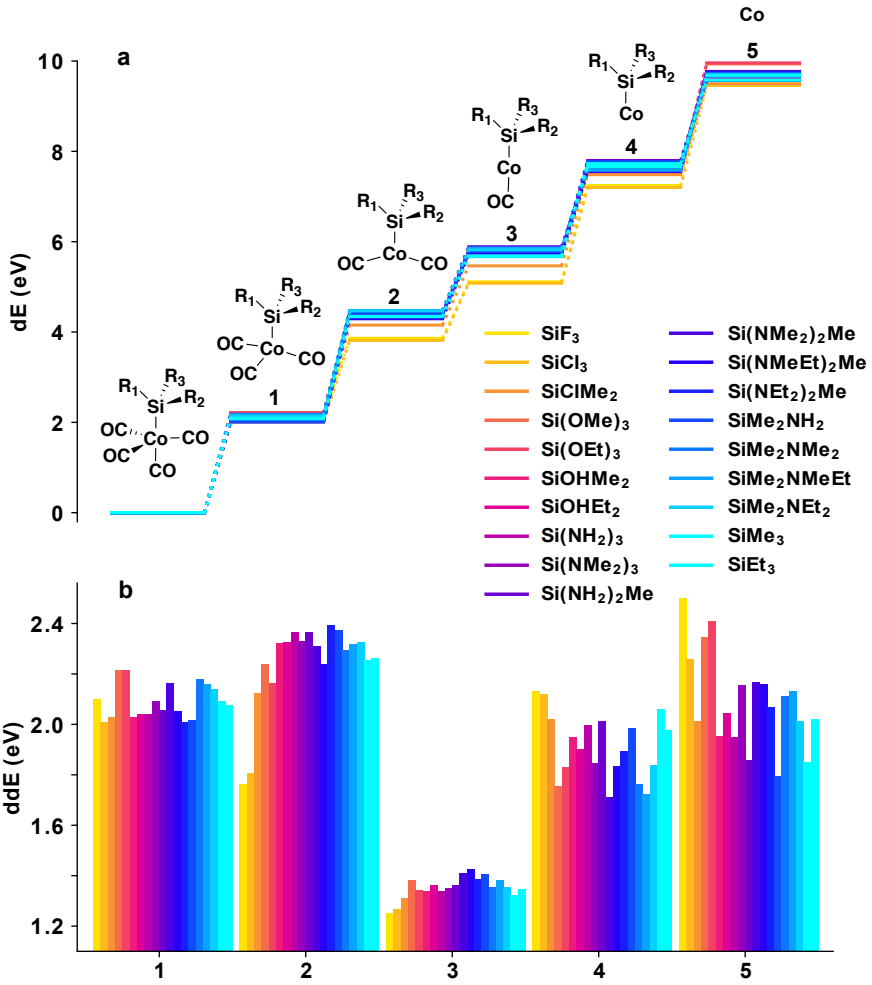

Figure 4.13: The gas phase decomposition of all 19 CoSi precursors. Plot a shows the dE over the course of gas phase decomposition via loss of CO. Plot b compares the ddEs for each step across all precursors. Precursors were ordered by approximated electronegativity spanning R groups from halogens (yellow) to alkoxy groups (red) to amino groups (purple) to alkyl groups (blue).

Pathway A which offers more interaction with the metal center whereas SiO_2 shows preference for Pathway B which involves the silyl group. This results strongly suggests that CoSi will offer better reactivity with SiO_2 than traditional Co precursors which are designed to bind to the surface directly through the metal center.

A closer look at individual deposition pathways reveals the effect of the silyl groups. In the case of Cu, the preferred pathway not only changed across different precursors but there was often crossover during middle deposition steps. Figure 4.15 shows the *dE*s for depositon pathways A, B and C on copper for each CoSi precursor along with the optimized geometries. CoSi1 and CoSi4 are the most sta-

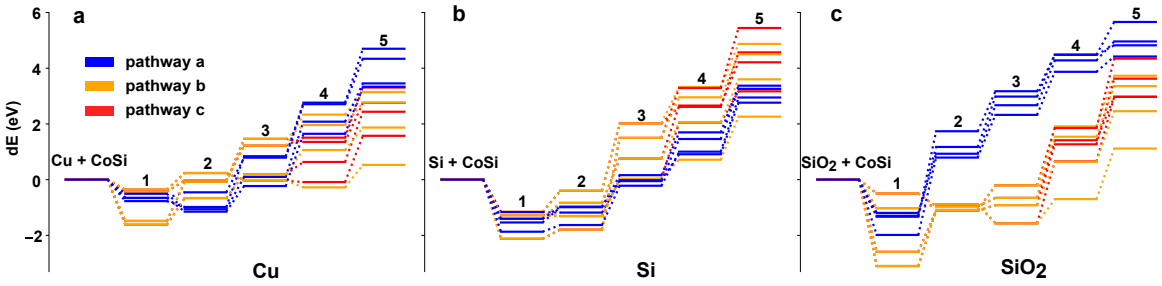

Figure 4.14: The surface deposition pathways of all 4 CoSi precursors. The *dE* of deposition for pathway a (blue), b (orange) and c (red) are compared on Cu (a), Si (b) and SiO_2 (c) and show that pathway selectivity is largely determined by the surface type.

bilized by Cu surface during deposition. However, CoSi1 observes a crossover in optimal pathways between steps 2 and 4. Both Co and Si coordinate strongly to the Cu surface as the reaction progresses. From these results, it is not apparent that a silyl group serves a mechanistic purpose for deposition of Co onto Cu. Existing precursors such as $Co_2(CO)_8$ or CCTBA already[cite] perform well on copper.

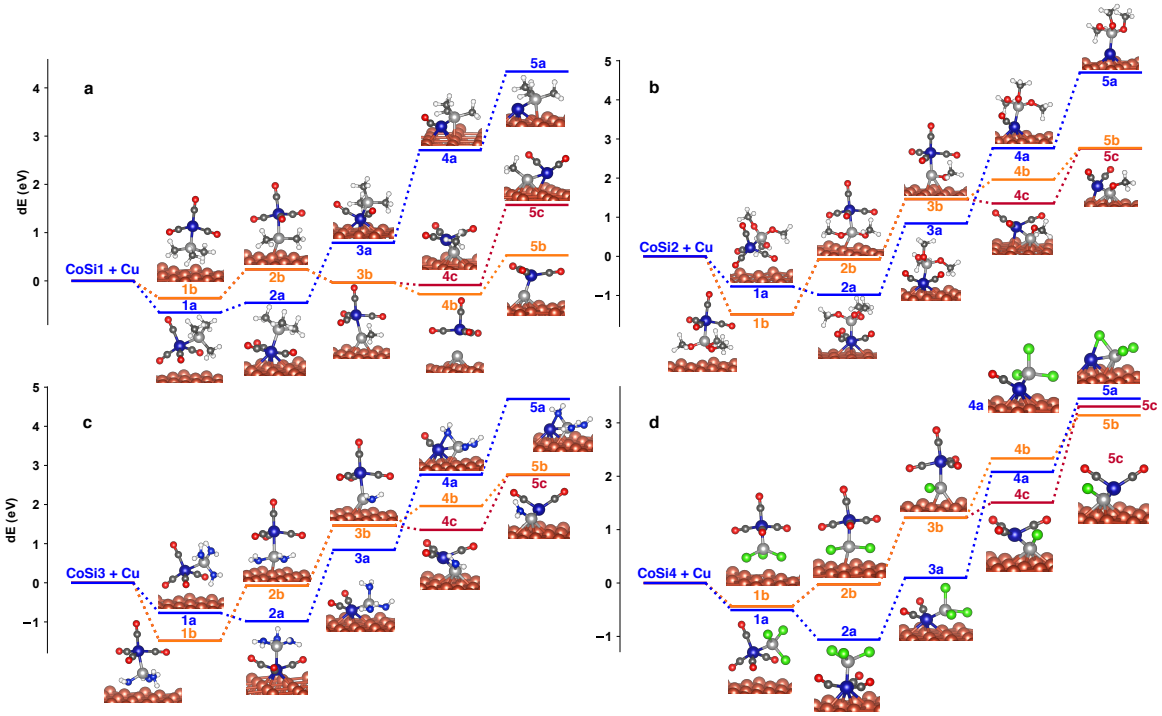

Figure 4.15: The deposition of CoSi precursors onto Cu. Pathway A (blue), B (orange), and C (red) are overlaid for the precursors ($SiMe_3$ (**a**), $Si(OMe)_3$ (**b**), $Si(NH_2)_3$ (**c**), and $SiCl_3$ (**d**).

As shown in Figure 4.14, deposition of CoSi precursors on the silicon surface favors Pathway A which directly involves the metal center rather than the silyl. However, CoSi1 is the exception where Pathway B is preferred during the decomposition steps on Si(100) (Figure 4.17). The strong affinity for a pathway involving Co corroborates experimental evidence, where relatively good reactivity permits deposition of Co precursors at lower temperatures ($<$100 °C). The most stabilized decomposition pathways on Si were seen for deposition of CoSi3 via Pathway A and CoSi1 for Pathway B. CoSi4 has the greatest separation in energies between pathways for steps 2 and 3. Despite the selectivity for Pathway A, selecting a CoSi precursor for ALD may still provide some advantages. The incorporation of carbon impurities into silicon can be avoided by using an chloro or amine-based silyl ligand. Secondly, CoSi precursors offer the control of stepwise ALD using a reductant since Co is oxidized unlike cobalt carbonyl which undergoes thermal ALD.

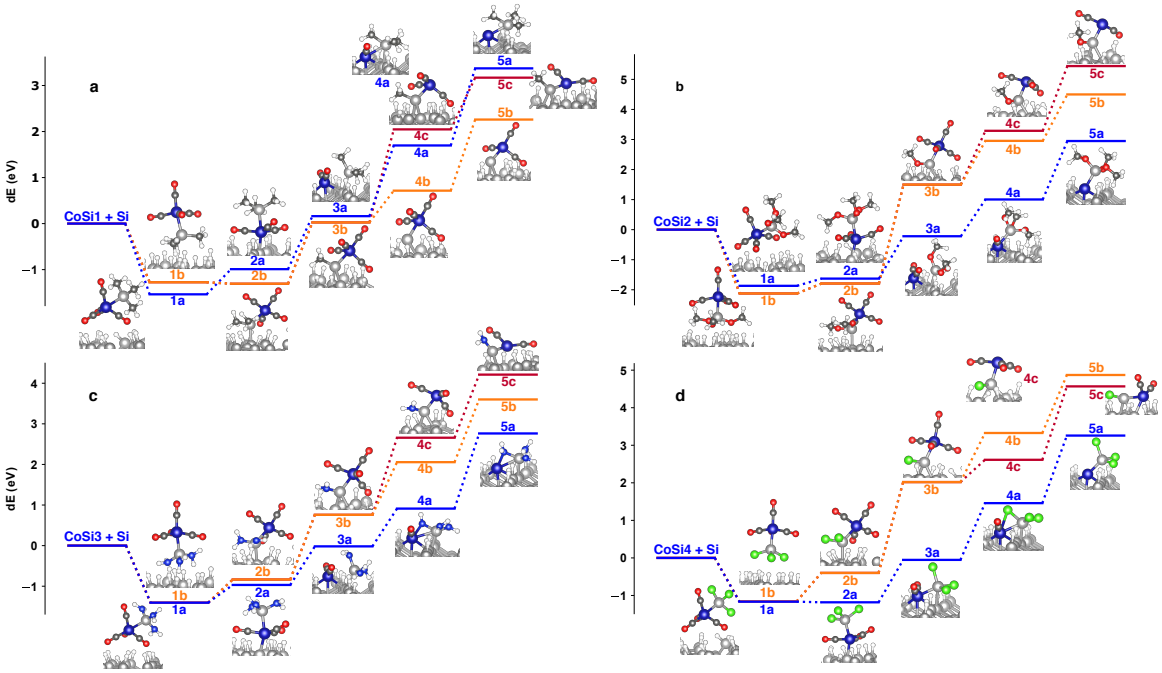

Figure 4.16: Deposition of CoSi precursors onto silicon. Pathway A (blue), B (orange), and C (red) are overlaid for the precursors ($SiMe_3$ (**c**), $Si(OMe)_3$ (**b**), $Si(NH_2)_3$ (**c**), and $SiCl_3$). The Si surface shows a general preference for Pathway A (blue) except in the case of CoSi1.

Finally, modelling CoSi depositing onto SiO_2 exhibited the potential for a silyl group to facilitate reactivity. No matter the R group, involving the silyl in deposition through Pathway B or c resulted in much lower energies throughout the

entire pathway. The most surface-stabilized decomposition pathway once again involved CoSi1, however, to avoid exposing the surface to reactive carbon species (methyls), any of the other CoSi precursors showed good separation between pathways. In this case, Pathway B was modelled with the silyl only coordinating to one oxygen to form intermediate 2b (Figure 4.17). However in practice, intermediate 3 can coordinate to a second oxygen to eliminate HR. This may drive the deposition pathway to even lower energies. Based on these results, CoSi precursors should be considered very promising candidates for assisting the deposition of Co onto SiO_2. It is worth noting that CoSi only needs to be used for the initial cycles of ALD to obtain good coverage of SiO_2 and once the substrate is Co, conventional precursors can be used for further film growth.

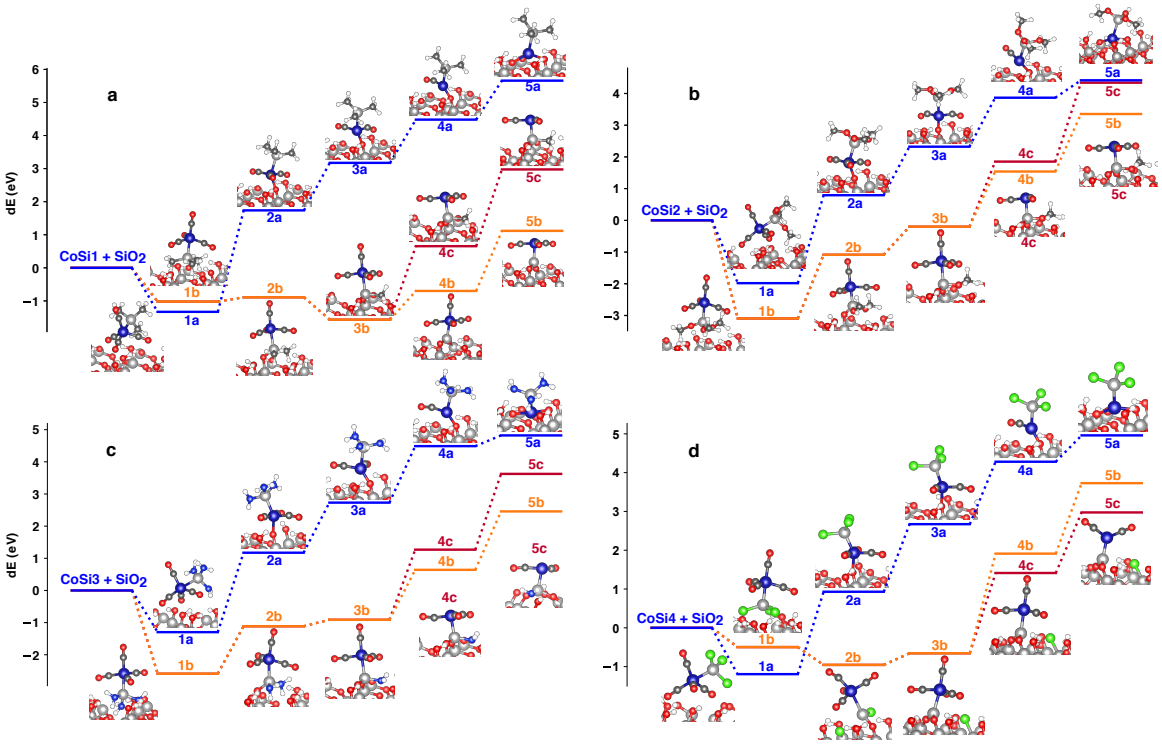

Figure 4.17: Deposition of CoSi precursors onto SiO_2. Pathway A (blue), b (orange), and c (red) are overlaid for the precursors ($SiMe_3$ (**a**), $Si(OMe)_3$ (**b**), $Si(NH_2)_3$ (**c**), and $SiCl_3$). SiO_2 shows a high selectivity for Pathway C (orange) and B (red) to involve the silyl group.

Computational results showed no evident benefits from using CoSi for deposition onto Cu. However, the results from modelling deposition onto silicon favors a metal-surface bond during decomposition. While this result in particular may not

indicate a need for the silyl to deposit Co onto Si, a carbon-free precursor such as CoSi3 or CoSi4 may offer a solution for avoiding carbon-silicon impurities that plague ALD of common Co precursors. Finally, as illustrated in Figure 4.17, the SiO_2 surface shows a stunning selectivity for involving the silyl group in deposition rather than the Co. Rather than forcing reactivity between the Co center and terminal OH groups, using a silyl linkage between Co and the surface offers a creative solution to avoid high temperatures and poor surface coverage.

4.3.3 AIMD simulations on the surface

AIMD provides a glimpse into the interactions at the surfaces. Dissociation of silyls and carbonyls, tenacious surface binding through the Co center, strong van der Waals interactions and side reactions were some of the interactions showcased in the hundreds of simulations performed. Through AIMD interactions, the dynamics of adsorption processes were determined. For example, how many carbonyls needed to be lost before Co becomes reactive with silicon versus copper versus silica surfaces (1-2 for Cu, 1 for Si and 3 for SiO_2). Treated silicon and copper surfaces show reactivity towards CoSi precursors, while the strong stability of the silica surface, makes it a more inert environment. Therefore, surface interactions were least observed in simulations involving SiO_2. In fact, while atomic Co freely incorporated itself into Cu and Si surfaces, strong bonding to the SiO_2 required initiation by either placing the atom beyond the guarding OH groups or by running AIMD. Once the barrier of approaching the first bridging layer of SiO_2 was overcome, a much stronger bond formed between Co and the silica surface (Figure 4.18).

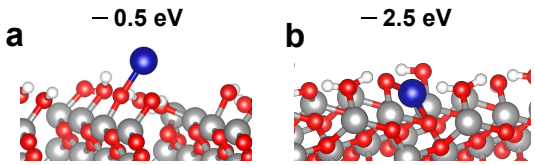

Figure 4.18: Two geometry optimizations of Co on SiO2. Initializing a couple angstroms apart result in a 2 eV difference in binding energy.

The strong coordination between atomic CO and Si was also captured with AIMD when starting from the step 5a intermediate for CoSi1 (Figure 4.19**c**). The Co readily dissociates from $SiMe_3$ to dig into the Si surface as seen for atomic Co.

Since this was not observed for other CoSi precursors, it may indicate a more reactive Co-silyl bond when electron donating groups are attached to the silyl group. Furthermore, the silicon surface is an electron-rich environment which may destabilize the Co-silyl bond.

Reaction steps such as free loss of carbonyls were successfully captured by AIMD (Figure 4.19**a**). the loss of a carbonyl is necessary to initialize reactivity with the surface by freeing a coordination site on Co. Furthermore, the loss of subsequent carbonyls during later stages of deposition is also observed (Figure 4.19**b**). In late stages of Pathway A, an intact silyl ligand forms a bridging R group to temporarily satisfy vacant coordination sites on Co (Figure 4.19**b**). This is regularly observed for all R groups during AIMD except for OMe.

Finally, chlorine of CoSi4 is an exciting R group to observe during AIMD. It will dissociate from the silyl to strongly interact with all surfaces, including SiO_2. In an extreme example, it dissociated from the silyl group during a geometry optimization (Figure 4.19**d**). While chlorine is corrosive towards metal surfaces, $SiCl_4$ is a common precursor for deposition of both silicon and silica. The question remains whether Cl will interfere with the successful deposition of cobalt. While a $Co(CO)_4SiCl_3$ complex was successfully synthesized and crystallized by a colleague, it remains to be determined whether it is suitable for ALD.

AIMD simulations provided some insight on the behaviors of each precursor on various substrates. Now that likely intermediates have been established by AIMD and geometry optimizations, reaction barriers can be obtained to quantitate the reactivity of each reaction step. While the silyl group shows favored reactivity towards the SiO_2 surface, it is shown that carbonyls readily dissociate, frequently leaving open coordination sites to interact with the substrate. Measuring the activation barriers for the elimination of target R groups (Figure 4.2) during deposition will provide further insight on which R groups best facilitate the silyl-down pathway.

4.4 Conclusion

The cobalt-silyl family of precursors are strong candidates because (i) they are easy to synthesize and have good volatility, (ii) they offer a Co—CO reactive center which is a common choice for metal precursors because the carbonyls can leave as neutral ligands, and (iii) the silyl group is easily functionalized, offering an alter-

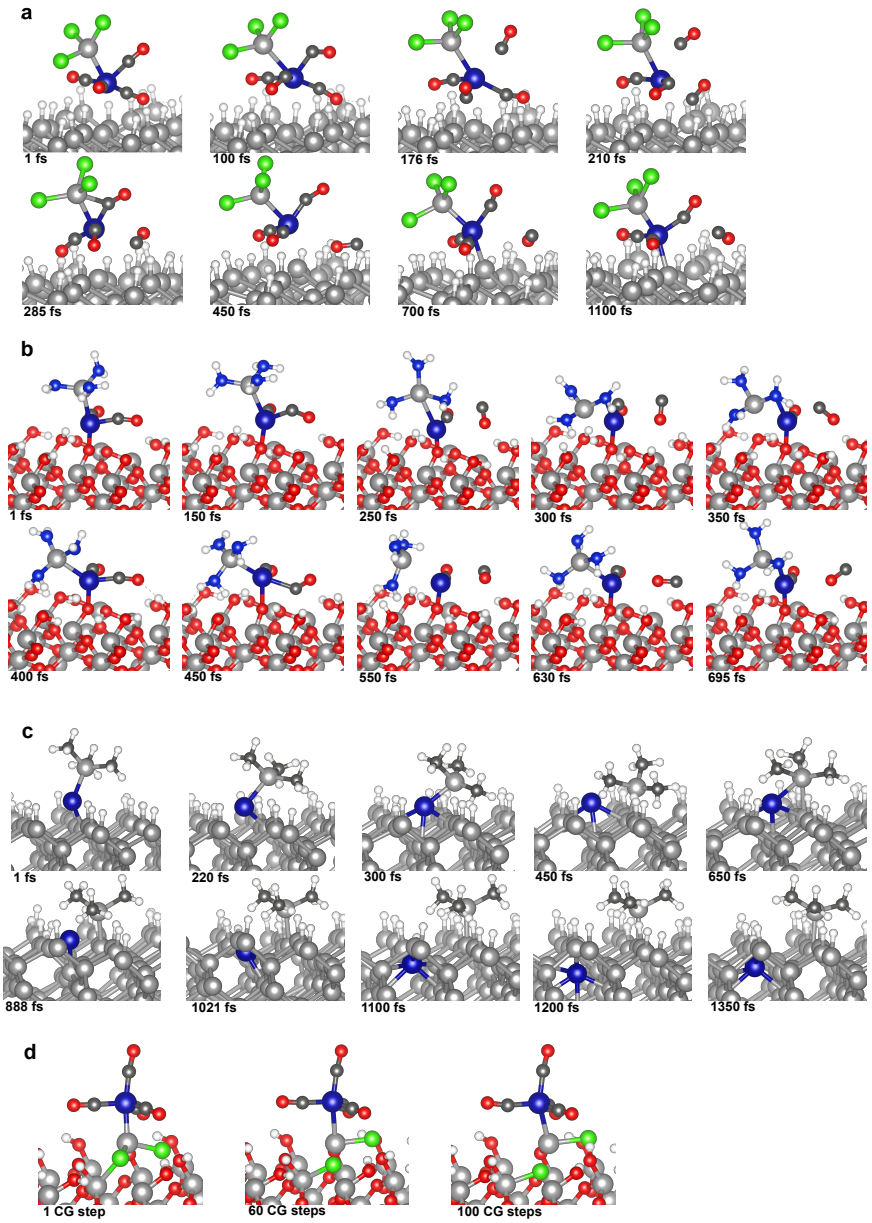

Figure 4.19: Snapshots from reaction steps which occurred in sequence during AIMD or geometry optimizations. Panel **a** shows the association/dissociation of CO from CoSi4 on Si in a trajectory starting from step 1. Panel **b** shows association/dissociation of a carbonyl from CoSi-3 in a trajectory starting from step 3 on SiO_2. Panel **c** shows the trajectory of CoSi1 after loss of all carbonyls as depicted by Pathway A. Panel **d** shows a geometry optimization of CoSi4 during step 2 of Pathway B. All Si surfaces were modelled at 250 K, while SiO_2 system was simulated at 110 K to achieve reasonable atom velocities.

native reactive handle for binding to the surface.

In all cases, the silyl-down pathway was lower in energy during deposition onto SiO_2. In particular, the initial steps of deposition are consistently more favorable which is important for tethering the gas phase precursors evenly across the surface sites. NH_2 and OMe groups exhibit strong dispersion interactions with the surface during the initial adsorption step onto silica. These results all suggest that the alternate deposition pathway offered by the silyl groups may improve ALD deposition over traditional Co-down mechanism involving sequential loss of carbonyls.

AIMD is a useful tool for observing dynamic behaviour between precursors and the surface. It can also assist in identifying optimal surface sites for coordination and sampling multiple binding configurations. The configurations generated from AIMD often provided lower energy structures in geometry optimizations compared to starting structures.

The mechanisms were observed for deposition of Co-down species. One which did not involve the silyl coordinating to the surface, one in which the Co and silyl both formed strong interactions with the surface and a third where a carbonyl or R group from the silyl formed a bridging configuration between the Co and Silyl. In some instances, the Co-silyl bond was broken as both species bound to the surface. Common trends and binding pathways were identified across precursors and surfaces. While the Si surface prefers deposition Pathway A which directly coordinates Co to the surface, the CoSi precursors can offer an alternative to carbon-based precursors and avoid the incorporation of carbon impurities. Unless incorporation of silicon is desired, CoSi precursors showed no advantages for deposition onto Cu. For most CoSi precursors, the deposition pathways showed energetic crossover partway through deposition, indicating very little selectivity towards a particular mechanism.

The limited success of Co ALD onto SiO_2 can be tackled by seeking to understand the reaction mechanisms that take place on the surface. By directly addressing the problem of inherent poor reactivity between Co and the surface oxygen atoms, and seeking an alternative mechanism, the challenges of ALD can be overcome. The deposition of CoSi precursors shows potential for improving the reactivity with SiO2, resulting in better coverage and allowing for lower deposition temperatures. If these precursors show success in practice, the CoSi model can be applied to improve deposition of other transition metals onto SiO_2.

The computational methods employed to simulate CoSi on various surfaces

provided insight over the promise of a new precursor to overcome challenges with Co ALD. Understanding the mechanisms by which Co precursors deposit onto surfaces will guide the design of new precursors. Issues with SiO_2 coverage during ALD arise because (i) the binding energy between Co and the terminal groups is not strong and (ii) the binding sites on the surface are widely spaced compared to other substrates such as Si and Cu (Figure A.1) If impurities occupy a single coordination site, it disrupts the buildup across a larger area.

Chapter 5

Benchmarking methods, system size and predicted performance of high spin metal systems during oxygen reduction

This chapter discusses an ongoing project with colleague Brett Henderson which was initiated through a MITACS Accelerate internship partnering with OTI Lumionics and the Quantum Algorithms Institute. The work was shared equally between us. Generally, my role was generating the geometries and energies of periodic and molecular systems. The optimization of atomic systems were performed by us both for different metals. Henderson performed subsequent single point calculations using various methods including CCSD(T). Initially, I was the primarirly person corresponding with OTI and generating one- and two-electron integrals of neutral single-metal systems for iQCC. However, Henderson took on the correspondence along with the method development for preparing alkaline systems for OTI. Section 5.3.3 and 5.3.4, discuss work still underway and are therefore somewhat inconclusive.

5.1 Introduction

Several barriers stand in the way of widespread adoption of Proton-exchange membrane fuel cells (PEMFCs) in commercial vehicles, including durability, power

density, and cost. Fuel cell stack durability is reduced by factors such as membrane degradation, carbon electrode corrosion, and catalyst instability.[199, 200, 201] Power density relies on good transport of O_2, high catalyst activity, and high electrochemical surface areas,[202] of which the latter two factors often conflict with the final barrier to PEMFC adoption: cost. While the US Department of Energy has set ultimate cost targets at $30/kW,[200, 203] current PEMFCs have an estimated cost between $50/kW and $75/kW.[200]

One contributor to persistent high costs is the use of platinum, typically in the form of platinum nanoparticles dispersed on a porous carbon substrate, as a catalyst of both the hydrogen oxidation reaction at the anode and the oxygen reduction reaction at the cathode.[200, 202, 204, 205, 206] In addition, platinum catalysts are prone to degradation from contaminants, such as carbon monoxide and NO_x compounds.[205, 206] While PEMFCs typically rely on platinum catalysts at both electrodes, in practice, areal loadings of platinum are roughly four times higher at the cathode to compensate for the slower oxygen reduction reaction.[202] Therefore, much research has gone into reducing platinum group metal (PGM) loadings at the cathode or replacing Pt altogether in order to reduce costs and make PEMFCs a viable commercial product.

Typical strategies to reduce PGM catalyst reliance include increasing the mass activity of the platinum or eliminating PGM catalysts altogether. Increased mass activities can be achieved by engineering the platinum nanostructure to increase the number of catalytic sites, as by generating cage structures[207] or synthesizing especially reactive surface planes.[208, 209] In addition, shape-controlled nanoparticles of platinum alloyed with base metals like nickel can increase specific activities while reducing platinum content.[210, 211, 212] A related strategy involves passivating the surface of nanoparticles of other less expensive materials, including platinum alloys, with a thin layer of reactive platinum.[202, 210, 211, 213, 214] The most successful approach to eliminating PGM catalysts altogether has been the use of catalysts containing iron or cobalt coordinated to nitrogen and carbon, or Fe/Co-N-C catalysts. In 2017, Ballard Power Systems and Nisshinbo commercialized the first PEMFC with a non-PGM catalyst at the cathode,[205] but much work remains to make these catalysts competitive with PGM cathode catalyst layers, especially for EV applications with large power requirements.

Despite their promise, PGM-free catalysts generally demonstrate activities about 10-fold lower than platinum-based catalysts and poor durability.[205] Because of

the lower activity of PGM-free catalysts, catalyst layers are made significantly thicker than their PGM counterparts.[202, 205] At high current densities, this can result in degraded power output due to poor mass transport of O_2, protons, and electrons through the thicker layer.[202, 205, 206] Possible remedies to this situation include optimizing the mass transport properties of the catalyst layer by tuning the porosity of the carbon support,[215] increasing the turnover frequency of catalytic sites by carefully tuning the electronic structure and morphology of the M-N coordination complexes, or increasing site density. The latter two approaches are quite amenable to computational study via electronic structure methods.

The initial development of Fe/CoNC catalysts was guided largely by chemical intuition. However, recent computational studies have been crucial in driving rational catalyst design by investigating the electronic and geometric structure of catalyst sites and linking them to experimental activities. A combination of advanced spectroscopic techniques such as X-ray absorption near edge structure and *ab initio* calculations using density functional theory have helped identify FeN_4 sites as the most stable and catalytically active constituents of FeNC catalysts.[206, 216] Since then, density functional theory has been used to examine how the electronic structure and catalytic activity changes upon the presence of solvent,[216] additional ligands,[217, 218, 219, 220] metal supports,[221] and bimetallic catalytic sites containing either a second Fe atom or different metals such as Co, Ni, Cu, and Pt.[217, 218, 222]

Furthermore, molecular hosts have been shown to host active sites for ORR with good stability. Porphyrin and phthalocyanine-based macrocycles are common scaffolds for various metal centers and have been shown to catalyze ORR as molecular catalysts.[223, 224, 225] These macrocycles also offer opportunities for ligand functionalization to tune catalyst properties before being incorporated onto a conductive matrix through pyrolisys, polymerization or more gentle self-assembly procedures.

Despite these advances in understanding, many open questions remain in the rational design of PGM-free oxygen reduction catalysts. For one, it is critical to gain a better understanding of how the coordination chemistry and specific ligands bound to catalytic metal sites affect their activity in order to improve it. In addition, most computational studies have supposed a pristine graphene or graphene nanoribbon support. While this can offer insight into the stability and activity of catalysts at edge vs bulk sites, more work needs to be done to understand how de-

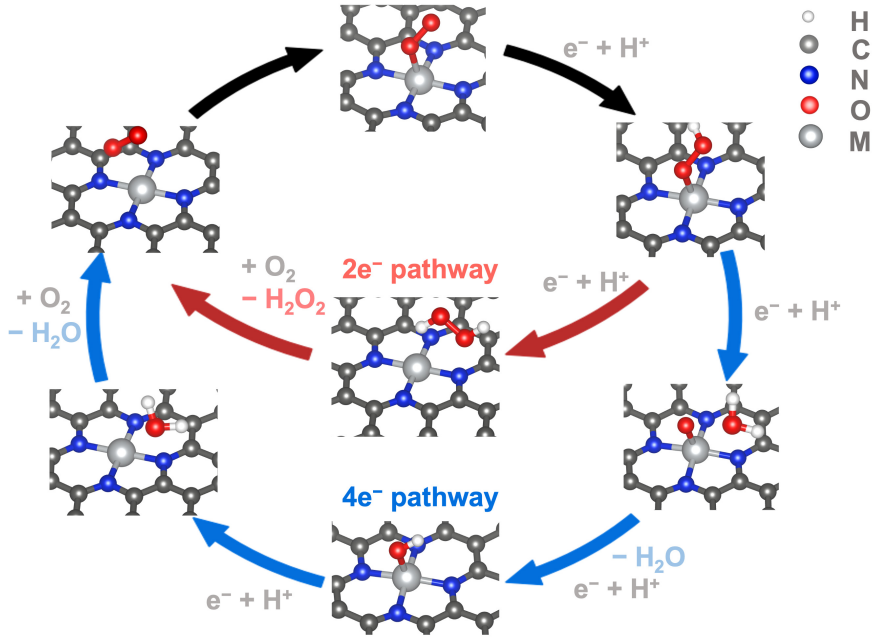

Figure 5.1: Two- and four-electron pathways on a graphene-embedded MN_4 catalyst of the associative pathway for the oxygen reduction reaction. Blue arrows depict the four-electron pathway and red arrows depict the two-electron pathway.

fects in the local graphene environment, such as vacancies or substitutions, impact the chemistry of the active site. As poor durability is known to plague PGM-free devices, further investigation into the various mechanisms for degradation, including catalyst poisoning and structural changes in the operating environment, is also necessary.

Finally, although density functional theory has proven an invaluable methodology in investigating these catalysts, its accuracy in treating transition metal catalysis can be called into question. For instance, Anderson and Holby found that the H–O, H–OH, H–OO, and HO–O bond strengths calculated while examining the oxygen reduction pathway on these catalysts was significantly overestimated relative to experiment, leading to incorrect reaction potentials.[219, 220] In addition to the limitations of simplified solvent models, some of the calculation errors can be attributed to the approximations made by the exchange-correlation functionals used, which fail to consistently capture electronic correlations in these systems to a desired accuracy. These approximate functionals are derived from simpler sys-

tems of non-interacting electrons and sometimes parameterized with experimental data,[226, 227] meaning there are many flavors to choose from. Unfortunately, it can be hard to know *a priori* which functional will perform best for a given system, and the accuracy of DFT generally degrades when studying systems far from equilibrium (e.g. bond dissociation and some transition states) and transition metal chemistry, which often involves highly correlated states.[226, 228] Therefore, DFT can leave much to be desired when studying the catalysis of the electrochemical reactions at fuel cell electrodes. The importance of the computational modeling of fuel cell catalysts warrants the exploration of higher-level methods that escape the approximations and system-dependent parameterization of density functional theory.

In contrast, higher level methods such as coupled cluster theory or Quantum Monte Carlo compute this correlation energy to greater accuracy but are only accessible for small molecular systems on the order of tens of atoms using existing classical hardware.[228, 229] In addition, to make them more tractable, practical implementations of coupled cluster usually involve truncations of the theory that reduce its accuracy in describing states with large correlation energies.[227] In order to study heterogeneous catalysis in fuel cell electrodes, models are needed that can accurately represent nanostructured transition metal catalysts embedded in carbon scaffolding.

This work sets out to benchmark a multitude of computational approaches to describe the ORR pathway. Periodic MNC catalysts are simulated for multiple transition metals that have been experimentally tested as PGM-free alternatives. Furthermore, molecular scale catalysts with porphyrin and phthalocyanine scaffolds are simulated at a slightly higher level of theory. Finally, single metals were modeled using a variety of methods to i) test the consistency between these methods, ii) identify if any trends were replicated from larger systems and iii) compare the electronic energies along the ORR pathway between the metals.

5.2 Models and methods

5.2.1 Computational models

Three different types of models for non-PGM ORR catalysts were investigated and are hereafter referred to as the *periodic system*, *molecular systems*, and *single-*

atom systems. The periodic model consisted of a graphene sheet with six carbon sites replaced by an MN_4 unit, where M is Fe, Co, Mn, or Ni (Figure 5.2a). This type of system is well studied using DFT as a model for catalysts formed by pyrolysis of precursors such as porphyrins.[230, 231, 232] Our particular model contained 122 carbon atoms and a single MN_4 site per supercell to allow for adequate spacing between active sites. The molecular models studied consist of phthalocyanine- and porphyrin-metal complexes, where the metal site was also substituted with Fe, Co, Mn, or Ni (Figure 5.2b-d). Such complexes are easily synthesized and functionalized and they have demonstrated experimental promise in ORR.[230, 231, 232, 233, 224] Finally, the atomic model consisted of a single metal atom of the element types listed above (Figure 5.2e).

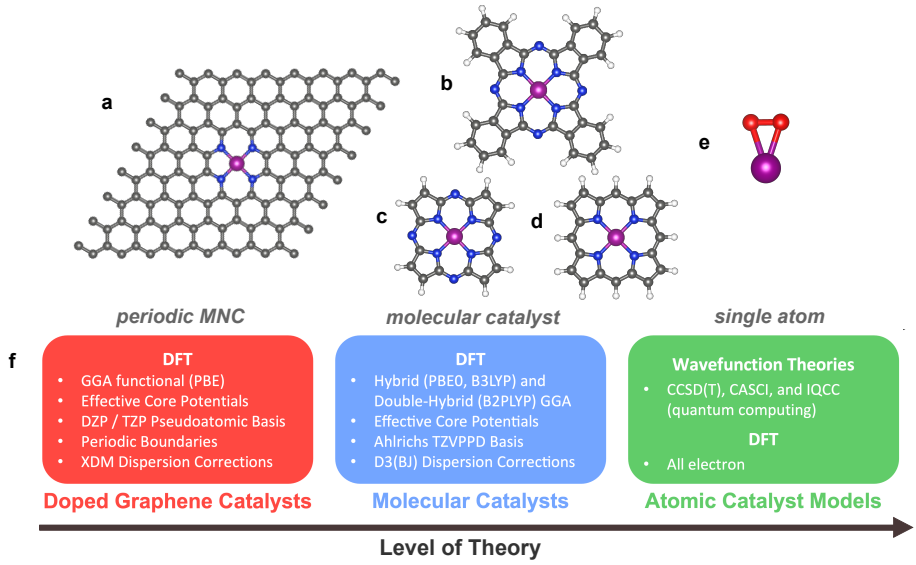

Figure 5.2: Model systems and methods. In the periodic MNC catalysts (**a**), the transition metal is embedded in a periodic graphene scaffold. Molecular systems include phthalocyanine (**b**), an abbreviated phthalocyanine catalyst (**c**) with missing aryl groups and porphyrin (**c**). The single-atom system (**e**) shows Mn bound to O_2 in the first step of ORR. A summary of the computational methods surveyed for each of the three system types is provided below (**d**).

5.2.2 Computational methods

In studying the models described above, the computational methods employed followed the expected trade-off between system size and theoretical accuracy (Figure

5.2f). For each system-type, geometries and single-point electronic energies were computed along the two- and four-electron pathways stemming from the associative pathway. To assess the free energy along each ORR pathway, the energy of free $H^+ + e^-$ can approximated as being equal to half of the Gibbs free energy of gaseous H_2. This strategy was first introduced by Nørskov as the computational hydrogen electrode model.[234, 235] In the following reaction pathways, we adapt this model for electronic structure calculations. Only the electronic components of the free energies for ΔEs are used in order to benchmark the various methods used to assess the electronic structure specifically.

Periodic system calculations employed spin-polarized DFT under periodic boundary conditions using numerical atomic orbitals, as implemented in the SIESTA code [131]. Exchange and correlation were treated with the generalized gradient approximation using the PBE functional [135] and vdW-TS dispersion corrections were applied.[236] Troullier-Martins effective core potentials from the SIESTA database [182] were used alongside a TZP basis for atomic and cell optimizations. A spacing of 50 $\mathring{A}$ was included between sheets and a single K-point was used. The orbital energy shift was set to a cutoff energy of 0.001 Ry and the real-space mesh cutoff was set to 300 Ry.

Molecular systems were studied using open-shell DFT in the NWChem code and ORCA.[157, 153] Exchange and correlation were treated using hybrid (PBE0 [237] and B3LYP [238]) and double-hybrid (B2PLYP [115]) GGA functionals with D3(BJ) dispersion corrections [181, 239]. Single point energy calculations included all electrons and used a def2-TZVPPD basis after geometry optimizations were done using a def2-TZVP basis.[240] Single-atom systems were also studied in NWChem by applying the same DFT methodologies as for molecular catalysts.

Brett Henderson also performed coupled cluster calculations with explicit single and double excitations and perturbative triples (CCSD(T)) on the PBE0 equilibrium geometries using the ORCA code, version 5.0.3. Because the correlation energy in post Hartree-Fock calculations is known to converge more slowly than the Hartree-Fock or DFT energy,[241] a def2-QZVPPD basis set was used for all elements. For closed shell species, restricted Hartree-Fock references were used. For open shell species, unrestricted Hartree-Fock (UHF) calculations were performed. However, the actual reference determinant was formed from a transformation of the UHF orbitals quasi-restricted ones[242] to mitigate spin contamination. In all cases, the integral threshold was decreased to 10^{-15}, the overlap threshold increased to 10^{-7}

to reduce potential linear dependencies for diffuse basis set, and the finest default ORCA grid, defined by the keyword 'DEFGRID3' was used. In addition, the stability of all Hartree-Fock solutions with respect to orbital coefficients was examined using the ORCA "STABPERFORM" keyword in the SCF block to ensure the calculation had reached a minimum. The calculation was restarted until the resulting solution was stable. It is noted that several reaction intermediates displayed rather large T_1 diagnostic values $>>$ 0.02, which is indicative of significant multireference character. T_1 values are a reliable measure of the appropriateness of a single-reference treatment of correlation.[243] Values larger than 0.02 indicate the result should be treated with skepticism and that a multi-reference approach may be more appropriate This is not altogether unexpected for such transition-metal complexes and warrants further investigation with multireference methods.

Furthermore, the anionic ORR pathway was used to benchmark the iterative qubit cluster method. In the anionic pathway, $4OH^-$ molecules are produced:

$$O_2 + 2H_2O + 4e^- \rightarrow 4OH^- \tag{5.1}$$

It is well established that anions are notoriously difficult to simulate due to their diffuse properties.[244, 245] Therefore, a more diffuse basis set is required compared to neutral or cationic species along with a better treatment of electronic correlation to capture the elusive electronic structure of these species. The preparation of one- and two-electron integrals for iQCC was performed using PySCF, version 2.0.1. ROHF was performed on each set of intermediates, followed by unrestricted MP2 to obtain the MP2 natural orbitals. From these, an active space of 30 spatial orbitals and either 29 (for species with odd numbers of electrons) or 30 (even numbers) electrons was selected. one- and two electron integrals were calculated and printed to a standard FCIDUMP format, then converted to the Microsoft Broombridge (0.2) format for sending to OTI.

CAS methods for reaction ΔE's require special attention to ensure that the CAS is consistent across different intermediates. We performed our calculations stepwise, performing the above preparation steps for all reactants and all products for each reaction step, with all species participating in the step included in each calculation. Spectator species were omitted from each step to enforce that the CAS only included relevant orbitals. Thus, each intermediate was actually computed twice. Once as a product for a given step, and then again as a reactant for the next

step.

A number of methods were tested to study transition states and minimum energy spin crossings in the atomic catalyst model reaction pathways. Using the DFT methodology described above, NEB and CI-NEB calculations were performed using between 10 and 20 beads between each pair of intermediates. Transition state estimates from these strings were then optimized using saddle point searches. For transitions between intermediates with different spin multiplicities, regular NEB was performed for the reaction step with both the starting and ending spin multiplicity to obtain estimates for the minimum energy spin transitions. In select cases, unrelaxed scans over two internal coordinates were executed to generate two potential energy surfaces at the different spin multiplicities and their intersections were evaluated. Transition state methods which account for spin crossings are not well-established. However, we based our methods off of multiple spin-state NEB introduced by Zhao et al.[246] Our first objective is to identify which spin results in the lowest saddle point of a reaction. Then the saddle point can be fixed as an endpoint to perform further NEB calculations on the side which the spin transition occurs. Fixing two images between which a spin transition occurs and performing NEB between them can be done iterative until a satisfactory spin-transition is obtained. Examples of this approach will be shown in Section 5.3.4.

5.3 Results and discussion

5.3.1 Model reduction

The effect of model reduction was compared for a number of cases. First, the periodic MNCs computed using the SIESTA method were directly compared to single atom catalysts treated with the same methods (Figure 5.3). The adsorption and desorption steps are expected to have far different ΔE values in the unsaturated metal compared to the embedded metal. Adsorption steps (0$\rightarrow$1) are more negative and desorption steps (4$\rightarrow$5 and H_2O_2 desorption in step 2$\rightarrow$3 of the 2e$^-$ pathway) are more positive. Binding geometries generally demonstrate more tenacious coordination between the intermediate and the catalyst (Figure 5.3e-f). In the M$-$O$_2$ complex, η^2 binding is observed on the single-atom catalyst (Figure 5.3e, step 1) while the MNC catalysts engage O_2 in κ^1 side-on binding (Figure 5.3f, step 1). A similar configurational change is observed in the M$-$OOH intermediate, how-

ever the η^2 binding to the atomic catalyst remains slightly asymmetric (Figure 5.3e, step 2).

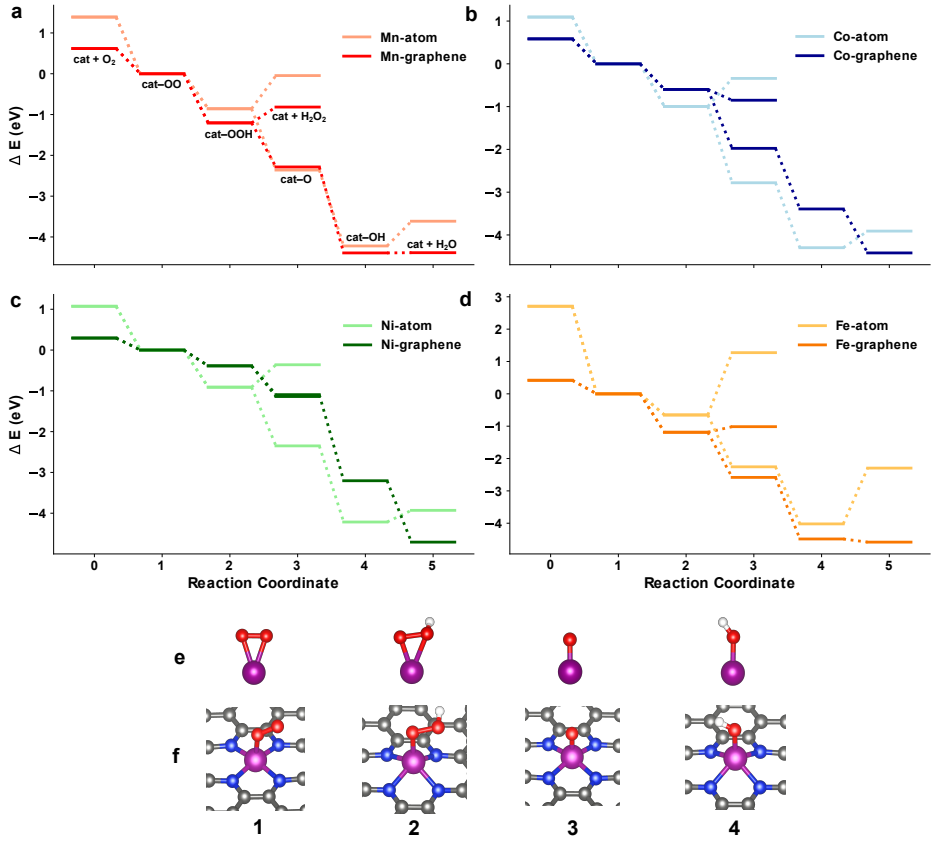

Figure 5.3: Two and four-electron pathways of oxygen reduction on an embedded graphene catalyst model and single-atom catalyst model are shown relative to reaction step 1. Dark colours depict periodic systems and light colours depict single atom pathways for Mn (**a**), Co (**b**), Ni (**c**) and Fe (**d**). The optimized binding configuration for each intermediate step are shown for both systems (**e, f**). Both systems were optimized using the PBE/TZP vdW-TS method in SIESTA.

While differences can be deduced from plotting ΔEs of a reaction path, $\Delta\Delta E$s are a better way to compare difference in energy for a given step in the pathway. Figure 5.4 shows $\Delta\Delta E$s for each ORR step for the atomic and periodic systems of the 4e$^-$ pathway. As discussed, the largest differences are seen in adsorption and desorption steps (0$\rightarrow$1 and 4$\rightarrow$5), however intermediate energies are also affected by the system. There were no consistent trends reflected between the atomic and periodic systems across different metals. The formation of M$-$OOH is less favored by the NiNC and CoNC systems but this is not replicated in the single-atom catalysts, where the $\Delta\Delta E$ of Fe in step 1$\rightarrow$2 (M$-$OOH formation) is

the least negative in the atomic case whereas NiNC and CoNC are by far the least negative in the periodic case. The formation of the first H_2O molecule leaves behind an M−O intermediate. The single-atom catalysts see a tighter spread of energetic change in this step (ranging from −1.5 eV to −1.9 eV), but the $\Delta\Delta E$s in the MNC systems range from −0.7 eV in CoNC to −1.4 for FeNC. The formation of M−OH in step 3→4 was in closest energetic agreement between systems and metals, where the only outlier is Co for which the single-atom system favors the step more than CoNC. Finally, the H_2O desorption step (4→5) showed somewhat consistent trends between the two systems, where the smallest positive desorption energies on the single-atom catalysts (Co and Ni) correspond to the most negative desorption energies for the same transition metals in the periodic systems. We expected to see systematic differences between the pathways of single-metal and periodic MNC catalysts. However, these differences are not consistent between steps nor metals. While the general energetic profile of the pathway is reproduced for the intermediate species with a single-atom catalyst, it is not enough to make assumptions about the performance of the corresponding MNC system.

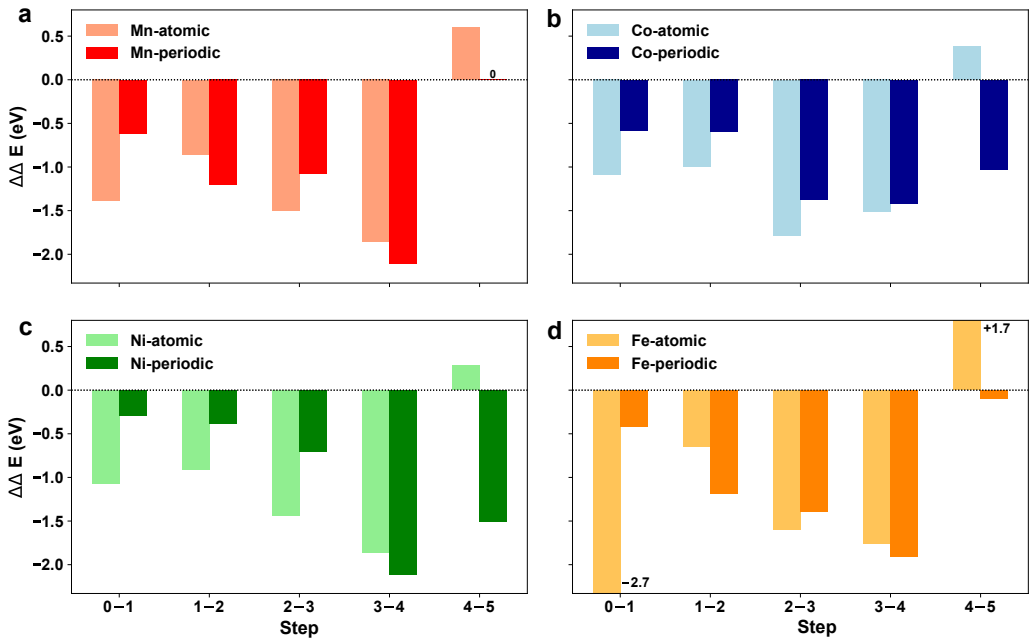

Figure 5.4: The $\Delta\Delta Es$ plotted for periodic MNC catalysts and single-atom catalysts. Dark colours depict periodic systems and light colours depict single atom step energies for Mn (**a**), Co (**b**), Ni (**c**) and Fe (**d**).

A more subtle comparison was made between ORR pathways catalyzed by molecular phthalocyanine catalysts and an abbreviated version where the four

outer aryl groups are omitted from the geometry (Figure 5.5 **e,f**). Binding configurations of the intermediates remained nearly identical between each system and as did the ΔEs for the two- and four-electron pathways. This is expected since the immediate binding environment of the metal center is unchanged. Optimizing the electronic structure of the catalysts without the aryl groups reduced the walltime by more than three-fold in the final DFT optimization step for the same number of resources (40 core single node, Table A.2). Despite a similar electronic structure, the full phthalocyanine systems were much more difficult to converge in geometry optimizations due to their larger size.

Both catalyst systems show very similar ΔEs, however, there are a handful of steps in disagreement. This may be attributed to poor convergence upon the correct electronic structure during single-point and geometry optimizations, despite multiple attempts with newly optimized geometries. Spin contamination was also present in a number of steps, with the calculated s^2 differing by up to 0.05 from the expected values. It is interesting to note that steps with strong disagreement (Mn step 0, Mn$-$O in step 4 and Fe$-$OH in step 5) all claim the full phthalocyanine to be at a higher energy. The negative values for H_2O_2 and H_2O desorption steps in the periodic system metal can be attributed to the increased stability of the metal center. But these values are also important indicators for rate of desorption which is an indicator of catalytic activity.

The $\Delta\Delta Es$ were plotted to compare the the phthalocyanine and abbreviated phthalocyanine catalyst systems (Figure 5.6). In this case, there is very strong agreement between each system and the abbreviated phthalocyanine catalysts replicate the trends for each metal. The exception is step 3 for Mn (Mn$-$O), where the full phthalocyanine is higher in energy.

The comparison between the molecular and atom-scale catalysts calculated using PBE0 also showed large differences as seen in the SIESTA PBE comparisons discussed for periodic and single-atoms (Figure 5.3). The ΔE and ΔEs did not replicate trends for different metals consistently and served as poor indicators for the performance of the corresponding metal within the macrocycle. These results emphasize the importance of including ligands to represent the local binding environment at the site of catalysis. Both the periodic and molecular MNC catalysts coordinate with two x-type Ns and two L-type Ns. While the neutral single-metal catalysts were not good indicators of the trends observed in periodic or molecular catalysts, applying a +2 charge to the metal center to match the catalyst oxidation

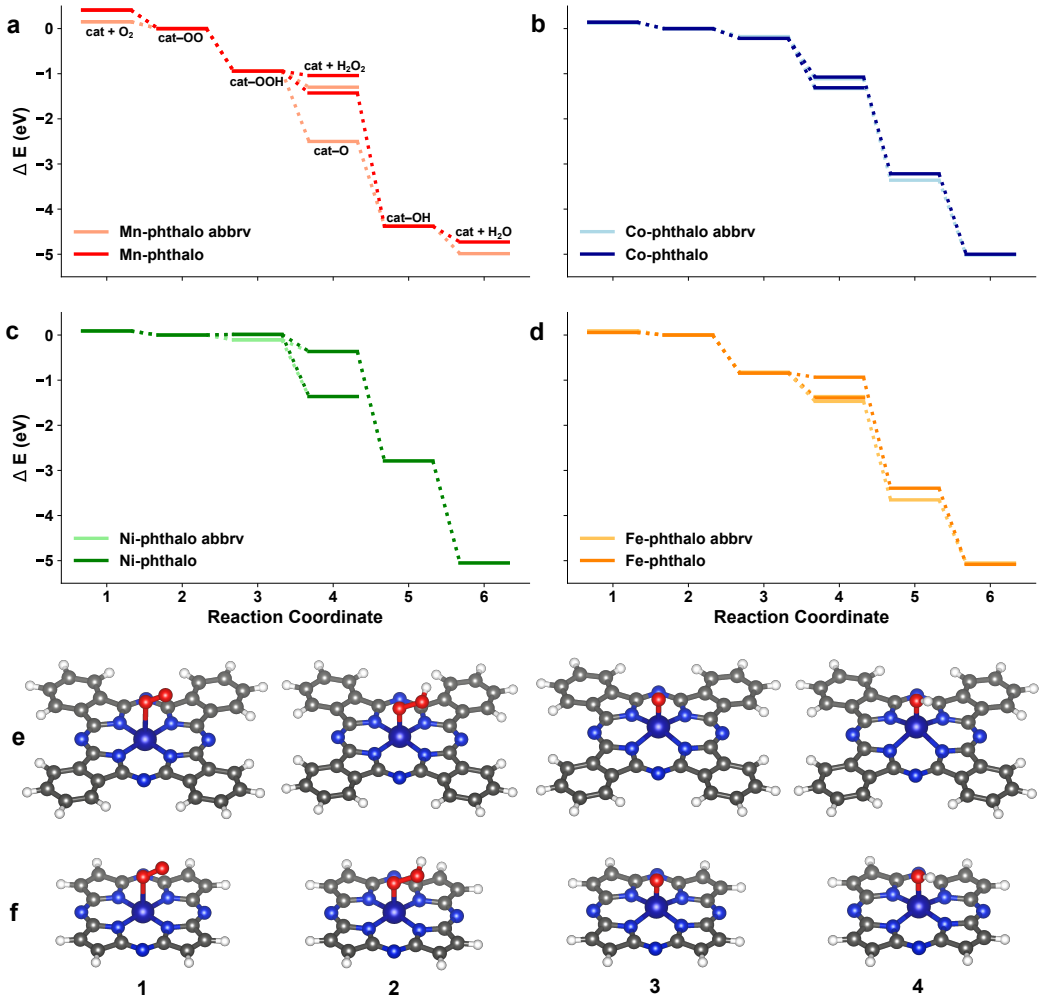

Figure 5.5: Two and four-electron pathways of oxygen reduction on a phthalocyanine-embedded catalyst are compared to a reduced model. ΔEs are plotted relative to reaction step 1. Dark colours depict full systems and light colours depict abbreviated phthalocyanine models for Mn (**a**), Co (**b**), Ni (**c**) and Fe (**d**). The optimized binding configuration for each intermediate step are shown for the Mn case in both systems (**e,f**).

state could improve these results (which is currently being investigated). Furthermore, it would be interesting to see if geometry optimizations with such an oxidation state will produce binding configurations more similar to the intermediates of the larger systems (ie. side-on binding of O_2 in the first intermediate).

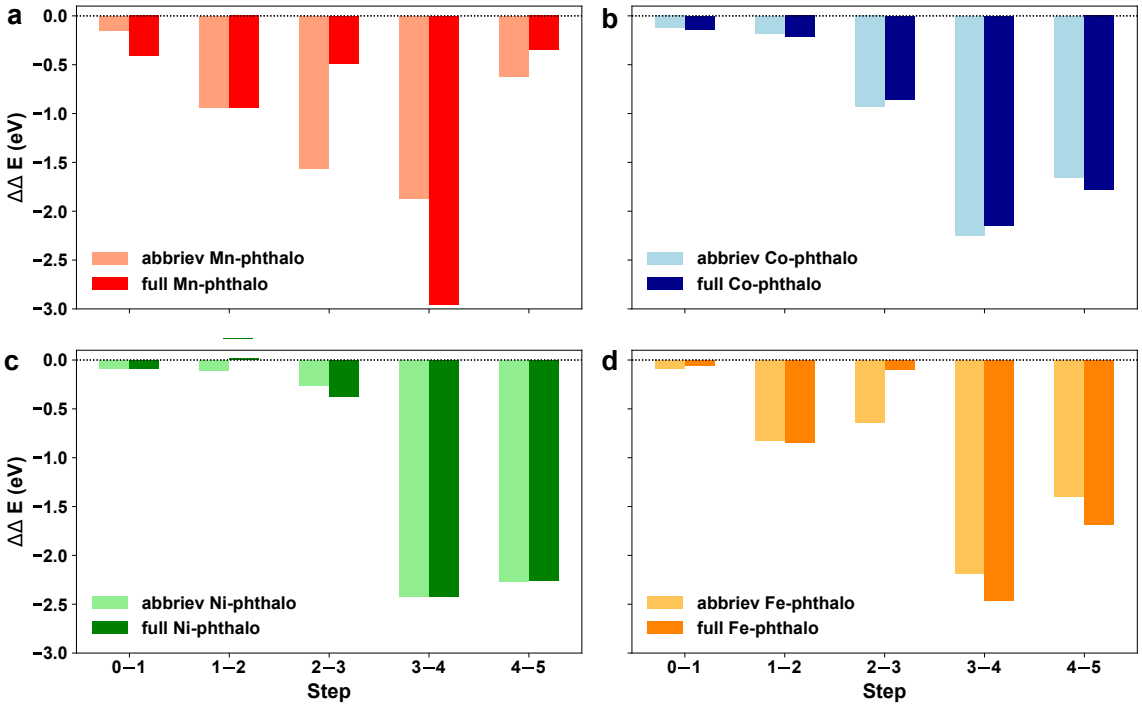

Figure 5.6: The $\Delta\Delta Es$ plotted for full and abbreviated phthalocyanine-embedded catalysts. Dark colours depict periodic systems and light colours depict single atom step energies for Mn (**a**), Co (**b**), Ni (**c**) and Fe (**d**).

5.3.2 Impact of exchange-correlation functional

While the importance of catalyst ligands on the calculated trends for ORR are irrefutable, single-metal catalysts are ideal subjects for benchmarking a large field of methods for describing the catalyzed ORR pathway. Their small size yet high complexity and large number of near-degenerate states makes them a challenge for most methods. Establishing the level of theory required to describe these high-spin systems consistently is important for validating the results obtained for larger systems. Can PBE0 compete with double-hybrid functionals and coupled-cluster methods? Lower levels of theory are capable of describing more realistically scaled model systems which contain the ligands and proper coordination environment on the catalyst center. However, it is necessary to validate the accuracy of these methods to ensure the metal-oxygen interactions are captured sufficiently.

We note first that the net ΔH for the overall $4e^-$ reaction pathway is relatively consistent among all three functionals. Thermodynamic calculations were also performed to compare the 0 K reaction enthalpies against experimental values from the National Institute of Standards and Technology (NIST) database.[247] Both

electronic energies and thermodynamic energies are benchmarked in Table 5.1. CCSD(T) shows remarkable agreement with the experimental value to within 0.05 eV.

method	ΔE	ΔH (0 K)
PBE0	−5.22	−4.65
B3LYP	−5.13	−4.62
B2PLYP	−5.25	−4.73
CCSD(T)	−5.48	−4.91
Exp.[247]		−4.95

Table 5.1: H_2O formation energies (in eV) benchmarked for various methods. The electronic energy is shown as well as the thermodynamic ΔH value at 0 K which can be benchmarked against the experimental reference.

While there is good agreement on the net reaction, the functionals show greater discrepancies for intermediate steps. In particular, intermediate 3 shows disagreement of up to $\pm$0.5 eV between functionals for some metals. However, the difference is not systematic. The lack of a systematic trend between functionals seems to be the rule, as the relative over and underestimation of energy changes between functionals varies from step to step even when they do agree on the sign of the energy change.

To evaluate the DFT functionals, we first optimized geometries of all metal pathways using each functional to identify discrepancies in the energy and binding configurations in each step. Bond lengths and angles for each step were also tabulated in subsection A.0.2 to identify differences in geometries. Figure 5.7 shows the ΔEs of the ORR pathways on single-atom catalysts. There is good overall agreement between functionals for most steps, however, as mentioned, intermediate 3 shows a large spread of ΔEs for Fe and Co. The Ni pathway boasts the tightest agreement between functionals over the course of the entire pathway (Figure 5.7**c**), with M−O in step 3 having the worst agreement. In general, step 1→2 to form M−OOH shows the best energetic agreement across all systems (Figure 5.8).

The range of bond M−O lengths calculated by each functional varied for each metal and step (Table 5.2). The range was acquired by taking the difference between the longest and shortest bond length among the set of PBE0, B3LYP and B2PLYP optimized geometries. The greatest disagreement was observed in intermediates 2 and 3 (M−OOH and M−O), while step 4 (M−OH) reports the highest agreement. Mn showed the highest consesus among the metals, how-

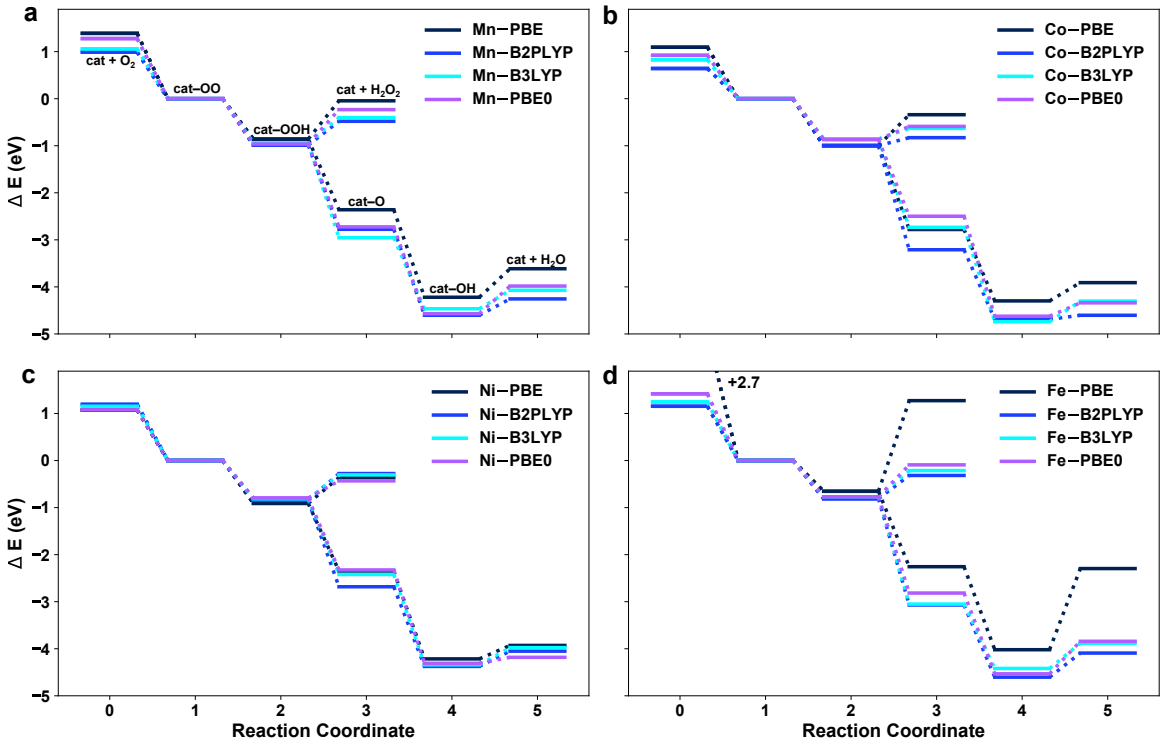

Figure 5.7: ΔEs for pathways where geometry optimizations were performed with four common DFT functionals. PBE (dark blue), B2PLYP (blue), B3LYP (light blue), and PBE0 are plotted for Mn (**a**), Co (**b**), Ni (**c**) and Fe (**d**).

ever each metal contained a step where the functionals disagreed by over 0.4 Angstroms. For reference, these same functionals agree within 0.021 Angstroms for the O_2 molecule, spanning 1.193−1.214 Angstroms which contains the experimental value of 1.2075 Ang.[248]

	M−O range			
atom	**M−O_2**	**M−OOH**	**M−O**	**M−OH**
Mn	0.020	0.016	0.041	0.010
Co	0.036	0.070	0.011	0.013
Ni	0.007	0.054	0.012	0.026
Fe	0.014	0.018	0.056	0.009

Table 5.2: The difference of M−O bond lengths (ΔM−O) in geometries optimized using PBE0, B3LYP and B2PLYP for each ORR step intermediate. For each step, the spread between the longest and shortest M−O bond length across all optimized structures are reported. Note that PBE structures were excluded due to the difference in method (different basis set and dispersion treatment).

The geometries of reaction steps for atomic catalysts were optimized at the

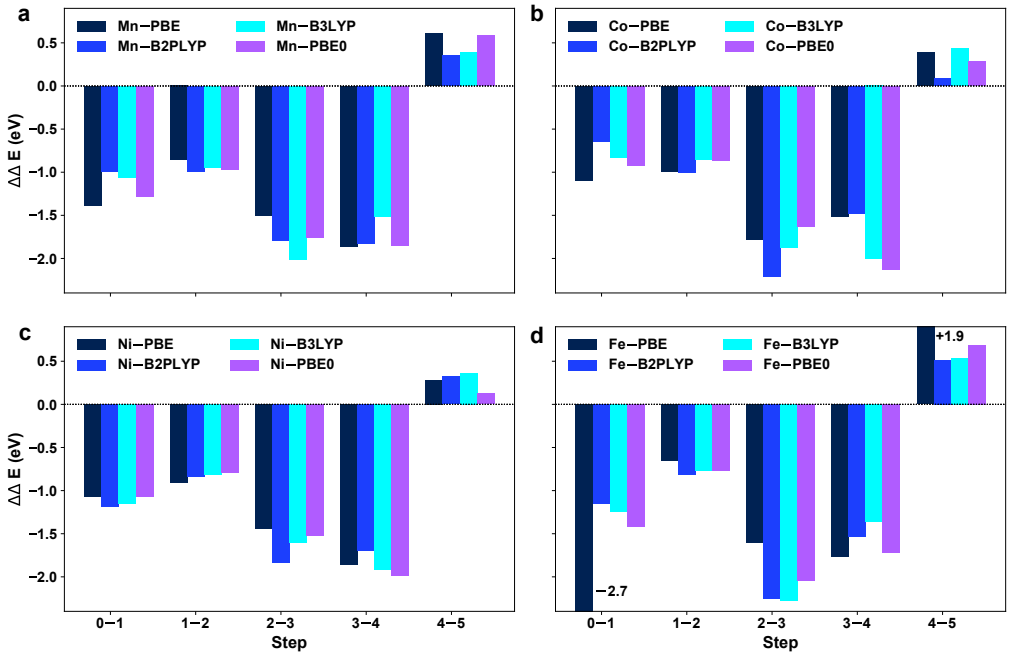

Figure 5.8: $\Delta\Delta Es$ for pathways where geometry optimizations were performed with four common DFT functionals. PBE (dark blue), B2PLYP (blue), B3LYP (light blue), and PBE0 are plotted for Mn (**a**), Co (**b**), Ni (**c**) and Fe (**d**).

PBE0-D3(BJ)/def2-TZVPPD level of theory. These energies were re-computed using PBE0-D3(BJ), B3LYP-D3(BJ) and B2PLYP-D3(BJ) functionals with the same basis set. This enables us to evaluate energies on a set of identical geometries. Surprisingly, these DFT functionals show greater disagreement for single-point calculations on identical geometries. Figure 5.9 plots the ΔEs from PBE0-D3(BJ)/def2-TZVPPD (violet), B2PLYP-D3(BJ)/def2-TZVPPD//PBE0-D3(BJ)/def2-TZVPPD (blue), B3LYP-D3(BJ)/def2-TZVPPD//PBE0-D3(BJ)/def2-TZVPPD (light blue), and coupled cluster (CCSD(T)/def2-QZVPPD//PBE0-D3(BJ)/def2-TZVPPD) single point calculations for each catalyzed pathway.

While PBE0 and B3LYP remain in good agreement, the double hybrid functional shows the most outstanding energetic disagreement. Once again, ΔEs involving the M−O intermediate (3) show the largest spread of energies for all metal types. Coupled cluster results stray from the PBE0 results in a few steps. The Mn metal is found to be less stable by CCSD(T), driving up the energy of intermediates involving free catalyst (intermediates 0 and 5) (Figure 5.9**a**). Steps 1→2 and 2→3 are predicted to be more downhill for the Ni pathway by CCDS(T) while the final desorption step (4→5) is assigned to be more positive (Figure 5.9**c**). In the case

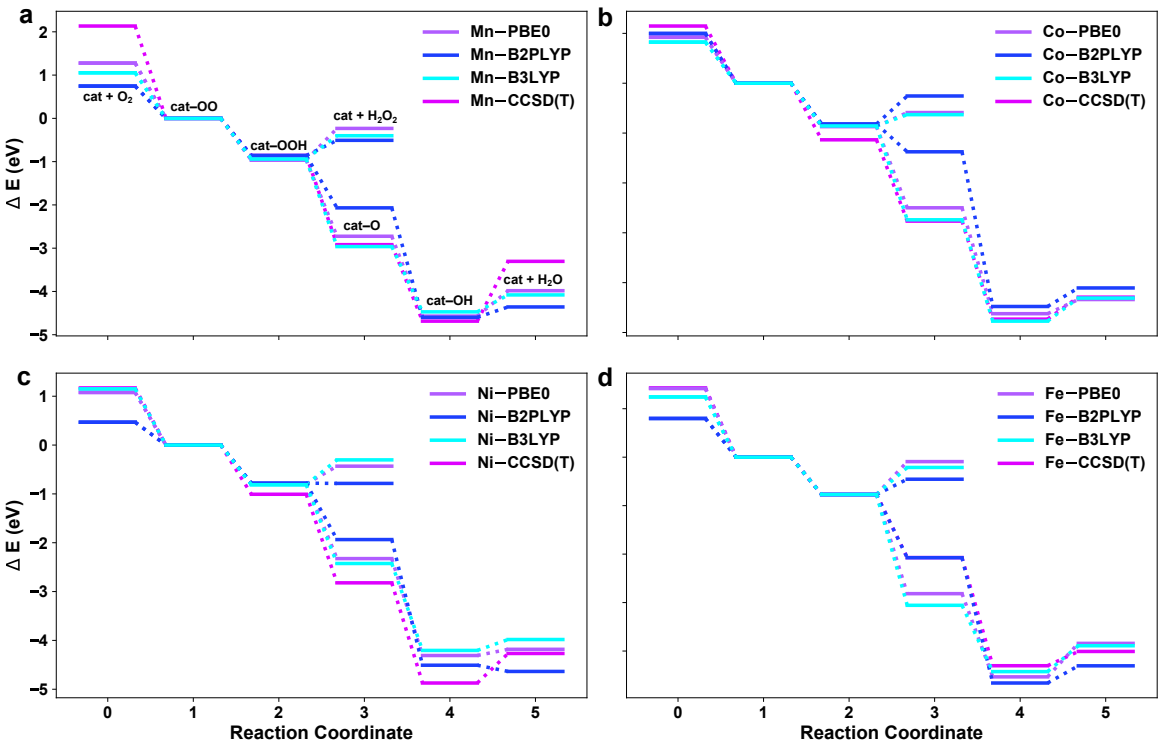

Figure 5.9: ΔEs resulting from mixed method calculations. PBE0-D3(BJ)/def2-TZVPPD (violet), B2PLYP-D3(BJ)/def2-TZVPPD//PBE0-D3(BJ)/def2-TZVPPD (blue), B3LYP-D3(BJ)/def2-TZVPPD//PBE0-D3(BJ)/def2-TZVPPD (light blue), and coupled cluster (CCSD(T)/def2-QZVPPD//PBE0-D3(BJ)/def2-TZVPPD, fuchsia) results were benchmarked for Mn (**a**), Co (**b**), Ni (**c**) and Fe (**d**).

of Fe, CCSD(T) matches the higher B2PLYP energy for the M−O intermediate (3) but shows good agreement with PBE0 otherwise.

The increased differences in energies do not necessarily correspond to steps with larger ranges in M−O bond length from the functional-specific geometry optimizations. For example, in Table 5.2 the M−O bond length in the M−OOH intermediate showed the largest disagreement among functionals, however the agreement in energy does not grow worse from single point calculations on the PBE0 geometry. On the other hand, intermediate 4 (M−OH) shows tight agreement in M−OH bond lengths across functionals yet the single-point energies on the PBE0 geometry result in greater energetic disagreement. This suggests that geometric and energetic agreement across functionals are independent for these systems.

The single point energies calculated with B2PLYP are generally higher relative to other functionals and relative to the energy with a B2PLYP optimized geometry. However, a handful of steps showed improved agreement between the DFT $\Delta\Delta E$

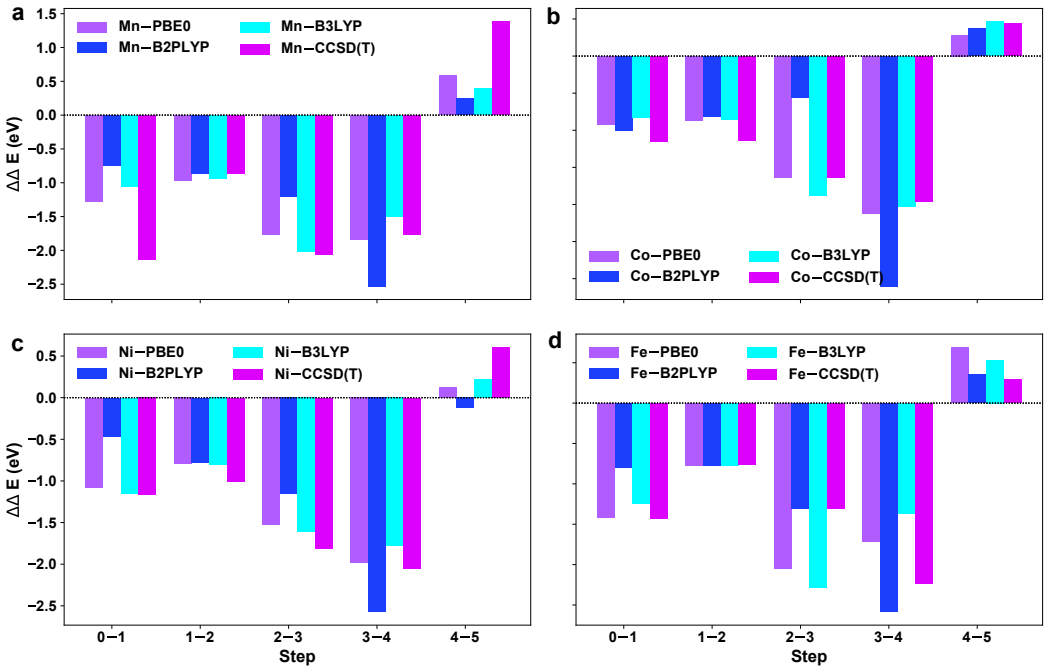

Figure 5.10: $\Delta\Delta Es$ for single point calculations on each atom-catalyzed ORR pathway for PBE0-optimized geometries. PBE0 (violet), B2PLYP (blue), B3LYP (light blue), and coupled cluster (CCSD(T)/def2-QZVPPD, fuchsia) results were benchmarked for Mn (**a**), Co (**b**), Ni (**c**) and Fe (**d**).

values with the same geometry. The formation of M−OOH (step 1→2) in Figure 5.10 for Co (**b**), Ni (**c**), and Fe (**d**) show slightly closer $\Delta\Delta E$ values (note, this observation excludes CCSD(T) results plotted in fuchsia). However, most steps would suggest it is better to calculate the energy using the geometry optimized with the same functional. This is particularly the case for B2PLYP energies, which are far different for the PBE0 geometry than for B2PLYP-optimized structures presented in Figure 5.8 and Figure 5.7. In both cases, the energies obtained by B3LYP and PBE0 are in highest agreement for the single-atom pathways. There is better agreement between functionals when the geometries are optimized using each respective functional.

5.3.3 Benchmarking the alkaline pathway for Ni

Ongoing collaborative work with OTI Lumionics has involved benchmarking their iterative qubit coupled cluster method.[102] As mentioned in Chapter 2, it is important to keep CAS selection as consistent as possible when obtaining any in-

formation from ΔEs. Keeping the CAS-size the same is simple but selecting consistent orbitals to treat fully is important to obtain meaningful comparisons across the entire pathway. To keep CAS selection consistent along the entire pathway, Henderson generated the following set of reactants/products to benchmark:

$$Ni + O_2 \rightarrow Ni - O_2 \tag{5.2}$$

$$Ni - O_2 + H_2O + e^- \rightarrow Ni - OOH + OH^- \tag{5.3}$$

$$Ni - OOH + e^- \rightarrow Ni - O + OH^- \tag{5.4}$$

$$Ni - O + H_2O + e^- \rightarrow Ni - OH + OH^- \tag{5.5}$$

$$Ni - OH + e^- \rightarrow Ni + H_2O \tag{5.6}$$

Figure 5.11 shows computational results from the alkaline pathway. 19 iterations of iQCC were followed up with PT2 projections for the expected convergence upon a ground-state energy. For step 1 and 2, iQCC performs better than ROHF, however we believe that testing a larger CAS may be needed to improve the converged electronic structure across all the steps. Testing a larger basis than TZVPPD may also improve results.

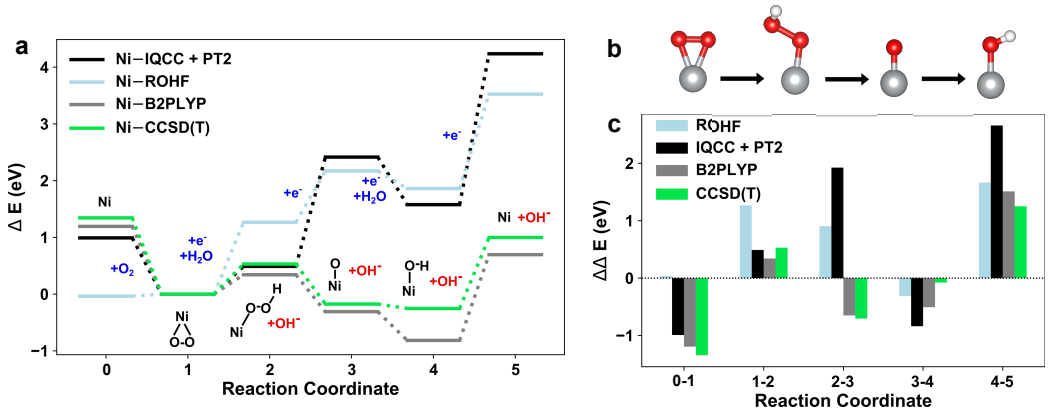

Figure 5.11: ΔEs for the anionic ORR pathway on atomic Ni were benchmarked for iQCC (black), ROHF (light blue), DFT (grey), and CCSD(T) (green) (**a**). The energies have all been zeroed relative to the first intermediate. PBE0/Def2-TZVPPD-optimized geometries were used for energetic evaluation and the intermediate complexes are shown in **b**. $\Delta\Delta Es$ are plotted in **c**.

This work is ongoing as we continue to improve the starting wavefunction used. Starting from the CCSD(T) solution along with using a larger basis set will provide

a better starting wavefunction for the iQCC optimization. The multireference character of the M−O step makes it challenging to converge which may need to be addressed by incorporating multireference methods. Testing the pathway of lower-valence metals such as Mn may show better convergence. However, it may be that a larger CAS selection is necessary to fully capture the electronic interactions.

5.3.4 Transition state and spin transition calculations

Another ongoing avenue of research is identifying transition state barriers for the splitting of O_2. The separation of oxygen atoms upon O_2 adsorption is another catalytic pathway hypothesized to occur MNC systems.[219] If the catalyst sufficiently lowers the barrier of O_2 bond activation, the formation of a M−OOH intermediate is avoided which may reduce the formation of H_2O_2.

We sought to compute the transition state for O_2 activation in the dissociative pathway following step 1, M−O_2→ O−M−O. Finding transitions states for most ORR steps is complicated by spin transitions which also must occur. A spin transition occurs when both the energy and coordinates of two spin states intersect and is not to be confused with the transition state. As mentioned in subsection 5.2.2, conventional methods such as NEB and CI-NEB (climbing image) do not facilitate spin-transitions in common software, which calls for a manual approach and multiple calculations when a spin-transition occurs during the reaction step.

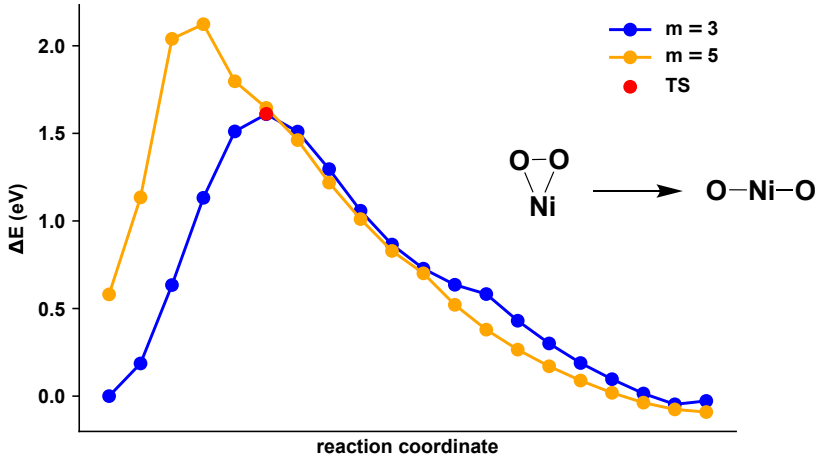

Figure 5.12: Coarse NEB scans performed for both spin states separately. The lowest barrier is identified for multiplicty 3 (orange) after which a spin transition is expected to bring the system to the lowest multiplicty of the product (m=5, orange).

Initial coarse NEB scans were performed with both reactant and product multiplicities for M$-$O$_2$$\rightarrow$O$-M-$O. Figure 5.12 plots the initial NEB results for Ni$-$O$_2$ $\rightarrow$ O$-$Ni$-$O. 20 beads were optimized with both multiplicities and the lowest barrier was selected for a saddlepoint optimization, which in the case of Ni, was the pathway with multiplicity 3. Using the optimized saddlepoint, further NEB calculations can performed using the transition state as a fixed endpoint to learn more about the spin transition and to form a more continuous set of images. Since the spin remains the same between the optimized transition state and either the reactant or product (in the case of Ni, the lowest transition state matches the multiplicity of the starting), further calculations are not necessary on the side of the transition state where the spin remains the same. However, in the case of the Ni reaction step, further calculations are required between the transition state and product to narrow down where the spin transition occurs between those endpoints. Figure 5.13**b** shows the result from 20 bead NEB calculations connecting the TS to the product (an additional calculation was performed to obtain higher resolution between the reactant and transition state but is not necessary). The orange m5 pathway is slightly lower in energy than the m3 pathway and it seems that a spin transition occurs immediately after the transition state. Since the geometries are fixed and identical at the transition state for both spins, the coordinates are very similar in the beads immediately proceeding the transition state where the energy of the blue and orange trace intersect. To obtain an exact spin transition point, the energy must be identical for both multiplicities for the same geometry which can be verified by single point optimizations at both spins. In the case of Ni, these NEB calculations strongly suggest that a spin transition from multiplicity 3 to 5 occurs in the bead directly following the TS.

The same procedure was applied to Mn which resulted in a much different energy surface (Figure 5.13**a**). In the case of Mn, we found that the spin transition occurs before the optimized saddlepoint. Therefore, NEB scans were performed with multiplicities 8 and 4 to connect the reactant and transition state. According to the scans, the lowest possible spin transition energy was found to be 1.3 eV however further single point calculations should be performed to force geometric overlap.

Locating spin transitions can be useful, however the most practical aspect of these calculations is determining whether a spin transition occurs on the reactant or products side of a saddle point. Knowing the multiplicity of a transition state is

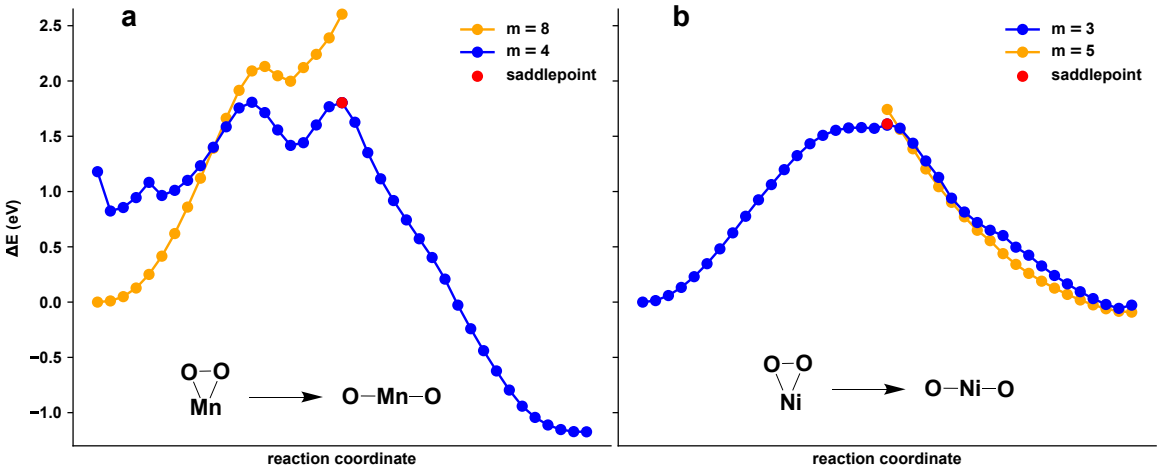

Figure 5.13: NEB scans to identify where spin-transitions likely occur. Each figure shows three 20-bead NEB calculations, each of which has a fixed endpoint on the transition state geometry (red). The reaction step is plotted for Mn (**a**) starting at multiplicity 8 (blue) and ending at multiplicity 4, as well as for Ni (**a**) going from multiplicity 3 (blue) to 5 (orange).

necessary for determining the correct energetic barrier of a reaction step. However, finding the exact point of energetic and geometric crossing between two spin systems is expensive and less useful than determining accurate reaction barriers.

5.3.5 Metal substitution and catalytic activity

Finally, we sought to gain some chemical insight from the metals and systems we studied. The electronic structure calculations shed some light on the differences between each metal. In the neutral single-atom catalysts (Figure 5.14a), Pt was included as a reference metal. Interestingly, the Pt atom shows the strongest affinity for O_2 along with Fe while also having one of the lower energies in the formation and dissociation of H_2O from M−OH after Ni (Figure 5.15a). In general, Fe is in closest agreement with Pt for steps 0→1, 1→2, and 2→3, however Fe has the highest H_2O dissociation energy followed by Mn in 4→5.

Mn, Co, Ni, and Fe are compared in the periodic graphene lattice (Figure 5.14b). While atomic Co has the lowest affinity for O_2 in step 0→1, in the MNC system, Ni has the lowest O_2 affinity while Co and Mn have the strongest O_2 binding energy (Figure 5.15b). Mn has a value close to 0 eV for the formation and desorption of H_2O while Ni and Co have decidedly negative $\Delta\Delta E$ values, reaching below −1 eV. Fe is only slightly more negative than Mn, suggesting that these metals have a low

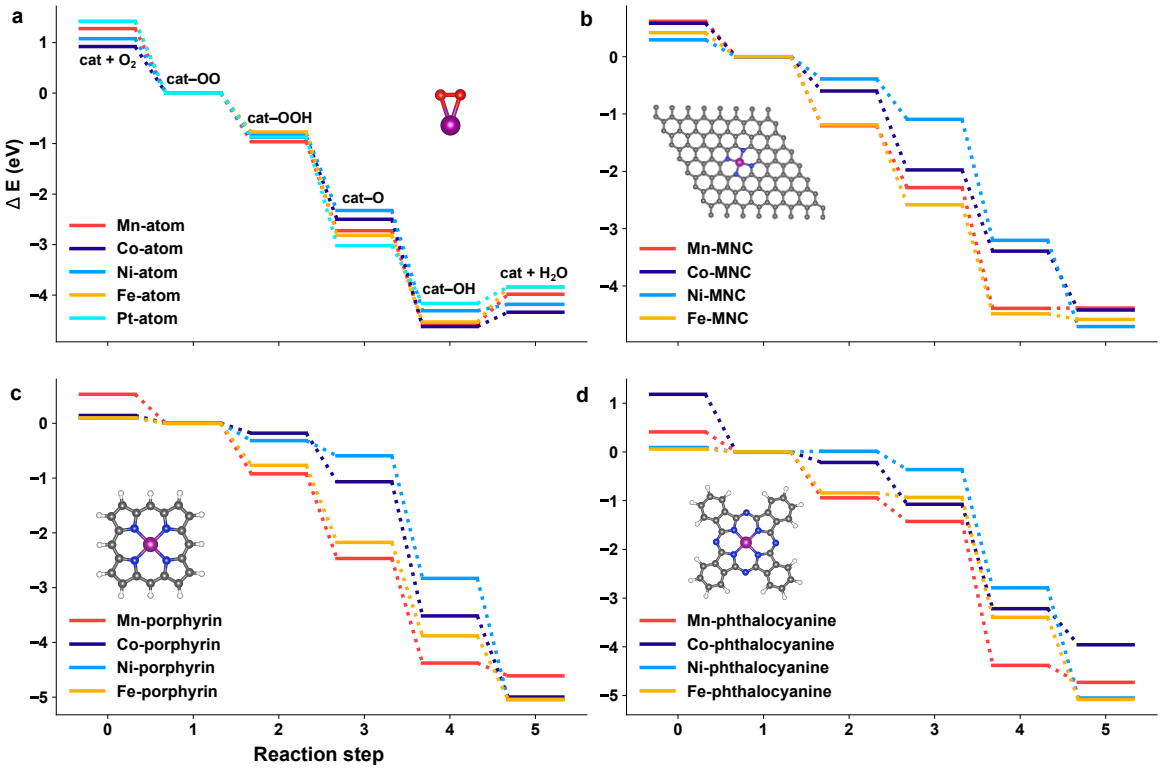

Figure 5.14: A comparison of the metal performance across different systems. Single-atoms **a**, periodic MNC **b**, porphyrin **c** and phthalocyanine **d** catalysts are plotted for Mn (red), Co (dark blue), Ni (blue), and Fe (orange). Platinum is compared to other single atoms in **a** (light blue).

drive for converting M−OH to M + H_2O.

When comparing metal trends between the single-atom systems and porphyrins, steps 2→3, 3→4 and 4→5 reflect a similar ordering of energies. In both systems, Mn and Fe exhibit the strongest drive towards for formation of M−O and H_2O and Ni the weakest. In step 3→4, when M−OH is formed, Co exhibits the most negative $\Delta\Delta E$, followed by Ni. Fe is the least negative step of the four metals in both the single atom and porphyrin case. Finally, while the formation of water from M−OH in step 4→5 is positive for the single-metal systems, the ordering of the metals is shared across all four systems. Ni exhibits the most negative $\Delta\Delta E$ followed by Co. In all system except for the single-atoms, Mn favors step 4→5 the least.

Interestingly, the phthalocyanine system only shares energetic trends with porphyrin for the initial steps M + O_2 → M−OOH (0→1, 1→2) and the final step (4→5) while the middle steps involving M−O and M−OH (2→3→4) are quite different. However, the general energetic ordering of the metal pathways during the initial

association of O_2 to the metal show good agreement between all three systems for most steps. The four added nitrogen atoms about the metal have a notable effect on these middle steps (since the abbreviated phthalocyanine closely matched the ΔEs of the full system, we can determine that the added aryl groups do not have a strong effect on the reaction paths). Adding functional groups to tune the pathway can be easily done on the aryl groups of phthalocyanine. The effect of electron withdrawing versus donating ligands may achieve desirable outcomes such as enhancing O_2 association energies, reducing the overpotential and decreasing H_2O dissociation energies, and will be among the next areas of investigation in this work.

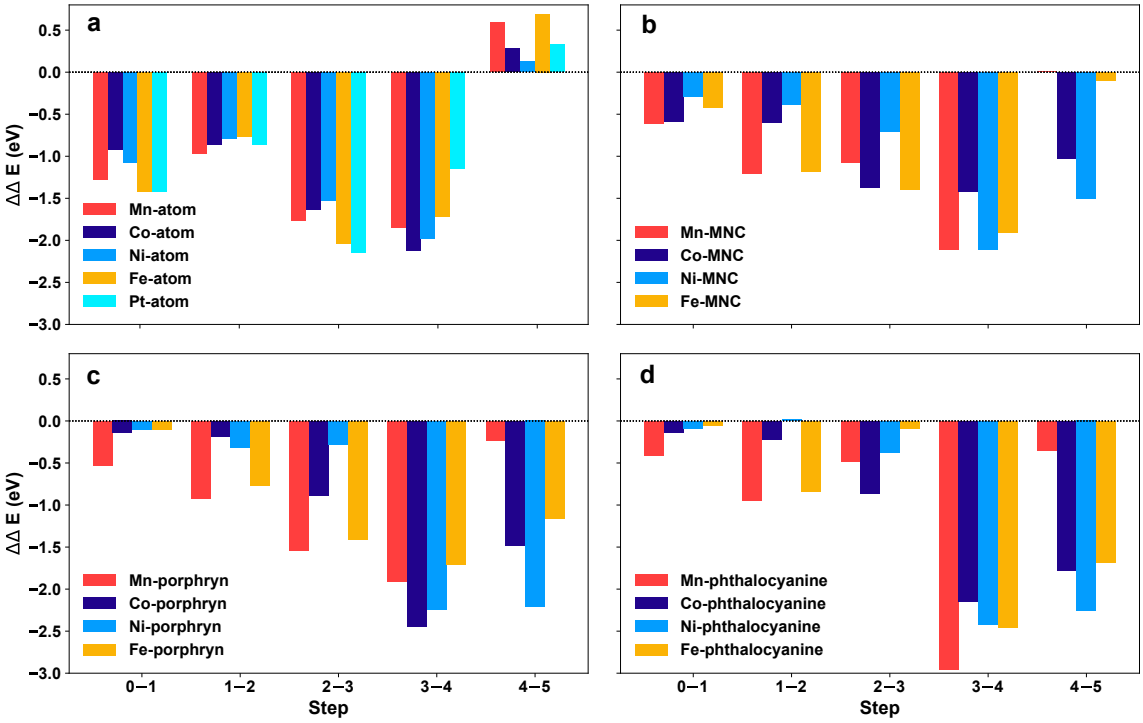

Figure 5.15: The $\Delta\Delta Es$ compared for each metal across different systems. Single-atoms **a**, periodic MNC **b**, porphyrin **c** and phthalocyanine **d** catalysts are plotted for Mn (red), Co (dark blue), Ni (blue), and Fe (orange). Platinum is compared to other single atoms in **a** (light blue).

Further analysis of free energies and limiting potentials are underway for these systems using computational methods introduced by Nørskov.[233] For the time being, we have shown that hybrid DFT functionals perform relatively well for geometry optimizations (Table 5.2) and that system-reduction can improve computational costs and convergence of electronic structure methods without sacrificing

accuracy as long as the ligands about the metal center are retained. However, the high-spin character of these systems makes them challenging for electronic structure methods to converge. In particular, transition state calculations are limited because each step also sees a spin-transition. As shown in the previous section, the spin transition can be roughly located after two NEB calculations which allows one to identify whether the transition state shares the multiplicity of the reactant or products. Finding accurate reaction barriers for key reaction steps is important for determining useful trends and making deductions about catalytic activity.

5.3.6 Conclusion

In this chapter, the ORR pathway was used to benchmark a variety of computational methods on compact, yet difficult systems. Single-atom centers were benchmarked using DFT and wavefunciton methods, revealing challenging steps and metals. CCSD(T) results obtained by Henderson suggest high multireference character for a handful of steps, illustrating the challenge of simulating these systems accurately.

Single-atom systems were also used to test transition state methods on reaction steps where a spin transition occurs. While requiring multiple NEB calculations, identifying saddlepoints was relatively seamless. We hope to extend this method to larger systems to identify catalyzed O_2 bond activation energies for different metals and systems.

We showed that while trends for single-atoms are a poor reflection of larger systems, less extreme reductions such as removal of the outer aryl groups on the phthalocyanine catalysts not only preserves metal trends but also reproduces very similar ΔEs to the original system. The removal of these 16 carbons and 8 hydrogens sped up the calculations a considerable amount. Unfortunately, including the aryl groups is necessary for testing the effect of functionalization as they serve as handles for new groups.

Overall, DFT performs relatively well for most steps. Good starting geometries and awareness of challenging steps is important when simulating these systems. Furthermore, keeping tabs on the multiplicities is important. In many steps, multiple spin states were close in energy (within 0.2 eV), illustrating how complex these systems are.

Chapter 6

Additional projects and collaborations

Several collaborative projects are summarized in this chapter. Several have resulted in peer reviewed publications. There are four sections dedicated to separate collaborations followed by a short fifth section summarizing other work. In the cases where the collaboration led to a publication, a brief background and motivation for the project is given followed by relevant results and figures which highlight my contributions. In the first section, a python tool for handling kinetic data and accounting for catalyst poinsoning is introduced. This project has not been published but a manuscript is in preparation. In section 6.2, a recent collaboration with Dave Leitch and Jingru Li is summarized. My major contribution was computing minimum and transition state structures of a large Pd catalyst. These structures were then used for further ESP analysis by Li. More computational work formed another collaboration with Gilian Thomas who performed mass spectrometric analysis of isobaric platinate species in the gas phase. My contributions to this publication is summarized in 6.3 Finally, computational analysis of reactive metallocenes was paired with mass spectrometric analysis by Anuj Joshi for a publication in Dalton Transations and is presented in section 6.4.3. In 6.5, Catacycle is introduced, which is an arrow drawing tool used across the chemical community today.

6.1 Accounting for catalyst poisoning during kinetic analysis

6.1.1 Background

Variable time normalization analysis (VTNA) is a visual tool recently introduced by Bures in 2016 for analyzing the kinetics of a reaction.[186] VTNA allows the order of a reaction with respect to a reagent to be determined. The time axis is scaled by the relative concentration of the reagent raised to a variable power Equation 6.1. When the exponent, α, equals the correct order with respect to the reagent, the kinetic component is cancelled, and the traces will overlay. Applying this normalization to each component of the system produces a linear trace can be obtained of which the slope corresponds to the observed rate constant for the reaction.

$$\int_{t=0}^{t} [A]^{\alpha} dt \tag{6.1}$$

VTNA has proven to be a convenient way for comparing entire abundance reaction profiles in a figure by overlaying multiple reaction traces. It's simple visual delivery also makes it appealing to an audience less familiar with kinetic analysis. In collaboration with fellow lab mates, a Python-powered web tool was designed whereby users can upload their data and manipulate them into the VTNA format by use of simple sliding scales. It also allows for auto-fitting of the data. The tool will be made freely available online for all users at *www.catacycle.com/vtna*. It includes a modification to the method to account for catalyst poisoning, a phenomenon that disproportionately affects reactions conducted at low catalyst loadings.

When using conventional kinetic analyses, it has often been noted that reactions are slower than expected at low catalyst loadings. Particularly, when running experiments at the low concentrations required for ESI-MS, even very low levels of catalyst poisons reduce the effective concentration of the catalyst to a noticeable extent. For example, drying solvents much below 5 ppm in H_2O is challenging, yet this concentration level is typical of analyses using ESI-MS. The underperformance of low catalyst loadings phenomenon is also commonly observed even at higher concentrations, in cases where the substrate is impure and contains substances capable of deleteriously binding to the catalyst. We have implemented

a correction in VTNA that may prove useful to chemists who are trying to account for these deviations from model behavior. The correction is simple to implement and understand, it reduces the catalyst concentration by a fixed amount regardless of catalyst loading (i.e. 1, 2 and 4% catalyst loadings might all be reduced by 0.5% to give effective catalyst loadings of 0.5, 1.5 and 3.5%). There are many examples in the literature of catalyst poisoning in both homo and heterogenous catalysis.[249, 250, 251]

What distinguishes poisoning from other catalytic deactivation processes such as decomposition and side reactions, is that it immediately consumes the catalyst when it is added. It does not add complexity to the reaction traces but to simply lower the effective concentration of the catalyst by a set amount upon addition of the catalyst. Other mechanisms such as catalyst decomposition processes will affect the reaction in a non-linear fashion since they affect the catalyst over the course of the reaction. Therefore, we can extend the VTNA method to account for catalyst poisoning during time normalization Equation 6.2.

$$\int_{t=0}^{t} [A - poison]^{\alpha} dt \tag{6.2}$$

6.1.2 Methods

In collaboration with Brett Henderson, a python script was created to perform VTNA and correct for catalyst poison. Two generations of the code exist. The first generation is a jupyter notebook which uses four python packages: matplotlib for data visualization, pandas and numpy for data manipulation and ipywidgets for the user interface. The first user interaction with the program is a prompt for the .xsls data file. When prompting the user for their file, instructions on the specific format are included. Then the user is prompted to specify which type of normalization method should be applied to their data. Maximum value normalization is ideal for data where the measure of a species' abundance is directly comparable to the absolute value of the measurement. For example, we can use the magnitude of change in an NMR peak integration over the course of a reaction to make direct comparisons with measurements taken over time. The second option, total (ion) count normalization, normalizes each data point by the sum of all data points in that time-step. This results in a series of individually normalized data points, each marking the percent abundance of the species at that point in time. This is useful for meth-

ods where the nature of measurement causes variations in the absolute counts recorded because the relative abundance of species can be used as an internal standard. Normalizing by the total ion count (TIC) is applicable in mass spectrometry (MS) where values reported are not an absolute representation of concentration in a sample. If the user deems neither of these options suitable for their data, their data won't be normalized. Another input required is the relative concentrations of the reagent they wish to test. These values must be given without units as they are stored as floats for later calculations.

There are a few other adjustments that need to be made to the dataset before the reaction order can be determined. Firstly, all experiments that will be compared need to have the same starting point. Because each sheet describes a separate experiment, the start times may not align. Secondly, the data should be smoothed if it is noisy. Because each experiment is performed separately, the quality of the data may vary, and some experiments may require more averaging. The user manually defines when time equals zero by picking the point on their trace when the reaction begins. They also select the degree of smoothing for each experiment in the first interactive plot using ipywidgets. Both the translation and the smoothing can be done using a slider bar that is directly above the plot, updating the figure each time the bar is moved. The smoother widget is used to adjust the window size of a rolling mean. The rolling mean finds the average value of all data points within the specified range (window size) of each data point. Every data point then becomes the average of its neighbors. This smoothing is handy because it retains the same data density regardless of how much smoothing is performed. However, this may also falsely portray high quality data and should be used in moderation.

The final two widgets are used to adjust the order of the reaction until the traces align for each reaction and to correct for poisoning. A widget for time normalization adjusts the x-axis values for each trace so that the time column is normalized by the concentration of the reagent raised to the power of the widget value. Once the correct order has been selected, the value is stored in a variable to be used in the final plot along with all the other adjustments previously made to the dataset. A second widget allows users to find the degree of poison by subtracting a fixed "poisoned" concentration of reactant.

In a second edition, Brett Henderson implemented an auto-fit function which allows the user to select from a number of different cost function they can to use fit a reaction order. These tools are being made available on GitHub and hopefully

as a web-interface on Catacycle.com as well.

6.1.3 Discussion

Two datasets were tested using the VTNA tool with and without a poisoning. To apply VTNA, 1^HNMR data of zirconium catalyzed hydroamination[252] (Figure 6.1**a**) was normalized by the measured concentration of Zr added raised to the first power (Figure 6.1**b**). Though the reaction is first order with respect to the Zr catalyst, normalizing the time axis did not result in a perfect overlay due to catalyst poisoning. By subtracting a constant amount of catalyst from all measured concentrations, a better fit was achieved (Figure 6.1**c**).

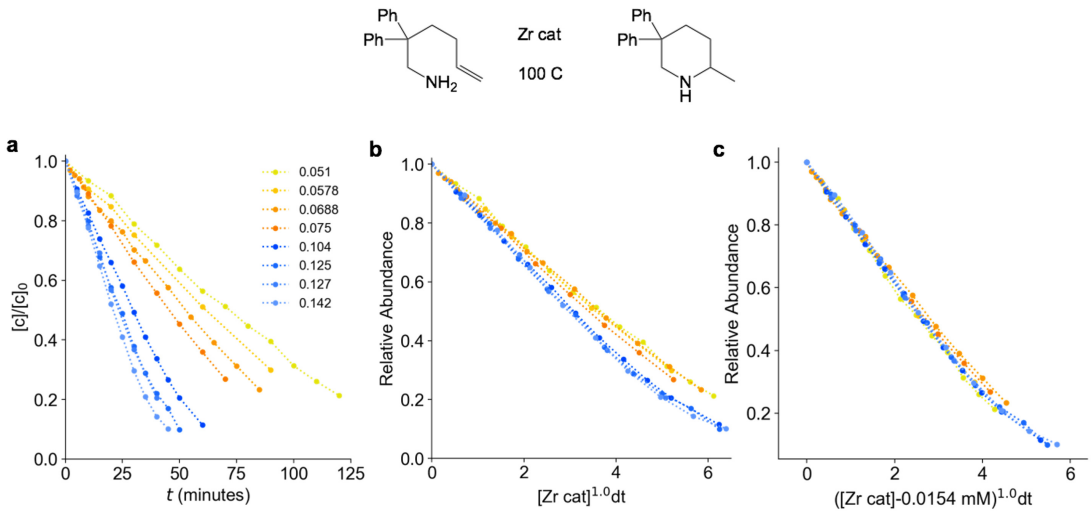

Figure 6.1: An example of VTNA applied to hydramination experiments. The plots show overlaid raw data from each experiment in **a**, time normalized to first order in catalyst concentration in plot **b** and **c** shows improved overlay after adjusting for a constant amount catalyst poisoning across all experiments.

The second dataset assessed by VTNA was that of the formation of a charged cobalt carbonyl alkynyl complex (Figure 6.2) which is found to be first order in $Co_2(CO)_8$. Since the $Co_2(CO)_8$ is in 100-fold excess to the charged alkyne its concentration approximated as constant during the reaction. Once again, the low concentration reaction was slower than expected but when a poison correction of 0.16 mM is applied, the traces overlay (Figure 6.2**c**).

The correction for an unknown amount of poisoning is only meaningful if multiple experiments are conducted in identical conditions. It is particularly important

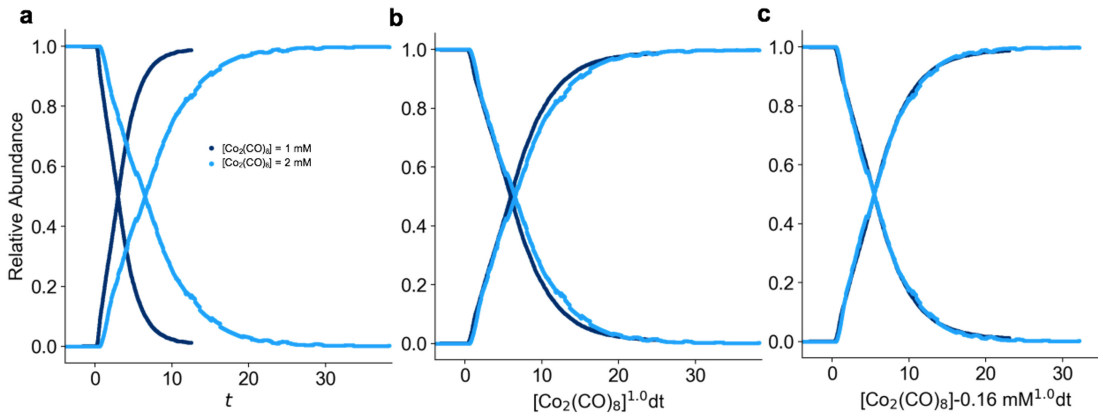

Figure 6.2: VTNA applied to the formation of a bridging alkynyl complex. The formation of the charged analog to CCTBA was monitored by PSI-ESI-MS at 1 mM (dark blue) and 2 mM (light blue) $Co_2(CO)_8$ (**a**). Good overlay is achieved when the time axis is normalized by the concentration of $Co_2(CO)_8$ raised to the first order (**b**). An excellent fit is achieved after adjustments are made for poisoning (**c**).

to have more than two experiments to determine the exact poison levels when the reaction order is also not previously determined. In some cases, a reaction is not exactly first order but somewhere between. Knowing the amount of poison in a reaction and applying adjusting the effective catalyst loading accordingly can be very helpful in kinetic analysis. Purifying solvents and reagents from persistent impurities becomes more difficult the higher the desired purity and in some cases, purchased reagents can be difficult to purify further. Poisoning corrections to kinetic analysis can provide a useful substitute when catalyst loadings are within the limit of the impurities present. This work is in preparation for publication.

6.2 Mechanistic trends in the oxidative addition of aryl halides to palladium

In collaboration with David Leitch and Jingru Lu, the mechanism and reactivity dependencies of oxidative addition (OA) was investigated and our work was published in RSC.[253] Catalytic cross-coupling is one of the most versatile and widely-used methods to link molecular fragments.[254] Using the mechanistic features of oxidative addition to Pd(0) as a guide, Lu considered molecular descriptors that would provide mechanistically meaningful correlations between substrate structures and oxidative addition reactivity (Figure 3).[255] I performed transition state calculations on a number of OA substrates to provide structural and electronic information to back Lu's linear regression model. A brief introduction is given, followed by passage and figures extracted from the SI of the published manuscript.

6.2.1 Background

The oxidative addition of aryl halides to Pd(0) has been studied experimentally[256, 257, 258, 259] and computationally.[260, 261, 262, 263] The mechanism of this catalytic step is generally thought to proceed through a 3-centered transition state where Pd-C and Pd-X formation occurs simultaneously. However, transition state (TS) calculations reveal that the degree of polarization in a heterocycle influences the transition state. For the highly polar substrates, we observed a minimum energy path proceeding through C-X bond cleavage followed by Pd-X bond formation, resembling the mechanism for nucleophilic aromatic substitution (S_NAr).[260, 263] The mechanisms are illustrated by Lu and Leitch in Figure 6.3.

For both pathways, four steps are considered: the free catalyst and substrate, the π-complex intermediate, the oxidative addition transition state and the oxidative addition product. The π-complex intermediate structures of ten substrates were computed and the binding energy was calculated. Based on the structural and electronic features of the intermediates and transition states calculated for the oxidative addition pathway, Lu built a reactivity map from a combination of molecular descriptors such as electrostatic potentials (ESP) for specific atoms in the substrate,[264, 265, 266, 267, 268, 269] A-values to describe sterics,[270] and the intrinsic bond strength index (IBSI).[271]

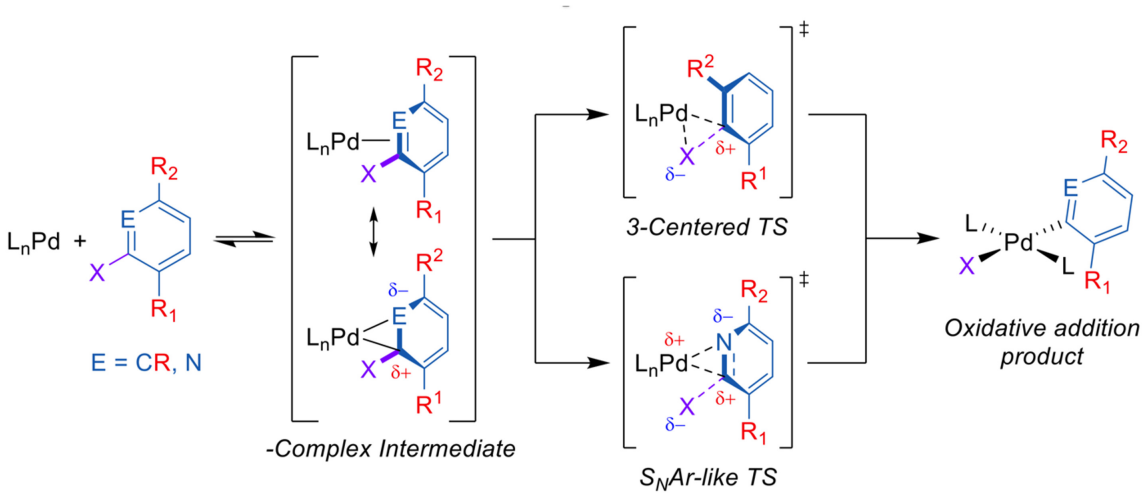

Figure 6.3: The general mechanism for oxidative addition to $L_nPd(0)$, with the π-complex intermediate preceding either Pd insertion into C–X bond, or an S_NAr-like displacement of X (where X=Cl, Br, OTf). Figure and caption reproduced from published manuscript.[253]

6.2.2 Methods

To locate transition states for oxidative addition, different reaction coordinates were scanned depending on the nature of the aromatic substrate. For chlorinated pyridine substrates, the transition state of the oxidative addition step was found by stretching along the Cl-C2 bond axis to locate the "S_NAr-like" transition state. To locate the "3-centered" oxidative addition transition state for aryl bromides, we used a relaxed scan opening the C1-Pd-Br angle from the π-complex intermediate to the cis oxidative addition product; this cis complex then isomerizes to the more stable trans geometry (which is the experimentally observed geometry).

Transition state structures used in this work were obtained in ORCA 4.0.1.2[153] using relaxed scans with an RI BP86/def2-SVP approach with D3BJ dispersion for all atoms except for Pd, for which a def2- TZVP basis set was used. Subsequent electronic structure calculations were then performed with a RI-B2PLYP/def2-TZVP approach with D3 dispersion to calculate TS energies. The same approach was used to generate starting, intermediate and product structures. Lu generated average ESP values using transition state structures. An example input file to compute a geometry is provided below.

Geometry:

```
! RI BP86 def2-SVP def2/J D3BJ TIGHTSCF Opt Grid3 FinalGrid5
%basis newgto Pd "def2-TZVP" end end
```

Energy:

```
! RI-B2PLYP D3 def2-TZVP def2-TZVP/C TIGHTSCF
```

Figure 6.4: Example input files for geometry and electronic structure calculations.

6.2.3 Results and Discussion

The energies of the six intermediates and their corresponding transition states and products are given in 6.1. The simplified reaction coordinates for oxidative addition of the 2-chloropyridine and bromobenzene substrates are given in Figure 4. Overall, the trends in reactivity mirror those observed experimentally. One minor discrepancy is the transition state energy for 4-bromoanisole is slightly lower than for bromobenzene (3 kJ/mol difference), whereas the experimental $\Delta\Delta G^{\ddagger}$ is $\sim$1.5 kJ/mol with bromobenzene lower than 4-bromoanisole. The bent geometry of the $Pd(PCy_3)_2$ starting structure P–Pd–P bond angle of 160.3° agrees with geometries previously reported in the literature.[272] Our π-complex intermediate structures and transition states are also consistent with previously reported geometries for related systems.[260]

The reaction pathways calculated for aryl chlorides (Figure 6.5**a**) show an elevated intermediate energy and transition state barrier during oxidative addition 2-chloro-6-aminopyridine (orange). For aryl bromides (Figure 6.5**b**), bromobenzene boasts the highest transition state barriers closely followed by 4-bromoanisole. In both cases, electron withdrawing cyano groups stabilize the intermediate and transition state structures.

These electronic energies provide a benchmarking tool and suggest that intermediate structures along with simple molecular descriptors suffice in predicting the reactivity of any aryl substrate for oxidative addition. Lu also found that ESP values found on atoms in intermediate structures successfully reproduced trends from transition state structures. The reactivity model developed by Lu demonstrates that a quantitative structure–reactivity model for oxidative addition enables accurate predictions for the outcome of various cross-coupling reactions. By correlating relative reaction rates with easily-obtained molecular descriptors, Lu's model can predict the reactivity of diverse (hetero)aryl electrophiles toward oxidative addition

△E (kJ/mol)	π complex intermediate	transition state	product (cis)	product (trans)
2-chloro-6-cyanopyridine	+14	+27	−103	−198
2-chloropyridine	+18	36	−125	−164
2-chloro-6-aminopyridine	+45	+57	−101	−179
4-bromobenzonitrile	-9	+15	−128	−206
bromobenzene	+11	+34	−110	−190
4-bromoanisole	+7	+31	−108	−157

△E (kJ/mol)	π complex intermediate
2-chloro-3-methylpyridine	−3
2-chloro-6-methylpyridine	+6
2-chloro-3-trifluoromethylpyridine	+3
2-chloro-6-trifluoromethylpyridine	+2
2-chloro-3-cyanopyridine	−41

Table 6.1: Tabulated energies (kJ/mol) of key species in the oxidative addition pathway relative to the unbound substrate and $Pd(PCy_3)_2$. The top table shows step energies from full reaction steps. The energy of forming the intermediate precursor complex was also calculated for six additional substrates (bottom table).

to Pd(0) before performing cumbersome reactions or transition state calculations.

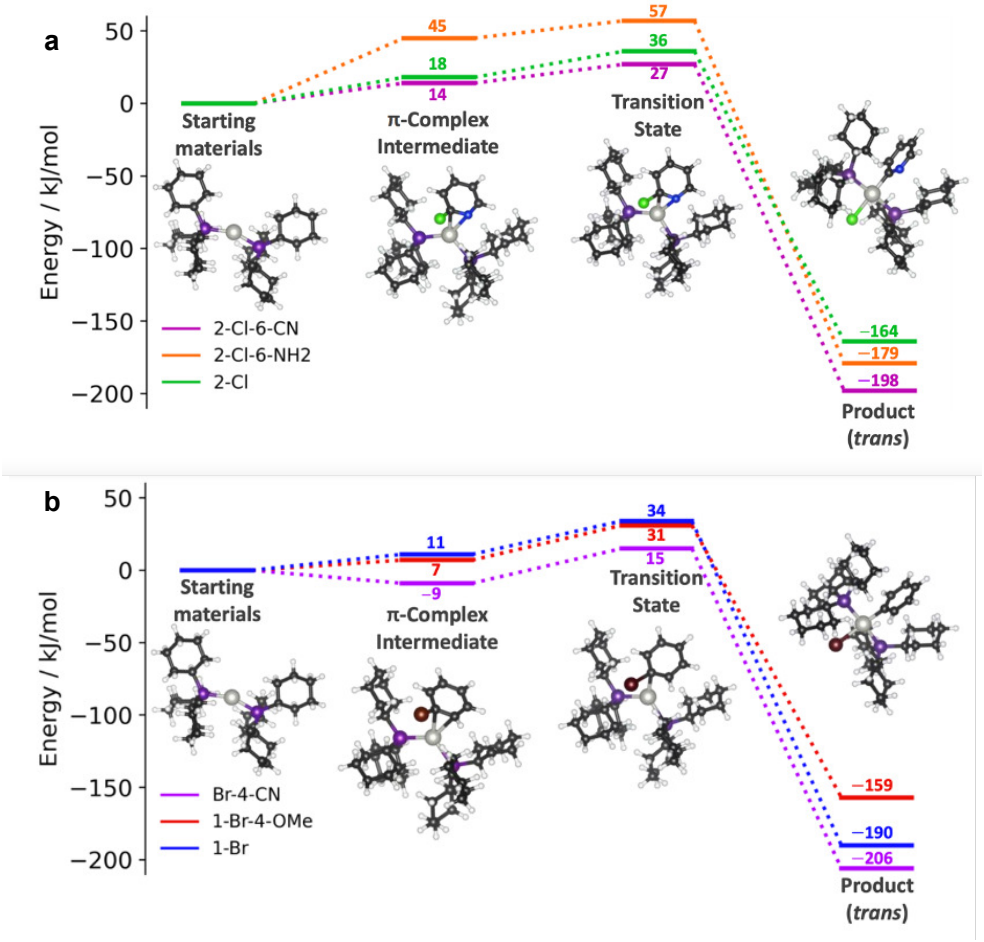

Figure 6.5: Simplified calculated reaction coordinate for oxidative addition of chloro and bromo substrates. Panel **a** shows 2-chloro-6-cyanopyridine (purple), 2-chloro-6-aminopyridine (orange), and 2-chloropyridine (green) to $Pd(PCy_3)_2$. The calculated structures for 2-chloropyridine derivatives are shown as representative. Panel **b** shows the reaction path energies of 4-bromobenzonitrile (purple), 4-bromoanisole (red), and bromobenzene (blue). Calculated structures for the bromobenzene derivatives are shown as representative. The cis oxidative addition products are not shown.(**b**).

6.3 Trichloro(Dinitrogen)Platinate(II)

In a collaboration with Gilian Thomas, the existence of a dinitriogen ligand on trichloroplatinate was investigated and the findings were pubished.[273] I performed DFT calculations to compare the binding energies of various isobaric species to supplement mass spectrometric results. Excerpts related to my contributions have

been selected from the published manuscript, and are summarized below.

6.3.1 Background

Zeise's salt is the oldest known organometallic complex, first isolated in 1830 after boiling platinum tetrachloride in ethanol.[274] However, the complex has since been made using ethylene.[275] Crystallographic data [276, 277] shows that the ethylene binds in a side-on a bonding mode as described by the Dewar–Chatt–Duncanson model.[278] Zeise's salt marks the beginning of organometallic chemistry research. A variety of derivatives have been prepared since where the ethylene is replaced by another 2-electron ligand.[279, 278, 280, 281] Monodentate alkenes tend to bind weakly to metal centers, and it is generally difficult to preserve their coordination even under the mildest of ESI-MS conditions.[282, 283] Since ethylene ligand binds tenaciously to the platinum, Thomas set out to investigate whether it would remain bound throughout the desolvation process during electrospray ionization mass spectrometry (ESI-MS). However, when Thomas prepared a $[PtCl_4]^{2-}$ solution in water a minor peak with the expected *m/z* and isotope pattern for $[PtCl_3(C_2H_4)]^-$ was observed in the absence of ethylene. Collision-induced dissociation (CID) experiments of the unexpected peak resulted in the loss of a neutral species with a molecular weight of 28 Da, as would be expected for the ethylene species. Since Nitrogen also has the same molecular weight as ethylene (28 Da), it was a probable explanation for this ion. Dinitrogen is present in abundance during ESI-MS experiments thanks to its use as a desolvation gas. Dinitrogen complexes have been reported for metals in Groups 3–9,[284, 285, 286, 287, 288] some with carefully constructed coordination environments,[289, 290, 291, 292, 293, 294, 295, 296, 297] and others evolved for nitrogen fixation,[298, 299, 300, 301] dinitrogen complexes are far less common for Groups 10 and 11. However, dinitrogen complexes involving platinum have not been isolated. Some mass spectrometric studies have been performed to study PtN_2 bonds under specialized conditions.[302, 303, 304, 305] There is ample interest in metal centers which will bind to dinitrogen species due to the inherent difficulty of activating the dinitrogen bond.[306] The robustness of the observed gasphase $[PtCl_3(N_2)]^-$ species was probed using accurate mass analysis, MS/MS studies, ion-mobility spectrometry (IMS), and computational chemistry by myself. All experiential work was conducted by Thomas. We compared all molecules of mass 28 Da that can act as a ligand

for the $[PtCl_3]^-$ fragment: ethylene, dinitrogen, and carbon monoxide. The resulting $[PtCl_3(L)]^-$ complexes are numbered **1** (L=C_2H_4), **2** (L=N_2) and **3** (L=CO). The binding energies and configurations of these complexes were investigated computationally as well as a number of adducts with common solvents.

6.3.2 Methods

Ion-mobility data for each of the three complexes was collected on a Waters Synapt G2-Si instrument by Thomas. Computational analysis of the three ions allows us to assess the strength of binding of the ligands in the gas phase, and in keeping with the tandem mass spectrometric results, the calculations showed the order of binding strength to be CO>C_2H_4 >N_2. Because of the low number of atoms, calculations could be performed at a high level. Binding energies of N_2, CO, and C2H4 to $[PtCl_3]^-$ were calculated using density functional theory (DFT) at the RI-UB2PLYP/def2-TZVPP level of theory,[115] with D3 dispersion corrections[307] using ORCA 4.0 software.[152]

6.3.3 Results and Discussion

The difference in drift time in the ion-mobility spectra for **3** and **1** (Figure 6.6) is somewhat surprising, given the similarities in size of the two complexes (same nominal mass and number of atoms), but drift times are dependent on factors including ion-neutral interactions,[308] drift gas polarizability,[309, 310] shape,[311] and charge state.[312] Additionally, ions with a more delocalized charge are less prone to forming short-lived heterodimers with the drift gas molecules.[313, 314, 315] Because CO is more highly polarized than N_2 (see Figure 6.6 insets of electrostatic potentials mapped on to the electron density isosurface), it exhibits a longer drift time despite their similarity in collisional cross-section. The computational results predict the strongest bond energies for CO, then ethylene, then dinitrogen, in full agreement with the MS/MS and ion-mobility results obtained by Thomas.

The ligand dissociation energies for L ligands in complexes **1**, **2**, and **3** were compared to solvent molecules and O_2 for context (Figure 6.7 and Figure 6.8). N_2 was found to exhibit stronger coordination to Pt than methanol and slightly weaker binding than acetonitrile. Other polar ligands examined were water and dimethylformamide (DMF), and these both have markedly lower binding energies than N_2.

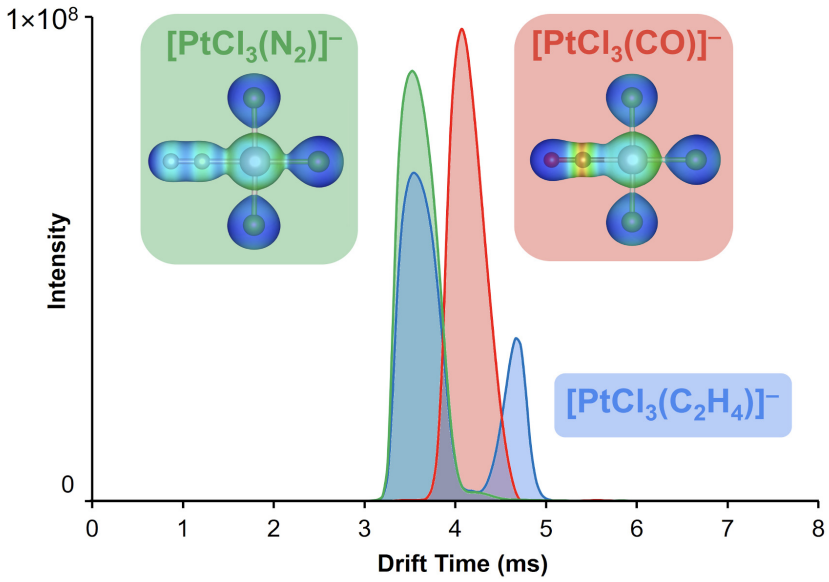

Figure 6.6: Ion-mobility spectrum for $[PtCl_3(C_2H_4)]^-$ (blue), $[PtCl_3(N_2)]^-$ (green) and $[PtCl_3(CO)]^-$ (red). The area of each trace has been normalized to the same value. Structures of $[PtCl_3(N_2)]^-$ (left) and $[PtCl_3(CO)]^-$ (right) show the electrostatic potential (red=0.8, blue=0.1) calculated with the orca_vpot keyword and plotted as a cube file mapped onto the electron density isosurface (0.1 e$Å^{-3}$).

Dioxygen was the weakest binder of all, with less than half the binding strength of N_2 (unlike N_2, the strongest binding mode for O_2 was side-on rather than end-on).

Frontier molecular orbitals were plotted for **1**, **2**, and **3** (Figure 6.9). All exhibited the synergistic π back-bonding that is a feature of all three ligands, with filled ligand orbitals σ-donating into empty metal orbitals of appropriate symmetry, and filled metal orbitals donating π electron density back to the ligand into empty π^* orbitals.[316, 317] Comparing the calculated N_2 bond length of 1.112 $Å$ in **2** to established bond lengths in structurally characterized dinitrogen complexes is instructive. Examination of iridium (the closest analogue to Pt) complexes of dinitrogen in the Cambridge Structural Database (36 unique bond lengths are known), we find the N_2 distance falls in the range 0.982 $Å$[318] to 1.183 $Å$,[319] with an average of 1.117 $Å$, strikingly close to that calculated for **2**. The bond length in **2** is most similar to that in an iridium pincer complex prepared by Brookhart and co-workers in which the dinitrogen ligand (N-N distance 1.119 $Å$) is bound to two iridium centers.[320]

Given the surprisingly high gas-phase and calculated stability of this platinum

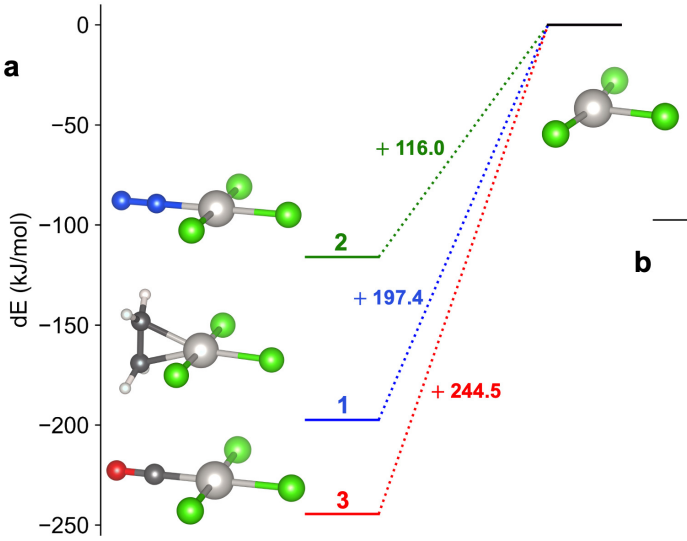

b

L	L Dissociation (kJ/mol)
C_2H_4	+197
N_2	+116
CO	+244
ACN	+119
MeOH	+111
H_2O	+98
DMF	+93
O_2	+49

Figure 6.7: Ligand dissociation energies (LDE) calculated as reaction enthalpies for the dissociation reaction $PtCl_3{-}L \rightarrow PtCl_3{+}L$. Comparison of C_2H_4, N_2 and CO (diagram) to that of common readily available compounds (table **b**)

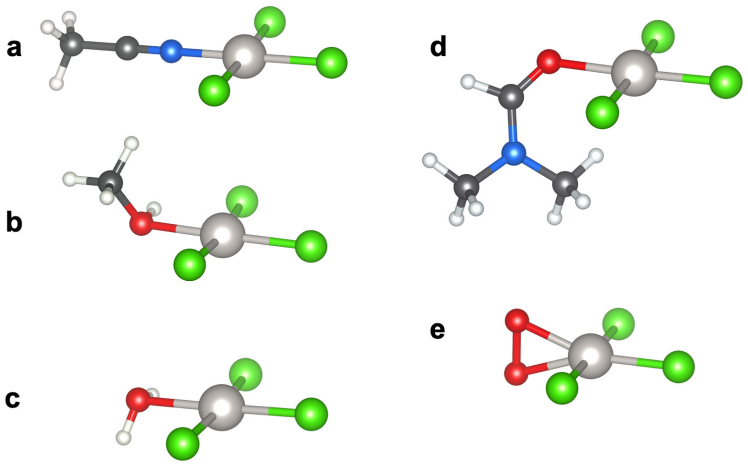

Figure 6.8: Optimized structures of PtCl3 coordinating with common ligands. The additional ligands considered were O_2 (**a**), H_2O (**b**), MeOH **c**, MeCN (**d**), e) NMe_2CHO (**f**)

dinitrogen complex, **2** makes for a feasible synthetic target. The relatively high strength of binding may provide exploitable levels of activation of the dinitrogen molecule in water, leading to new opportunities in functionalization and catalysis.

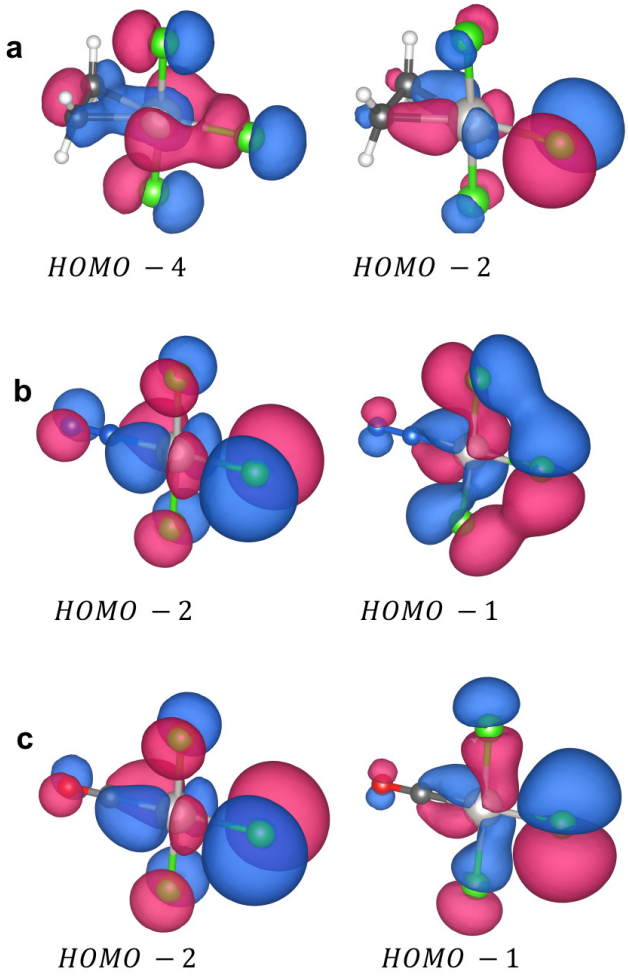

Figure 6.9: Occupied molecular frontier orbitals from complex **1** (**a**), **2** (**b**), and **3** (**c**) involved in binding to their respective ligands.

6.4 Reactive metallocene cations as sensitive indicators of gas-phase oxygen and water

Nitrogen generators are becoming increasingly popular as a gas source for mass spectrometric applications.[321] Nitrogen generators supply nitrogen on demand and save a significant amount of money in labs that require a continuous N_2 supply. However, in order to conduct air sensitive chemistry, the supply of N_2 must be of high enough purity.[322] The McIndoe lab had recently installed a factory-refurbished, N_2 generator, supplied by Peak Scientific. Reduced titanocene(III) complexes and cationic zirconocene(IV) alkyls were used as indicators for oxygen

and water in the N_2 supply.

6.4.1 Background

Nitrogen generators are becoming increasingly popular as a gas source for mass spectrometric applications.[321] Nitrogen generators supply nitrogen on demand and save a significant amount of money in labs that require a continuous N_2 supply. However, in order to conduct air sensitive chemistry, the supply of N_2 must be of high enough purity. The McIndoe lab had recently installed a factory-refurbished, N_2 generator, supplied by Peak Scientific. Reduced titanocene(III) complexes and cationic zirconocene(IV) alkyls were used as indicators for oxygen and water in the N_2 supply. The gas phase reactivity of $[Cp_2ZrMe]^+$ is limited to the work published by Richardson et al.[323, 324, 325] and Chen.[326] Other than comments about the hydrolytic sensitivity in the experimental sections there is lacking work published that discusses the reaction with O_2. Therefore, the reaction of formation of $[Cp_2ZrO_2]^+$ from $[Cp_2ZrMe]^+$ in the gas phase was investigated computationally.

6.4.2 Methods

The oxidation reactions observed by mass spectrometry were modelled computationally. Reaction paths for the oxidation of $[Cp_2Ti(CH_3CN)_2]^+$ and $[Cp_2ZrMe]^+$ were estimated a series of DFT functionals in the SIESTA 4.0.1 and ORCA 4.0 codes.[131, 152] A spin-polarized UPBE/DZP formalism was used in SIESTA, with Troullier–Martins norm-conserving pseudopotentials, and dispersive interactions included at the D2 level of Grimme, which is appropriate for gas-phase metal species.[236, 115] The effects of Hartree-Fock exchange and basis set size were considered by using a series of unrestricted methods available in the ORCA software. Single point energies for SIESTA-optimized ground and transition state structures were confirmed using UPBE0/TZVP, UPBE0-D2/TZVP, UPBE0-D3/TZVP, and RI-UB2PLYP-D3/TZVP in ORCA . The structural convergence of relevant, stable Ti complexes was confirmed by comparison to RI-UB2PLYP-D3/TZVP-level calculations in ORCA. Given the agreement between SIESTA-based UPBE/DZP calculations and ORCA-based RI-UB2PLYP-D3/TZVP, all Zr calculations were performed in SIESTA.

Transition states were estimated using relaxed scans (linear transit) in SIESTA,

using a homemade Python script that reduced and fixed the distance between an oxygen molecule and the metal complex. Methyl groups are quite energetic, so the presence of possible methyl-scavenging molecules (O_2, N_2, methyl radical) was also considered in the case of $[Cp_2ZrMe]^+$ oxidation. Additional ab initio molecular dynamics (AIMD) calculations were performed in SIESTA at the PBE/DZP level, to follow the behavior of the complexes under ambient temperature conditions. The AIMD procedure in SIESTA used a Nose-Hoover thermostat ramping from 0 to 300 K, with 1 fs timestep. Between 500 and 1000 timesteps were considered, until the simulation completed. All SIESTA calculations used a pseudo-atomic orbital (PAO) confinement energy of 1 mRy.[327]

6.4.3 Results and discussion

Mass spectrometric results obtained by Joshi suggest that $[Cp_2Ti(NCMe)]^+$ is the primary source of the oxygen-containing complex $[Cp_2TiO_2]^+$. Ab initio molecular dynamics (AIMD) simulations37 at 300 K of $[Cp_2Ti(NCMe)]^+$+O_2 and $[Cp_2Ti(NCMe)_2]^+$+O_2 support this hypothesis, as the titanium in the $[Cp_2Ti(NCMe)_2]^+$ complex is inert to O_2 while the Ti of $[Cp_2Ti(NCMe)]^+$ readily binds to O_2 (Figure 6.10).

Since the concerted pathway from $[Cp_2Ti(NCMe)_2]^+$ to $[Cp_2TiO_2(NCMe)]^+$ or $[Cp_2TiO_2]^+$ is not likely, we calculated energy diagrams for two possible mechanisms, both involving the initial dissociation of acetonitrile from $[Cp_2Ti(NCMe)_2]^+$ to form $[Cp_2Ti(NCMe)]^+$. A concerted mechanism wherein O_2 replaces CH_3CN as a ligand was considered as well as a stepwise mechanism where the second O_2 binds in a monodentate fashion prior to loss of the second CH_3CN and O_2 reorientation to η^2-O_2 (Figure 6.11). Changes in energy for the different steps along the Ti reaction paths are reported, at various levels of theory (Table 6.2). Energy differences obtained from the PBE-D2/DZP methodology in SEISTA were consistent with higher-level B2PLYP-D3 calculations, thus validating the SIESTA approach for these systems. Loss of the first acetonitrile ligand in the first step destabilizes the complex, creating the opportunity for attack from the O_2 molecules present in the gas phase. Species **2**, **3**, and **4** were all observed in the mass spectrometry experiments. The most stable structure of **4** had O_2 in an η^2 configuration, replacing both monodentate CH_3CN ligands (Figure 6.11). The **2** $\rightarrow$ **3** $\rightarrow$ **4** pathway is a sequence of bond dissociation and association steps and thus barrier-less, and the lowest energy pathway in the computational model. However, higher-energy

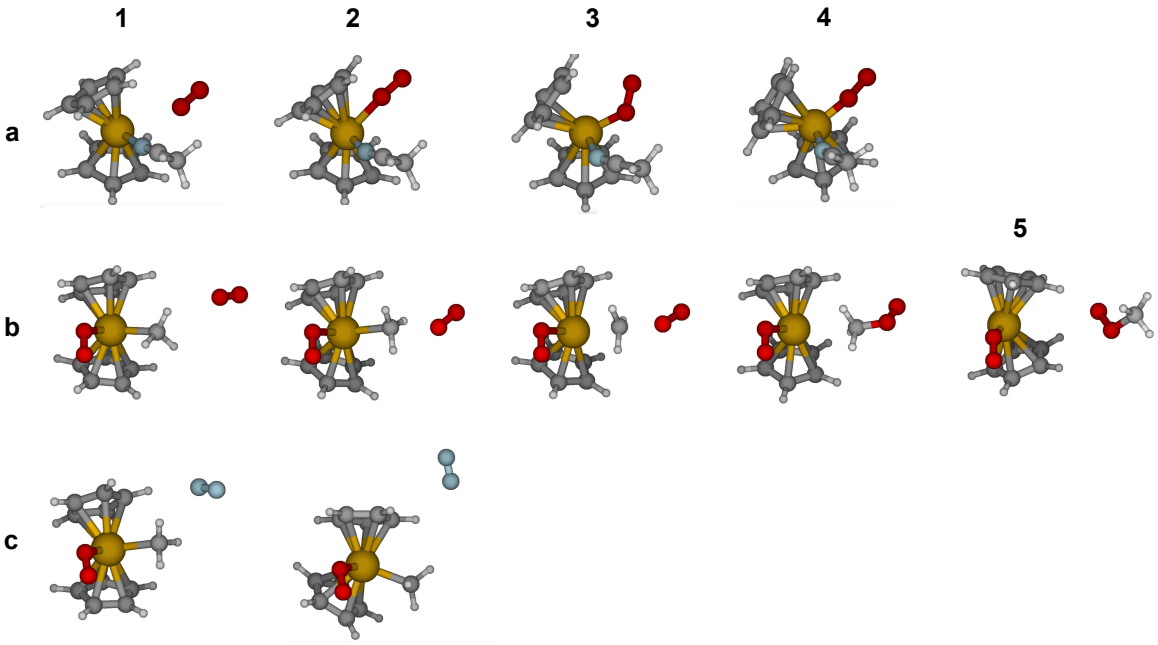

Figure 6.10: Snapshots from AIMD simulations at 300 K. Over the course of 1000 fs, **a** shows O_2 readily coordinating to $[Cp_2Ti(NCMe)_2]^+$, **b** shows O_2 abstracting a methyl group from $[Cp_2Zr(O_2)Me]^+$ and **c** shows N_2 inert towards the same complex.

species are accessible in the ESI-MS setup, making a concerted mechanism for the **2** $\rightarrow$ **4** pathway viable.

Step	PBE vdW-TS	PBE0/ TZVP vdW-TS	PBE0-D2/ TZVP	PBE0-D3/ TZVP	RI-B2PLYP-D3/TZVP	RI-B2PLYP-D3/TZVP
1 $\rightarrow$ **2**	+137	+102	+207	+150	+122	+129
2 $\rightarrow$ **3**	-86	-97	-155	-140	-94	-104
3 $\rightarrow$ **4**κ^1	+159	+112	+145	+128	+167	+143
3 $\rightarrow$ **4**η^2	+77	+52	+79	+67	+55	+75

Table 6.2: The single point energies (kJ/mol) calculated in SIESTA (column one) were benchmarked against a range of functionals in Orca. The final column shows results from unrestricted RI-B2PLYP-D3/TZVP to optimize the geometry and electronic structure. Note that all calculations are unrestricted DFT.

The possibility of a monodentate binding by O_2 was considered in the product **4**, in addition to the bidentate mode. The $\kappa 1 - O_2$ form is less stable than the $\eta^2 - O_2$ binding mode. This is reflected in the shapes of the highest occupied molecular orbitals (HOMO) of the two species. Greater overlap between the metal center

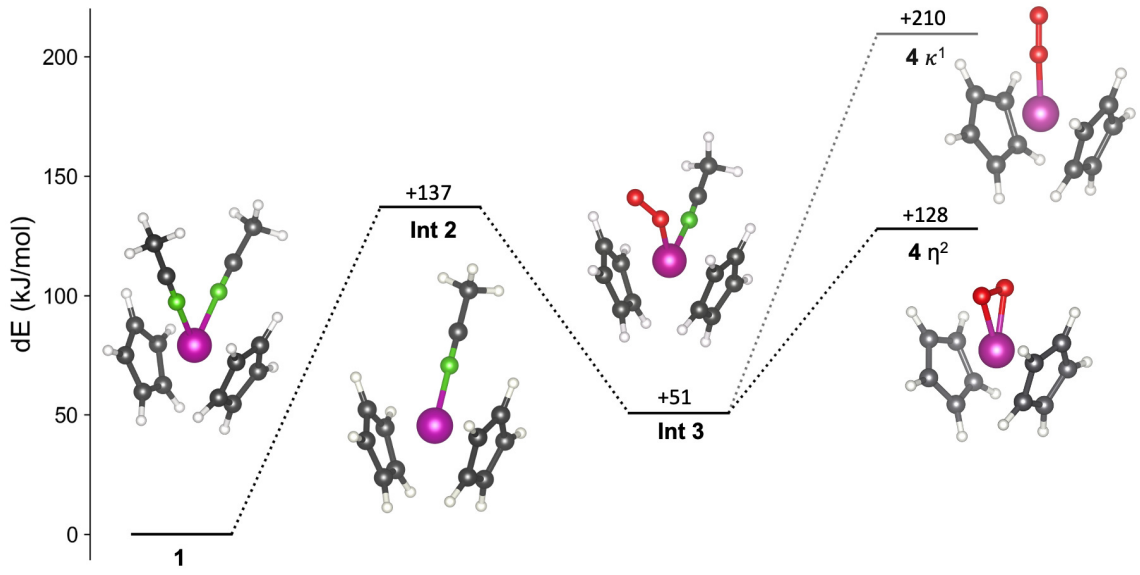

Figure 6.11: The $[Cp_2Ti(NCMe)_2]^+$+ O_2 reaction pathway calculated with SIESTA (UPBE-D2). In the stepwise mechanism for Ti ligand exchange, the reaction pathway can be modelled as a series of bond association/dissociation steps **1** $\rightarrow$ **2** $\rightarrow$ **3** $\rightarrow$ **4**. All steps are single bond dissociation or association steps and are therefore barrier-less. Although a concerted pathway from **2** to **4** may occur when the Ti/O_2 bond forms as the CH_3CN breaks away, there is no saddle point along the PES because the minimum energy of this transition state results in structure **3**.

and two of the lone pair orbitals of the bidentate O_2 molecule is evidenced in the HOMO of the $\eta 2 - O_2$ complex (Figure 6.12**b**), compared to the single lone-pair participating in binding of the $\kappa 1 - O_2$ mode (Figure 6.12**a**).

On the other hand, reaction coordinate analysis through linear transit scans at 0 K identified a stable intermediate where Zr is bound to both O_2 and Me (Int**6** in Figure 6.13), which was not observed experimentally. The gas phase calculations of the possible $[Cp_2ZrMe]^+$ + O_2 $\rightarrow$ $[Cp_2ZrO_2]^+$ + $Me^\bullet$ reaction via a concerted mechanism found that the methyl radical was too reactive to present as an independent leaving group. Instead, the metal center accommodated both ligands as $[Cp_2ZrMeO_2]^+$, an intermediate species that is not observed in the mass spectra. Instead, $[Cp_2ZrO_2]^+$ is observed directly in the experiment, suggesting that the methyl group has to leave through a stabilized pathway, such as by attaching to a scavenging group. Gas phase scavenging reactions have been observed in MS previously.[328, 329]

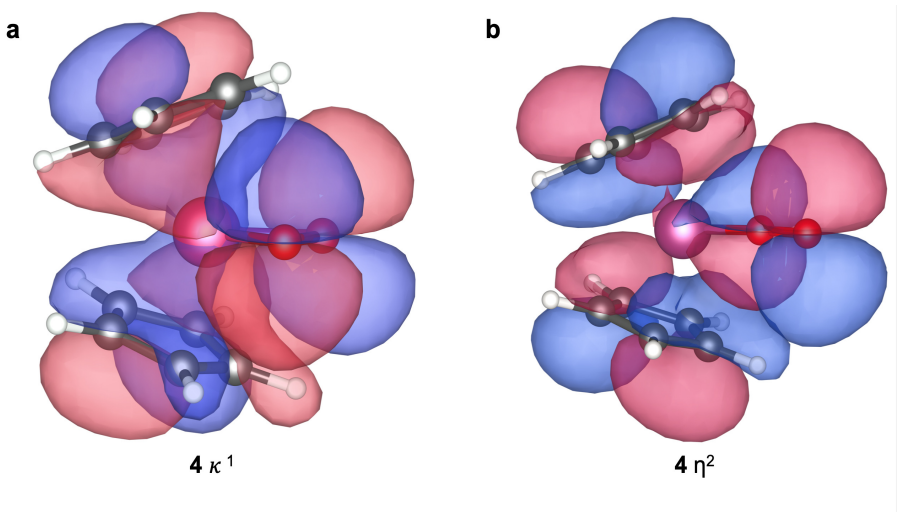

Figure 6.12: HOMO in (a) monodentate and (b) bidentate bound O2 in [Cp2TiO2]+

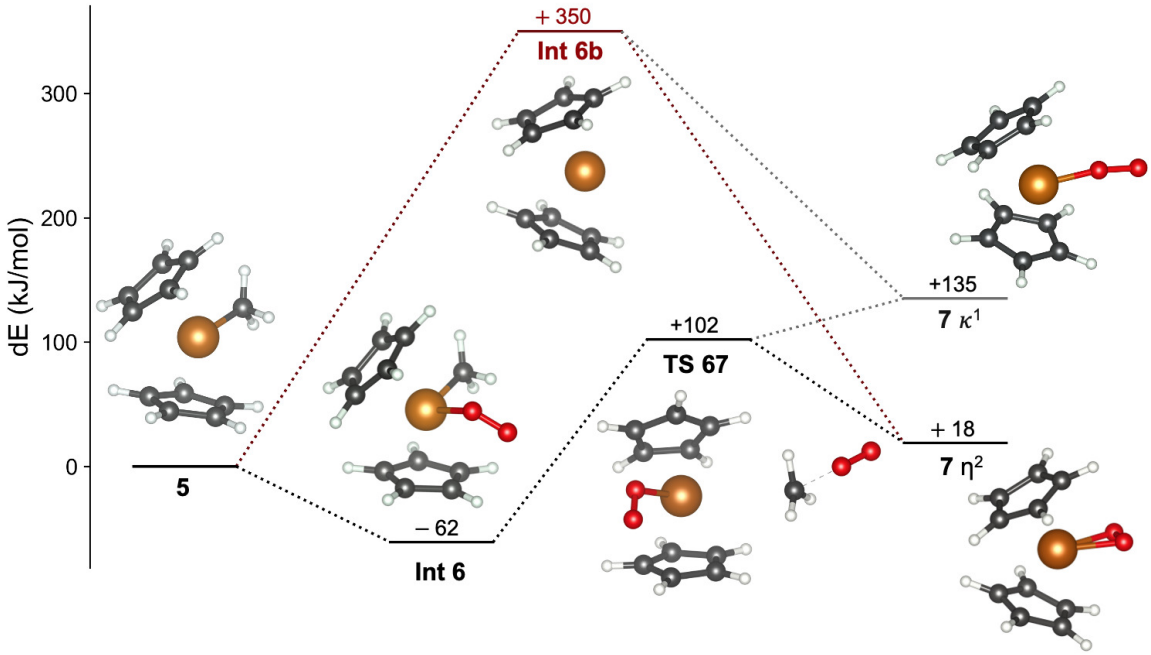

Figure 6.13: The $[Cp_2ZrMe]^+ + O_2$ reaction pathways calculated with SIESTA (UPBE-D2). The Zr ligand exchange is assisted by stabilizing the Me leaving group (TS**67**).

Ab initio molecular dynamics calculations of the reactions between $[Cp_2ZrMeO_2]^+$ and possible scavengers were carried out at the PBE-vdwTS/DZP level in SIESTA, at a temperature of 300K, for 2 ps. Fluorobenzene (solvent), N_2 and O_2 (present

in the desolvation gas) being the only species present in abundance during the transfer from solution phase to the high vacuum of the mass spectrometer were all considered as scavenger candidates. Fluorobenzene and N_2 were inert to the $[Cp_2Zr(O_2)Me]^+$ complex (Figure 6.10**c**) but O_2 readily facilitates the removal of the methyl radical (Figure 6.10**b**) and formation of $[Cp_2ZrO_2]^+$.

Like the Ti complex, O_2 as a side-on ligand is more favorable than end-on. From MO diagrams (Figure 6.14), we can make a qualitative argument that this is due to favorable overlap from p_x and p_z orbitals in the two highest occupied molecular orbitals (HOMOs) in the side-on conformation. The end-on binding mode provides the Zr center overlap with the p_z and p_y from only one oxygen.

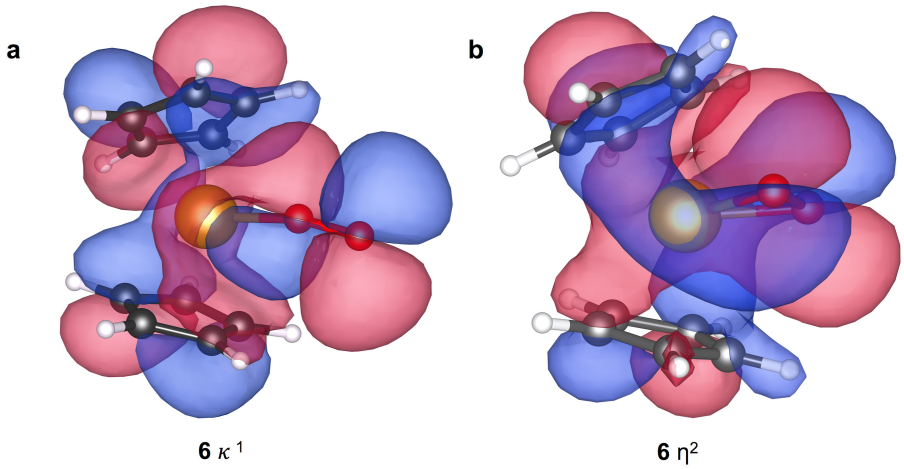

Figure 6.14: HOMOs of the zirconocene complexes: (**a**) and (**b**) show HOMO for monodentate and bidentate-bound O_2 in $[Cp_2ZrO_2]^+$.

Only the most reactive ions generate byproduct ions attributable to gas-phase oxygenation, and in the case of an indicator developed for detection of O_2,[330, 331] the extent of oxidation is $<$4% at the highest flow rate examined by Joshi. Extremely reactive ions such as the 14e$^-$ $[Cp_2ZrMe]^+$ complex are much more reactive towards oxygen and water; using such ions as probes, the source(s) of contamination within the spectrometer can be readily discovered and corrected for as in the present work. Computational work provided insight into how the observed oxidation chemistry proceeded in the absence of species intermediate between the species injected and that observed, which in the case of the zirconocene species required the involvement of another oxygen molecule to mediate the removal of the methyl group. Calculations pointed to both the oxidized titanocene and zirconocene

species having dioxygen coordinated in a side-on binding mode.

6.5 Other collaborative work

Finally, Catacycle.com was a collaboration with Brett Henderson and James McFarlane in which we launched a python-powered website, *catacylce.com*.[332] The information conveyed by catalytic arrows has not evolved much in recent years.[333] The concept of Catacycle is to convey rate information through the thickness of the arrow, where thicker arrows are drawn for faster steps and the thinnest arrows assigned to the rate limiting steps. Furthermore, unlimited color options, reversibility, perfect circles and many more features are available to chemists seeking to make attractive figures without much fuss. The Catacycle webtool has been widely used to produce figures since its launch in 2019.[334, 335, 336, 337, 338, 339, 340]

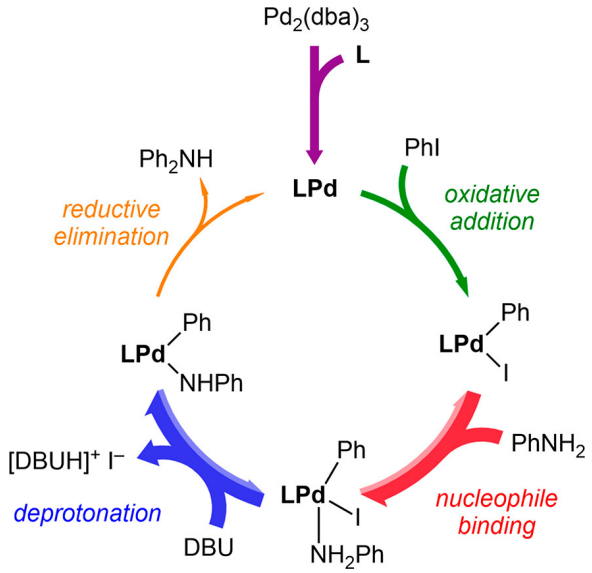

Figure 6.15: Catalytic cycle for the Buchwald–Hartwig amination. Catalyst activation (fuschia) is relatively slow, as is oxidative addition (green). Addition of the aniline (red) and deprotonation (blue) are both very fast and reversible. The reductive elimination (orange) is the slowest step and is the point at which the catalyst rests.

Additional collaborations include a methodology review article on PSI[184] and filming tutorials for PythoMS.[341] In the review article, figures were produced to demonstrate the smoothing effect of normalization on a noisy dataset in mass spectrometry. In collaboration with Lars Yunker on his python tool for the analysis of raw mass spectrometric data, tutorials were filmed to aid users in accessing and using the package in a MacOS environment.[341] Several handy python scripts

generated over the course of my PhD are made publicly available in Appendix B and on Github at *github.com/sofiadonnecke* along with the PyVTNA package. A special thank you goes to Brett Henderson who assisted me with writing and troubleshooting many of the complex scripts and python packages.

Chapter 7

Conclusion

A vast number of important processes take place on surfaces, however many of these chemical reaction pathways are poorly understood. In this dissertation, a variety of organometallic surface reactions were visited, ranging from catalysis to atomic layer deposition processes, with the purpose of understanding their mechanisms and benchmarking the methods used to describe them. From atomic layer deposition to catalytic processes, reaction pathways were investigated using both periodic and finite models. A mechanistic understanding of ALD deposition pathways allowed us to identify promising cobalt precursors to address the challenge of producing cobalt thin films for complex nanodevices. Theoretical and experimental methods were applied in combination to study the elementary steps taking place in the gas phase and on the surface guide the rational design of new precursors for ALD.

Besides mechanistic understanding, this thesis also focused on method selection, refinement and benchmarking for these complex processes. The tradeoff between system size and computational expense governs the selection of methods applied to each system. However, PBE0 stood out as a consistent performer for finite transition metal systems when paired with Ahlrich's def2 basis sets. Moreover, the remarkable scaling of the SIESTA method allows us to simulate large periodic systems with surprising accuracy. ESI-MS allowed us to experimentally observe the gas phase decomposition pathways of Co ALD precursors in Chapter 3.

Experimental and computational techniques used in combination to study a system are a powerful tool for better understanding the reaction pathways that take place. In Chapter 3, the decomposition pathways of CCTBA and CCTMA were studied in the gas phase by mass spectrometry and revealed very similar

pathways aside from a stronger alkyne-Co bond in the case of CCTBA. Further computational simulations of the deposition revealed stronger surface interactions between CCTMA and the Si(111) surface. The reaction barriers were assessed for the incorporation of carbon impurities and revealed a lower reactivity between the internal alkyne. These results strongly suggest that CCTMA may be a more desirable precursor for atomic layer deposition onto silicon and other substrates where CCTBA incorporates high amounts of carbon. Experimental testing should be performed to identify whether CCTMA does in fact outperform CCTBA during ALD on Si and SiO_2.

A novel approach to studying Co ALD precursors was taken to better identify trends in their gas-phase decomposition pathways. Although mass spectrometry has been used to monitor the biproducts in some ALD processes, direct analysis of Co precursors by ESI-MS has not been used to observe their gas phase behaviour. The use of CID to study transition metal complexes can determine factors such as their gas phase stability, the reactivity of their ligands, and the order in which ligands are lost. Performing such an analysis for other precursors such as the CoSi species can determine trends in gas phase reactivity as the silyl ligand varies.

These cobalt silyl precursors are explored computationally in Chapter 4. While these precursors have been patented, their reactivity has not yet been systematically studied. In this chapter, the reactivities of various CoSi precursors were assessed on common surfaces for ALD. The computed pathways suggest that incorporating a silyl ligand unlocks a new deposition mechanism which incorporates a Si$-$Co layer rather than a Co layer on the substrate. According to computed ΔEs, these cobalt silyl species offer a more favorable deposition pathway onto SiO_2 compared to the pathway initiated by M$-$CO loss. This enhanced deposition pathway on the SiO_2 surface offers a new avenue of depositing the initial layer of Co onto silica, which has been problematic in practice. Improving the reactivity between the substrate and the precursors during initial ALD cycles will reduce island growth and increase the uniformity of the initial layers. Moreover, in this chapter a streamlined procedure for obtaining robust binding structures on complex surfaces was developed. By sampling the local PES through AIMD simulations and starting new geometry optimizations from selected time steps, the structure and energy become less biased by the initial structure generated manually. In several cases, this procedure has resulted in significant stabilization for surface binding configurations along energetic pathways. On the other hand, when a more stable binding

geometry is not found, it offers confidence that the original binding configuration is a satisfactory minimum on the PES. These results suggest that AIMD simulations should become a standard approach for exploring stable adsorption configurations for complex molecules and/or surfaces. This dissertation explains a streamlined approach for doing so.

In Chapter 5, the oxygen reaction is modeled on a variety of non-precious metal catalysts. We set out to benchmark the electronic energies and assess the tradeoff between method and system size. We showed that while trends for single-atoms are a poor reflection of larger systems, less extreme reductions such as removal of the outer aryl groups on the molecular phthalocyanine catalysts not only preserves metal trends but also reproduces very similar Δ Es to the original system. However, even when modeled at the atomic scale, these high-spin and high-valent systems pose a challenge for conventional DFT optimization methods. The large number of degenerate orbitals and closely interacting valence electrons make it difficult to converge on a solution for the electronic structure of the reactive center. Even more challenging than finding minima is to find transition state barriers, which is an important measure of catalytic activity. Conventional transition state methods do not accommodate spin transitions along a reaction step, so a manual approach for handling TS calculations is applied to find barriers. Wavefunction methods including CCSD(T) were also benchmarked showing good agreement with DFT for most steps. New questions have opened up from this research such as what to do when we encounter a particularly challenging species such as the M$-$O intermediate with high multi-reference character. Furthermore, we showed that single-atom systems cannot replicate trends found for larger systems but would applying an oxidation state and/or pseudopotentials in place of ligands to the single-metal systems improve the system? Using the tested and benchmarked methods, ligand functionalization, applying solvent models to systems and calculating their free energies will provide practical insight on the performance of these catalysts.

The remainder of my collaborative work is presented in Chapter 6, spanning from python tools to aid kinetic analysis to DFT calculations of molecular-scale organometallic systems. In three published projects, DFT methods were applied to study reactive complexes, their reaction pathways, ligand binding energies and transition states, and results were paired with experimental data obtained by collaborators. Computational findings were in good agreement with experimental results for all three projects. A common theme across several projects is the compatibility

of mass spectrometry with DFT for analyzing gas phase species. Unlike solution-phase reactions, CID experiments occur in the gas phase, which eliminates the need for solvent models to obtain ΔEs consistent with experiment.

There are endless avenues for further exploration for these systems thanks to the multitude of computational techniques available in today's day and age. However, a number of reaction pathways were modelled on the surface which ranged from benchmarking the energetics of known reactions to new systems and their unexplored reaction pathways. In this dissertation promising Co ALD precursors were identified to be tested experimentally. Working with such complex systems led to a computational approach which enhances the process of modelling complex interactions between molecules and surface sites using AIMD. The approach outlined in Chapter 4 offers a simple way to significantly improve adsorption geometries and can be used for any system. The next steps in this research should involve finding reaction barriers of the various CoSi species using the NEB approach as done in Chapter 3. These reaction barriers will provide insight on precursor stability, reactivity towards different surfaces and the effect of ligands on their reactivity. Expanding the computational analysis to include the precursors which were only studied in the gas phase, particularly the family of amines, should also be done to provide specific recommendations for experimental testing. The most important lesson from these projects is to learn as much as possible about the system at hand before setting out to model it. This is important for both identifying all the possible pathways but also to reduce time spent tackling unlikely reaction pathways or steps. If no or very little *a priori* knowledge exists about a pathway, modeling its mechanism can seem daunting. Identifying similar systems which are known to base models off of and to validate reaction intermediates can offer an enormous leg up. In complex systems it is often impractical to model every possible step or pathway the system could take and relying on chemical intuition to pioneer an initial guess for an unexplored pathway is a necessary first step towards understanding the chemistry at hand.

Bibliography

[1] Werner Stumm. Reactivity at the mineral-water interface: Dissolution and inhibition. *Colloids and Surfaces A: Physicochemical and Engineering Aspects*, 120(1-3):143–166, feb 1997.

[2] Ralph T. Yang. Adsorbents: Fundamentals and Applications. *Adsorbents: Fundamentals and Applications*, apr 2003.

[3] J. C. Abanades, B. Arias, A. Lyngfelt, T. Mattisson, D. E. Wiley, H. Li, M. T. Ho, E. Mangano, and S. Brandani. Emerging CO2 capture systems. *International Journal of Greenhouse Gas Control*, 40:126–166, sep 2015.

[4] Arunkumar Samanta, An Zhao, George K.H. Shimizu, Partha Sarkar, and Rajender Gupta. Post-combustion CO 2 capture using solid sorbents: A review. *Industrial and Engineering Chemistry Research*, 51(4):1438–1463, feb 2012.

[5] Sunho Choi, Jeffrey H. Drese, and Christopher W. Jones. Adsorbent materials for carbon dioxide capture from large anthropogenic point sources. *ChemSusChem*, 2(9):796–854, sep 2009.

[6] Peter Strasser and Hirohito Ogasawara. Surface electrochemistry. *Chemical Bonding at Surfaces and Interfaces*, pages 397–455, jan 2008.

[7] Egill Skúlason, Vladimir Tripkovic, Mårten E. Björketun, Sigrídur Gudmundsdóttir, Gustav Karlberg, Jan Rossmeisl, Thomas Bligaard, Hannes Jónsson, and Jens K. Nørskov. Erratum: Modeling the electrochemical hydrogen oxidation and evolution reactions on the basis of density functional theory calculations (Journal of Physical Chemistry C (2010) 114C (18182)). *Journal of Physical Chemistry C*, 114(50):22374, oct 2010.

[8] Zhi Wei She, Jakob Kibsgaard, Colin F. Dickens, Ib Chorkendorff, Jens K. Nørskov, and Thomas F. Jaramillo. Combining theory and experiment in electrocatalysis: Insights into materials design. *Science*, 355(6321), jan 2017.

[9] Sharon Mitchell, Ruixuan Qin, Nanfeng Zheng, and Javier Pérez-Ramírez. Nanoscale engineering of catalytic materials for sustainable technologies. *Nature Nanotechnology*, 16(2):129–139, nov 2021.

[10] Anders Nilsson, Lars G.M. Pettersson, and Jens K. Nørskov. *Chemical Bonding at Surfaces and Interfaces*. Elsevier, 2008.

[11] Jens Hagen. Heterogeneously Catalyzed Processes in Industry. *Industrial Catalysis*, pages 261–298, sep 2015.

[12] By H Stott T and Associate Professor of Physical Chemistry. A theory of the catalytic surface. *Proceedings of the Royal Society of London. Series A, Containing Papers of a Mathematical and Physical Character*, 108(745):105–111, may 1925.

[13] T. Zambelli, J. Wintterlin, J. Trost, and G. Ertl. Identification of the 'active sites' of a surface-catalyzed reaction. *Science*, 273(5282):1688–1690, sep 1996.

[14] R. C. Egeberg, S. Dahl, A. Logadottir, J. H. Larsen, J. K. Noørskov, and I. Chorkendorff. N2 dissociation on Fe(1 1 0) and Fe/Ru(0 0 0 1): What is the role of steps? *Surface Science*, 491(1-2):183–194, sep 2001.

[15] Jens K. Nørskov, Thomas Bligaard, Britt Hvolbæk, Frank Abild-Pedersen, Ib Chorkendorff, and Claus H. Christensen. The nature of the active site in heterogeneous metal catalysis. *Chemical Society Reviews*, 37(10):2163–2171, 2008.

[16] John Humphreys, Rong Lan, and Shanwen Tao. Development and Recent Progress on Ammonia Synthesis Catalysts for Haber–Bosch Process. *Advanced Energy and Sustainability Research*, 2(1):2000043, 2021.

[17] Lionel Delaude and Alfred F. Noels. Metathesis. *Kirk-Othmer Encyclopedia of Chemical Technology*, dec 2005.

[18] Bo Yang, Robbie Burch, Christopher Hardacre, Gareth Headdock, and P. Hu. Origin of the increase of activity and selectivity of nickel doped by Au, Ag, and Cu for acetylene hydrogenation. *ACS Catalysis*, 2(6):1027–1032, jun 2012.

[19] Felix Studt, Frank Abild-Pedersen, Thomas Bligaard, Rasmus Z. Sørensen, Claus H. Christensen, and Jens K. Nørskov. On the Role of Surface Modifications of Palladium Catalysts in the Selective Hydrogenation of Acetylene. *Angewandte Chemie*, 120(48):9439–9442, 2008.

[20] Felix Studt, Frank Abild-Pedersen, Thomas Bligaard, Rasmus Z. Sørensen, Claus H. Christensen, and Jens K. Nørskov. Identification of non-precious metal alloy catalysts for selective hydrogenation of acetylene. *Science*, 320(5881):1320–1322, jun 2008.

[21] L. Carrette, K. A. Friedrich, and U. Stimming. Fuel Cells - Fundamentals and Applications. *Fuel Cells*, 1(1):5–39, 2001.

[22] Kaustav Saikia, Biraj Kumar Kakati, Bibha Boro, and Anil Verma. Current advances and applications of fuel cell technologies. In *Recent Advancements in Biofuels and Bioenergy Utilization*, pages 303–337. Springer Singapore, jan 2018.

[23] Jens K. Nørskov, Felix Studt, Frank Abild-Pedersen, and Thomas Bligaard. Fundamental Concepts in Heterogeneous Catalysis. *Fundamental Concepts in Heterogeneous Catalysis*, 9781118888:1–196, oct 2014.

[24] Suhas G. Jadhav, Prakash D. Vaidya, Bhalchandra M. Bhanage, and Jyeshtharaj B. Joshi. Catalytic carbon dioxide hydrogenation to methanol: A review of recent studies. *Chemical Engineering Research and Design*, 92(11):2557–2567, nov 2014.

[25] T. Bligaard, J. K. Nørskov, S. Dahl, J. Matthiesen, C. H. Christensen, and J. Sehested. The Brønsted-Evans-Polanyi relation and the volcano curve in heterogeneous catalysis. *Journal of Catalysis*, 224(1):206–217, may 2004.

[26] C. R. Henry, C. Chapon, and C. Duriez. Precursor state in the chemisorption of CO on supported palladium clusters. *The Journal of Chemical Physics*, 95(1):700–705, 1991.

[27] Qing Hua Wang, Kourosh Kalantar-Zadeh, Andras Kis, Jonathan N. Coleman, and Michael S. Strano. Electronics and optoelectronics of two-dimensional transition metal dichalcogenides. *Nature Nanotechnology 2012 7:11*, 7(11):699–712, nov 2012.

[28] Yi Zhang, Luyao Zhang, and Chongwu Zhou. Review of chemical vapor deposition of graphene and related applications. *Accounts of Chemical Research*, 46(10):2329–2339, oct 2013.

[29] Zhengyang Cai, Bilu Liu, Xiaolong Zou, and Hui Ming Cheng. Chemical Vapor Deposition Growth and Applications of Two-Dimensional Materials and Their Heterostructures. *Chemical Reviews*, 118(13):6091–6133, jul 2018.

[30] Vera Steinmann, Rupak Chakraborty, Paul H. Rekemeyer, Katy Hartman, Riley E. Brandt, Alex Polizzotti, Chuanxi Yang, Tom Moriarty, Silvija Gradečak, Roy G. Gordon, and Tonio Buonassisi. A Two-Step Absorber Deposition Approach to Overcome Shunt Losses in Thin-Film Solar Cells: Using Tin Sulfide as a Proof-of-Concept Material System. *ACS Applied Materials and Interfaces*, 8(34):22664–22670, aug 2016.

[31] Richard W Johnson, Adam Hultqvist, and Stacey F Bent. A brief review of atomic layer deposition: from fundamentals to applications. *Materials Today*, 17(5):236–246, 2014.

[32] H. Van Bui, F. Grillo, and J. R. Van Ommen. Atomic and molecular layer deposition: off the beaten track. *Chemical Communications*, 53(1):45–71, dec 2016.

[33] Tuomo Suntola and Jorma Antson. Method for producing compound thin films, nov 1977.

[34] Esko Ahvenniemi, Andrew R Akbashev, Saima Ali, Mikhael Bechelany, Maria Berdova, Stefan Boyadjiev, David C Cameron, Rong Chen, Mikhail Chubarov, Veronique Cremers, Anjana Devi, Viktor Drozd, Liliya Elnikova, Gloria Gottardi, Kestutis Grigoras, Dennis M Hausmann, Cheol Seong Hwang, Shih-Hui Jen, Tanja Kallio, Jaana Kanervo, Ivan Khmelnitskiy, Do Han Kim, Lev Klibanov, Yury Koshtyal, A Outi I Krause, Jakob Kuhs,

Irina Kärkkänen, Marja-Leena Kääriäinen, Tommi Kääriäinen, Luca Lamagna, Adam A Łapicki, Markku Leskelä, Harri Lipsanen, Jussi Lyytinen, Anatoly Malkov, Anatoly Malygin, Abdelkader Mennad, Christian Militzer, Jyrki Molarius, Małgorzata Norek, Çağla Özgit-Akgün, Mikhail Panov, Henrik Pedersen, Fabien Piallat, Georgi Popov, Riikka L Puurunen, Geert Rampelberg, Robin H A Ras, Erwan Rauwel, Fred Roozeboom, Timo Sajavaara, Hossein Salami, Hele Savin, Nathanaelle Schneider, Thomas E Seidel, Jonas Sundqvist, Dmitry B Suyatin, Tobias Törndahl, J Ruud van Ommen, Claudia Wiemer, Oili M E Ylivaara, and Oksana Yurkevich. Review Article: Recommended reading list of early publications on atomic layer deposition—Outcome of the "Virtual Project on the History of ALD". *Journal of Vacuum Science Technology A*, 35(1):10801, 2017.

[35] Anatolii A Malygin, Victor E Drozd, Anatolii A Malkov, and Vladimir M Smirnov. From V. B. Aleskovskii's "Framework" Hypothesis to the Method of Molecular Layering/Atomic Layer Deposition. *Chemical Vapor Deposition*, 21(10-11-12):216–240, 2015.

[36] Steven M George. Atomic Layer Deposition: An Overview. *Chemical Reviews*, 110(1):111–131, 2010.

[37] Andrew L Johnson and James D Parish. Recent developments in molecular precursors for atomic layer deposition. In *Organometallic Chemistry: Volume 42*, volume 42, pages 1–53. The Royal Society of Chemistry, 2019.

[38] A J M Mackus, A A Bol, and W M M Kessels. The use of atomic layer deposition in advanced nanopatterning. *Nanoscale*, 6(19):10941–10960, 2014.

[39] Jinhee Kwon, Mark Saly, Mathew D Halls, Ravindra K Kanjolia, and Yves J Chabal. Substrate selectivity of (tBu-Allyl)Co(CO) 3 during thermal atomic layer deposition of cobalt. *Chemistry of Materials*, 24(6):1025–1030, 2012.

[40] Adriaan J.M. Mackus, Marc J.M. Merkx, and Wilhelmus M.M. Kessels. From the Bottom-Up: Toward Area-Selective Atomic Layer Deposition with High Selectivity †. *Chemistry of Materials*, 31(1):2–12, jan 2019.

[41] Ali Haider, Shaoren Deng, Wouter Devulder, Jan Willem Maes, Jean Marc Girard, Gabriel Khalil El Hajjam, Gouri Sankar Kar, Karl Opsomer,

Christophe Detavernier, Michael Givens, Ludovic Goux, Sven Van Elshocht, Romain Delhougne, Annelies Delabie, Matty Caymax, and Johan Swerts. Pulsed chemical vapor deposition of conformal GeSe for application as an OTS selector. *Materials Advances*, 2(5):1635–1643, mar 2021.

[42] M Knez, K Nielsch, and L Niinistö. Synthesis and Surface Engineering of Complex Nanostructures by Atomic Layer Deposition. *Advanced Materials*, 19(21):3425–3438, 2007.

[43] Peter Ozaveshe Oviroh, Rokhsareh Akbarzadeh, Dongqing Pan, Rigardt Alfred Maarten Coetzee, and Tien-Chien Jen. New development of atomic layer deposition: processes, methods and applications. *Science and Technology of Advanced Materials*, 20(1):465–496, 2019.

[44] Karla Bernal Ramos, Mark J Saly, and Yves J Chabal. Precursor design and reaction mechanisms for the atomic layer deposition of metal films. *Coordination Chemistry Reviews*, 257(23):3271–3281, 2013.

[45] Thomas J. Knisley, Lakmal C. Kalutarage, and Charles H. Winter. Precursors and chemistry for the atomic layer deposition of metallic first row transition metal films, 2013.

[46] Nicola Pinna and Mato Knez. *Atomic Layer Deposition of Nanostructured Materials*. Wiley-VCH, jan 2012.

[47] Seán T Barry, Andrew V Teplyakov, and Francisco Zaera. The Chemistry of Inorganic Precursors during the Chemical Deposition of Films on Solid Surfaces. *Accounts of Chemical Research*, 51(3):800–809, 2018.

[48] E Langereis, S. B.S. Heil, H. C.M. Knoops, W Keuning, M. C.M. Van De Sanden, and W. M.M. Kessels. In situ spectroscopic ellipsometry as a versatile tool for studying atomic layer deposition. *Journal of Physics D: Applied Physics*, 42(7):73001, 2009.

[49] Jolien Dendooven and Christophe Detavernier. Basics of Atomic Layer Deposition: Growth Characteristics and Conformality. In *Atomic Layer Deposition in Energy Conversion Applications*, pages 1–40. 2017.

[50] Laurent Henn-Lecordier, Wei Lei, Mariano Anderle, and Gary W. Rubloff. Real-time sensing and metrology for atomic layer deposition processes and manufacturing. *Journal of Vacuum Science Technology B: Microelectronics and Nanometer Structures*, 25(1):130, jan 2007.

[51] Jaakko Niinistö, Antti Rahtu, Matti Putkonen, Mikko Ritala, Markku Leskelä, and Lauri Niinistö. In situ quadrupole mass spectrometry study of atomic-layer deposition of ZrO2 using Cp2Zr(CH3)2 and water. *Langmuir*, 21(16):7321–7325, aug 2005.

[52] Raija Matero, Antti Rahtu, and Mikko Ritala. In situ reaction mechanism studies on the atomic layer deposition of Al2O3 from (CH3)2AlCl and water. *Langmuir*, 21(8):3498–3502, apr 2005.

[53] Antti Rahtu, Teemu Alaranta, and Mikko Ritala. In situ quartz crystal microbalance and quadrupole mass spectrometry studies of atomic layer deposition of aluminum oxide from trimethylaluminum and water. *Langmuir*, 17(21):6506–6509, oct 2001.

[54] J Aarik, A Aidla, and K Kukli. In situ characterization of ALE growth by reagent pulse delay times in a flow-type reactor. *Applied Surface Science*, 75(1-4):180–184, 1994.

[55] Jolien Dendooven, Sreeprasanth Pulinthanathu Sree, Koen De Keyser, Davy Deduytsche, Johan A. Martens, Karl F. Ludwig, and Christophe Detavernier. In situ X-ray fluorescence measurements during atomic layer deposition: Nucleation and growth of TiO2 on planar substrates and in nanoporous films. *Journal of Physical Chemistry C*, 115(14):6605–6610, apr 2011.

[56] Y. Wang, M. T. Ho, L. V. Goncharova, L. S. Wielunski, S. Rivillon-Amy, Y. J. Chabal, T. Gustafsson, N. Moumen, and M. Boleslawski. Characterization of ultra-thin hafnium oxide films grown on silicon by atomic layer deposition using tetrakis(ethylmethyl-amino) hafnium and water precursors. *Chemistry of Materials*, 19(13):3127–3138, jun 2007.

[57] David N. Goldstein, Jarod A. McCormick, and Steven M. George. Al2O3 Atomic layer deposition with trimethylaluminum and ozone studied by in situ transmission FTIR spectroscopy and quadrupole mass spectrometry. *Journal of Physical Chemistry C*, 112(49):19530–19539, dec 2008.

[58] Xun Luo, Chun-Yi Chen, Tso-Fu Mark Chang, Keunwoo Lee, Taeyong Park, Jaesang Lee, Jinwoo Kim, Jeongtae Kim, Nohjung Kwak, Seungjin Yeom, and Hyeongtag Jeon. Characteristics of Cobalt Films Deposited by Metal Organic Chemical Vapor Deposition Method Using Dicobalt Hexacarbonyl tert-Butylacetylene. *Japanese Journal of Applied Physics Keunwoo Lee et al*, 47:5396, 2008.

[59] Keunjun Kim, Keunwoo Lee, Sejin Han, Wooho Jeong, and Hyeongtag Jeon. Characteristics of Cobalt Thin Films Deposited by Remote Plasma ALD Method with Dicobalt Octacarbonyl. *Journal of The Electrochemical Society*, 154(3):H177, jan 2007.

[60] Igor Iatsunskyi, Mateusz Kempiński, Mariusz Jancelewicz, Karol Załęski, Stefan Jurga, and Valentyn Smyntyna. Structural and XPS characterization of ALD Al2O3 coated porous silicon. *Vacuum*, 113:52–58, mar 2015.

[61] Guo Yong Fang, Li Na Xu, Yan Qiang Cao, Lai Guo Wang, Di Wu, and Ai Dong Li. Self-catalysis by aminosilanes and strong surface oxidation by O2 plasma in plasma-enhanced atomic layer deposition of high-quality SiO2. *Chemical Communications*, 51(7):1341–1344, jan 2015.

[62] Aleksandra Zydor and Simon D. Elliott. TiCp*(OMe) 3 versus Ti(OMe) 4 in atomic layer deposition of TiO 2 with water - Ab initio modelling of atomic layer deposition surface reactions. *Journal of Nanoscience and Nanotechnology*, 11(9):8089–8093, sep 2011.

[63] Chaitanya Krishna Ande, Harm C.M. Knoops, Koen De Peuter, Maarten Van Drunen, Simon D Elliott, and Wilhelmus M.M. Kessels. Role of Surface Termination in Atomic Layer Deposition of Silicon Nitride. *Journal of Physical Chemistry Letters*, 6(18):3610–3614, 2015.

[64] Ciaran A Murray, Simon D Elliott, Dennis Hausmann, Jon Henri, and Adrien Lavoie. Effect of reaction mechanism on precursor exposure time in atomic layer deposition of silicon oxide and silicon nitride. *ACS Applied Materials and Interfaces*, 6(13):10534–10541, 2014.

[65] Woojin Choi, Sungwoo Lee, Dong Hoon Han, Hong Taek Lim, Hwanyeol Park, and Gun Do Lee. Reaction mechanisms of chlorine reduction on hy-

droxylated alumina in titanium nitride growth: First principles study. *Applied Surface Science*, 550, 2021.

[66] S D Elliott, G Dey, and Y Maimaiti. Classification of processes for the atomic layer deposition of metals based on mechanistic information from density functional theory calculations. *The Journal of Chemical Physics*, 146(5):52822, 2017.

[67] Guoyong Fang, Lina Xu, Yanqiang Cao, and Aidong Li. Theoretical design and computational screening of precursors for atomic layer deposition, 2016.

[68] Timothy P. Holme and Fritz B. Prinz. Atomic layer deposition and chemical vapor deposition precursor selection method application to strontium and barium precursors. *Journal of Physical Chemistry A*, 111(33):8147–8151, aug 2007.

[69] Marissa M. Kerrigan, Joseph P. Klesko, and Charles H. Winter. Low Temperature, Selective Atomic Layer Deposition of Cobalt Metal Films Using Bis(1,4-di-tert-butyl-1,3-diazadienyl)cobalt and Alkylamine Precursors. *Chemistry of Materials*, 29(17):7458–7466, sep 2017.

[70] Chi Vo-Van, Zoukaa Kassir-Bodon, Hongxin Yang, Johann Coraux, Jan Vogel, Stefania Pizzini, Pascale Bayle-Guillemaud, Mairbek Chshiev, Laurent Ranno, Valérie Guisset, Philippe David, Violaine Salvador, and Olivier Fruchart. Ultrathin epitaxial cobalt films on graphene for spintronic investigations and applications. *New Journal of Physics*, 12(10):103040, oct 2010.

[71] Chi Vo-Van, Stefan Schumacher, Johann Coraux, Violetta Sessi, Olivier Fruchart, Nick B Brookes, Philippe Ohresser, and Thomas Michely. Magnetism of cobalt nanoclusters on graphene on iridium. *Applied Physics Letters*, 99(14):142504, 2011.

[72] Jinhee Kwon, Mark Saly, Ravindra K Kanjolia, and Yves J Chabal. Surface reactions of μ2-η2-(tBu-acetylene)dicobalthexacarbonyl with Oxidized and H-terminated Si(111) Surfaces. *Chemistry of Materials*, 23(8):2068–2074, 2011.

[73] Thomas J Knisley, Mark J Saly, Mary Jane Heeg, John L Roberts, and Charles H Winter. Volatility and High Thermal Stability in Mid- to

Late-First-Row Transition-Metal Diazadienyl Complexes. *Organometallics*, 30(18):5010–5017, 2011.

[74] David Zanders, Ji Liu, Jorit Obenlüneschloß, Claudia Bock, Detlef Rogalla, Lukas Mai, Michael Nolan, Seán T. Barry, and Anjana Devi. Cobalt Metal ALD: Understanding the mechanism and role of zinc alkyl precursors as reductants for low-resistivity co thin films. *Chemistry of Materials*, 33(13):5045–5057, jul 2021.

[75] David J H Emslie, Preeti Chadha, and Jeffrey S Price. Metal ALD and pulsed CVD: Fundamental reactions and links with solution chemistry. *Coordination Chemistry Reviews*, 257(23):3282–3296, 2013.

[76] Alain E Kaloyeros, Youlin Pan, Jonathan Goff, and Barry Arkles. Cobalt Thin Films: Trends in Processing Technologies and Emerging Applications. *ECS Journal of Solid State Science and Technology*, 8(2):P119–P152, 2019.

[77] Anthony Cartner, Brian Robinson, and Peter J Gardner. Heat of formation of dicobalt octacarbonyl and the metal-carbon monoxide bond strength in carbonyls. *Journal of the Chemical Society, Chemical Communications*, (9), 1973.

[78] David A Brown. Substitution reactions of metal, carbonyl compounds, 1967.

[79] H. Werner. Kinetische Untersuchungen der Substitutionsreaktionen von Carbonylmetall-Komplexen. *Angewandte Chemie*, 80(24):1017–1028, 1968.

[80] Arthur A. Blanchard. The volatile metal carbonyls. *Chemical Reviews*, 21(1):3–38, aug 1937.

[81] Joseph P. Klesko, Marissa M. Kerrigan, and Charles H. Winter. Low Temperature Thermal Atomic Layer Deposition of Cobalt Metal Films. *Chemistry of Materials*, 28(3):700–703, feb 2016.

[82] Jing Yang, Kecheng Li, Jun Feng, and Roy G. Gordon. Direct-liquid-evaporation chemical vapor deposition of smooth, highly conformal cobalt and cobalt nitride thin films. *Journal of Materials Chemistry C*, 3(46):12098–12106, nov 2015.

[83] Jaehong Yoon, Han-Bo-Ram Lee, Doyoung Kim, Taehoon Cheon, Soo-Hyun Kim, and Hyungjun Kim. Atomic Layer Deposition of Co Using N2H2 Plasma as a Reactant. *Journal of The Electrochemical Society*, 158(11):H1179, oct 2011.

[84] Han Bo Ram Lee and H. Kim. High-quality cobalt thin films by plasma-enhanced atomic layer deposition. *Electrochemical and Solid-State Letters*, 9(11):G323, aug 2006.

[85] Tyler D.M. Elko-Hansen and John G. Ekerdt. XPS investigation of the atomic layer deposition half reactions of bis(N-tert-butyl-N-ethylpropionamidinato) cobalt(II). *Chemistry of Materials*, 26(8):2642–2646, apr 2014.

[86] C. Georgi, A. Hildebrandt, T. Waechtler, S. E. Schulz, T. Gessner, and H. Lang. A cobalt layer deposition study: Dicobaltatetrahedranes as convenient MOCVD precursor systems. *Journal of Materials Chemistry C*, 2(23):4676–4682, may 2014.

[87] Booyong S. Lim, Antti Rahtu, and Roy G. Gordon. Atomic layer deposition of transition metals. *Nature Materials 2003 2:11*, 2(11):749–754, oct 2003.

[88] M Coulomb and Balance While. A First Memoir on Electricity and Magnetism. pages 1–8, 2000.

[89] M. Born and R. Oppenheimer. Zur Quantentheorie der Molekeln. *Annalen der Physik*, 389(20):457–484, jan 1927.

[90] Jensen Frank. Introduction to Computational Chemistry, 3rd Edition — Wiley. *WILEY*, page 660, 2017.

[91] Laurie J Butler. CHEMICAL REACTION DYNAMICS BEYOND THE BORN-OPPENHEIMER APPROXIMATION. *Annu. Rev. Phys. Chem*, 49:125–71, 1998.

[92] D. R. Hartree. The Wave Mechanics of an Atom with a Non-Coulomb Central Field Part II Some Results and Discussion. *Mathematical Proceedings of the Cambridge Philosophical Society*, 24(1):111–132, 1928.

[93] D. R. Hartree. The Wave Mechanics of an Atom with a Non-Coulomb Central Field Part I Theory and Methods. *Mathematical Proceedings of the Cambridge Philosophical Society*, 24(1):89–110, 1928.

[94] J. C. Slater. The self consistent field and the structure of atoms. *Physical Review*, 32(3):339–348, 1928.

[95] J. A. Pople and R. K. Nesbet. Self-consistent orbitals for radicals, dec 1954.

[96] C. C.J. Roothaan. Self-Consistent Field Theory for Open Shells of Electronic Systems. *Reviews of Modern Physics*, 32(2):179, apr 1960.

[97] N. C. Handy, P. J. Knowles, and K. Somasundram. On the convergence of the Møller-Plesset perturbation series. *Theoretica Chimica Acta*, 68(1):87–100, jul 1985.

[98] Ross H. Nobes, John A. Pople, Leo Radom, Nicholas C. Handy, and Peter J. Knowles. Slow convergence of the møller-plesset perturbation series: the dissociation energy of hydrogen cyanide and the electron affinity of the cyano radical. *Chemical Physics Letters*, 138(5):481–485, jul 1987.

[99] Chr Møller and M. S. Plesset. Note on an Approximation Treatment for Many-Electron Systems. *Physical Review*, 46(7):618, oct 1934.

[100] C. David Sherrill and Henry F. Schaefer. The Configuration Interaction Method: Advances in Highly Correlated Approaches. *Advances in Quantum Chemistry*, 34(C):143–269, jan 1999.

[101] Jiří Čížek. On the Correlation Problem in Atomic and Molecular Systems. Calculation of Wavefunction Components in Ursell-Type Expansion Using Quantum-Field Theoretical Methods. *J. Chem. Phys*, 45:4256, 1966.

[102] Ilya G. Ryabinkin, Tzu Ching Yen, Scott N. Genin, and Artur F. Izmaylov. Qubit Coupled Cluster Method: A Systematic Approach to Quantum Chemistry on a Quantum Computer. *Journal of Chemical Theory and Computation*, 14(12):6317–6326, dec 2018.

[103] P. Hohenberg and W. Kohn. Inhomogeneous electron gas. *Physical Review*, 136(3B):B864, nov 1964.

[104] Tom Ziegler. Density functional theory as a practical tool for the study of elementary reaction steps in organometallic chemistry. *Pure Appl. Chern*, 63(6):873–878, 1991.

[105] Tom Ziegler. Approximate Density Functional Theory as a Practical Tool in Molecular Energetics and Dynamics. *Chem. Rev*, 91:651–667, 1991.

[106] Narbe Mardirossian and Martin Head-Gordon. Thirty years of density functional theory in computational chemistry: an overview and extensive assessment of 200 density functionals. *Molecular Physics*, 115:2315–2372, 2017.

[107] Lorena Vega, Judit Ruvireta, Francesc Viñes, and Francesc Illas. Jacob's Ladder as Sketched by Escher: Assessing the Performance of Broadly Used Density Functionals on Transition Metal Surface Properties. *Journal of Chemical Theory and Computation*, 14(1):395–403, 2018.

[108] David C. Langreth and John P. Perdew. Theory of nonuniform electronic systems. I. Analysis of the gradient approximation and a generalization that works. *Physical Review B*, 21(12):5469–5493, jun 1980.

[109] David C. Langreth and M. J. Mehl. Beyond the local-density approximation in calculations of ground-state electronic properties. *Physical Review B*, 28(4):1809–1834, aug 1983.

[110] X. J. Kong, C. T. Chan, K. M. Ho, and Y. Y. Ye. Cohesive properties of crystalline solids by the generalized gradient approximation. *Physical Review B*, 42(15):9357–9364, 1990.

[111] B Hammer, K W Jacobsen, and J. K. Nørskov. Role of nonlocal exchange correlation in activated adsorption. *Physical Review Letters*, 70(25):3971–3974, 1993.

[112] Lars Goerigk and Stefan Grimme. A thorough benchmark of density functional methods for general main group thermochemistry, kinetics, and noncovalent interactions. *Physical Chemistry Chemical Physics*, 13(14):6670–6688, 2011.

[113] Viktor N Staroverov, Gustavo E Scuseria, Jianmin Tao, and John P Perdew. Comparative assessment of a new nonempirical density functional:

Molecules and hydrogen-bonded complexes. *Journal of Chemical Physics*, 119(23):12129–12137, 2003.

[114] Sérgio Filipe Sousa, Pedro Alexandrino Fernandes, and Maria João Ramos. General performance of density functionals. *Journal of Physical Chemistry A*, 111(42):10439–10452, oct 2007.

[115] Stefan Grimme. Semiempirical hybrid density functional with perturbative second-order correlation. *Journal of Chemical Physics*, 124(3):034108, jan 2006.

[116] Marc Steinmetz and Stefan Grimme. Benchmark study of the performance of density functional theory for bond activations with (Ni,Pd)-based transition-metal catalysts. *ChemistryOpen*, 2(3):115–124, jun 2013.

[117] Valentina Vetere, Carlo Adamo, and Pascale Maldivi. Performance of the 'parameter free' PBE0 functional for the modeling of molecular properties of heavy metals. *Chemical Physics Letters*, 325(1-3):99–105, jul 2000.

[118] Jianmin Tao, John P Perdew, Viktor N Staroverov, and Gustavo E Scuseria. Climbing the density functional ladder: Nonempirical meta–generalized gradient approximation designed for molecules and solids. *Physical Review Letters*, 91(14), 2003.

[119] S. F. Boys. Electronic wave functions - I. A general method of calculation for the stationary states of any molecular system. *Proceedings of the Royal Society of London. Series A. Mathematical and Physical Sciences*, 200(1063):542–554, feb 1950.

[120] Frank Jensen. Atomic orbital basis sets. *Wiley Interdisciplinary Reviews: Computational Molecular Science*, 3(3):273–295, 2013.

[121] Frank Jensen. Polarization consistent basis sets: II. Estimating the Kohn-Sham basis set limit. *Journal of Chemical Physics*, 116(17):7372–7379, 2002.

[122] Frank Jensen. Polarization consistent basis sets: Principles. *Journal of Chemical Physics*, 115(20):9113–9125, 2001.

[123] Jingjing Zheng, Xuefei Xu, and Donald G. Truhlar. Minimally augmented Karlsruhe basis sets. *Theoretical Chemistry Accounts*, 128(3):295–305, feb 2011.

[124] Dmitrij Rappoport and Filipp Furche. Property-optimized Gaussian basis sets for molecular response calculations. *Journal of Chemical Physics*, 133(13):134105, oct 2010.

[125] Florian Weigend and Reinhart Ahlrichs. Balanced basis sets of split valence, triple zeta valence and quadruple zeta valence quality for H to Rn: Design and assessment of accuracy. *Physical Chemistry Chemical Physics*, 7(18):3297–3305, aug 2005.

[126] Ewa Papajak, Jingjing Zheng, Xuefei Xu, Hannah R. Leverentz, and Donald G. Truhlar. Perspectives on basis sets beautiful: Seasonal plantings of diffuse basis functions, oct 2011.

[127] J. Grant Hill. Gaussian basis sets for molecular applications, jan 2013.

[128] Markus Bursch, Jan-Michael Mewes, Andreas Hansen, and Stefan Grimme. Best-Practice DFT Protocols for Basic Molecular Computational Chemistry**. *Angewandte Chemie*, 134(42):e202205735, oct 2022.

[129] Arnim Hellweg and Dmitrij Rappoport. Development of new auxiliary basis functions of the Karlsruhe segmented contracted basis sets including diffuse basis functions (def2-SVPD, def2-TZVPPD, and def2-QVPPD) for RI-MP2 and RI-CC calculations. *Physical Chemistry Chemical Physics*, 17(2):1010–1017, dec 2015.

[130] D. Andrae, U. Häußermann, M. Dolg, H. Stoll, and H. Preuß. Energy-adjusted ab initio pseudopotentials for the second and third row transition elements. *Theoretica Chimica Acta*, 77(2):123–141, mar 1990.

[131] José M. Soler, Emilio Artacho, Julian D. Gale, Alberto García, Javier Junquera, Pablo Ordejón, and Daniel Sánchez-Portal. The SIESTA method for ab initio order-N materials simulation. *Journal of Physics Condensed Matter*, 14(11):2745–2779, 2002.

[132] Rutger A Van Santen. Introduction to Computational Chemistry Handbook of Heterogeneous Catalysis Computational Chemistry of Solid State Materials Computational Modeling for Homogeneous and Enzymatic Catalysis Molecular Heterogeneous Catalysis. In *Computational Methods in Catalysis and Materials Science: An Introduction for Scientists and Engineers*. 2009.

[133] Philippe Sautet and Françoise Delbecq. Catalysis and surface organometallic chemistry: A view from theory and simulations, 2010.

[134] Cláudio M. Lousada and Pavel A. Korzhavyi. Surface chemistry of oxygen on aluminum - Performance of the density functionals: PBE, PBE0, M06, and M06-L. *Journal of Computational Chemistry*, 37(9):787–794, apr 2016.

[135] John P. Perdew, Kieron Burke, and Matthias Ernzerhof. Generalized gradient approximation made simple. *Physical Review Letters*, 77(18):3865–3868, oct 1996.

[136] Stefan Grimme, Andreas Hansen, Jan Gerit Brandenburg, and Christoph Bannwarth. Dispersion-Corrected Mean-Field Electronic Structure Methods. *Chemical Reviews*, 116(9):5105–5154, 2016.

[137] Werner Reckien, Florian Janetzko, Michael F. Peintinger, and Thomas Bredow. Implementation of empirical dispersion corrections to density functional theory for periodic systems. *Journal of Computational Chemistry*, 33(25):2023–2031, sep 2012.

[138] Noa Marom, Alexandre Tkatchenko, Mariana Rossi, Vivekanand V. Gobre, Oded Hod, Matthias Scheffler, and Leeor Kronik. Dispersion interactions with density-functional theory: Benchmarking semiempirical and interatomic pairwise corrected density functionals. *Journal of Chemical Theory and Computation*, 7(12):3944–3951, dec 2011.

[139] Stefan Grimme. Accurate description of van der Waals complexes by density functional theory including empirical corrections. *Journal of Computational Chemistry*, 25(12):1463–1473, sep 2004.

[140] Victor G. Ruiz, Wei Liu, and Alexandre Tkatchenko. Density-functional theory with screened van der Waals interactions applied to atomic and molec-

ular adsorbates on close-packed and non-close-packed surfaces. *Physical Review B*, 93(3):35118, 2016.

[141] Peter Schwerdtfeger. The pseudopotential approximation in electronic structure theory. *ChemPhysChem*, 12(17):3143–3155, 2011.

[142] N. Troullier and José Luriaas Martins. Efficient pseudopotentials for plane-wave calculations. *Physical Review B*, 43(3):1993–2006, jan 1991.

[143] William G. Hoover. Canonical dynamics: Equilibrium phase-space distributions. *Physical Review A*, 31(3):1695–1697, mar 1985.

[144] Graeme Henkelman, Blas P. Uberuaga, and Hannes Jónsson. A climbing image nudged elastic band method for finding saddle points and minimum energy paths. *The Journal of Chemical Physics*, 113(22):9901, nov 2000.

[145] Baron Peters, Andreas Heyden, Alexis T. Bell, and Arup Chakraborty. A growing string method for determining transition states: Comparison to the nudged elastic band and string methods. *Journal of Chemical Physics*, 120(17):7877–7886, apr 2004.

[146] Graeme Henkelman and Hannes Jónsson. Improved tangent estimate in the nudged elastic band method for finding minimum energy paths and saddle points. *Journal of Chemical Physics*, 113(22):9978–9985, nov 2000.

[147] Graeme Henkelman, Blas P. Uberuaga, and Hannes Jónsson. Climbing image nudged elastic band method for finding saddle points and minimum energy paths. *Journal of Chemical Physics*, 113(22):9901–9904, nov 2000.

[148] Graeme Henkelman and Hannes Jónsson. A dimer method for finding saddle points on high dimensional potential surfaces using only first derivatives. *Journal of Chemical Physics*, 111(15):7010–7022, oct 1999.

[149] Rachid Malek and Normand Mousseau. Dynamics of Lennard-Jones clusters: A characterization of the activation-relaxation technique. *Physical Review E - Statistical Physics, Plasmas, Fluids, and Related Interdisciplinary Topics*, 62(6):7723–7728, dec 2000.

[150] Jon Baker. An algorithm for the location of transition states. *Journal of Computational Chemistry*, 7(4):385–395, aug 1986.

[151] R. A. Olsen, G. J. Kroes, G. Henkelman, A. Arnaldsson, and H. Jónsson. Comparison of methods for finding saddle points without knowledge of the final states. *Journal of Chemical Physics*, 121(20):9776–9792, nov 2004.

[152] Frank Neese. The ORCA program system. *Wiley Interdisciplinary Reviews: Computational Molecular Science*, 2(1):73–78, jan 2012.

[153] Frank Neese, Frank Wennmohs, Ute Becker, and Christoph Riplinger. The ORCA quantum chemistry program package. *Journal of Chemical Physics*, 152(22):224108, jun 2020.

[154] Ask Hjorth Larsen, Jens JØrgen Mortensen, Jakob Blomqvist, Ivano E. Castelli, Rune Christensen, Marcin Dułak, Jesper Friis, Michael N. Groves, BjØrk Hammer, Cory Hargus, Eric D. Hermes, Paul C. Jennings, Peter Bjerre Jensen, James Kermode, John R. Kitchin, Esben Leonhard Kolsbjerg, Joseph Kubal, Kristen Kaasbjerg, Steen Lysgaard, Jón Bergmann Maronsson, Tristan Maxson, Thomas Olsen, Lars Pastewka, Andrew Peterson, Carsten Rostgaard, Jakob SchiØtz, Ole Schütt, Mikkel Strange, Kristian S. Thygesen, Tejs Vegge, Lasse Vilhelmsen, Michael Walter, Zhenhua Zeng, and Karsten W. Jacobsen. The atomic simulation environment - A Python library for working with atoms, jun 2017.

[155] Qiming Sun, Timothy C. Berkelbach, Nick S. Blunt, George H. Booth, Sheng Guo, Zhendong Li, Junzi Liu, James D. McClain, Elvira R. Sayfutyarova, Sandeep Sharma, Sebastian Wouters, and Garnet Kin Lic Chan. PySCF: the Python-based simulations of chemistry framework. *Wiley Interdisciplinary Reviews: Computational Molecular Science*, 8(1):e1340, jan 2018.

[156] Qiming Sun, Xing Zhang, Samragni Banerjee, Peng Bao, Marc Barbry, Nick S. Blunt, Nikolay A. Bogdanov, George H. Booth, Jia Chen, Zhi Hao Cui, Janus J. Eriksen, Yang Gao, Sheng Guo, Jan Hermann, Matthew R. Hermes, Kevin Koh, Peter Koval, Susi Lehtola, Zhendong Li, Junzi Liu, Narbe Mardirossian, James D. McClain, Mario Motta, Bastien Mussard, Hung Q. Pham, Artem Pulkin, Wirawan Purwanto, Paul J. Robinson, Enrico Ronca, Elvira R. Sayfutyarova, Maximilian Scheurer, Henry F. Schurkus, James E.T. Smith, Chong Sun, Shi Ning Sun, Shiv Upadhyay, Lucas K. Wagner, Xiao Wang, Alec White, James Daniel Whitfield, Mark J. Williamson, Sebastian Wouters, Jun Yang, Jason M. Yu, Tianyu Zhu, Timothy C. Berkelbach,

Sandeep Sharma, Alexander Yu Sokolov, and Garnet Kin Lic Chan. Recent developments in the P y SCF program package. *Journal of Chemical Physics*, 153(2):024109, jul 2020.

[157] M. Valiev, E. J. Bylaska, N. Govind, K. Kowalski, T. P. Straatsma, H. J.J. Van Dam, D. Wang, J. Nieplocha, E. Apra, T. L. Windus, and W. A. De Jong. NWChem: A comprehensive and scalable open-source solution for large scale molecular simulations. *Computer Physics Communications*, 181(9):1477–1489, sep 2010.

[158] John B. Fenn, Matthias Mann, Chin Kai Meng, Shek Fu Wong, and Craig M. Whitehouse. Electrospray ionization for mass spectrometry of large biomolecules, 1989.

[159] Matthias Wilm. Principles of electrospray ionization, jul 2011.

[160] Malcolm Dole, L L Mack, R L Hines, Department Of Chemistry, R C Mobley, L D Ferguson, and M B Alice. Molecular beams of macroions. *The Journal of Chemical Physics*, 49(5):2240–2249, 1968.

[161] Antonios O Aliprantis, James W Canary, and A V J Am. Observation of Catalytic Intermediates in the Suzuki Reaction by Electrospray Mass Spectrometry Ar-Af. *J. K. Angew. Chem., Int. Ed. Engl*, 116(2):1345–1347, 1994.

[162] Andries P Bruins. Mechanistic aspects of electrospray ionization. *Journal of Chromatography A*, 794:345–357, 1998.

[163] J. V. Iribarne and B. A. Thomson. On the evaporation of small ions from charged droplets. *The Journal of Chemical Physics*, 64(6):2287–2294, aug 1976.

[164] M. Gamero-Castaño and J. Fernández De La Mora. Direct measurement of ion evaporation kinetics from electrified liquid surfaces. *Journal of Chemical Physics*, 113(2):815–832, jun 2000.

[165] B. A. Thomson and J. V. Iribarne. Field induced ion evaporation from liquid surfaces at atmospheric pressure. *The Journal of Chemical Physics*, 71(11):4451–4463, 1979.

[166] F. W. Röllgen, E Bramer-Weger, and L Bütfering. FIELD ION EMISSION FROM LIQUID SOLUTIONS : ION EVAPORATION AGAINST ELECTRO-HYDRODYNAMIC DISINTEGRATION. *Le Journal de Physique Colloques*, 48(C6):C6–253–C6–256, 1987.

[167] Matthias S. Wilm and Matthias Mann. Electrospray and Taylor-Cone theory, Dole's beam of macromolecules at last? *International Journal of Mass Spectrometry and Ion Processes*, 136(2-3):167–180, sep 1994.

[168] Lekha Sleno and Dietrich A. Volmer. Ion activation methods for tandem mass spectrometry, oct 2004.

[169] Zohrab Ahmadi, Lars P E Yunker, Allen G Oliver, and J Scott McIndoe. Mechanistic features of the copper-free Sonogashira reaction from ESI-MS. *Dalton Trans.*, 44(47):20367–20375, 2015.

[170] Lars P E Yunker, Zohrab Ahmadi, Jessamyn R Logan, Wenzhao Wu, Tengfei Li, A Martindale, Allen G Oliver, and J Scott McIndoe. Real-Time Mass Spectrometric Investigations into the Mechanism of the Suzuki–Miyaura Reaction. *Organometallics*, 37(22):4297–4308, 2018.

[171] Alan An Jung Wei, Anuj Joshi, Yuxuan Chen, and J. Scott McIndoe. Strategies for avoiding saturation effects in ESI-MS. *International Journal of Mass Spectrometry*, 450:116306, apr 2020.

[172] Jiang Lu, Hyoung-Chan Ha, Paul Ma, Seshadri Ganguli, Joseph F. Aubuchon, Sang-Ho Yu, and Murali K. Narasimhan. Cobalt deposition on barrier surfaces, aug 2015.

[173] Charles Alan Cooper, Segei Ivanov, and Moo-Sung Kim. Disubstituted Alkyne Dicobalt Hexacarbonyl Compounds, Method of Making and Method of Use Thereof, dec 2018.

[174] Byeol Han, Kyu Ha Choi, Kwangmin Park, Won Seok Han, and Won Jun Lee. Low-temperature atomic layer deposition of cobalt oxide thin films using dicobalt hexacarbonyl tert-butylacetylene and ozone. *Electrochemical and Solid-State Letters*, 15(2):D14, dec 2012.

[175] S. B. Kang, H. S. Kim, K. J. Moon, W. H. Sohn, G. H. Choi, S. H. Kim, N. J. Bae, U. I. Chung, and J. T. Moon. CVD-Cobalt for the Next Generation of Source/Drain Salicidation and Contact Silicidation in Novel MOS Device Structures with Complex Shape. *Technical Digest - International Electron Devices Meeting*, pages 501–504, 2003.

[176] Jae Hyung Park, Dae Yong Moon, Dong Suk Han, Yu Jin Kang, So Ra Shin, Hyung Tag Jeon, and Jong Wan Park. Plasma-enhanced atomic layer deposition (PEALD) of cobalt thin films for copper direct electroplating. *Surface and Coatings Technology*, 259(PA):98–101, 2014.

[177] Heinz W. Sternberg, Julius G. Shukys, Charles Delle Donne, Raymond Markby, Robert A. Friedel, and Irving Wender. Addition of Carbon Monoxide to Acetylene Dicobalt Hexacarbonyl. A New Type of Complex. *Journal of the American Chemical Society*, 81(10):2339–2342, 1959.

[178] Danielle M. Chisholm and J. Scott McIndoe. Charged ligands for catalyst immobilisation and analysis. *Dalton Transactions*, (30):3933–3945, jul 2008.

[179] Matthew A Henderson, Jingwei Luo, Allen Oliver, and J Scott Mcindoe. The Pauson-Khand Reaction: A Gas-Phase and Solution-Phase Examination Using Electrospray Ionization Mass Spectrometry. *Organometallics*, 30:5471–5479, 2011.

[180] Anuj Joshi, Charles Killeen, Tanner Thiessen, Harmen Zijlstra, and Scott McIndoe. Handling considerations for the mass spectrometry of reactive organometallic compounds By Anuj Joshi, Charles Killeen, Tanner Thiessen, Harmen S. Zijlstra and J. Scott McIndoe. *Journal of Mass Spectrometry*, 57(3):e4740, mar 2022.

[181] Stefan Grimme, Jens Antony, Stephan Ehrlich, and Helge Krieg. A consistent and accurate ab initio parametrization of density functional dispersion correction (DFT-D) for the 94 elements H-Pu. *The Journal of Chemical Physics*, 132(15):154104, 2010.

[182] N Troullier and José Lu´Martins. Efficient pseudopotentials for plane-wave calculations. II. Operators for fast iterative diagonalization. *Phys. Rev. B*, 43(11):8861–8869, apr 1991.

[183] D J Evans and B L Holian. The Nose–Hoover thermostat. *The Journal of Chemical Physics*, 83(8):4069–4074, 1985.

[184] Gilian T. Thomas, Sofia Donnecke, Ian C. Chagunda, and J. Scott McIndoe. Pressurized Sample Infusion. *Chemistry - Methods*, 2(1):e202100101, jan 2022.

[185] Krista L Vikse, Zohrab Ahmadi, Jingwei Luo, Nicole Van Der Wal, Kevin Daze, Nichole Taylor, and J. Scott McIndoe. Pressurized sample infusion: An easily calibrated, low volume pumping system for ESI-MS analysis of reactions. *International Journal of Mass Spectrometry*, 323-324:8–13, 2012.

[186] Jordi Burés. Variable Time Normalization Analysis: General Graphical Elucidation of Reaction Orders from Concentration Profiles. *Angewandte Chemie International Edition*, 55(52):16084–16087, 2016.

[187] P. C. Leung and P. Coppens. Experimental charge density study of dicobalt octacarbonyl and comparison with theory. *Acta Crystallographica Section B*, 39(5):535–542, oct 1983.

[188] Ray L. Sweany and Theodore L. Brown. Infrared Spectra of Matrix-Isolated Dicobalt Octacarbonyl. Evidence for the Third Isomer. *Inorganic Chemistry*, 16(2):415–421, feb 1977.

[189] Thelma Y Garcia, James C Fettinger, Marilyn M Olmstead, and Alan L Balch. Splendid symmetry: Crystallization of an unbridged isomer of Co 2(CO)8 in Co2(CO)8 ·c 60. *Chemical Communications*, (46):7143–7145, 2009.

[190] Michael I. Bruce, Maryka Gaudio, Benjamin C. Hall, Brian K. Nicholson, Gary J. Perkins, Brian W. Skelton, and Allan H. White. Structural Studies of Some Compounds Containing C2 Fragments Attached to Various Metal-Ligand End-Groups. *Zeitschrift für anorganische und allgemeine Chemie*, 637(9):1207–1212, jul 2011.

[191] K.M. Nicholas and R. Pettit. An alkyne protecting group. *Tetrahedron Letters*, 12(37):3475–3478, jan 1971.

[192] Robert H Crabtree. Robert H. Crabtree The Organometallic Chemistry of the Transition Metals, 5th edn John Wiley and Sons, 2009, 520 pp. (hardback)

ISBN 978-0-470-25762-3. *Applied Organometallic Chemistry*, 24(9):667–667, sep 2010.

[193] Masahiko Kinebuchi, Ryohei Uematsu, and Keiji Tanino. Synthetic studies on psiguadial B: Construction of bicyclo[4.3.1]decane skeleton via double cyclization reaction of alkyne dicobalt complex. *Tetrahedron Letters*, 58(14):1382–1386, 2017.

[194] Jian Li, Georg Schreckenbach, and Tom Ziegler. A Reassessment of the First Metal—Carbonyl Dissociation Energy in M(CO)4 (M = Ni, Pd, Pt), M(CO)5(M = Fe, Ru, Os), and M(CO)6 (M = Cr, Mo, W) by a Quasirelativistic Density Functional Method. *Journal of the American Chemical Society*, 117(1):486–494, 1995.

[195] Jae Min Park, Se Jin Jang, Luchana L. Yusup, Won Jun Lee, and Sang Ick Lee. Plasma-Enhanced Atomic Layer Deposition of Silicon Nitride Using a Novel Silylamine Precursor. *ACS Applied Materials and Interfaces*, 8(32):20865–20871, aug 2016.

[196] Rajesh J Odera, Cunhai Dong, and Shaun Cembella. Organometalic Compounds Useful for Chemical Phase Deposition, nov 2016.

[197] Thao T. Nguyen, Tufan K. Mukhopadhyay, Samantha N. Macmillan, Michael T. Janicke, and Ryan J. Trovitch. Synthesis of Aminosilane Chemical Vapor Deposition Precursors and Polycarbosilazanes through Manganese-Catalyzed Si-N Dehydrocoupling. *ACS Sustainable Chemistry and Engineering*, 10(13):4218–4226, apr 2022.

[198] Strem Chemicals. Applications of Metal Halide Precursors in CVD/ALD Processes.

[199] Rod Borup, Jeremy Meyers, Bryan Pivovar, Yu Seung Kim, Rangachary Mukundan, Nancy Garland, Deborah Myers, Mahlon Wilson, Fernando Garzon, David Wood, Piotr Zelenay, Karren More, Ken Stroh, Tom Zawodzinski, James Boncella, James E. McGrath, Minoru Inaba, Kenji Miyatake, Michio Hori, Kenichiro Ota, Zempachi Ogumi, Seizo Miyata, Atsushi Nishikata, Zyun Siroma, Yoshiharu Uchimoto, Kazuaki Yasuda, Ken Ichi Kimijima, and Norio Iwashita. Scientific aspects of polymer electrolyte fuel cell durability and degradation, oct 2007.

[200] Michael M Whiston, Inês L Azevedo, Shawn Litster, Kate S Whitefoot, Constantine Samaras, and Jay F Whitacre. Expert assessments of the cost and expected future performance of proton exchange membrane fuel cells for vehicles. *Proceedings of the National Academy of Sciences of the United States of America*, 116(11):4899–4904, 2019.

[201] Mohammed Jourdani, Hamid Mounir, and Abdellatif El Marjani. Compilation of factors affecting durability of proton exchange membrane fuel cell (PEMFC). *Proceedings of 2014 International Renewable and Sustainable Energy Conference, IRSEC 2014*, pages 542–547, mar 2014.

[202] Anusorn Kongkanand and Mark F Mathias. The Priority and Challenge of High-Power Performance of Low-Platinum Proton-Exchange Membrane Fuel Cells. *Journal of Physical Chemistry Letters*, 7(7):1127–1137, 2016.

[203] Department of Energy. Fuel Cell 2016 Multi-Year Research, Development, and Demonstration Plan. Technical report, Department of Energy, 2016.

[204] Wolfgang Bernhart, Stefan Riederle, Manuel Yoon, and Wilfried G Aulbur. Fuel Cells — A Realistic Alternative for Zero Emission? *Auto Tech Review*, 3(3):18–23, 2014.

[205] Dustin Banham, Ja Yeon Choi, Takeaki Kishimoto, and Siyu Ye. Integrating PGM-Free Catalysts into Catalyst Layers and Proton Exchange Membrane Fuel Cell Devices. *Advanced Materials*, 31(31):1–6, 2019.

[206] Yanghua He, Shengwen Liu, Cameron Priest, Qiurong Shi, and Gang Wu. Atomically dispersed metal-nitrogen-carbon catalysts for fuel cells: Advances in catalyst design, electrode performance, and durability improvement. *Chemical Society Reviews*, 49(11):3484–3524, 2020.

[207] Chen Chen, Yijin Kang, Ziyang Huo, Zhongwei Zhu, Wenyu Huang, Huolin L Xin, and Joshua D Snyder. Highly Crystalline Multimetallic Nanoframes with Three-Dimensional Electrocatalytic Surfaces. *Science*, 343(6177):1339–1343, 2014.

[208] Jeffrey Yue, Zheng Du, and Minhua Shao. Mechanisms of Enhanced Electrocatalytic Activity for Oxygen Reduction Reaction on High-Index Platinum

n(111)-(111) Surfaces. *Journal of Physical Chemistry Letters*, 6(17):3346–3351, 2015.

[209] T Katsuyama, K Hiruma, K Ogawa, T W Odom, C M Lieber, P Werner, M Zacharias, W C Ellis, V Schmidt, S Senz, S Fan, R S Williams, D P Basile, T Hesjedal, J S Harris, H J Gassen, M Hirata, H Dai, X Li, L J Lauhon, M S Gudiksen, a F Marshall, C E D Chidsey, P C Mcintyre, J C Harmand, G Patriarche, L Travers, G E Cirlin, S M Prokes, R C Cammarata, J Tersoff, M C Reuter, F M Ross, L Yang, D Li, a Majumdar, R Abbaschian, J L Murray, L H Bennett, H Baker, Metals Park, W C Carter, W C Johnson, Materials Society, Boca Raton, S Guha, and M a Aziz. Synthesis of Tetrahexahedral Platinum. *Handbook of Chemistry and Physics*, (May):732–735, 2007.

[210] Oliver Gröger, Hubert A Gasteiger, and Jens-Peter Suchsland. Review—Electromobility: Batteries or Fuel Cells? *Journal of The Electrochemical Society*, 162(14):A2605—-A2622, 2015.

[211] Minna Cao, Dongshuang Wu, and Rong Cao. Recent advances in the stabilization of platinum electrocatalysts for fuel-cell reactions. *ChemCatChem*, 6(1):26–45, 2014.

[212] Vojislav R Stamenkovic, Ben Fowler, Bongjin Simon Mun, Guofeng Wang, Philip N Ross, Christopher A Lucas, and Nenad M Markovic. Improved oxygen reduction activity on Pt3Ni(111) via increased surface site availability. *Science*, 315(5811):493–497, 2007.

[213] Binghong Han, Christopher E Carlton, Anusorn Kongkanand, Ratandeep S Kukreja, Brian R Theobald, Lin Gan, Rachel O'Malley, Peter Strasser, Frederick T Wagner, and Yang Shao-Horn. Record activity and stability of dealloyed bimetallic catalysts for proton exchange membrane fuel cells. *Energy and Environmental Science*, 8(1):258–266, 2015.

[214] Yu Zhang, Yu Chi Hsieh, Vyacheslav Volkov, Dong Su, Wei An, Rui Si, Yimei Zhu, Ping Liu, Jia X Wang, and Radoslav R Adzic. High performance Pt monolayer catalysts produced via core-catalyzed coating in ethanol. *ACS Catalysis*, 4(3):738–742, 2014.

[215] Fatemeh Razmjooei, Jeong Hoon Yu, Ha Young Lee, Byong June Lee, Kiran Pal Singh, Tong Hyun Kang, Hyoung Juhn Kim, and Jong Sung Yu.

Single-atom iron-based electrocatalysts for high-temperature polymer electrolyte membrane fuel cell: Organometallic precursor and pore texture tailoring. *ACS Applied Energy Materials*, 3(11):11164–11176, 2020.

[216] Edward F Holby, Gang Wu, Piotr Zelenay, and Christopher D Taylor. Structure of Fe-Nx-C Defects in Oxygen Reduction Reaction Catalysts from First-Principles Modeling. *Journal of Physical Chemistry C*, 118:14388–14393, 2014.

[217] Meiling Xiao, Yongting Chen, Jianbing Zhu, Hao Zhang, Xiao Zhao, Liqin Gao, Xian Wang, Jin Zhao, Junjie Ge, Zheng Jiang, Shengli Chen, Changpeng Liu, and Wei Xing. Climbing the Apex of the ORR Volcano Plot via Binuclear Site Construction: Electronic and Geometric Engineering. *Journal of the American Chemical Society*, 141(44):17763–17770, nov 2019.

[218] Edward F Holby and Christopher D Taylor. Activity of N-coordinated multi-metal-atom active site structures for Pt-free oxygen reduction reaction catalysis: Role of OH ligands. *Scientific Reports*, 5:1–4, 2015.

[219] Alfred B. Anderson and Edward F. Holby. Pathways for O2 Electroreduction over Substitutional FeN4, HOFeN4, and OFeN4 in Graphene Bulk Sites: Critical Evaluation of Overpotential Predictions Using LGER and CHE Models. *Journal of Physical Chemistry C*, 123(30):18398–18409, 2019.

[220] Hoon T Chung, David A Cullen, Drew Higgins, Brian T Sneed, Edward F Holby, Karren L More, and Piotr Zelenay. Direct atomic-level insight into the active sites of a high-performance PGM-free ORR catalyst. *Science*, 357(6350):479–484, 2017.

[221] Zhen Jiang and Vitaly Alexandrov. Enhancing Oxygen Electroreduction Activity of Single-Site Fe-N-C Catalysts by a Metal Support. *Journal of Physical Chemistry C*, 123(50):30335–30340, dec 2019.

[222] Jiayi Xu, Ayyappan Elangovan, Jun Li, and Bin Liu. Graphene-Based Dual-Metal Sites for Oxygen Reduction Reaction: A Theoretical Study. *The Journal of Physical Chemistry C*, 125(4):2334–2344, 2021.

[223] Shuai Yuan, Jiayu Peng, Yirui Zhang, Daniel J. Zheng, Sujay Bagi, Tao Wang, Yuriy Román-Leshkov, and Yang Shao-Horn. Tuning the Catalytic

Activity of Fe-Phthalocyanine-Based Catalysts for the Oxygen Reduction Reaction by Ligand Functionalization. *ACS Catalysis*, 12(12):7278–7287, jun 2022.

[224] Michel Lefèvre, Eric Proietti, Frédéric Jaouen, and Jean Pol Dodelet. Iron-Based catalysts with improved oxygen reduction activity in polymer electrolyte fuel cells. *Science*, 324(5923):71–74, apr 2009.

[225] Xiang Wang, Zhen Feng Cai, Dong Wang, and Li Jun Wan. Molecular Evidence for the Catalytic Process of Cobalt Porphyrin Catalyzed Oxygen Evolution Reaction in Alkaline Solution. *Journal of the American Chemical Society*, 141(19):7665–7669, may 2019.

[226] R O Jones. Density functional theory: Its origins, rise to prominence, and future. *Reviews of Modern Physics*, 87(3), 2015.

[227] Yudong Cao, Jonathan Romero, Jonathan P Olson, Matthias Degroote, Peter D Johnson, Mária Kieferová, Ian D Kivlichan, Tim Menke, Borja Peropadre, Nicolas P D Sawaya, Sukin Sim, Libor Veis, and Alán Aspuru-Guzik. Quantum Chemistry in the Age of Quantum Computing. *Chemical Reviews*, 119(19):10856–10915, 2019.

[228] Bela Bauer, Sergey Bravyi, Mario Motta, and Garnet Kin-Lic Chan. Quantum Algorithms for Quantum Chemistry and Quantum Materials Science. *Chemical Reviews*, 120(22):12685–12717, 2020.

[229] Alan Ho, Jarrod McClean, and Shyue Ping Ong. The Promise and Challenges of Quantum Computing for Energy Storage. *Joule*, 2(5):810–813, 2018.

[230] Zhong Shuai Wu, Long Chen, Junzhi Liu, Khaled Parvez, Haiwei Liang, Jie Shu, Hermann Sachdev, Robert Graf, Xinliang Feng, and Klaus Müllen. High-performance electrocatalysts for oxygen reduction derived from cobalt porphyrin-based conjugated mesoporous polymers. *Advanced Materials*, 26(9):1450–1455, mar 2014.

[231] Xiaoyang Cui, Shubin Yang, Xingxu Yan, Jiugou Leng, Shuang Shuang, Pulickel M. Ajayan, and Zhengjun Zhang. Pyridinic-Nitrogen-Dominated Graphene Aerogels with Fe–N–C Coordination for Highly Efficient Oxygen

Reduction Reaction. *Advanced Functional Materials*, 26(31):5708–5717, aug 2016.

[232] Minmin Liu, Linlin Wang, Kangning Zhao, Shanshan Shi, Qinsi Shao, Lei Zhang, Xueliang Sun, Yufeng Zhao, and Jiujun Zhang. Atomically dispersed metal catalysts for the oxygen reduction reaction: Synthesis, characterization, reaction mechanisms and electrochemical energy applications, 2019.

[233] Chang Xin Zhao, Bo Quan Li, Jia Ning Liu, and Qiang Zhang. Intrinsic Electrocatalytic Activity Regulation of M–N–C Single-Atom Catalysts for the Oxygen Reduction Reaction. *Angewandte Chemie - International Edition*, 60(9):4448–4463, feb 2021.

[234] J K Nørskov, J Rossmeisl, A Logadottir, L Lindqvist, J R Kitchin, T Bligaard, and H Jónsson. Origin of the Overpotential for Oxygen Reduction at a Fuel-Cell Cathode. *The Journal of Physical Chemistry B*, 108(46):17886–17892, 2004.

[235] Andrew A Peterson, Frank Abild-Pedersen, Felix Studt, Jan Rossmeisl, and Jens K Nørskov. How copper catalyzes the electroreduction of carbon dioxide into hydrocarbon fuels. *Energy Environ. Sci.*, 3(9):1311–1315, 2010.

[236] Alexandre Tkatchenko and Matthias Scheffler. Accurate molecular van der Waals interactions from ground-state electron density and free-atom reference data. *Physical Review Letters*, 102(7):073005, feb 2009.

[237] Carlo Adamo and Vincenzo Barone. Toward reliable density functional methods without adjustable parameters: The PBE0 model. *The Journal of Chemical Physics*, 110(13):6158–6170, 1999.

[238] Axel D Becke. Density-functional thermochemistry. III. The role of exact exchange. *The Journal of Chemical Physics*, 98(7):5648–5652, 1993.

[239] Stefan Grimme, Stephan Ehrlich, and Lars Goerigk. Effect of the damping function in dispersion corrected density functional theory. *Journal of Computational Chemistry*, 32(7):1456–1465, 2011.

[240] Dmitrij Rappoport and Filipp Furche. Property-optimized Gaussian basis sets for molecular response calculations. *The Journal of Chemical Physics*, 133(13):134105, 2010.

[241] Frank Neese and Edward F Valeev. Revisiting the atomic natural orbital approach for basis sets: Robust systematic basis sets for explicitly correlated and conventional correlated ab initio methods? *Journal of Chemical Theory and Computation*, 7(1):33–43, 2011.

[242] Frank Neese. Importance of direct spin-spin coupling and spin-flip excitations for the zero-field splittings of transition metal complexes: A case study. *Journal of the American Chemical Society*, 128(31):10213–10222, aug 2006.

[243] Timothy J. Lee and Peter R. Taylor. A diagnostic for determining the quality of single-reference electron correlation methods. *International Journal of Quantum Chemistry*, 36(23 S):199–207, apr 1989.

[244] Herbert B. Shore, J. H. Rose, and E. Zaremba. Failure of the local exchange approximation in the evaluation of the H- ground state. *Physical Review B*, 15(6):2858–2861, mar 1977.

[245] Karlheinz Schwarz. Instability of stable negative ions in the Xα method or other local density functional schemes. *Chemical Physics Letters*, 57(4):605–607, aug 1978.

[246] Liming Zhao, K. Jiro Watanabe, Naoki Nakatani, Akira Nakayama, Xin Xu, and Jun Ya Hasegawa. Extending nudged elastic band method to reaction pathways involving multiple spin states. *The Journal of Chemical Physics*, 153(13):134114, oct 2020.

[247] Branko Ruscic. Active thermochemical tables: Water and water dimer. *Journal of Physical Chemistry A*, 117(46):11940–11953, nov 2013.

[248] K. P. Huber and G. Herzberg. *Molecular Spectra and Molecular Structure*. Springer US, 1979.

[249] Paolo Marcazzan, Brian O. Patrick, and Brian R. James. Amine products and catalyst poisoning in the homogeneous H2 hydrogenation of imines catalyzed by the [Rh(COD)(PPh3)2]PF6 precursor. *Organometallics*, 22(6):1177–1179, mar 2003.

[250] Ercan Bayram and Richard G Finke. Quantitative 1,10-phenanthroline catalyst-poisoning kinetic studies of Rh(0) nanoparticle and Rh 4 cluster benzene hydrogenation catalysts: Estimates of the poison K association binding constants, of the equivalents of poison bound and of the number of ca. *ACS Catalysis*, 2(9):1967–1975, 2012.

[251] Eduardo E. Wolf and Eugene E. Petersen. On the kinetics of self-poisoning catalytic reactions. *Journal of Catalysis*, 47(1):28–32, apr 1977.

[252] David C Leitch, Rachel H Platel, and Laurel L Schafer. Mechanistic Elucidation of Intramolecular Aminoalkene Hydroamination Catalyzed by a Tethered Bis(ureate) Complex: Evidence for Proton-Assisted C–N Bond Formation at Zirconium. *Journal of the American Chemical Society*, 133(39):15453–15463, 2011.

[253] Jingru Lu, Sofia Donnecke, Irina Paci, and David C. Leitch. A reactivity model for oxidative addition to palladium enables quantitative predictions for catalytic cross-coupling reactions. *Chemical Science*, 13(12):3477–3488, mar 2022.

[254] Louis Charles Campeau and Nilay Hazari. Cross-Coupling and Related Reactions: Connecting Past Success to the Development of New Reactions for the Future. *Organometallics*, 38(1):3–35, jan 2019.

[255] Christopher Sandford, Lydia R. Fries, Tyler E. Ball, Shelley D. Minteer, and Matthew S. Sigman. Mechanistic Studies into the Oxidative Addition of Co(I) Complexes: Combining Electroanalytical Techniques with Parameterization. *Journal of the American Chemical Society*, 141(47):18877–18889, nov 2019.

[256] Claire L. McMullin, Jesús Jover, Jeremy N. Harvey, and Natalie Fey. Accurate modelling of Pd(0) + PhX oxidative addition kinetics. *Dalton Transactions*, 39(45):10833–10836, nov 2010.

[257] Mårten Ahlquist and Per Ola Norrby. Oxidative addition of aryl chlorides to monoligated palladium(0): A DFT-SCRF study. *Organometallics*, 26(3):550–553, jan 2007.

[258] Hans Martin Senn and Tom Ziegler. Oxidative addition of aryl halides to palladium(0) complexes: A density-functional study including solvation. *Organometallics*, 23(12):2980–2988, jun 2004.

[259] Christophe Coperet, Christopher P. Gordon, and Myuto Kashihara. Reactivity of substituted benzenes toward oxidative addition relates to NMR chemical shift of the ipso-carbon. *Organic Letters*, 22(22):8910–8915, nov 2020.

[260] Bert U.W. Maes, Stefan Verbeeck, Tom Verhelst, Audrey Ekomié, Niklas Von Wolff, Guillaume Lefèvre, Emily A. Mitchell, and Anny Jutand. Oxidative Addition of Haloheteroarenes to Palladium(0): Concerted versus SNAr-Type Mechanism. *Chemistry – A European Journal*, 21(21):7858–7865, may 2015.

[261] Emily A. Mitchell, Philip G. Jessop, and Michael C. Baird. A kinetics study of the oxidative addition of bromobenzene to Pd(PCy 3)2 (Cy = cyclohexyl) in a nonpolar medium: The influence on rates of added PCy3 and bromide ion. *Organometallics*, 28(23):6732–6738, dec 2009.

[262] Fabiola Barrios-Landeros, Brad P. Carrow, and John F. Hartwig. Effect of ligand steric properties and halide identity on the mechanism for oxidative addition of haloarenes to trialkylphosphine Pd(0) complexes. *Journal of the American Chemical Society*, 131(23):8141–8154, jun 2009.

[263] Moshe Portnoy and David Milstein. Mechanism of Aryl Chloride Oxidative Addition to Chelated Palladium(0) Complexes. *Organometallics*, 12(5):1665–1673, 1993.

[264] Yuning Shen, Julia E. Borowski, Melissa A. Hardy, Richmond Sarpong, Abigail G. Doyle, and Tim Cernak. Automation and computer-assisted planning for chemical synthesis. *Nature Reviews Methods Primers 2021 1:1*, 1(1):1–23, mar 2021.

[265] Cherumuttathu H. Suresh, P. Alexander, K. Periya Vijayalakshmi, P. K. Sajith, and Shridhar R. Gadre. Use of molecular electrostatic potential for quantitative assessment of inductive effect. *Physical Chemistry Chemical Physics*, 10(43):6492–6499, nov 2008.

[266] Fareed Bhasha Sayyed and Cherumuttathu H. Suresh. Quantification of substituent effects using molecular electrostatic potentials: Additive nature and proximity effects. *New Journal of Chemistry*, 33(12):2465–2471, dec 2009.

[267] Geetha S. Remya and Cherumuttathu H. Suresh. Quantification and classification of substituent effects in organic chemistry: A theoretical molecular electrostatic potential study. *Physical Chemistry Chemical Physics*, 18(30):20615–20626, jul 2016.

[268] Stephanie A. Grimmel and Markus Reiher. The electrostatic potential as a descriptor for the protonation propensity in automated exploration of reaction mechanisms. *Faraday Discussions*, 220(0):443–463, dec 2019.

[269] Shridhar R. Gadre, Cherumuttathu H. Suresh, and Neetha Mohan. Electrostatic potential topology for probing molecular structure, bonding and reactivity. *Molecules*, 26(11):3289, may 2021.

[270] Ernest L. Eliel and Samuel H. Wilen. Topics in Stereochemistry. *Topics in Stereochemistry*, 20:1–344, 2007.

[271] Johanna Klein, Hassan Khartabil, Jean Charles Boisson, Julia Contreras-Garciá, Jean Philip Piquemal, and Eric Hénon. New Way for Probing Bond Strength. *Journal of Physical Chemistry A*, 124(9):1850–1860, mar 2020.

[272] Bai Amutha Anjali and Cherumuttathu H. Suresh. Interpreting Oxidative Addition of Ph-X (X = CH3, F, Cl, and Br) to Monoligated Pd(0) Catalysts Using Molecular Electrostatic Potential. *ACS Omega*, 2(8):4196–4206, aug 2017.

[273] Gilian T. Thomas, Sofia Donnecke, Irina Paci, and J. Scott McIndoe. Trichloro(Dinitrogen)Platinate(II). *Chemistry - A European Journal*, 26(54):12359–12362, sep 2020.

[274] W. C. Zeise. Von der Wirkung zwischen Platinchlorid und Alkohol, und von den dabei entstehenden neuen Substanzen. *Annalen der Physik*, 97(4):497–541, jan 1831.

[275] L B Hunt. The First Organometallic Compounds. *Platinum Metals Review*, 28(2):76–83, 1984.

[276] M. Black, R. H. B. Mais, and P. G. Owston. The crystal and molecular structure of Zeise's salt, KPtCl3.C2H4.H2O. *Acta Crystallographica Section B Structural Crystallography and Crystal Chemistry*, 25(9):1753–1759, sep 1969.

[277] Richard A. Love, Robert Bau, Thomas F. Koetzle, Graheme J.B. Williams, and Lawrence C. Andrews. Neutron Diffraction Study of the Structure of Zeise's Salt, KPtCl3(C2H4).H2O. *Inorganic Chemistry*, 14(11):2653–2657, nov 1975.

[278] Otto J. Scherer and Andreas Nahrstedt. Synthesis of a Zeise Salt Derivative with a Phosphorus Nitrogen Ylide as Chelate Ligand. *Angewandte Chemie International Edition in English*, 18(3):234–235, mar 1979.

[279] Alexander Weninger, Daniel Baecker, Victoria Obermoser, Dorothea Egger, Klaus Wurst, and Ronald Gust. Synthesis and Biological Evaluation of Zeise's Salt Derivatives with Acetylsalicylic Acid Substructure. *International Journal of Molecular Sciences 2018, Vol. 19, Page 1612*, 19(6):1612, may 2018.

[280] Sandra Meieranz, Maria Stefanopoulou, Gerhard Rubner, Kerstin Bensdorf, Dominic Kubutat, William S. Sheldrick, and Ronald Gust. Untersuchungen zur biologischen Aktivität des Zeise-Salzes und seiner Derivate. *Angewandte Chemie*, 127(9):2876–2879, feb 2015.

[281] Gary A. Foulds and David A. Thornton. Application of spectroscopic techniques to substituted aniline derivatives of Zeise's salt. *Journal of Molecular Structure*, 98(3-4):309–314, apr 1983.

[282] Jingwei Luo, Yang Wu, Harmen S. Zijlstra, David A. Harrington, and J. Scott McIndoe. Mass transfer and convection effects in small-scale catalytic hydrogenation. *Catalysis Science Technology*, 7(12):2609–2615, jun 2017.

[283] Jingwei Luo, Robin Theron, Laura J. Sewell, Thomas N. Hooper, Andrew S. Weller, Allen G. Oliver, and J. Scott McIndoe. Rhodium-Catalyzed Selective Partial Hydrogenation of Alkynes. *Organometallics*, 34(12):3021–3028, jun 2015.

[284] D. E. Harrison and H. Taube. The Formation of Ru(NH3)5N22+ in Aqueous Solution by Direct Action of Molecular Nitrogen. *Journal of the American Chemical Society*, 89(22):5706–5707, oct 1967.

[285] M. Hidai, K. Tominari, Y. Uchida, and A. Misono. A trans-dinitrogen complex of molybdenum. *Journal of the Chemical Society D: Chemical Communications*, (23):1392–1392, jan 1969.

[286] B. Bell, J. Chatt, and G. J. Leigh. A new route to hydride, carbonyl, and bis-dinitrogen complexes of tungsten. *Journal of the Chemical Society D: Chemical Communications*, (13):842a–842a, jan 1970.

[287] J. Chatt, J. R. Dilworth, and G. J. Leigh. A series of nitrogen complexes of rhenium(I). *Journal of the Chemical Society D: Chemical Communications*, (13):687–688, jan 1969.

[288] A. Yamamoto, S. Kitazume, L. S. Pu, and S. Ikeda. Study of the fixation of nitrogen. Isolation of tris(triphenylphosphine)cobalt complex co-ordinated with molecular nitrogen. *Chemical Communications (London)*, (2):79–80, jan 1967.

[289] Samuel M. Bhutto and Patrick L. Holland. Dinitrogen Activation and Functionalization Using β-Diketiminate Iron Complexes. *European Journal of Inorganic Chemistry*, 2019(14):1861–1869, apr 2019.

[290] Patrick L. Holland. Metal-dioxygen and metal-dinitrogen complexes: Where are the electrons? *Dalton Transactions*, 39(23):5415–5425, jun 2010.

[291] Amanda C. Bowman, Carsten Milsmann, Crisita Carmen Hojilla Atienza, Emil Lobkovsky, Karl Wieghardt, and Paul J. Chirik. Synthesis and molecular and electronic structures of reduced bis(imino)pyridine cobalt dinitrogen complexes: Ligand versus metal reduction. *Journal of the American Chemical Society*, 132(5):1676–1684, feb 2010.

[292] Joseph Chatt, Jonathan R. Dilworth, and Raymond L. Richards. Recent Advances in the Chemistry of Nitrogen Fixation. *Chemical Reviews*, 78(6):589–625, 1978.

[293] Erli Lu, Benjamin E. Atkinson, Ashley J. Wooles, Josef T. Boronski, Laurence R. Doyle, Floriana Tuna, Jonathan D. Cryer, Philip J. Cobb, Inigo J. Vitorica-Yrezabal, George F.S. Whitehead, Nikolas Kaltsoyannis, and Stephen T. Liddle. Back-bonding between an electron-poor, high-oxidation-state metal and poor π-acceptor ligand in a uranium(v)–dinitrogen complex. *Nature Chemistry*, 11(9):806–811, aug 2019.

[294] Christopher M. Kozak and Philip Mountford. Revelations in dinitrogen activation and functionalization by metal complexes, feb 2004.

[295] William J. Evans, Tamara A. Ulibarri, and Joseph W. Ziller. Isolation and X-ray Crystal Structure of the First Dinitrogen Complex of an f-Element Metal, [(C5Me5)2Sm]2N2. *Journal of the American Chemical Society*, 110(20):6877–6879, 1988.

[296] Dieter Sellmann. Dinitrogen-Transition Metal Complexes: Synthesis, Properties, and Significance. *Angewandte Chemie International Edition in English*, 13(10):639–649, oct 1974.

[297] Erin A. MacLachlan and Michael D. Fryzuk. Synthesis and reactivity of side-on-bound dinitrogen metal complexes. *Organometallics*, 25(7):1530–1543, mar 2006.

[298] Frank B. Simpson and Robert H. Burris. A nitrogen pressure of 50 atmospheres does not prevent evolution of hydrogen by nitrogenase. *Science*, 224(4653):1095–1097, 1984.

[299] Hannah L. Rutledge and F. Akif Tezcan. Electron Transfer in Nitrogenase, jun 2020.

[300] Douglas C. Rees and James B. Howard. Nitrogenase: Standing at the crossroads, oct 2000.

[301] Barbara K. Burgess and David J. Lowe. Mechanism of molybdenum nitrogenase. *Chemical Reviews*, 96(7):2983–3011, 1996.

[302] JCS Dalton, By J K Burdett, M A Graham, J J Turner, A D Allen, F Bottomley, Accounts Chem Research, Yu G Borod, A E Shilov, J K Burdett, Chem Comm, G Blyholder, and J D Richardson. Binary compounds of dinitrogen

with nickel, chromium, platinum, and copper: a vibrational investigation of the metal–dinitrogen linkage. *Journal of the Chemical Society, Dalton Transactions*, (15):1620–1625, jan 1972.

[303] Angelo Citra, Xuefeng Wang, William D. Bare, and Lester Andrews. Reactions of laser-ablated platinum with nitrogen: Matrix infrared spectra of platinum nitride, complexes, and anions. *Journal of Physical Chemistry A*, 105(33):7799–7811, aug 2001.

[304] E P Kundig, M Moskovits, A N D, and G A Ozin. Binary Transition Metal Dinitrogen Complexes. Part II. Matrix Infrared and Raman Spectra, Structure, and Bonding of Pt(N2)n (where n=1–3). *https://doi.org/10.1139/v73-407*, 51(16):2710–2721, aug 2011.

[305] G. A. Ozin and W. E. Klotzbuecher. Binary Mixed Dioxygen Dinitrogen Complexes of Nickel, Palladium, and Platinum, (O2)M(N2)n (where M = Ni, Pd, or Pt; n = 1 or 2). *Journal of the American Chemical Society*, 97(14):3965–3974, jul 1975.

[306] Matthew J. Chalkley, Marcus W. Drover, and Jonas C. Peters. Catalytic N2-to-NH3(or -N2H4) Conversion by Well-Defined Molecular Coordination Complexes. *Chemical Reviews*, 120(12):5582–5636, jun 2020.

[307] Sebastian Kozuch, David Gruzman, and Jan M.L. Martin. DSD-BLYP: A general purpose double hybrid density functional including spin component scaling and dispersion correction. *Journal of Physical Chemistry C*, 114(48):20801–20808, dec 2010.

[308] Thomas Wyttenbach, Gert Von Helden, Joseph J. Batka, Douglas Carlat, and Michael T. Bowers. Effect of the long-range potential on ion mobility measurements. *Journal of the American Society for Mass Spectrometry*, 8(3):275–282, mar 1997.

[309] G. Reid Asbury and Herbert H. Hill. Using different drift gases to change separation factors (a) in ion mobility spectrometry. *Analytical Chemistry*, 72(3):580–584, 2000.

[310] Kristyn M. Roscioli, Xing Zhang, Shelly X. Li, Gilles H. Goetz, Guilong Cheng, Zhongli Zhang, William F. Siems, and Herbert H. Hill. Real time

pharmaceutical reaction monitoring by electrospray ion mobility-mass spectrometry. *International Journal of Mass Spectrometry*, 336:27–36, feb 2013.

[311] Helko Borsdorf and Gary A. Eiceman. Ion mobility spectrometry: Principles and applications. *Applied Spectroscopy Reviews*, 41(4):323–375, 2006.

[312] Abu B. Kanu, Prabha Dwivedi, Maggie Tam, Laura Matz, and Herbert H. Hill. Ion mobility–mass spectrometry. *Journal of Mass Spectrometry*, 43(1):1–22, jan 2008.

[313] Nicole J. Rijs, Thomas Weiske, Maria Schlangen, and Helmut Schwarz. Effect of Adduct Formation with Molecular Nitrogen on the Measured Collisional Cross Sections of Transition Metal-1,10-Phenanthroline Complexes in Traveling Wave Ion-Mobility Spectrometry: N2 Is Not Always an ”Inert” Buffer Gas. *Analytical Chemistry*, 87(19):9769–9776, sep 2015.

[314] Priscila M. Lalli, Bernardo A. Iglesias, Henrique E. Toma, Gilberto F. De Sa, Romeu J. Daroda, Juvenal C. Silva Filho, Jan E. Szulejko, Koiti Araki, and Marcos N. Eberlin. Protomers: formation, separation and characterization via travelling wave ion mobility mass spectrometry. *Journal of Mass Spectrometry*, 47(6):712–719, jun 2012.

[315] Z. Karpas, M. J. Cohen, R. M. Stimac, and R. F. Wernlund. On the effects of structure and charge distribution on the mobility of ions. *International Journal of Mass Spectrometry and Ion Processes*, 74(2-3):153–159, dec 1986.

[316] J. Chatt. Molecular nitrogen as a ligand. *Pure and Applied Chemistry*, 24(2):425–442, jan 1970.

[317] Mariusz Mitoraj and Artur Michalak. Donor-acceptor properties of ligands from the natural orbitals for chemical valence. *Organometallics*, 26(26):6576–6580, dec 2007.

[318] Christina Y. Tang, Amber L. Thompson, and Simon Aldridge. Dehydrogenation of saturated CC and BN bonds at cationic N-heterocyclic carbene stabilized M(III) centers (M = Rh, Ir). *Journal of the American Chemical Society*, 132(30):10578–10591, aug 2010.

[319] Hongyun Fang, Yoong Kee Choe, Yonghua Li, and Shigeru Shimada. Synthesis, Structure, and Reactivity of Hydridoiridium Complexes Bearing a Pincer-Type PSiP Ligand. *Chemistry – An Asian Journal*, 6(9):2512–2521, sep 2011.

[320] Inigo Göttker-Schnetmann, Peter S. White, and Maurice Brookhart. Synthesis and Properties of Iridium Bis(phosphinite) Pincer Complexes (p-XPCP)IrH 2, (p-XPCP)Ir(CO), (p-XPCP)Ir(H)(aryl), and (p-XPCP)IrH 2μ-N 2 and Their Relevance in Alkane Transfer Dehydrogenation. *Organometallics*, 23(8):1766–1776, apr 2004.

[321] Tiedong Guo, Robert L Taylor, Ravinder J Singh, and Steven J Soldin. Simultaneous determination of 12 steroids by isotope dilution liquid chromatography-photospray ionization tandem mass spectrometry. *Clinica Chimica Acta*, 372(1-2):76–82, 2006.

[322] Arthur I. Shirley and Norberto O. Lemcoff. High-Purity Nitrogen by Pressure-Swing Adsorption. *AIChE Journal*, 43(2):419–424, feb 1997.

[323] Charles S. Christ, John R. Eyler, and David E. Richardson. Insertion, Adduct Formation, and Elimination of Alkenes in Gas-Phase Reactions of Bis(η5-cyclopentadienyl)methylzirconium(1+) with Nitriles. *Journal of the American Chemical Society*, 112(12):4778–4787, 1990.

[324] Charles S. Christ, John R. Eyler, and David E. Richardson. Insertion and σ-Bond Metathesis Pathways in Gas-Phase Reactions of Bis(η5-cyclopentadienyl)methylzirconium(1+) with Dihydrogen and Unsaturated Hydrocarbons. *Journal of the American Chemical Society*, 112(2):596–607, 1990.

[325] Charles S. Christ, John R. Eyler, and David E. Richardson. Gas-Phase Reactions of Bis(η5-cyciopentadienyl)methylzirconium(1+) with Dihydrogen, Ethylene, and Propylene. *Journal of the American Chemical Society*, 110(12):4038–4039, 1988.

[326] D. Feichtinger, D. A. Plattner, and P. Chen. Ziegler-Natta-like tiefin oligomerization by alkylzirconocene cations in an electrospray ionization tandem mass spectrometer [13], jul 1998.

[327] Chris R.L. Chapman, Elvis C.M. Ting, Ashley Kereszti, and Irina Paci. Self-assembly of cysteine dimers at the gold surface: A computational study of competing interactions. *Journal of Physical Chemistry C*, 117(38):19426–19435, sep 2013.

[328] Christopher K. Barlow, Adam Wright, Christopher J. Easton, and Richard A.J. O'Hair. Gas-phase ion-molecule reactions using regioselectively generated radical cations to model oxidative damage and probe radical sites in peptides. *Organic and Biomolecular Chemistry*, 9(10):3733–3745, may 2011.

[329] Olaf Böge, Anke Mutzel, Yoshiteru Iinuma, Pasi Yli-Pirilä, Ariane Kahnt, Jorma Joutsensaari, and Hartmut Herrmann. Gas-phase products and secondary organic aerosol formation from the ozonolysis and photooxidation of myrcene. *Atmospheric Environment*, 79:553–560, nov 2013.

[330] Sharon J. Nieter Burgmayer. Use of a Titanium Metallocene as a Colorimetric Indicator for Learning Inert Atmosphere Techniques. *Journal of Chemical Education*, 75(4):460, apr 1998.

[331] Darien Yeung, Johanne Penafiel, Harmen S. Zijlstra, and J. Scott McIndoe. Oxidation of Titanocene(III): The Deceptive Simplicity of a Color Change. *Inorganic Chemistry*, 57(1):457–461, jan 2018.

[332] James McFarlane, Brett Henderson, Sofia Donnecke, and J. Scott McIndoe. An Information-Rich Graphical Representation of Catalytic Cycles. *Organometallics*, 38(21):4051–4053, nov 2019.

[333] A Zecchina and S Califano. The Development of Catalysis: A History of Key Processes and Personas in Catalytic Science and Technology by Adriano Zecchina and Salvatore Califano. *MRS Bulletin*, 43(4):309–309, 2018.

[334] Andrew J. Medford, Poul Georg Moses, Karsten Wedel Jacobsen, and Andrew A. Peterson. A Career in Catalysis: Jens Kehlet Nørskov. *ACS Catalysis*, 12(15):9679–9689, aug 2022.

[335] Venkadesh Balakrishnan, Vetrivelan Murugesan, Bincy Chindan, and Ramesh Rasappan. Attenuation of Ni(0) Decomposition: Mechanistic In-

sights into AgF-Assisted Nickel-Mediated Silylation. *Inorganic Chemistry*, 61(3):1438–1446, jan 2022.

[336] He Xin Xiao, Wan Yun Hsu, Siou Wei Liang, Yingjie Guo, Wan Ching Lee, I. Chung Lu, and Yu Chang Chang. Bulky Di(1-adamantyl)phosphinous Acid-Ligated Pd(II) Precatalysts for Suzuki Reactions of Unreactive Aryl Chlorides. *ACS Omega*, 6(50):35134–35143, dec 2021.

[337] Samantha M. Brewer, Timothy M. Schwartz, Magy A. Mekhail, Lara S. Turan, Timothy J. Prior, Timothy J. Hubin, Benjamin G. Janesko, and Kayla N. Green. Mechanistic Insights into Iron-Catalyzed C-H Bond Activation and C-C Coupling. *Organometallics*, 40(15):2467–2477, aug 2021.

[338] Swathi Swaminathan, Jitendra K. Bera, and Manabendra Chandra. Simultaneous Harvesting of Multiple Hot Holes via Visible-Light Excitation of Plasmonic Gold Nanospheres for Selective Oxidative Bond Scission of Olefins to Carbonyls. *Angewandte Chemie International Edition*, 62(7):e202215933, feb 2023.

[339] Isaac Omari, Mathias Paul, and J. Scott McIndoe. Standardized Stirring for Small Scale Surveys. *Chemistry - Methods*, 1(3):173–176, mar 2021.

[340] Mathias Paul, Katarina Laketic, and J. Scott McIndoe. Disulfonated xantphos for mass spectrometric mechanistic analysis. *Canadian Journal of Chemistry*, 99(2):87–92, 2021.

[341] Lars P.E. Yunker, Sofia Donnecke, Michelle Ting, Darien Yeung, and J. Scott McIndoe. PythoMS: A Python Framework to Simplify and Assist in the Processing and Interpretation of Mass Spectrometric Data. *Journal of Chemical Information and Modeling*, 59(4):1295–1300, apr 2019.

Appendix A

Additional Information

A.0.1 Surface simulations

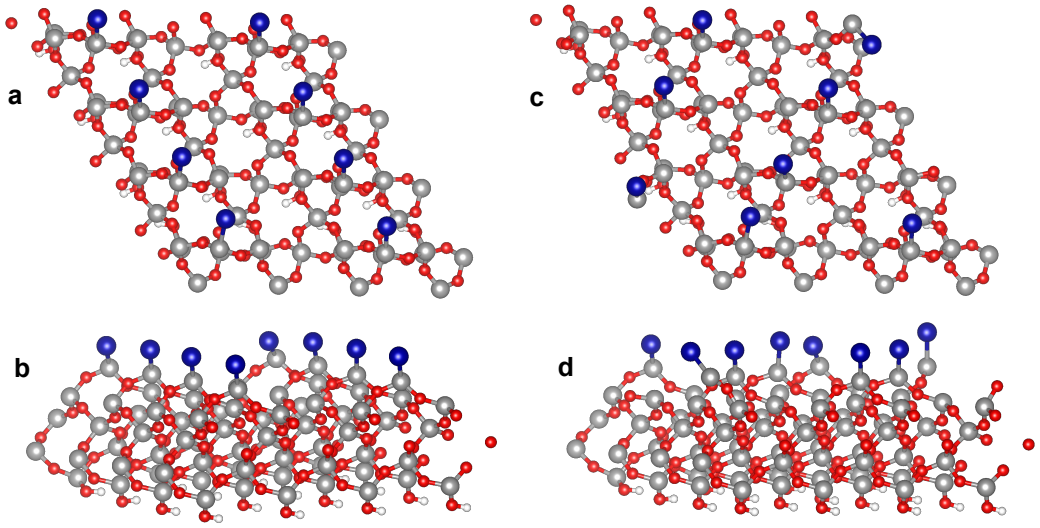

Figure A.1: Surface coverage for the initial layer of Co. As OH groups are bound, the surface becomes less repulsive (Figure 14). Next steps would be to test whether Pathway B is still preferred after the initial layer of OH is occupied.

A.0.2 ORR supplementary data

Bond lengths and angles from ORR pathways

(100)surface	literature	SIESTA optimized
Cu	a=3.61	a=3.73
Co	a=2.51, c=4.07	a=2.49, c=4.15
Si	a = 5.43	a=5.30
SiO_2	a=4.91, c=5.40	a=5.17, c=5.40

Table A.1: Optimized lattice parameters for the Cu, Si and SiO_2(100) surfaces compared to crystallographic literature values. Optimizations were performed with SIESTA as described in 4.

metal	abbreviated catalyst	full catalyst
Mn	323.8	10704.5
Co	752.5‡	2602.7
Ni	1094.6	7592.1
Fe	1874.8	15736.3

‡ 2 nodes with 40 cores were allocated rather than 4 nodes.

Table A.2: Walltimes in seconds for the final optimization step in the DFT calculations of abbreviated and full phthalocyanine catalysts.

method	O−O
lit[248]	**1.2075**
PBE	1.243
PBE0	1.193
B3LYP	1.204
B2PLYP	1.214

Table A.3: O_2 bond lengths in Angstroms. Note PBE results were paired with a TZP basis set and vdW-TS dispersion corrections as discussed in the methodology section.

Step 1 M−O

metal	slab	phthalo	a. phthalo	porph
Mn	2.001	2.188	2.206	2.171
Co	2.030	2.562	2.374	2.510
Ni	2.452	3.515	3.427	3.255
Fe	1.906	3.367	3.229	3.152

atom	PBE	PBE0	B3LYP	B2PLYP
Mn	2.129	2.061	2.081	2.071
Co	1.832	1.980	2.010	1.974
Ni	1.881	1.891	1.897	1.890
Fe	1.988	1.973	1.987	1.985

Step 1 O−O

metal	slab	phthalo	a. phthalo	porph
Mn	1.310	1.284	1.281	1.289
Co	1.280	1.193	1.196	1.194
Ni	1.264	1.193	1.193	1.193
Fe	1.319	1.193	1.193	1.193

atom	PBE	PBE0	B3LYP	B2PLYP
Mn	1.374	1.317	1.332	1.353
Co	1.326	1.301	1.312	1.343
Ni	1.315	1.323	1.341	1.360
Fe	1.390	1.318	1.335	1.355

Table A.4: Step 1 bond lengths reported in Angstroms. The upper sections tabulate values for periodic, phthalocyanine, abbreviated phthalocyanine (a. phthalo) and porphyrin catalysts while the lower half reports the values for single atom pathways optimized with different DFT functionals.

Step 1 M−O−O°

metal	slab	phthalo	a. phthalo	porph
Mn	121.6	72.9	73.1	72.7
Co	118.3	119.6	120.5	119.8
Ni	116.2	109.8	107.0	108.7
Fe	118.2	107.0	107.4	108.2

atom	PBE	PBE0	B3LYP	B2PLYP
Mn	71.2	71.4	71.3	71.0
Co	120.2	70.9	71.0	70.2
Ni	115.5	69.5	69.3	69.1
Fe	69.7	70.5	70.4	70.0

Table A.5: Step 1 M−O−O bond angles. The upper sections tabulate values for periodic, phthalocyanine, abbreviated phthalocyanine (a. phthalo) and porphyrin catalysts while the lower half reports the values for single atom pathways optimized with different DFT functionals.

Step 2 M−OOH

metal	slab	phthalo	a. phthalo	porph
Mn	1.941	1.943	1.950	1.864
Co	1.901	1.904	1.864	1.944
Ni	2.134	3.127	3.072	2.236
Fe	1.914	1.886	1.891	1.894

atom	PBE	PBE0	B3LYP	B2PLYP
Mn	2.002	1.941	1.952	1.957
Co	1.811	1.803	1.814	1.873
Ni	1.847	1.768	1.771	1.822
Fe	1.944	1.842	1.851	1.860

Step 2 MO−OH

metal	slab	phthalo	a. phthalo	porph
Mn	1.473	1.423	1.423	1.431
Co	1.439	1.359	1.375	1.372
Ni	1.425	1.308	1.308	1.302
Fe	1.482	1.410	1.413	1.417

atom	PBE	PBE0	B3LYP	B2PLYP
Mn	1.528	1.465	1.490	1.504
Co	1.500	1.423	1.443	1.491
Ni	1.482	1.436	1.460	1.516
Fe	1.514	1.433	1.454	1.481

Table A.6: Step 2 bond lengths reported in Angstroms. The upper sections tabulate values for periodic, phthalocyanine, abbreviated phthalocyanine (a. phthalo) and porphyrin catalysts while the lower half reports the values for single atom pathways optimized with different DFT functionals.

Step 2 M−O−OH°

metal	slab	phthalo	a. phthalo	porph
Mn	102.4	111.3	110.9	109.8
Co	112.8	114.2	113.4	113.4
Ni	112.6	93.0	90.5	108.7
Fe	101.0	113.1	112.6	111.9

atom	PBE	PBE0	B3LYP	B2PLYP
Mn	79.1	79.1	79.4	78.1
Co	109.7	115.0	116.5	77.8
Ni	109.2	111.0	111.3	77.2
Fe	80.8	110.0	112.0	99.2

Table A.7: Step 2 M−O−O bond angles. The upper sections tabulate values for periodic, phthalocyanine, abbreviated phthalocyanine (a. phthalo) and porphyrin catalysts while the lower half reports the values for single atom pathways optimized with different DFT functionals.

Step 3 M−O

metal	slab	phthalo	a. phthalo	porph
Mn	1.707	1.624	1.627	1.622
Co	1.685	1.736	1.740	1.727
Ni	1.782	1.963	1.969	1.708
Fe	1.700	1.742	1.912	1.608

atom	PBE	PBE0	B3LYP	B2PLYP
Mn	1.697	1.627	1.633	1.586
Co	1.671	1.579	1.590	1.580
Ni	1.710	1.614	1.626	1.618
Fe	1.662	1.600	1.610	1.554

Table A.8: Step 3 bond lengths reported in Angstroms. The upper section tabulates values for periodic, phthalocyanine, abbreviated phthalocyanine (a. phthalo) and porphyrin catalysts while the lower half reports the values for single atom pathways optimized with different DFT functionals.

Step 4 M−OH				
metal	**slab**	**phthalo**	**a. phthalo**	**porph**
Mn	1.903	1.774	1.901	1.901
Co	1.913	1.897	1.848	1.784
Ni	2.028	1.965	1.972	1.952
Fe	1.860	1.868	1.864	1.770

atom	**PBE**	**PBE0**	**B3LYP**	**B2PLYP**
Mn	1.893	1.839	1.844	1.849
Co	1.810	1.773	1.783	1.770
Ni	1.823	1.791	1.765	1.791
Fe	1.853	1.798	1.806	1.807

Table A.9: Step 4 bond lengths reported in Angstroms. The upper section tabulates values for periodic, phthalocyanine, abbreviated phthalocyanine (a. phthalo) and porphyrin catalysts while the lower half reports the values for single atom pathways optimized with different DFT functionals.

Appendix B

Additional Information

B.0.1 Input files

Orca input file example

```
! RI-B2PLYP D3 def2-TZVP def2-TZVP/C TIGHTSCF Opt Grid3 FinalGrid5
%scf
  MaxIter 550
end
%maxcore 3000
%pal
nprocs 40
end
*xyzfile 0 1 input.xyz
```

An NWChem input file example

The following input performs a PBE0/def2-TZVP geometry optimization followed by a single point calculations with a def2-TZVPPD basis set.

```
echo
start phthalo
title "phthalo PBE0"

memory total 3600 mb
```

```
permanent_dir ./perm
scratch_dir    ./perm

geometry units angstroms autosym
 load input.xyz
end

basis spherical
 * library def2-TZVP
end

dft
 direct
 cgmin
 odft
 xc pbe0
 mult 6
 disp vdw 4
 print low
 convergence fast
 iterations 501
end

scf
 print low
 semidirect memsize 100000000 filesize 0
end

driver
 maxiter 350
 xyz pbe0
end

task dft optimize
```

```
basis spherical
 * library def2-TZVPD
end
dft
  tolerances tight
  grid fine
end
task dft energy
```

B.0.2 SIESTA scripts

Generate SIESTA input

The following script was written to generate a set of siesta input files from an xyz and cell vectors file.

```
#!/cvmfs/soft.computecanada.ca/nix/var/nix/profiles/16.09/bin/python
import os
from shutil import copyfile as cp
import sys
import glob
import numpy as np
import pandas as pd
from itertools import combinations

sys.path.append("/home/i/ipaci/donnecke/pyscripts")
df=pd.read_csv('/home/i/ipaci/donnecke/pyscripts/tablegrimme.csv', sep

#element library
DIK = {
        "Co" : 27,
        "Si" : 14,
        "O" : 8,
        "H" : 1,
        "F" : 9,
```

```
        "C" : 6,
        "Cu" : 29,
        "N" : 7,
        "P" : 15,
        "S" : 16,
        "Cl" : 17,
        "Zr" : 40,
        "Pd" : 46,
        "Br" : 35,
        "Fe" : 26,
        "Ni" : 28,
        "Mn" : 25
        }

def getspeciesblock(species):
    block = ""
    keys = list(species.keys())
    keys.sort()
    for key in keys:
        block += species[key] + "\t" + str(DIK[key]) + "\t" + key + "\n
    return block

def getgrimmeline(a1,n1,a2,n2,a1screen=False,a2screen=False):
    if a1screen:
        a1_c6 = df[df['Element']==a1]['C6scr'].values[0]
        a1_r0 = df[df['Element']==a1]['R0scr'].values[0]
    else:
        a1_c6 = df[df['Element']==a1]['C6'].values[0]
        a1_r0 = df[df['Element']==a1]['R0'].values[0]
    if a2screen:
        a2_c6 = df[df['Element']==a2]['C6scr'].values[0]
        a2_r0 = df[df['Element']==a2]['R0scr'].values[0]
    else:
        a2_c6 = df[df['Element']==a2]['C6'].values[0]
        a2_r0 = df[df['Element']==a2]['R0'].values[0]
```

```
    pairC6 = np.sqrt(a1_c6*a2_c6)
    pair_R0 = (a1_r0+a2_r0)
    return "\t".join([str(n1), str(n2),"Grimme", "{:.2f}".format(pairC6

def getgrimmeblock(species):
    block = []
    pairs = list(combinations(species.keys(), 2))
    Co_screen = False
    Cu_screen = False
    for key in species.keys():
        if key == "Co":
            screen = "n" #input("is {} screened y/n? ".format(key))
            Co_screen = (screen == "y")
        elif key == "Cu":
            screen = "n" #input("is {} screened y/n? ".format(key))
            Cu_screen = (screen == "y")
    for key in species.keys():
        pairs.append((key, key))
    for pair in pairs:
        screen1, screen2 = False, False
        if pair[0] == "Cu":
            screen1 = Cu_screen
        if pair[1] == "Cu":
            screen2 = Cu_screen
        if pair[0] == "Co":
            screen1 = Co_screen
        if pair[1] == "Co":
            screen2 = Co_screen
        block.append(getgrimmeline(pair[0], species[pair[0]], pair[1],
    return "\n".join(block)

#user inputs
print("Default cell coor is 30.0 A cube")
sysname = 'job' #input("System Name: ")
```

```
dench = 'n' #input("Print WFS? (y/n): ")
if dench == "y":
    mini = input("Minimum Orbital: ")
    maxi = input("Maximum Orbital: ")
    denchar = "WriteDenchar .true.\nWriteDM.NetCDF .true.\nWriteDMHS.N
else:
    denchar = ""

#freeze atoms
freez = 'n'# input("freeze atoms(y/n): ")
if freez == "y":
    starts = input("starting from atom: ")
    ends = input("ending at atom: ")
    freeze = "%block GeometryConstraints\n     position from {} to {}\n%
else:
    freeze = ""

typerun = "CG" #input("TypeOfRun(CG or nose): ")
if typerun == "nose":
#    length = input("Total time: ")
    steps = input("Time steps: ")
    starttemp = input("initial temp: ")
    target = input("final temp: ")
    md = """
MD.InitialTimeStep 1
MD.FinalTimeStep {}
MD.LengthTimeStep 1 fs
MD.UseSaveXV .true.
MD.InitialTemperature {} K
MD.TargetTemperature {} K""".format(steps, starttemp, target)
else:
    md = ""
netcharge = '0' #input("Net Charge: ")
#spinpol
#spinpol = input("spinpolarized? (true/false) ")
```

```
#CobaltCase
slowconv = 'n' #input("high mixing & Pulay? y/n ")
if slowconv == "y":
    mixing = "0.05"
    pulay = "10"
else:
    mixing = "0.1"
    pulay = "7"
#generate at.coor
xyz = glob.glob('*.xyz')[0]
species = {}
counter = 1
numatoms = 0
with open(xyz, 'r') as f:
    with open("../at.coor", 'w+') as f2:
        for line in f.readlines():
            if len(line.split()) == 4:
                numatoms += 1
                cols = line.split()
                spec = cols[0]
                if spec not in species:
                    species[spec] = str(counter)
                    counter += 1
                f2.write('\t'.join(cols[1:] + [species[spec]]) + '\n')
#generate cell matrix
if os.path.isfile("cell.coor"):
    cp("cell.coor", "../cell.coor")
else:
    with open("../cell.coor", 'w+') as f3:
        f3.write("30.0\t 0.0\t 0.0\n 0.0\t30.0\t 0.0\n 0.0\t 0.0\t30.0

#generate .psf
for key in species.keys():
    cp("/home/i/ipaci/donnecke/pseudopotentials/{}.psf".format(key), "
# copy submission script
```

```
cp("/home/i/ipaci/donnecke/bin/sies.s", "../sies.s")
runtime = 'n' #input("edit pro.s? (y/n): ")
if runtime == "n":
    cp("/home/i/ipaci/donnecke/bin/sies.s", "../sies.s")
else:
    walltime = input("walltime (hrs up to 23): ")
    nodes = input("number of nodes: ")
    with open("../sies.s", "+w") as cedar:
        cedar.write("""#!/bin/bash
#SBATCH --nodes={}
#SBATCH --ntasks-per-node=48
#SBATCH --mem-per-cpu=2048M          # memory; default megabytes
#SBATCH --time=0-{}:00 # time (DD-HH:MM)
#SBATCH --job-name=siesta_job         # Name of job in queue
#SBATCH --output=job_info.out
#SBATCH --account=rrg-ipaci-ab        # group resource allocation

module load StdEnv/2016.4
module load nixpkgs/16.09  intel/2016.4  openmpi/2.1.1
module load siesta/4.0.1
mpiexec siesta <./file.fdf >> ./file.out""".format(nodes, walltime))

print("ready to run!")

foo = """
SystemName          {}
SystemLabel         {}
NumberOfAtoms       {}
NumberOfSpecies     {}
LatticeConstant     1.0 Ang
%block LatticeVectors < cell.coor
%block ChemicalSpeciesLabel
{}
%endblock ChemicalSpeciesLabel
```

```
%block MM.Potentials
{}
%endblock WW.Potentials
MM.Grimme.S6  1.0

AtomicCoordinatesFormat   Ang
%block  AtomicCoordinatesAndAtomicSpecies <  at.coor
{}
{}

MD.TypeOfRun   {}
{}
SpinPolarized  .true.
NetCharge {}
MD.NumCGsteps  1000
MD.VariableCell  .false.
MD.MaxForceTol  0.01  eV/Ang
SCF.DM.Tolerance  0.00001
SolutionMethod  diagon
XC.functional GGA
XC.authors  PBE
PAO.EnergyShift  0.001  Ry
PAO.BasisSize  TZP
Mesh.Cutoff  300  Ry
DM.NumberPulay {}
DM.MixingWeight {}
MaxSCFIterations  500
WriteMullikenPop  1
WriteCoorXmol  .true.
UseSaveData  .true.
Diag.Memory  5.0
WriteMDXmol  .true.
""".format(sysname, sysname, numatoms, len(species.keys()),
getspeciesblock(species), getgrimmeblock(species),freeze  ,denchar,
typerun, md, netcharge, pulay, mixing)
```

```
with open("../file.fdf", 'w+') as f3:
    f3.write(foo)

#submit
import subprocess as sp
submit = input("submit?(y/n): ")
if submit == "y":
    try:
        out = sp.check_output("(cd ... && sbatch sies.s)",stderr=sp.STDO
        print("{} has been submitted as {}".format(sysname, out))
    except sp.CalledProcessError as e:
        print("return code: {}".format(e.returncode))
        print("command: {}".format(e.cmd))
        print("output: {}".format(e.output))
```

Submit a large set of SIESTA jobs

The following bash script submits a list of separate siesta jobs from a directory of starting geometries. Note the naming system must be adjusted to work for the project at hand.

```
#!/bin/bash
module load scipy-stack

#for i in start/*.xyz;      #incase ya messed it up
#         do
#         job=${i:6:-4}
#        rm -r $job
#done

for i in start/*.out;
        do
        job=${i:6:-4}    #clip i down to name of the file for the job
        echo this works $job
        mkdir $job;
```

```
        mkdir $job/clean
        cp start/"$job".xyz "$job"/clean/"$job".xyz;
        cp start/"${job:1:3}"*.coor "$job"/clean/cell.coor;
        cd "$job"/clean;
        python ~/pyscripts/siesta.py
        cd ../..
done
```

Check for convergence and collect SIESTA output

The following script was written for collecting energies, optimized geometries and output files of the completed SIESTA jobs one directory down.

```
#!/bin/bash
module load CCEnv StdEnv/2020
module load scipy-stack

mkdir data
for i in start/*.out;
        do
        job=${i:6:-4}
        cp "$job"/job.xyz data/"$job".xyz
        cp "$job"/file.out data/"$job".out
done

python ~/pyscripts/collect_E.py
```

Extract a specific geometry from a sequence of AIMD xyz files

This script extracts a specified geometry step from an ANI file based on its step number and writes it to a single xyz file.

```
import numpy as np
import glob

ani = glob.glob('*.ANI')[0]
```

```
with open(ani, 'r') as f:
    lines = f.readlines()
    per_geo = int(lines[0])+2
    num_MD_steps = int(len(lines)/(per_geo))
extract = int(input(f"MD step to extract ({num_MD_steps} total)"))
start = (extract*per_geo)-per_geo
stop = (extract*per_geo)

with open(f'{extract}.xyz', 'w+') as f2:
    print(f'extracting lines {start} to {stop}')
    [f2.write(line) for line in lines[start:stop]]
    print(f'extracted geometry stored in "{extract}.xyz"')
```

Plot data from steps along a SIESTA AIMD trajectory.

The following python script obtains the energy and termperature from each snapshot of a SIESTA AIMD trajectory, tabulates the values in text files and plots the data as a scatter plot with twin axes.

```
#!/cvmfs/soft.computecanada.ca/nix/var/nix/profiles/16.09/bin/python
import os

#Temp="siesta: Temp_ion = "
#Energy='siesta: E_KS(eV) ='
if os.path.isfile('E.txt') == False:
    os.system("grep -i 'siesta: Temp_ion =' file.out > temp.txt")
    os.system("grep -i 'siesta: E_KS(eV) =' file.out > E.txt")

#plots Energy and termperature over course of run
import numpy as np
import matplotlib.pyplot as plt

print("PLOTTING EXTRACTED ENERGIES")
with open('E.txt') as f:
    lines = f.readlines()
```

```
    y = [float(line.split()[-1]) for line in lines]

x = np.arange(len(lines))
fig,ax1 = plt.subplots(figsize=(5,5))
ax1.scatter(x,y,color='b',label=f'E')
ax1.set_xlabel('MD-step')
ax1.set_ylabel('Energy (eV)')
ax1.legend(frameon=False)
ax1.set_title(os.getcwd().split('donnecke')[-1])
#overlay = input('overlay? y/n: ')
overlay="n"
if overlay == "y":
    with open('temp.txt') as f:
        lines = f.readlines()
        y2 = [float(line.split()[-2]) for line in lines]

    ax2 = ax1.twinx()
    ax2.scatter(x,y2,color='r',alpha=0.5,label='Temp')
    ax2.legend(loc='lower right',frameon=False)
    ax2.set_ylabel('Temp (K)')
    print("TEMP PLOTTED")
save = input("save figure as 'fig.png'? ")
if save == "y":
    plt.savefig("fig.png",dpi=500, transparent = True)
plt.show()
```